Strojniški vestnik
Journal of Mechanical Engineering

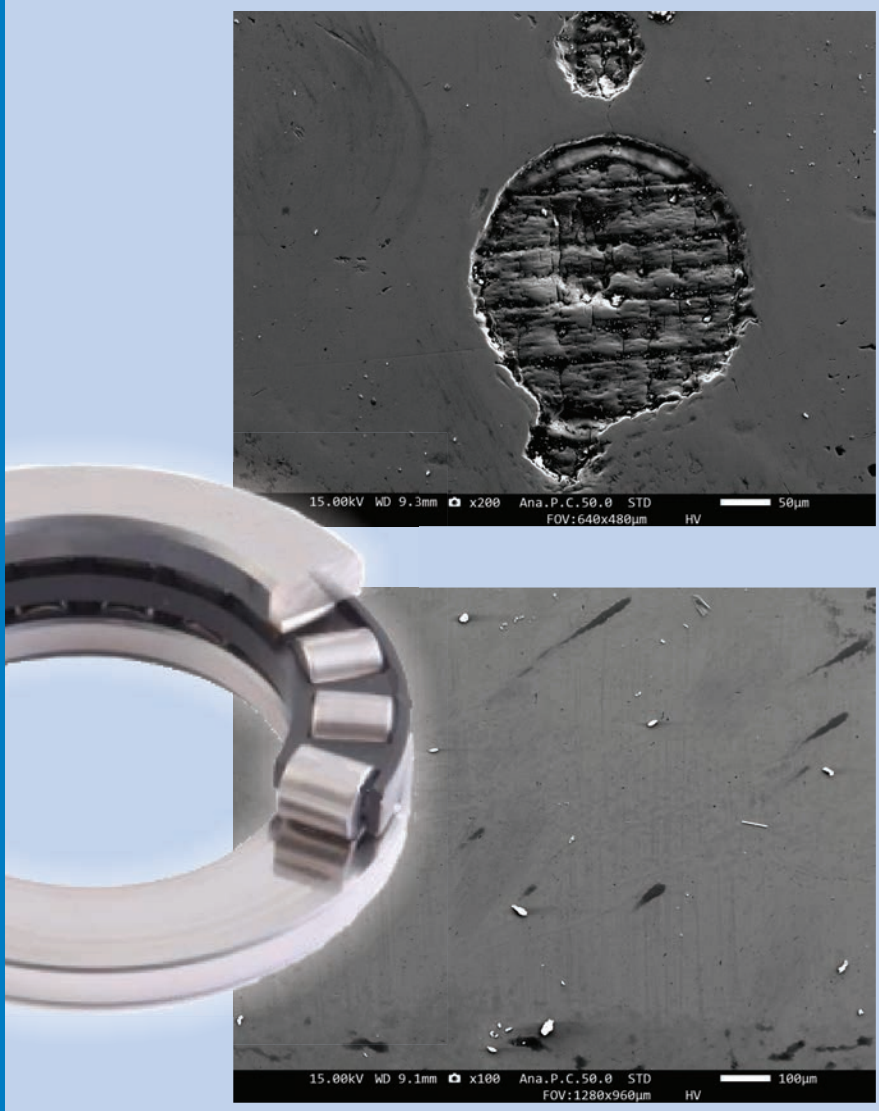

no. 3-4
year 2023
volume 69

Strojniški vestnik – Journal of Mechanical Engineering (SV-JME)

Aim and Scope
The international journal publishes original and (mini)review articles covering the concepts of materials science, mechanics, kinematics, thermodynamics, energy and environment, mechatronics and robotics, fluid mechanics, tribology, cybernetics, industrial engineering and structural analysis.
The journal follows new trends and progress proven practice in the mechanical engineering and also in the closely related sciences as are electrical, civil and process engineering, medicine, microbiology, ecology, agriculture, transport systems, aviation, and others, thus creating a unique forum for interdisciplinary or multidisciplinary dialogue.
The international conferences selected papers are welcome for publishing as a special issue of SV-JME with invited co-editor(s).

Editorial Office
University of Ljubljana, Faculty of Mechanical Engineering
SV-JME, Aškerčeva 6, SI-1000 Ljubljana, Slovenia
Phone: 386 (0)1 4771 137
Fax: 386 (0)1 2518 567
info@sv-jme.eu, http://www.sv-jme.eu

Print: Demat d.o.o., printed in 240 copies

Founders and Publishers
University of Ljubljana, Faculty of Mechanical Engineering, Slovenia
University of Maribor, Faculty of Mechanical Engineering, Slovenia
Association of Mechanical Engineers of Slovenia
Chamber of Commerce and Industry of Slovenia, Metal Processing Industry Association

President of Publishing Council
Mihael Sekavčnik
University of Ljubljana, Faculty of Mechanical Engineering, Slovenia

Vice-President of Publishing Council
Bojan Dolšak
University of Maribor, Faculty of Mechanical Engineering, Slovenia

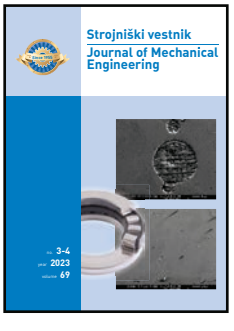

Cover:
To improve the reliability and service life of thrust cylindrical roller bearings, the pit-textured and non-textured bearings was carried out by using a universal friction and wear test rig, the effects of single/compound pit texture on tribological properties and on friction-induced vibration and noise were studied. The differences between the single/composite pit-textured and non-textured surfaces were studied in terms of the friction, wear, and vibration noise properties.

Image Courtesy:
The Authors,
Shenyang University of Chemical Technology,
Equipment Reliability Institute,
China

ISSN 0039-2480, ISSN 2536-2948 (online)

General information
Strojniški vestnik – Journal of Mechanical Engineering is published in 6 double issues per year.

Institutional prices include print & online access: institutional subscription price and foreign subscription €100,00 (the price of a single issue is €10,00); general public subscription and student subscription €50,00 (the price of a single issue is €5,00). Prices are exclusive of tax. Delivery is included in the price. The recipient is responsible for paying any import duties or taxes. Legal title passes to the customer on dispatch by our distributor. Single issues from current and recent volumes are available at the current single-issue price. To order the journal, please complete the form on our website. For submissions, subscriptions and all other information please visit: *http://www.sv-jme.eu.*

You can advertise on the inner and outer side of the back cover of the journal. The authors of the published papers are invited to send photos or pictures with short explanation for cover content.

We would like to thank the reviewers who have taken part in the peer-review process.

The journal is subsidized by Slovenian Research Agency.

SV-JME is indexed / abstracted in: SCI-Expanded, Compendex, Inspec, ProQuest-CSA, SCOPUS, TEMA. The list of the remaining bases, in which SV-JME is indexed, is available on the website.

Strojniški vestnik - Journal of Mechanical Engineering is available on *https://www.sv-jme.eu*.

Contents

Strojniški vestnik - Journal of Mechanical Engineering
volume 69, (2023), number 3-4
Ljubljana, March-April 2023
ISSN 0039-2480

Published monthly

Papers

Strojniški vestnik - Journal of Mechanical Engineering 69(2023)3-4, 87-99

DOI:10.5545/sv-jme.2022.455 Original Scientific Paper
Received for review: 2022-11-18
Received revised form: 2023-01-23
Accepted for publication: 2023-03-06

Effects of Single/Compound Pit Texture on the Friction-induced Vibration and Noise of Thrust Cylindrical Roller Bearings

Yueyong Wang[2] – Yimin Zhang[2,*] – Yibing Wang[2] – Risheng Long[1]
[1]Shenyang University of Chemical Technology, Equipment Reliability Institute, China
[2]Shenyang University of Technology, School of Mechanical Engineering, China

To improve the reliability and service life of thrust cylindrical roller bearings (TCRBs), the effects of single/compound pit texture on tribological properties and on friction-induced vibration and noise were studied. Laser marking equipment was used to create compound pit texture on a shaft washer. A universal friction and wear test rig was used to measure the friction force, vibration acceleration, and noise signals of TCRBs. The differences between the single/composite pit-textured and non-textured surfaces were studied in terms of the friction, wear, and vibration noise properties. The results revealed that the friction force and wear loss of the single/composite pit-textured surface were markedly lower than those of the non-textured surface. Compared to non-textured surface bearings, the friction force and wear loss for textured surface bearings were reduced by 39.6 % and 59.6 %, respectively, when the diameter, depth, and area density of the pit were 300 *μm*, 10 *μm*, and 10 %, respectively. The single/composite pit-textured surface exhibited good potential for vibration absorption and noise suppression. It could effectively interfere with the self-excited vibration of the TCRBs friction pair system, thereby reducing the degree of vibration noise of the TCRBs.
Keywords: thrust cylindrical roller bearings, single/compound pit texture, friction force, wear, friction-induced vibration and noise

Highlights
- *A single/compound surface pitting texture was applied to thrust cylindrical roller bearings under starved conditions.*
- *The friction and wear of single/compound pitted textured cylindrical roller bearings were significantly lower than those of non-textured surface bearings.*
- *Compound pitted textured contact surfaces with regular geometry were more likely to trap worn debris in the pits.*
- *Friction was closely related to vibration and noise, and both single and compound pits contributed to the vibration absorption and noise reduction.*

0 INTRODUCTION

In mechanical systems, thrust cylindrical roller bearings (TCRBs) are commonly used to bear friction losses, axial loads, and to support parts [1]. Bearings installed in heavy machines sometimes operate under mixed or starved lubrication; therefore, they show increased friction and wear [2]. Friction is caused when two solid surfaces in contact move (or tend to move) relative to each other; Wear is the phenomenon of continuous loss of surface materials in the process of relative movement of pairs, and wear is the inevitable result of friction. Friction causes energy consumption, wear leads to material loss, large material loss will lead to the failure of mechanical parts. Surface wear is a complex process. In an era of expanding energy demand and decreasing non-renewable resources, friction and wear will significantly increase fuel consumption, reduce the energy utilisation rate, and shorten the life of mechanical parts. To reduce these, it is essential to improve the wear resistance of TCRBs. New strategies for modifying friction and wear problems are more urgent now than in any previous era [3]. Wear is the inevitable result of friction, it is accompanied by friction process, can only be minimized but not completely avoided. With the development of science and technology, domestic and foreign scholars have found that the friction and wear cannot be greatly reduced if the roughness of the material surface is reduced, but the texture of the surface has better tribological properties. Surface texture has outstanding effects in reducing friction, reducing wear, and improving lubrication properties, which has attracted worldwide attention. Nature presents numerous multi-scale cases, such as the self-cleaning and superhydrophobicity of lotus leaves, adjustable adhesion of gecko feet, and drag reduction on dolphins and shark skin. These natural phenomena suggest that the compound surface pattern can effectively reduce friction and wear.

The lubrication condition of the working surface can be significantly improved by preparing micropits or microgrooves with specific geometries on the contact surface of the friction pair. The tribological properties of such contact surface were also significantly improved [4] and [5]. Laser surface texture (LST) [6], and [7] is one of the most successful methods owing to its flexibility, environmental protection, and economic advantages. Marian et al. [8] and [9] obtained an optimised and robust micro-texture design through friction simulation combined with advanced data analysis methods and corresponding

*Corr. Author's Address: Shenyang University of Chemical Technology, Equipment Reliability Institute, China, zhangyimin@syuct.edu.cn

tests. Costa et al. [10] emphasised the mechanism causing an increase in friction, pointing out existing deficiencies and future research directions. König et al. [11] numerically predicted the friction performance of journal bearings in single- and multi-scale surface patterns. They found that compared with unpatterned shaft sleeve, the wear of multi-scale patterns was reduced by θ % at most. The single-scale features of the microcoined and laser patterns reduced the wear by 8 % and 6 %, respectively. Grützmacher et al. [12] experimentally studied the influence of single- and multi-scale surface patterns on the friction properties of sliding bearings, and the coefficients of friction (COFs) of all patterns were significantly reduced. Other encouraging numerical and experimental results showed that multi-scale or hierarchical patterns/ textures were significantly improved compared to single pitted and non-textured surfaces [13] to [16]. Milčić et al. [17] studied the effects of shaft bush rotation frequency and radial load on Tegotenax V0 Stann-Babbabt bearings under hydrodynamic lubrication. Wrzochal et al. [18] introduced the basic assumption and mechanical design of a new type of friction torque measuring device for rolling bearings, and made a preliminary evaluation of its indexes.

Numerous studies have shown that friction-induced vibration noise was affected by factors such as the normal load, contact surface properties, and environmental conditions, particularly the microscopic morphology of the contact surface. Sudeep et al. [19], and [20] studied the influence of texture surfaces on friction wear and friction-induced vibration behaviour in the linear reciprocating motion of bearing steel point contact under different working conditions. For certain textures, the vibration amplitude was significantly reduced owing to the increase in the damping value compared to that of the smooth surface. Under starved and full lubrication conditions, Gupta et al. [21] conducted tribological and vibration studies on textured spur pairs. The results showed that the vibration amplitude, temperature rise, and mating surface wear decreased in the presence of a surface texture. Hu et al. [22] studied friction-screaming noise suppression using grooves and round-pit textures. The results indicated that both textured surfaces could reduce the high-frequency screaming noise of the friction system. Wrzochal et al. [23] pointed out that the cleanliness of bearings is a key factor to determine whether rolling bearings meet the quality requirements. Chernets et al. [24] proposed a computational method to solve the plane contact problem of elastic theory to determine the contact strength and tribological durability of plain bearings. Kydyrbekuly et al. [25] proposed a method for amplitude calculation and frequency characteristic construction of forced vibration and self-excited vibration of rotor-fluid-foundation system of nonlinear rolling bearing based on complex amplitude and harmonic balance method.

The relationship between the surface texture of rolling bearings and frictional vibration and noise, particularly for the surface compound texture, is insufficient. The novelty of this work lies in that there is little research on the relationship between surface texture and frictional vibration and noise, especially the relationship between tribological behavior of surface texture rolling bearings and frictional vibration and noise characteristics has not been reported. The research of this content can further study the generation mechanism of friction noise and put forward the optimized surface texture specification to reduce friction noise. An in-depth study and analysis of the mechanism of frictional vibration noise and interface behaviour characteristics of surface compound texture enriches the theory of friction-induced vibration and noise and has essential engineering application value.

1 EXPERIMENT

The TCRB had 8 roller elements (Detailed performance parameters are shown in Table 1), as shown in Fig. 1. Seven bearing sets labelled G01 to G07 (Table 2), were used to study the effects of single/compound pits on the tribological properties and friction-induced vibration noise of TCRBs. Non-textured TCRBs were introduced as a reference group and coded as G08 Each group contained three TCRBs. The friction force curve for each group was the mean. The wear loss for each group was the average of nine measurements from 24 TCRBs. All TCRBs were the same batch product from the same manufacturer, and

Table 1. *Detailed performance parameters of 81107TN thrust cylindrical roller bearing*

Material	Hardness	Density [g/cm³]	Elasticity modulus [MPa]	Poisson's ratio	Melting point [°C]	Pyroconductivity [W/(mK)]	Distortion temperature [°C]
GCr15	60 HRC to 65 HRC	7.81	2.07E5	0.29	1395 to 1403	40.11	—
PA66	95 HK to 105 HK	1.24	2.6E3	0.35	250 to 260	—	70

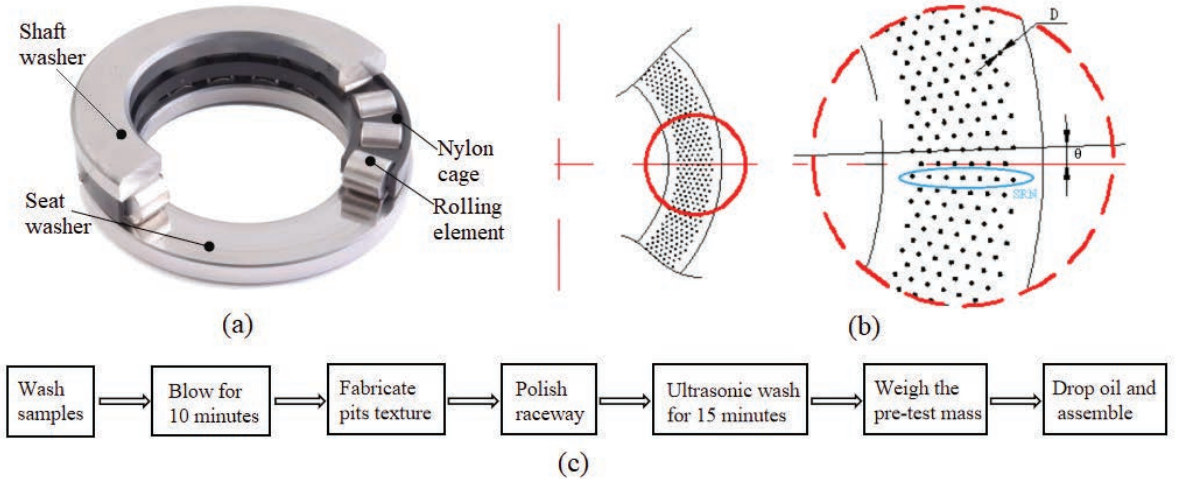

Fig. 1. *a) Components of 81107TN, b) pits texture parameters, and c) treatment process of bearings before wear tests*

the same sample was weighed three times to take the average value.

All TCRBs were prepared before the friction and wear tests according to the process shown in Fig. 1c. Laser marking equipment was used to fabricate compound pit texture on the shaft washer (WS). The textured surface was the surface in contact with the cylindrical roller. After laser texturing, use 800# 1000# 2000# sand-papers successively to remove the micro-bulges along the edges of pits by hand. Under the same conditions, the same person grinding with the same force, manual grinding was only the slightly convex edge produced by the pit texture, which did not reach the overall running in state of the bearing.

To reflect the ability of single/compound pits to collect and store debris [26], the effective volume of pits (EVP) was introduced and defined as:

Table 2. *Pits texture parameters and patterns of 81107TN TCRB groups*

Group Code	Diameter, D [μm]	Depth, H [μm]	Density, S [%]	Circumferential angle of pits, θ [°]	Single radial number, SRN	Effective volume of pits, EVP	Pit patterns
G01	100	10	10	1	35	9.891	
G02	300	10	10	1.8	7	9.891	
G03	500	10	10	5	7	9.891	
G04	100 / 300	10	10	2 / 2	35 / 5	11.304	
G05	100 / 500	10	10	2 / 6	35 / 5	10.833	
G06	100 / 100+300	10 / 20	18	1 / 2	35 / 7	17.804	
G07	100 / 100+500	10 / 20	13	1 / 5	35 / 7	18.793	
G08	—	—	—	—	—	—	

$$EVP = \pi \times \left(\frac{D}{2}\right)^2 \times H \times \frac{360^\circ}{\theta} \times SRN \times 10^{-8}. \quad (1)$$

The definition of the terms in Eq. (1) and the calculation results are shown in Fig. 1b and Table 1.

The laser texture parameters are listed in Table 3. The laser pulse duration, also known as Pulse-width, is a unit of time measurement, referring to the duration of laser action. In this study, pulse width ≤5 ms. The pit texture parameters are shown in Fig. 1b. The preparation of different parameters and patterns of the pits on the G01 to G07 shaft washers is shown in Table 1.

Table 3. *Parameters of laser marking equipment*

Indicators category	Parameter
Power [W]	3
Wavelength [nm]	1060
Engraving depth [mm]	0.01
Linear velocity [mm/s]	100
Laser frequency [kHz]	60
Repeated precision [mm]	±0.002

Frictional wear and vibration noise tests of the single/compound pit texture TCRBs were performed using a universal friction and wear test rig (MMW-1A, China) and a multifunctional vibration and noise acquisition system. The test apparatus was composed of friction and wear test system, signal acquisition, analysis system, etc., which could synchronously collect friction and vibration and noise signals in the process of friction and wear test.

The parameters of the universal friction and wear test rig were: longitudinal loading force (200± 100 N), rotational speed (200 rpm), and test time (10000 s). Usually, the rolling bearing is calculated according to the million speed or working hours, and the rotation speed calculated according to the number of revolutions of 200 rpm is 0.6 m/s. Within the test period, the middle distance of operation was 600 m. Taking into account the effect of sliding ratio, the sliding distance of G02 was 422.4 m and that of G08 was 607.2 m. Before each test, the shaft washer of the bearing was first weighed using an electronic balance (accuracy and readability of 0.1 mg and 0.01 mg, respectively). Drip 100 mg of commercial lubricant (Parameters are shown in Table 4) was applied on the pit-textured surface. All the friction, wear, vibration, and noise tests strictly implemented the above operating steps to ensure consistency in all the bearing tests. Lubricating oil was not used during the test.

Table 4. *Parameters of commercial lubricant*

Indicators category	Unit	Parameter
Dynamic viscosity @ 30 °C	mm²/s	14.45
Density @ 30 °C	kg/l	0.8678
Viscosity index, VI		163
Low temperature pumping viscosity, MRV @ –35 °C	mPa·s	18000
Flash point	°C	242
Pour point	°C	–45

The parameters of the triaxial piezoelectric acceleration sensor and microphone are presented in Table 5. The microphone was placed 30 mm from the friction pair. Vibration and noise signals were acquired using a 16 channel signalling system three times at 1 h intervals, with a sampling frequency and time of 12.8 kHz and 10 s, respectively.

Table 5. *Parameters of triaxial piezoelectric acceleration sensor and microphone*

Parameter	Triaxial piezoelectric acceleration sensor	Microphone
Range	±50 g	17 dB to138 dB
Frequency	0.5 kHz to7 kHz	3.15 Hz to 20 kHz
Sensitivity	10 mV/(m·s²)	50 mV/Pa
Mass	15 g	—

Three groups of bearings with the same texture style were tested under the same working conditions, and the test data (friction force, vibration acceleration, noise, etc.) were the average values of the three tests. All tests were performed under atmospheric conditions of 30±10 % relative humidity and room temperature of approximately 20 °C. The TCRB was cleaned after the tests using an ultrasonic cleaning machine containing an acetone solution. The bearing shaft washer was weighed using an electronic balance. The wear surface of the shaft washer was characterised using a scanning electron microscope. The relationship between the vibration and noise properties of the sample and its tribological behaviour were considered.

2 RESULTS AND DISCUSSION

2.1 Friction Force and Wear Analysis

Fig. 2 shows the friction force curve of TCRB G01 toG07 with single/compound pits under starved lubrication. This study was about friction-induced vibration noise, so we think it is more direct here to use friction rather than friction coefficient. The friction force curve of G08 is provided as a reference.

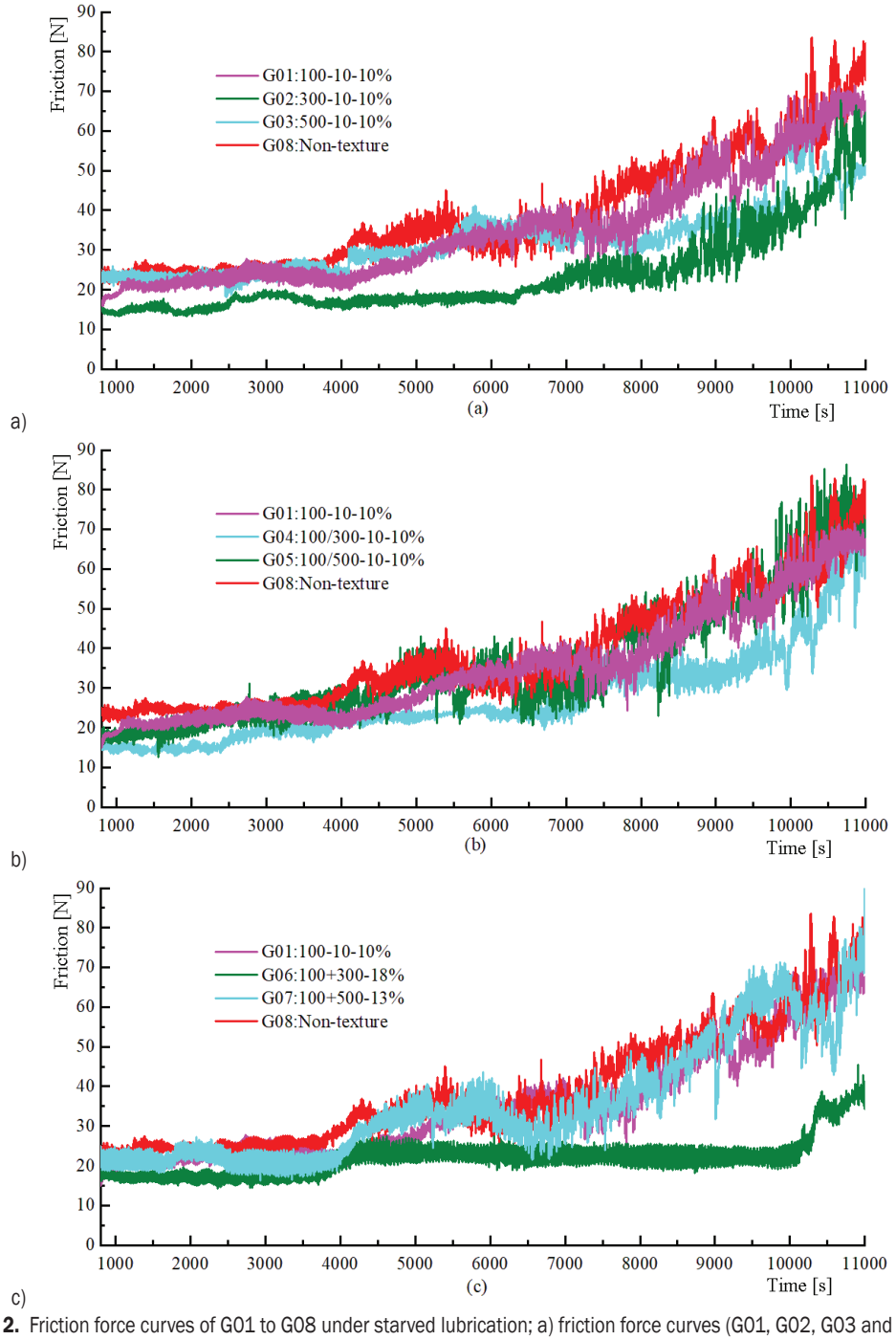

Fig. 2. Friction force curves of G01 to G08 under starved lubrication; a) friction force curves (G01, G02, G03 and G08), b) friction force curves (G01, G04, G05 and G08), and c) friction force curves (G01, G06, G07 and G08)

The label "G01 00- 0- 0% " stands for "Group number: diameter-depth-density".

From Fig. 2, the friction force of the TCRBs can be divided into three stages. Under starved lubrication conditions (initial 00 s, approximately), the steady-state stage is characterised by pit storage of lubricating oil, uniform lubrication film on the contact surface, good contact mechanics, and a stable friction curve. The contact surface was partially crushed at the defect initiation and development stage (00 s to 00 s), and pits captured the worn nylon powder and debris. Nylon powder might come

from the wear of cylindrical roller and cage pocket hole, self-aligning thrust bearing, wear of cage and friction pair running-in process, etc. The debris might come from unpolished texture edges or texture edges crushed during the test. The lubricating oil in the pits played a secondary lubrication role, and the friction curve started to show an upward trend. In the failure-increasing stage (800 s to 1000 s), the local crushing continued to deteriorate, the lubricating oil was gradually exhausted, and intermittent dry grinding occurred. The non-textured surface or pits could not store any more nylon powder and debris, and the wear was aggravated, leading to an accelerated increase in the friction curve. Taking Fig. 3c as an example, the friction curve of the texture bearing G06 was significantly lower than that of the smooth bearing G08, indicating that the texture can play a beneficial role in reducing friction and resisting wear.

Fig. 3 shows the wear loss on the shaft washer of each bearing group under starved lubrication conditions; the wear loss of the bearings containing single/compound pits was markedly reduced and lower than that of the non-textured surface bearing group. The wear loss for G02 was 3.38 mg, which was the lowest of all bearings tested. G03 and G06 reported a wear loss of 3.93 mg and 4.93 mg, respectively, at the medium level. The wear loss of G07 was 8.08 mg, which was identical to that of the non-textured G08 with a wear loss of 8.36 mg.

As shown in Fig. 3, an inflection point occurred when the pit diameter was 300 μm. The increase in the diameter of the pit indicates a reduction in the effective contact area, an increase in the contact stress (taking the texture bearing G02 and the non-textured smooth bearing G08 as examples, see Table 6), and an increase in the effective volume of the pit, serious collapse of the pit edge, and strong radial centrifugal movement of the nylon powder.

Fig. 4 shows the finite element analysis results of G02 and G08 thrust cylindrical roller bearings (1/8). In Fig. 4, the nodes of G02 were 40328, the elements were 34042, and the maximum contact stress was 889 MPa. In Fig. 4, the nodes of G08 were 42628, the elements were 35975, and the maximum contact stress was 722.8 MPa. The contact pressure value of finite element analysis was basically consistent with the theoretical calculation results in Table 6.

The worn surfaces of the shaft washers of G06 and G08 are shown in Fig. 5. From the wear marks and surfaces, in the compound textured bearing G06, the fatigue pitting was light, the debris on the contact surface was less and smaller, and the debris in the pit was larger. But in non-texture bearing G08, the fatigue

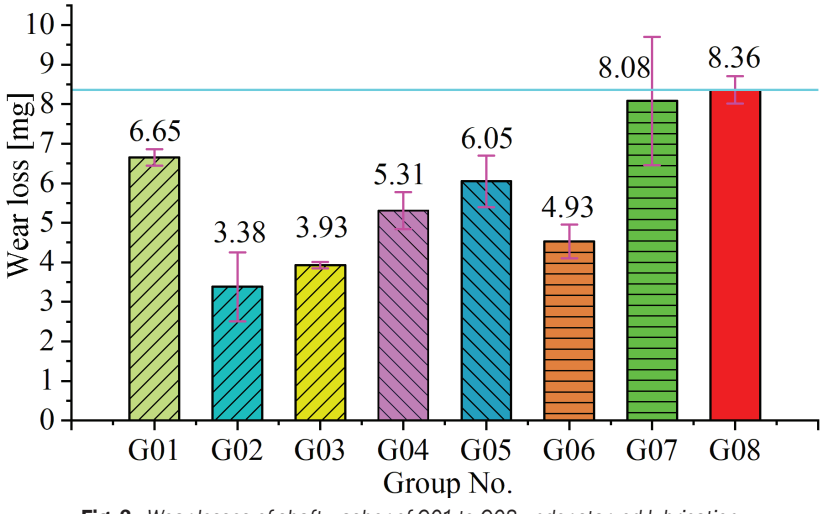

Fig. 3. *Wear losses of shaft washer of G01 to G08 under starved lubrication*

Table 6. *Contact pressure and contact area of single roller G02 and G08*

Group code	Load, Q [N]	Contact length, l [mm]	Elasticity modulus, E_1, E_2 [Pa]	Poisson's ratio μ_1, μ_2	Radius of roller, R_1 [mm]	Radius of contact surface of WS, R_2 [mm]	Contact half width, b [mm]	Contact pressure, [MPa]	Contact area, S [mm²]
G02	144.4	2.8	2.06E11	0.3	2.5	$+\infty$	0.038	864.66	0.213
G08	144.4	4	2.06E11	0.3	2.5	$+\infty$	0.032	718.75	0.256

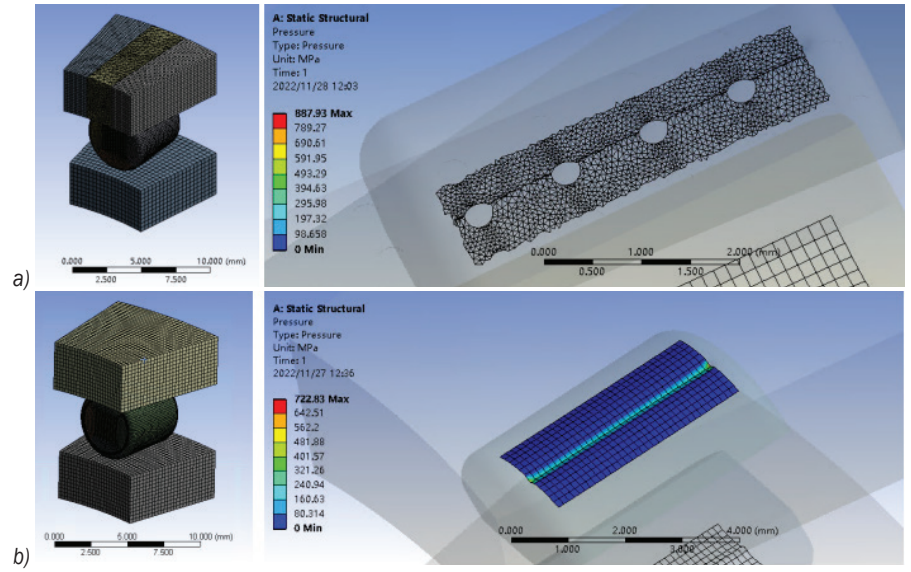

Fig. 4. *Finite element analysis (FEA) results of a) G02 and b) G08 thrust cylindrical roller bearings (1/18)*

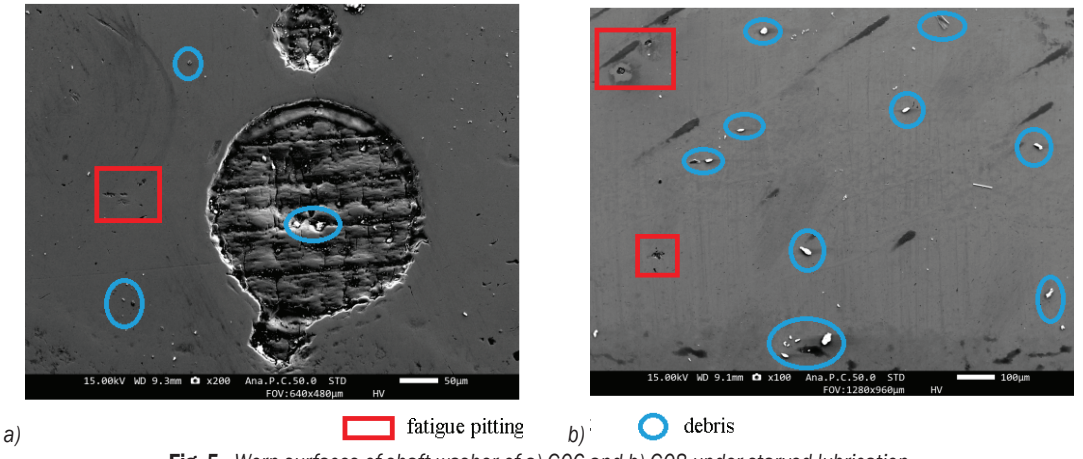

Fig. 5. *Worn surfaces of shaft washer of a) G06 and b) G08 under starved lubrication*

pitting was more serious and the debris was more and larger. Through comparative analysis, it can be seen that the pit texture can trap large debris and reduce the wear degree of the contact surface.

The effects of single/compound pits on the friction and wear performance of TCRBs were: (1) Compared to the non-textured TCRBs, the amount of debris left on the shaft washer of the single/compound pit texture was significantly reduced owing to the centrifugal throw effect during high-speed rotation [27]. This helped reduce the friction force and wear loss in the shaft washers in the TCRBs. (2) Single/compound pits reduced the effective contact area of the shaft washer [28]. The contact stress on the raceway was improved and the presence of surface pits reduced the contact area of the friction interface, thereby reducing the local contact stiffness. Simultaneously, the contact stress on the surface of the friction pair was distributed, improving the wear characteristics of the contact interface. (3) Laser surface texture technology improves fatigue and wear resistance and forms bionic anti-wear surfaces with "soft"–"hard" and "rigid"–"soft" phases. All bionic textured samples have positive effects on fatigue behavior through phase transformation and grain strengthening [29].

2.2 Effect of Single/Compound Pit Texture Surface on Friction-induced Vibration and Noise

The equivalent sound pressure level is defined as the sound pressure level averaged by the energy in a certain period of time. To evaluate the frictional

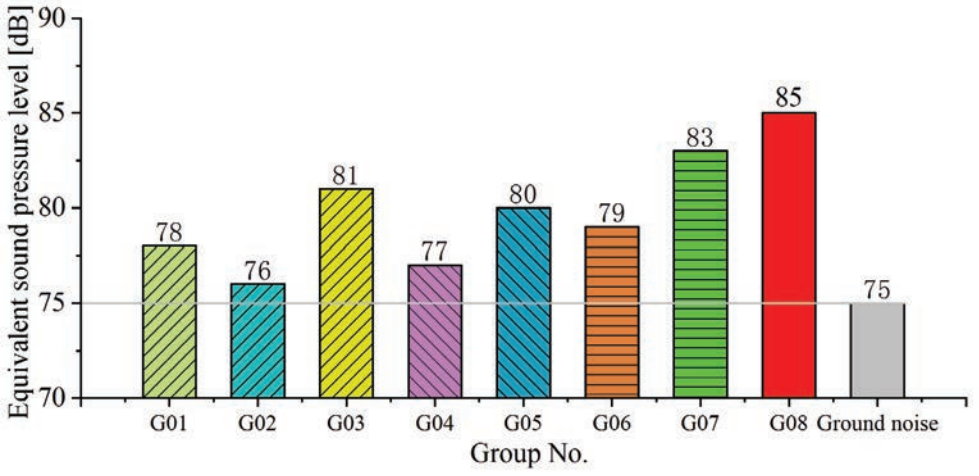

Fig. 6. *Equivalent sound pressure level of the non-textured surfaces and pit-textured surfaces*

noise level of the non-textured surface and single/compound pit-textured surface, an equivalent sound pressure level analysis was carried out on the noise sound pressure signals within 100 s in the stable stage, as shown in Fig. 6. The friction noise intensity of the non-textured bearing G08 was the highest at 85 dB, followed by single/compound pit-textured bearings G07, G03, and G05, at approximately 80 dB to -80 dB, all of which contained a texture with a pit diameter of 500 μm. In contrast, the intensity of the noise generated by the single-pit-textured bearing G02 was significantly lower (approximately 76 dB). This is similar to the background noise of 75 dB, indicating that approximately no noise was generated on the single pit-textured surface.

2.3 Time-frequency Analysis of Friction-induced Vibration and Noise

Time history records of the sound pressure signal and *Y*-direction acceleration were collected at approximately 3000 s. The pits can play a role in reducing vibration and noise [19], and [20].

Ming [30] studied a wavelet-spectrum autocorrelation method for rolling bearing composite-fault feature separation and concluded that under identical wavelet decomposition conditions, the wavelet-spectrum autocorrelation method was better than the wavelet-envelope spectrum feature separation. It had high engineering application value.

Wavelet transformation can select different time windows for different frequencies; a narrower time window for high-frequency signals and a wider time window for low-frequency signals. The wavelet transform of the known continuous signal $h(t)$ is defined as

$$W_{\varnothing}(a,\tau)=\frac{1}{\sqrt{|a|}}\int_{-\infty}^{+\infty}h(t)\varnothing^{*}\left[\frac{\tau-t}{a}\right]dt, \quad (2)$$

where a is the telescopic scale, τ is the shift factor, and $\varnothing(t)$ is a wavelet mother function, and it satisfies

$$C_{\varnothing}=\int_{-\infty}^{+\infty}\frac{\varnothing(\omega)}{\omega}d\omega<\infty, \quad C_{\varnothing}\neq 0. \quad (3)$$

The inverse transformation is defined as

$$h(t)=\frac{1}{C_{\varnothing}}\int_{-\infty}^{+\infty}\int_{0}^{+\infty}\frac{1}{a^{2}}W_{\varnothing}(a,\tau)\varnothing^{*}\left[\frac{\tau-t}{a}\right]dad\tau. \quad (4)$$

A time–frequency analysis of the noise and axial (*Y*) vibration acceleration was carried out to study the frequency variation of the test. As shown in Fig. 7, the change in the frictional contact caused by the roller element over the pit-textured surface did not change the dominant frequency of the sound pressure and vibration. However, significant energy distributions of G03, G07, and G08 were observed at a dominant frequency of 600 Hz, causing significant screaming noise. The energies of G04 and G06 at the dominant frequency of 5000 Hz were insignificant. Therefore, there were no high-frequency screams during the entire process.

2.4 Frequency Spectrum Analysis of Friction-induced Vibration and Noise

The pit morphology and friction force of the contact surface are closely related to friction-induced vibration noise. To further investigate the influence of

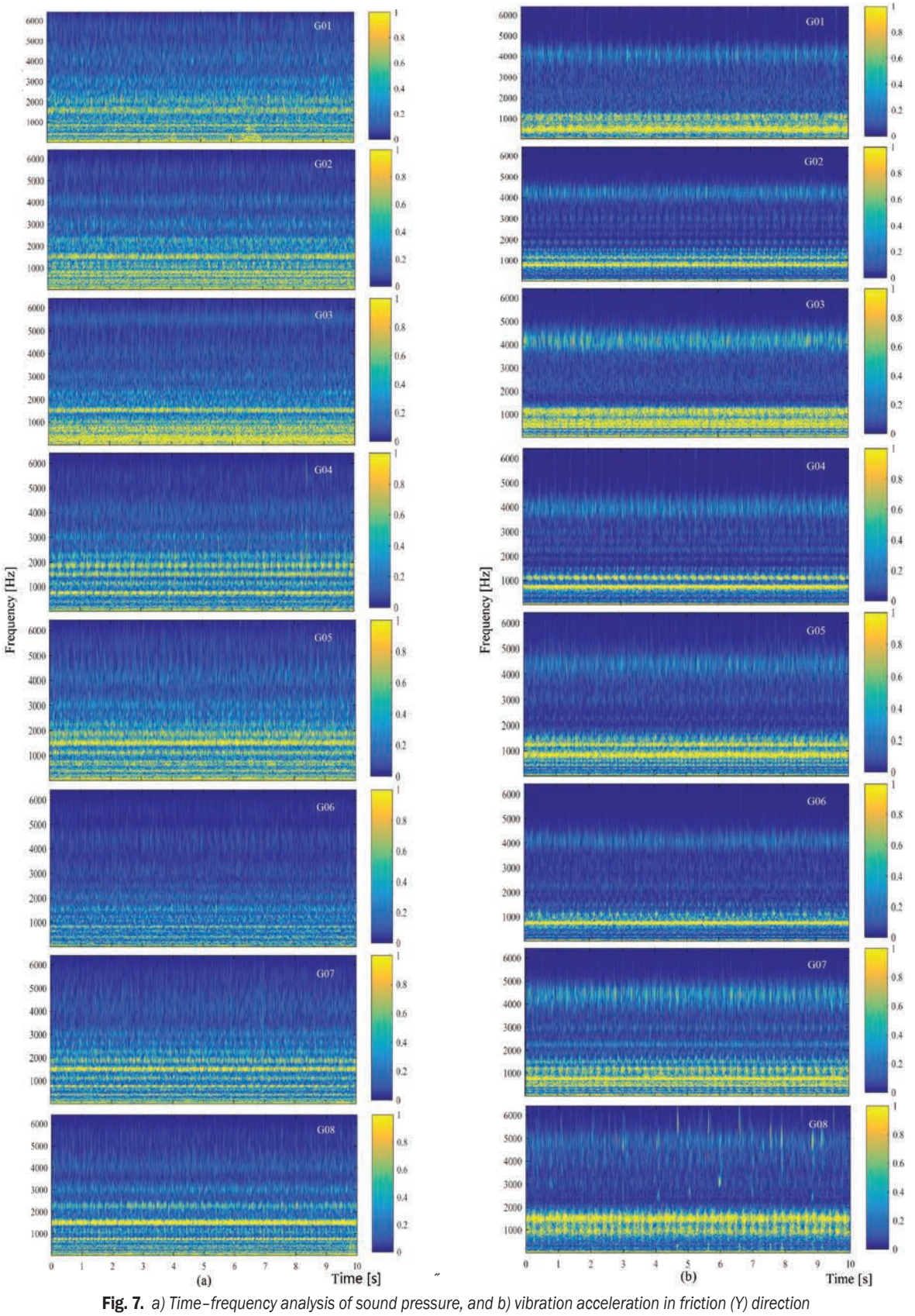

Fig. 7. *a) Time–frequency analysis of sound pressure, and b) vibration acceleration in friction (Y) direction*

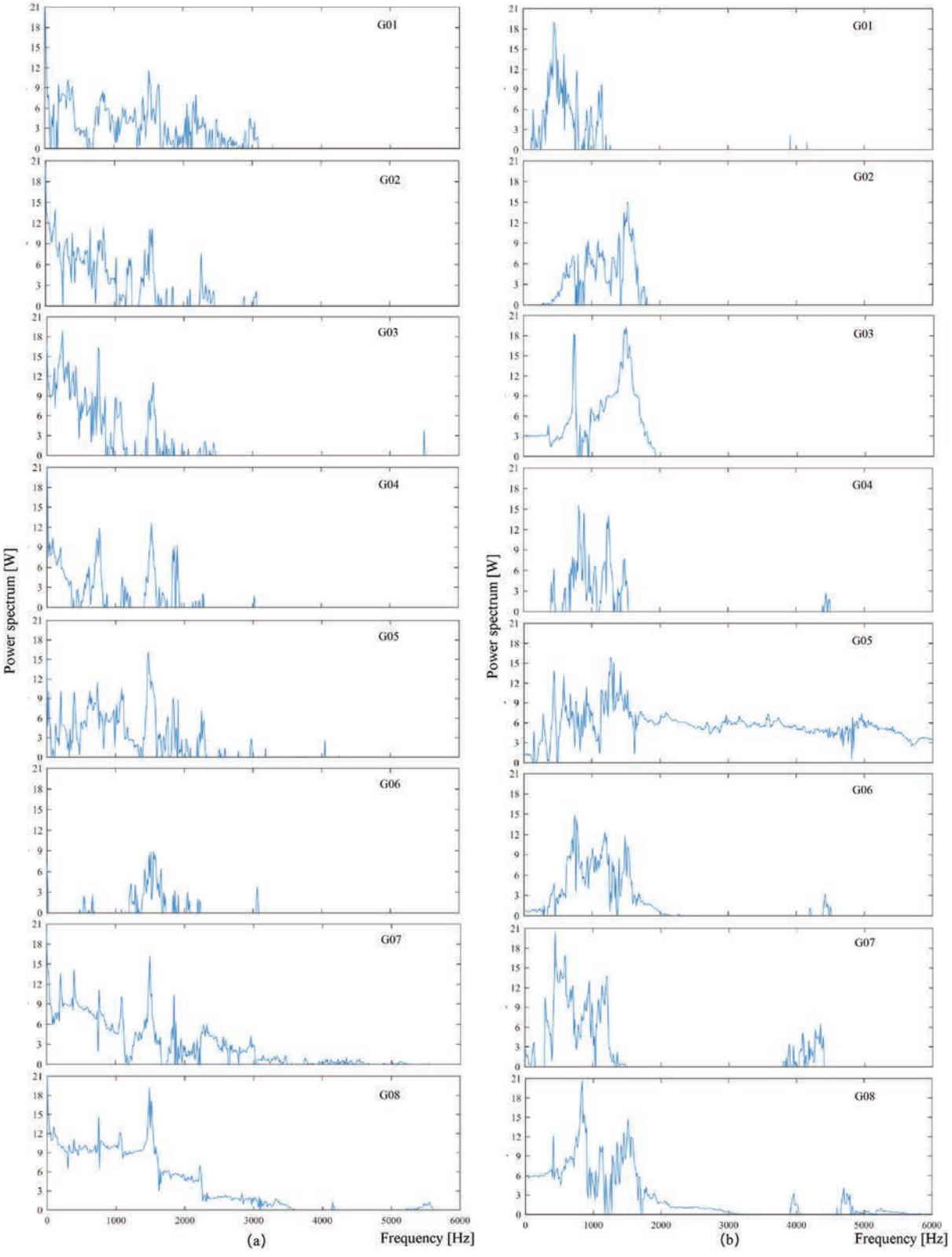

Fig. 8. *a) Power spectrum analysis diagram of noise pressure, and b) vibration acceleration in (Y) direction*

the single/compound pit-textured surface topography on vibration and noise, a frequency spectrum analysis of the friction-induced vibration noise signals and friction force was performed. The internal coherence of the signals is also discussed. Fig. 8 shows the power spectrum of noise pressure and vibration acceleration for non-textured surface bearings and different single/compound pit-textured bearings, reflecting the power distribution of these signals in the frequency domain (0–10 Hz). The signal power of all pit-textured surface bearings was low at the primary frequency. G06 exhibited the lowest power spectrum at 0–10 Hz.

2.5 Mechanism of Vibration and Noise Induced by Single/Compound Pit Texture Surface

The worn surface morphology of the single/compound pit-textured bearings consisted of macroscopic and microscopic pit morphologies. Macroscopic pits were composed of axial and radial spacing laws produced by laser marking equipment. The microscopic features include irregular features of the worn surfaces on the upper edges of the pits, such as wear debris layers, ploughing, and stripping. In this study, compared with the micro-irregular wear surface around the upper edge of the pits, the pits were the key reason for noise suppression.

The irregularity of the wear surface around the upper edge of the pit caused fluctuations in the friction force. It is often considered the actual excitation source of noise instability at the friction interface [31]. A pit-textured surface with specific geometries made it easier for wear debris to be trapped in pits and reduced noise tendencies. More importantly, pits can interrupt the continuous contact of the friction surface during rolling friction and reduce the effective contact area. Thus, they improve the surface-contact stress to suppress high-frequency friction fluctuations and interrupt the self-excited vibration of the friction system.

3 CONCLUSIONS

The effects of the single/compound pit texture on friction, wear performance, and friction-induced vibration noise characteristics of the TCRB were studied. The following conclusions were drawn.

1. Under starved lubrication, the friction force and wear loss on the single/compound pit-textured TCRBs were significantly lower than that on the non-textured surface bearings. The lowest wear loss was observed for G02. The friction force and wear loss were 39.6 % and 95.6 %, respectively, lower than the non-textured surface bearing.
2. Only 10 mg of lubricating oil was added to each test, with the operation of the TCRB, the lubricating oil at the contact between the shaft washer surface and the rolling elements was gradually exhausted. The lubricating oil stored in the pits was continuously removed and the lubrication state of the system was maintained. The single/compound pits played a role in storing the lubricating oil and providing secondary lubrication to the bearing system.
3. The frequencies of the friction force, noise pressure signals, and vibration acceleration signals were approximately equal (150 Hz) when there was significant noise. Friction force and vibration noise are closely related.
4. Noise and vibration were related to frictional fluctuations due to microscopic irregularities on wear surfaces, such as ploughing and abrasion debris layers. Single/compound pits texture contact surfaces with regular geometry made them easier to trap wear debris into the pits. Therefore, single and compound pits helped reduce irregularities and noise tendencies.

4 ACKNOWLEDGEMENTS

This work was supported by the National Key R&D Program of China (No. 2019YFB2004400) and the Chinese National Natural Science Foundation (No. U1708254). The authors sincerely thank the editors and reviewers for their efforts in improving this paper.

5 APPENDIX

The formula of contact pressure and contact area [32], since the thrust cylindrical roller bearing has 18 rollers, 1/18 of the bearing was taken for calculation. The meanings of the letters in the formula are shown in Table 4.

$$p_{\max} = \frac{2 \times Q}{\pi \times b \times l}, \tag{A1}$$

$$b = \sqrt{\frac{4}{\pi} \times \frac{1}{E^*} \times \frac{Q}{l} \times \frac{R_1 \times R_2}{R_1 + R_2}}, \tag{A2}$$

$$E^* = \frac{1-\mu_1^2}{E_1} + \frac{1-\mu_2^2}{E_2}, \tag{A3}$$

$$S = 2b \times l. \tag{A4}$$

5 REFERENCES

[1] Tala-ighil, N., Fillon, M. (2015). A numerical investigation of both thermal and texturing surface effects on the journal bearings static characteristics. *Tribology International*, vol. 90, p. 228-239, **DOI:10.1016/j.triboint.2015.02.032**.

[2] Wang, Q., Shi, F., Lee, S.C. (1997). A Mixed-TEHD model for journal-bearing conformal contact-Part II: Contact, film thickness, and performance analyses. *Journal of Tribology*, vol. 120, no. 2, p. 206-213, **DOI:10.1115/1.2834411**.

[3] Rosenkranz, A., Grützmacher, P.G., Murzyn, K., Mathieu, C., Mücklich, F. (2019). Multi-scale surface patterning to tune friction under mixed lubricated conditions. *Applied Nanoscience*, vol. 11, p. 751-762, **DOI:10.1007/s13204-019-01055-9**.

[4] Etsion, I. (2004). Improving tribological performance of mechanical components by laser surface texturing. *Tribology Letters*, vol. 17, p. 733-737, **DOI:10.1007/s11249-004-8081-1**.

[5] Mishra, S.P., Polycarpou, A.A. (2011). Tribological studies of unpolished laser surface textures under starved lubrication conditions for use in air-conditioning and refrigeration compressors. *Tribology International*, vol. 44, no. 12, p. 1890-1901, **DOI:10.1016/j.triboint.2011.08.005**.

[6] Olofinjana, B., Lorenzo-Martín, C., Ajayi, O.O., Ajayi, E.O. (2015). Effect of laser surface texturing (LST) on tribochemical films dynamics and friction and wear performance. *Wear*, vol. 332-333, p. 1225-1230, **DOI:10.1016/j.wear.2015.02.050**.

[7] Rodrigues, G.W., Bittencourt, M.L. (2020). Surface virtual texturing of the journal bearings of a three-cylinder ethanol engine. *Industrial Lubrication and Tribology*, vol. 72 no. 9, p. 1059-1073, **DOI:10.1108/ilt-09-2019-0380**.

[8] Marian, M., Grützmacher, P.G., Rosenkranz, A., Tremmel, S., Mücklich, F., Wartzack, S. (2019). Designing surface textures for EHL point-contacts - Transient 3D simulations, meta-modeling and experimental validation. *Tribology International*, vol. 137, p. 152-163, **DOI:10.1016/j.triboint.2019.03.052**.

[9] Marian, M., Almqvist, A., Rosenkranz, A, Fillon, M. (2022). Numerical micro-texture optimization for lubricated contacts-A critical discussion. *Friction*, vol. 10, p. 1772-1809, **DOI:10.1007/s40544-022-0609-6**.

[10] Costa, H.L., Schille, J., Rosenkranz, A. (2022). Tailored surface textures to increase friction-A review. *Friction*, vol. 10, p. 1285-1304, **DOI:10.1007/s40544-021-0589-y**.

[11] König, F., Rosenkranz, A., Grützmacher, P.G., Mücklich, F., Jacobs, G. (2020). Effect of single- and multi-scale surface patterns on the frictional performance of journal bearings - A numerical study. *Tribology International*, vol. 143, art. ID. 106041, **DOI:10.1016/j.triboint.2019.106041**.

[12] Grützmacher, P.G., Rosenkranz, A., Szurdak, A., König, F., Jacobs, G., Hirt, G., Mücklich, F. (2018). From lab to application - Improved frictional performance of journal bearings induced by single- and multi-scale surface patterns. *Tribology International*, vol. 127, p. 500-508, **DOI:10.1016/j.triboint.2018.06.036**.

[13] Segu, D.Z., Lu, C., Hwang, P., Kang, S. (2021). Optimization of tribological characteristics of a combined pattern textured surface using Taguchi design. *Journal of Materials Engineering and Performance*, vol. 30, p. 3786-3794, **DOI:10.1007/s11665-021-05673-9**.

[14] Segu, D.Z., Hwang, P. (2015). Friction control by multi-shape textured surface under pin-on-disc test. *Tribology International*, vol. 91, p. 111-117, **DOI:10.1016/j.triboint.2015.06.028**.

[15] Segu, D.Z., Hwang, P. (2016). Effectiveness of multi-shape laser surface texturing in the reduction of friction under lubrication regime. *Industrial Lubrication and Tribology*, vol. 68, p. 116-124, **DOI:10.1108/ILT-03-2015-0041**.

[16] Kim, J., Choi, S., Segu, D.Z., Jung, Y., Kim, S.S. (2014). Improvement of tribological characteristics of multi-scale laser-textured surface in terms of lubrication regime. *Tribology and Lubricants*, vol. 30, no. 1, p. 59-63, **DOI:10.9725/kstle.2014.30.1.59**.

[17] Milčić, D., Alsammarraie, A., Madić, M., Krstić, V., & Milčić, M. (2021). Predictions of Friction Coefficient in Hydrodynamic Journal Bearing Using Artificial Neural Networks. *Strojniški vestnik - Journal of Mechanical Engineering*, vol. 67, no. 9, p. 411-420, **DOI:10.5545/sv-jme.2021.7230**.

[18] Wrzochal, M., Adamczak, S., Domagalski, R., Piotrowicz, G., & Wnuk, S. (2022). New device proposed for industrial measurement of rolling bearing friction torque. *Strojniški vestnik - Journal of Mechanical Engineering*, vol. 68, no. 10, p. 610-622, **DOI:10.5545/sv-jme.2022.275**.

[19] Sudeep, U., Pandey, R.K., Tandon, N. (2013). Effects of surface texturing on friction and vibration behaviors of sliding lubricated concentrated point contacts under linear reciprocating motion. *Tribology International*, vol. 62, p. 198-207, **DOI:10.1016/j.triboint.2013.02.023**.

[20] Sudeep, U., Tandon, N., Pandey, R.K. (2016). Vibration studies of lubricated textured point contacts of bearing steels due to surface topographies: Simulations and experiments. *Tribology International*, vol. 102, p. 265-274, **DOI:10.1016/j.triboint.2016.05.040**.

[21] Gupta, N., Tandon, N., Pandey, R.K., Vidyasagar, K.E., Kalyanasundaram, D. (2020). Tribological and vibration studies of textured spur gear pairs under fully flooded and starved lubrication conditions. *Tribology Transactions*, vol. 63, p. 1103-1120, **DOI:10.1080/10402004.2020.1794093**.

[22] Hu, L., Mo, J., Wang, D., Yang, J., Chen, G., Zhu, M. (2016). Groove-textured and pit-textured surfaces to suppress friction-induced squeal noise. *China Mechanical Engineering*, vol. 27, no. 9, p. 1158-1164, **DOI:10.3969/j.issn.1004-132X.2016.09.004**. (in Chinese)

[23] Wrzochal, M., Adamczak, S., Piotrowicz, G., & Wnuk, S. (2022). Industrial experimental research as a contribution to the development of an experimental model of rolling bearing vibrations. *Strojniški vestnik - Journal of Mechanical Engineering*, vol. 68, no. 9, p. 552-559, **DOI:10.5545/sv-jme.2022.184**.

[24] Chernets, M., Opielak, M., Kornienko, A., & Radko, O. (2021). Predictive Estimation of Sliding Bearing Load-Carrying Capacity and Tribological Durability. *Strojniški vestnik - Journal of Mechanical Engineering*, vol. 67, no. 7-8, p. 363-368, **DOI:10.5545/sv-jme.2021.7139**.

[25] Kydyrbekuly, A., Ibrayev, G., Ospan, T., & Nikonov, A. (2021). Multi-parametric Dynamic Analysis of a Rolling Bearings

System. *Strojniški vestnik - Journal of Mechanical Engineering*, vol. 67, no. 9, p. 421-432, **DOI:10.5545/sv-jme.2021.7178**.

[26] Long, R., Ma, Q., Jin, Z., Zhang, Y., Han, H., Sun, S., Du, X. (2022). Tribological behavior of dimples textured rolling element bearings under stepped load and starved lubrication. *Industrial Lubrication and Tribology*, vol. 74, no. 7, p. 876-883, **DOI:10.1108/ilt-04-2022-0150**.

[27] Grützmacher, P.G., Rosenkranz, A., Rammacher, S., Gachot, C., Mücklich, F. (2017). The influence of centrifugal forces on friction and wear in rotational sliding. *Tribology International*, vol. 116, p. 256-263, **DOI:10.1016/j.triboint.2017.07.021**.

[28] Rosenkranz, A., Grützmacher, P.G., Gachot, C., Costa, H.L. (2019). Surface texturing in machine elements − a critical discussion for rolling and sliding contacts. *Advanced Engineering Materials*, vol. 21, no. 8, art. ID 1900194, **DOI:10.1002/adem.201900194**.

[29] Li, H., Zhou, H., Zhang, D.P., Zhang, P., Zhou, T. (2022). Influence of varying distribution distance and angle on fatigue wear resistance of 40Cr alloy steel with laser bionic texture. *Materials Chemistry and Physics*, vol. 277, art. ID 125515, **DOI:10.1016/j.matchemphys.2021.125515**.

[30] Ming, A. (2013). Compound fault features separation of rolling element bearing based on the wavelet decomposition and spectrum auto-correlation. *Journal of Mechanical Engineering*, vol. 49, no. 3, p. 80-87, **DOI:10.3901/jme.2013.03.080**.

[31] Mo, J., Wang, Z., Guangxiong, C., Shao, T., Zhu, M., Zhou, Z.R. (2013). The effect of groove-textured surface on friction and wear and friction-induced vibration and noise. *Wear*, vol. 301, no. 1-2, p. 671-681, **DOI:10.1016/j.wear.2013.01.082**.

[32] Popov, V.L. (2010). *Contact Mechanics and Friction: Physical Principles and Applications*. Springer, Springer Heidelberg **DOI:10.1007/978-3-642-10803-7**.

Strojniški vestnik - Journal of Mechanical Engineering 69(2023)3-4, 100-118
DOI:10.5545/sv-jme.2022.396
Original Scientific Paper
Received for review: 2022-10-02
Received revised form: 2023-01-19
Accepted for publication: 2023-02-14

Inverse Curves - Research on Two Quondam Inversor Mechanisms

Alina Duta[1]* – Iulian Popescu[2] – Ionut Daniel Geonea[1] – Simona-Mariana Cretu[1] – Ludmila Sass[1] – Dragos-Laurentiu Popa[1]

[1] University of Craiova, Faculty of Mechanics, Romania
[2] Academy of Technical Sciences, Romania

The field of research considered in this work is that of mechanisms generating inverse curves. We were motivated to approach this field, proposing variants of mechanisms based on Artobolevsky's inversor, in blocking conditions, due to the lack of recent applications related to inversor mechanisms that draw curves other than straight lines. Based on Crawford's inversor, Artobolevsky's inversor is structurally and kinematically analysed in what follows. Hence, we carried out the kinematic analysis and simulation of four inversor mechanisms derived from Artobolevsky's inversor, which draw different initial curves (a circle, a straight line, an ellipse and an Archimedes' spiral) were performed. Inverse curves were generated under limited operating conditions due to geometrical dimensions and kinematic parameters. Given the researchers' increasing interest in the development of applications related to inversor mechanisms (in fields such as: robotics, machine tools, visual arts and symbolic languages), as well as expanding databases of planar and spatial mechanisms, it is suggested that there is a need to create new mechanisms similar to those studied in this paper and to analyse their mode of operation.

Keywords: inversor mechanism, kinematic analysis, blocking positions

Highlights

- *Design and computational kinematic analysis of four new mechanisms that can be applied in current fields (e.g., lifting-lowering systems, conveyor belts, tool machines, suspension for electric wheels, walking and climbing robots, mechanisms for generating curves, gripping arms, kinetic light art).*
- *Addressing a topical area that is less studied but of interest to researchers.*
- *Establishing the conditions to avoid blocking with regard to the proposed inversor mechanisms.*
- *Computational kinematics analysis that identified the mechanisms used for fast movements.*

0 INTRODUCTION

Current challenges faced by researchers in various fields of Engineering can be supported by historical knowledge in the field of mechanisms and machines [1]. Attention is increasingly being paid to the creation and updating of databases containing information in various forms (text, image or diagram) in the field of planar and spatial mechanisms, including those generating curves. DMG Lib and thinkMOTION are examples of such databases [2].

In [1], several historical mechanisms for generating various curves are presented; their usefulness in a wide range of domains from engineering to the creation of new symbolic languages is highlighted. Among the mechanisms for generating curves, inversor mechanisms have been challenging specialists ever since. Two types of inversor mechanisms can be distinguished: some that direct the kinematic element in a forward-backward motion, and others in which one point moves along a given curve while another point describes an imposed curve, called the inverse curve.

For the mathematical definition of inverse curves, one should consider two curves given by polar coordinates. In Fig. 1, curve 1 is given by r_1, α and curve 2 is given by r_2, γ; P is the inversion centre of the inverse curves and β is the constant angle between r_1 and r_2.

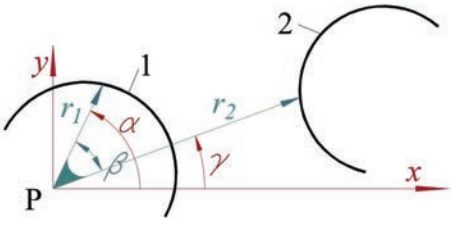

Fig. 1. *Inverse curves*

These curves are inverse to each other if Eq. (1) is verified [3].

$$r_1 \cdot r_2 = k^2, \tag{1}$$

where k is a positive number.

The inverse curves were first systematically investigated in 1824 by Steiner [4].

*Corr. Author's Address: University of Craiova, Craiova, 200512, Romania, alina.duta@edu.ucv.ro

Tables with the given direct curve / inverse curve are given in [3] (e.g., line/circle, Archimedean spiral/ Archimedean spiral, cardioid/ parabola, circle/circle, Diocles's cissoid/parabola, epi spiral/rose, hyperbola/ lemniscate, logarithmic spiral /logarithmic spiral, lituus/Fermat's spiral, sinusoidal spiral/sinusoidal spiral).

The specialized literature deals with many mechanisms that reverse the movement; they are made with levers (e.g., [5] to [7]), gears (e.g., [8] and [9]) and combinations of them (e.g., [10] and [11]). In [7], Artobolevsky presents descriptions, kinematic schemes and dimensional relationships between elements for several inversor mechanisms.

Patents for many inversor mechanisms have been obtained, e.g., lever mechanisms [12] to [14], a gear mechanism [15] and a hybrid mechanism [16].

Stephenson's popular mechanism of the steam locomotive also uses the reversing motion [17]. The first mechanism to draws a exactly straight line, invented by Peaucellier in 864 is an inversor mechanism that transforms a circular movement into an alternative linear one. These mechanisms still have various applications nowadays. For example, [18] and [19] present the generalization of Peaucellier's inversor and suggest the possibility of generalizing other inversor mechanisms.

Hart's inversor from 1874 transforms an alternative straight-line motion into another alternative rectilinear motion that is perpendicular to the initial axis [7]. Also, the Sylvester and Kempe inversors, conceived in 1874 and in 1875 respectively, represent improvements to Hart's cell.

Kinematic (e.g., [20] and [21]), kinetostatic (e.g., [22]) and dynamic analysis (e.g., [23] and [24]), synthesis studies (e.g., [20] and [25]) and different optimization types and techniques (e.g., [26] to [28]) were carried out for the inversor mechanisms. For example, a numerical method based on the mean-square minimization of the objective function [29] can be used for the kinematic synthesis of the Stephenson mechanism. Other modern methods can also be used to optimize these planar mechanisms (e.g., the genetic algorithm, approached in [28]).

Studies were also made for the inverse kinematics of the inversor mechanisms using various software tools (e.g., MATLAB/Simulink® [20]). Some studies present the connection between mathematics and mechanisms (including inversor mechanisms) as a resource for teaching mathematics (e.g., [30], [31] and [1]).

Inversor mechanisms are used in applications such as lifting-lowering systems (e.g., [12]), conveyor belts, tool machines, suspension for electric wheels (e.g., [14]), walking machines (with different numbers of legs: two [22], four [16], or six [13], [24] and [32]), climbing robots (e.g., [21]), mechanisms generating curves, gripping arms (e.g., [25], [27] and [33]), and kinetic light art (e.g., [34]).

In some cases, a mechanism with one degree of freedom was used for some robotic leg propulsion systems. It might involve one inversor mechanism (e.g., [16]) or can rely on an inversion linkage (e.g., [13]). In other cases, the mechanism of the robotic leg has several degrees of freedom and is able to describe lines and arcs with different centres of rotation (e.g., [24]).

In the field of interactive kinetic light art, in 2006 Ivo Schoofs presented a new kinetic structure, based on Peaucellier's inverted chain, i.e., the alternative form. He built it with his team on a large scale (area of 15 m × 15 m), and placed it in the Eindhoven square at 21 m height. This structure represents a special attraction for visitors who can draw their own characters [34].

Under the circumstances, we embarked upon an applied research study of other inversor mechanisms, able to draw geometric constructions in addition to lines.

In what follows we applied Crawford's mechanisms ([35] and [36]) and Artobolevsky's mechanisms ([5], [7] and [10]); four mechanisms that draw inverse curves were also studied. For the kinematic analysis and motion simulation of the studied inversor mechanisms under the imposed conditions, we used to GWBASIC®, SolidWorks® and ADAMS® software.

1 THE STUDY OF CRAWFORD'S INVERSOR

In the 18 th century, starting from one relation of inverse curves, Crawford invented two inversor mechanisms: one with the inversion centre between the two inverse curves and another with it outside them ([5], [8] and [37]). A structural and kinematic analysis of the inversor mechanism with the inversion centre between the curves, which has a circle as direct curve, is presented in this paper. The kinematic scheme of Crawford's inversor is depicted in Fig. 2.

The element 2 has the form of a T-shaped lever and turns about fixed axis A which is the inversing point of the inverse curves. The element 1 has the angle CBE of 90 degrees and is connected by the rotation joint B to the element 2. The sliders 3 and 4 are connected by the rotation joint C, and the sliders 5 and 6 are connected by the rotation joint E; these

move along elements 2 and 1. For any geometry of the mechanism, the points C, A and E are collinear. When one of the points E or C moves along an arbitrary curve, the other point describes the inverse curve.

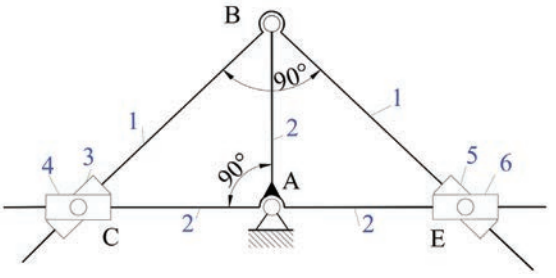

Fig. 2. *Crawford's inversor*

The mechanism performs inverse transformations because the dimensions of the mechanism verify the equation specific to inverse curves (Eq. (2)), where A is the inversion center and AC and AE are polar radii.

$$AE \cdot AC = AB^2. \tag{2}$$

The degree of mobility of this mechanism is calculated with Eq. (3), because the mechanism is not overconstrained [38].

$$M = 3 \cdot n - 2C_5 - C_4, \tag{3}$$

where n is the number of mobile elements, C_5 is the number of 5th class joints, and C_4 is the number of 4th class joints.

For $n = 6$, $C_5 = 8$ and $C_4 = 0$ the value for degree of mobility is 2, i.e., two leading elements are required.

If the position of one point on a given curve is imposed, e.g., the two coordinates of point C, the point E draws the inverse curve.

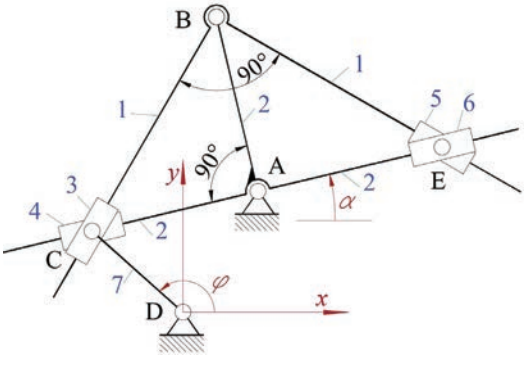

Fig. 3. *The kinematic scheme of the mechanism*

For the particular case when the direct curve is a circle, it is possible to impose the displacement of point C on it using the mechanism with the kinematic scheme from Fig. 3. The center of the circle is D and its radius equals the length of the element CD. The degree of mobility of the mechanism is equal to 1.

The structural scheme of the mechanism is depicted in Fig. 4. It can be seen that the mechanism consists of a driving element, a dyad TRT and a tetrad with 4 elements and 6 joints of the 5th class.

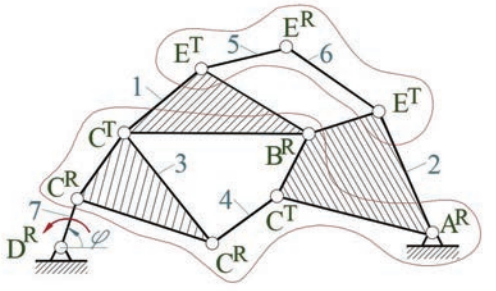

Fig. 4. *The structural scheme*

1.1 The Positions of the Mechanism

Considering as initial data DC = 31 mm, x_A = 24 mm, y_A = 29 mm, AB = 40 mm, φ = 125° and Eqs. (4) to (10), the kinematic scheme of the mechanism in GWBASIC® software was obtained (Fig. 5).

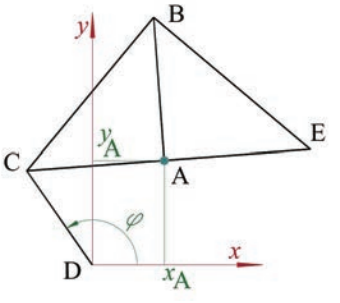

Fig. 5. *The mechanism for φ = 125 deg*

α and AC are calculated using Eq. (4).

$$\begin{cases} x_C = DC\cos\varphi = x_A + AC\cos(\alpha+\pi) \\ y_C = DC\sin\varphi = y_A + AC\sin(\alpha+\pi) \end{cases}. \tag{4}$$

Eq. (2) gives Eq. (5) that can be used to compute AE.

$$AE = AB^2 / AC. \tag{5}$$

The coordinates of B can be computed with Eqs. (6) and (7), BC is yielded by Eq. (8) and the position of E on the inverse curve is given by Eqs. (9) and (10).

$$x_B = x_A + AB\cos(\alpha+90), \tag{6}$$

$$y_B = y_A + AB\sin(\alpha+90), \tag{7}$$

$$BC^2 = AB^2 + AC^2, \quad (8)$$

$$x_E = x_A + AE\cos\alpha, \quad (9)$$

$$y_E = y_A + AE\sin\alpha. \quad (10)$$

For the kinematic analysis and simulation of the mechanism, the geometric model was performed in the SolidWorks® and imported into the ADAMS® software (Fig. 6).

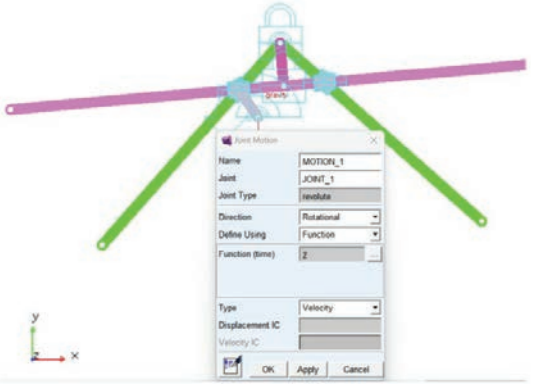

Fig. 6. *The model of the mechanism in the ADAMS® software*

1.2 Obtained Results

The rotation and translation joints were created and the motor was placed in the joint D, having angular velocity 2 rad/s (Fig. 6); taking into account the orientation of the system axes, the driving element moves in the trigonometric direction.

Fig. 7 shows the two circles drawn using the ADAMS® software: the direct curve described by point C in the trigonometric direction and the inverse one described by point E in the clockwise direction. The two circles have different areas.

The point C has uniform motion on the direct curve, its coordinates on the system axes are the trigonometric functions sine and cosine and its polar radius remains constant at 31 mm, being equal to the radius of the circle. The velocity of point C has constant modulus v = 62 mm/s and variable direction, being tangent to the trajectory. Because the velocity of the tracer point has a variable direction, it has a normal acceleration with constant modulus (Eq. (11)).

$$a^n = \omega^2 \cdot r = 124\ \text{mm/s}^2. \quad (11)$$

The inverse curve also has a circular trajectory, but, unlike the direct curve, the radius of the circle is larger; its polar radius is not constant because the center of the circle is not placed in the origin of the Cartesian system (Fig. 8). The coordinates of the tracer point E are shown in Fig. 8.

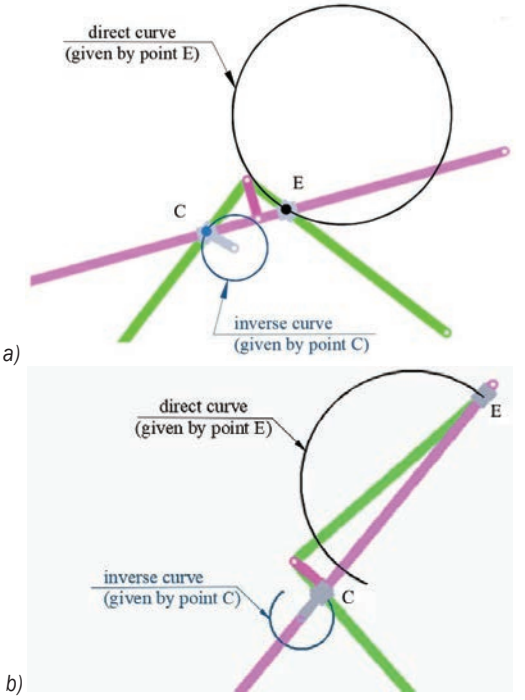

Fig. 7. *The inverse curves obtained in the ADAMS® software; a) entire curves, b) curves drawn at t = 2.5 s*

Unlike the point that draws the direct curve with uniform motion, the point that draws the reverse curve has variable motion.

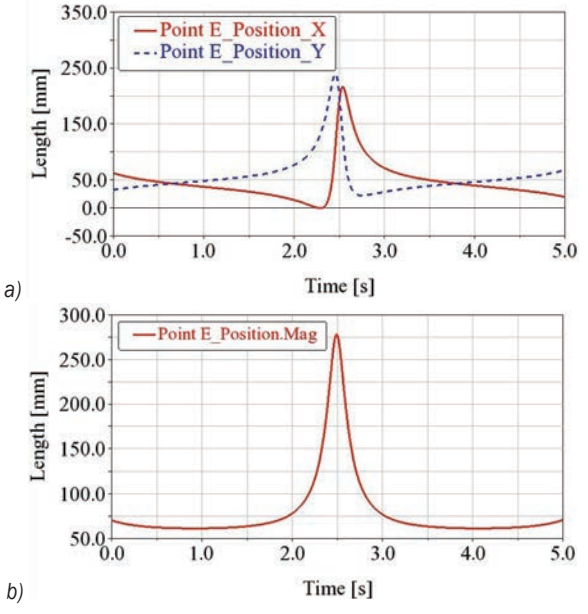

Fig. 8. *The diagram of coordinates for point E; a) the Cartesian coordinates, and b) the polar radius*

The velocity components are shown in Fig. 10a. At time t = 2.5 s, when the driving element performed

2[illegible] degrees from the initial position of 2[illegible]5 degrees (Fig. [illegible]7) , the velocity diagram of point E reveals a peak point of 22[illegible]0 mm/s when the polar radius of it reaches the maximum value (Fig. [illegible]9) ; because it is not a local maximum turning point of the function, the acceleration will not have the zero value and will appear as a peak point with the finite value of [illegible]900 m m/s² (Fig. [illegible]0) .

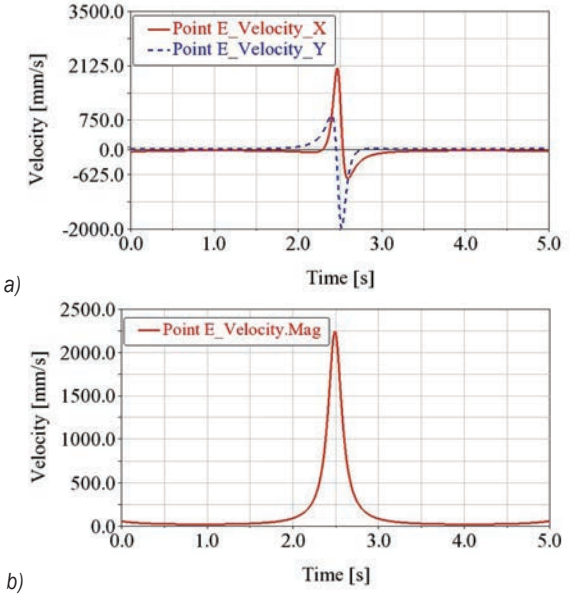

Fig. 9. *The diagram of velocity for point* E*; a) the projections on the system axes, and b) the magnitude*

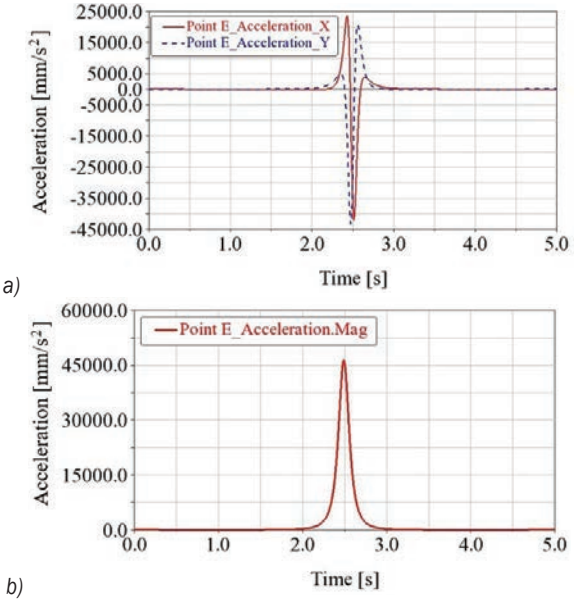

Fig. 10. *The diagram of acceleration for point* E*; a) the projections on the system axes, and b) the magnitude*

2 THE STUDY OF FOUR INVERSORS DERIVED FROM ARTOBOLEVSKY'S MECHANISM

An improvement of the Crawford's mechanism was provided by Artobolevsky (Fig. 1[illegible]) [10].

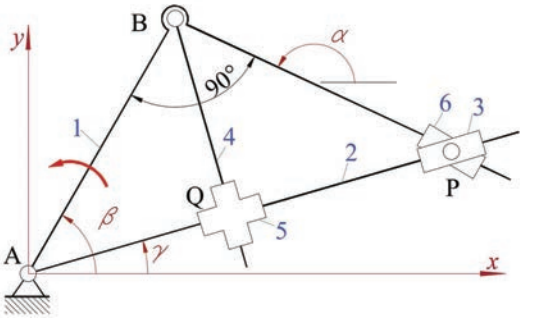

Fig. 11. *The Artobolevsky's inversor*

Our paper also focuses on the kinematic analysis and simulation of four mechanisms derived from Artobolevsky's inversor, which draw different initial curves (a circle, a straight line, an ellipse and an Archimedean spiral).

2.1 Circular Direct Curve

In order to obtain the circular trajectory of the direct curve described by point P, the rotating element CP is added to Artobolevsky's inversor mechanism (Fig. [illegible]2) . The inverse curve drawn by point Q is to be found.

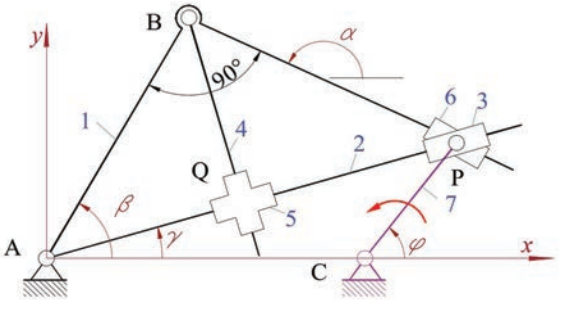

Fig. 12. *An improvement of Artobolevsky's inversor*

The equations for the position calculus are presented below (Eqs. ([illegible]2) to ([illegible]9).

$$x_P = x_C + CP\cos\varphi, \qquad ([illegible]2)$$

$$y_P = y_C + CP\sin\varphi, \qquad ([illegible]3)$$

$$\begin{cases} x_B = x_P + PB\cos\alpha = AB\cos\beta \\ y_B = y_P + PB\sin\alpha = AB\sin\beta, \\ \beta = \alpha - 90^0 \end{cases} \qquad ([illegible]4)$$

$$AP^2 = \left(x_P - x_A\right)^2 + \left(y_P - y_A\right)^2, \quad (5)$$

$$\sin\gamma = \frac{y_P}{AP}, \quad \cos\gamma = \frac{x_P}{AP}, \quad (6)$$

$$AQ = AB^2 / AP, \quad (7)$$

$$x_Q = AQ\cos\gamma, \quad (8)$$

$$y_Q = AQ\sin\gamma. \quad (9)$$

The position of P is calculated from Eqs. (2) and (3). α, β and PB are determined from Eq. (1), and γ results from Eq. (6). The relation given by Eq. (7) is the condition of inversion and yields AQ, making possible the computation of Q's coordinates, Eqs. (8) and (9).

The initial values for the mechanism are considered as follows: x_C = 103 mm, AB = 100 mm, CP = 43 mm. Fig. 13 shows the mechanism drawn in one position with the GWBASIC® software; the given curve, drawn by the point P appears in Fig. 14 and the inverse one, drawn by the point Q is given in Fig. 15.

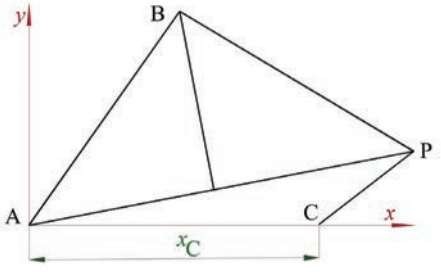

Fig. 13. *The mechanism in one position drawn with the GWBASIC® software*

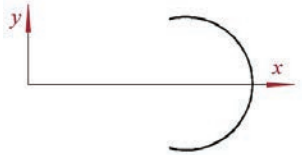

Fig. 14. *The curve drawn by point* P

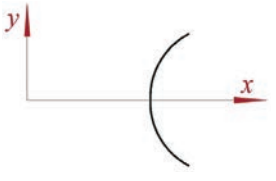

Fig. 15. *The inverse curve drawn by point* Q

The geometrical model of the mechanism it was obtained with the SolidWorks® and imported into the ADAMS® software for the kinematic analysis (Fig. 16).

After the simulation performed in ADAMS®, both direct and inverse curves were plotted. Point P does not draw a complete circle due to the dimensions of the mechanism; the arc of the circle is limited by the intersection points P_1 and P_2 between the circle drawn by point B and the circle drawn by point P (Fig. 17).

Fig. 16. *The model of the mechanism in the ADAMS® software*

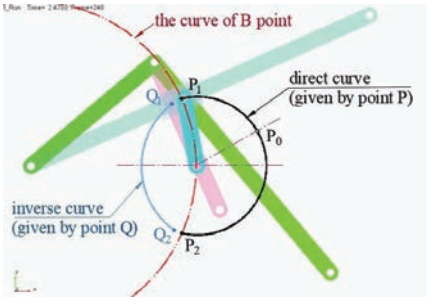

Fig. 17. *The curves drawn in the ADAMS® software*

For the mechanism from the Fig. 12, in order to avoid the operational blockage, the distance AC must be at least the sum of the radii AB and CP.

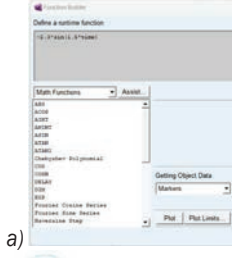

a)

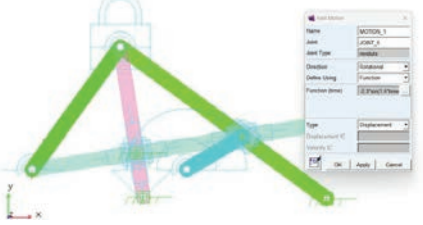

b)

Fig. 18. *The angular motion law for driving element; a) define a runtime function, and b) the joint motion*

Since the driving element has an oscillating motion, Eq. (20) was chosen as its angular motion law in the ADAMS® software (Fig. 18).

$$f\left(time\right)=-2.3\cdot\sin\left(1.5\cdot time\right). \qquad (20)$$

The value of the driving element angle was introduced in radians in Eq. (20) and displayed in degrees (Fig. 19a). The angular velocity of the driving element is within 0 deg/s to 200 deg/s (Fig. 19b) for 2.5 s. When the driving element moves 180 degrees clockwise during one second, the point P is starting from the initial position P_0 to the P_2 point. When the driving element reaches the point P_2, it stops and changes its direction of rotation (Fig. 17).

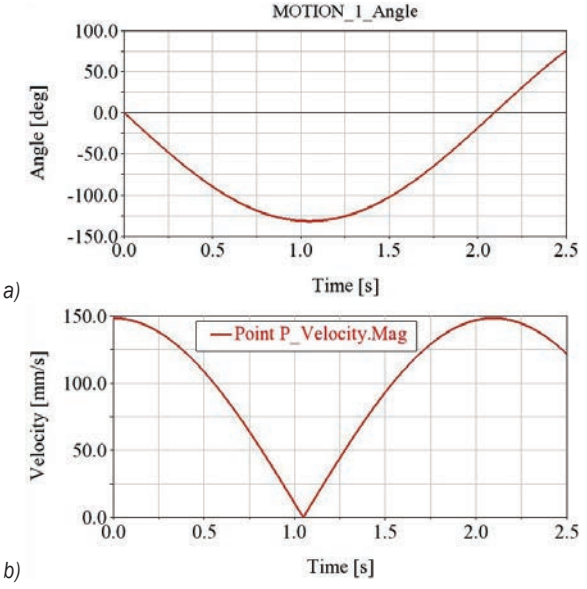

Fig. 19. *Kinematic diagrams for driving element; a) the angular position, and b) the angular velocity*

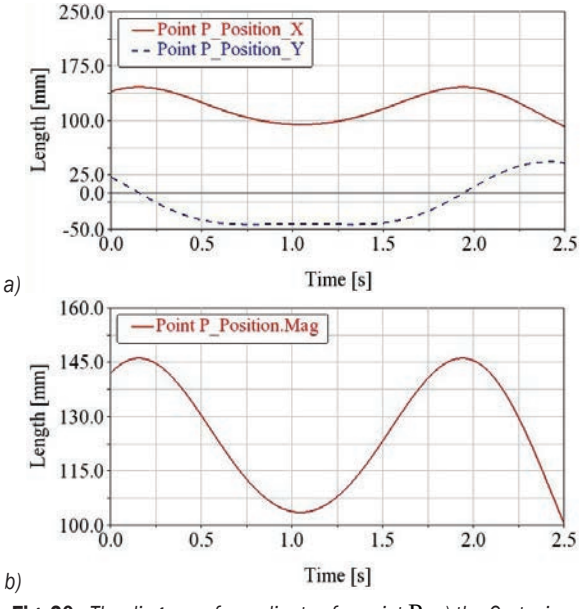

Fig. 20. *The diagram of coordinates for point P; a) the Cartesian coordinates; b) the polar radius*

Since the direct curve is a circular arc that does not have its centre at the origin of the Cartesian system, the polar radius is variable (Fig. 20b) and the Cartesian coordinates of the tracer point are represented in Fig. 20a.

For this law of motion, the velocity of the point P on the direct trajectory takes values between 0 mm/s and 600 mm/s (Fig. 21b) and its components on the system axes are represented in Fig. 21a.

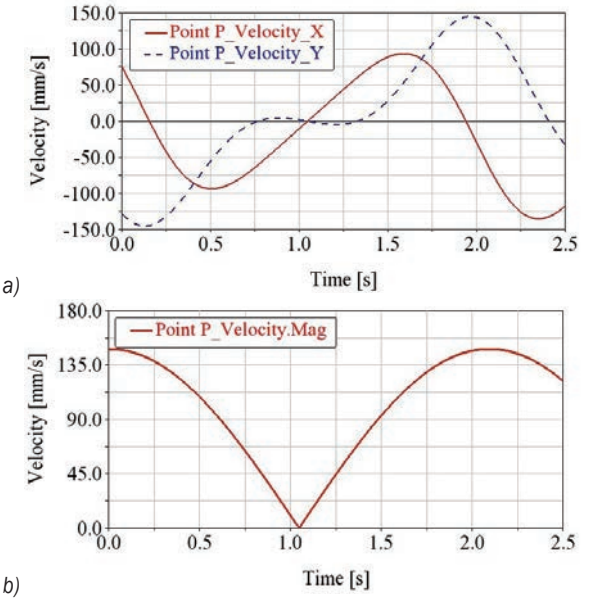

Fig. 21. *The diagram of velocity for point P; a) the projections on the system axes, and b) the magnitude*

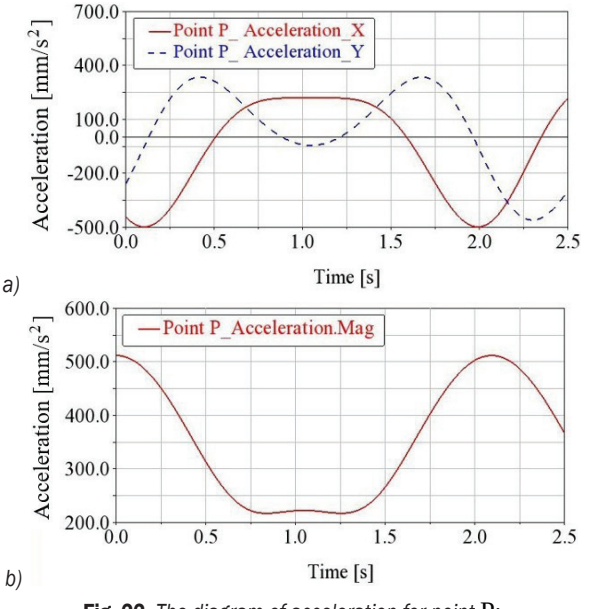

Fig. 22. *The diagram of acceleration for point P; a) the projections on the system axes, and b) the magnitude*

The acceleration takes values between 225 mm/s² to 230 mm/s² (Fig. 22b) and its projections on the system axes are represented in Fig. 22a.

Fig. 23 below indicates diagrams for the Cartesian coordinates and the polar radius for the inverse curve. The equations of the inverse curve are shown in the literature as functions of the direct curve variables [34]. One can check that the equation of the inverse curve is a circle, and also that its radius and centre can be determined from the ADAMS® software results. For this reason, one can consider the values of the Cartesian coordinates from the diagrams for any three points, and it is necessary to check the circle equation by them (Eq. (21)). One can determine the coordinates of the circle centre and its radius from this system of three equations and then the membership of other points to the circle can be verified.

$$\left(x_i - x_0\right)^2 + \left(y_i - y_0\right)^2 = R^2, \quad i = 1,2,3. \qquad (21)$$

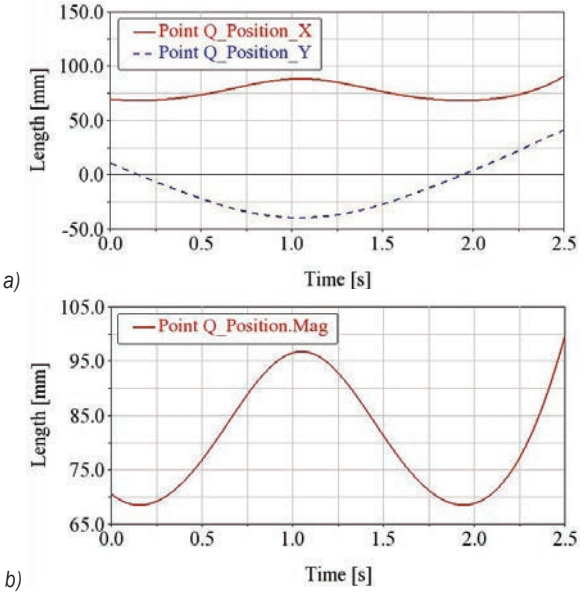

Fig. 23. *The diagram of coordinates for point Q; a) the Cartesian coordinates, b) the polar radius*

The animation and the velocity diagrams (Fig. 24) can reveal that point Q moves for one second on the inverse curve going in trigonometric direction; after stopping at point Q_2 (Fig. 7), the direction of rotation is changed.

Fig. 24 let us conclude that the circle ensures a slow decrease of the velocity up to the moment of an imposed stop (end point P_2) for the adopted law of motion of the driving element.

At the same time, the velocity diagram of the point Q shows a portion with an approximately constant velocity of 80 mm/s, which determines the acceleration of 0 mm/s² along the corresponding interval. Due to the velocity smooth slope before stopping, the maximum acceleration does not have a peak point in the end position P_2 (Fig. 25).

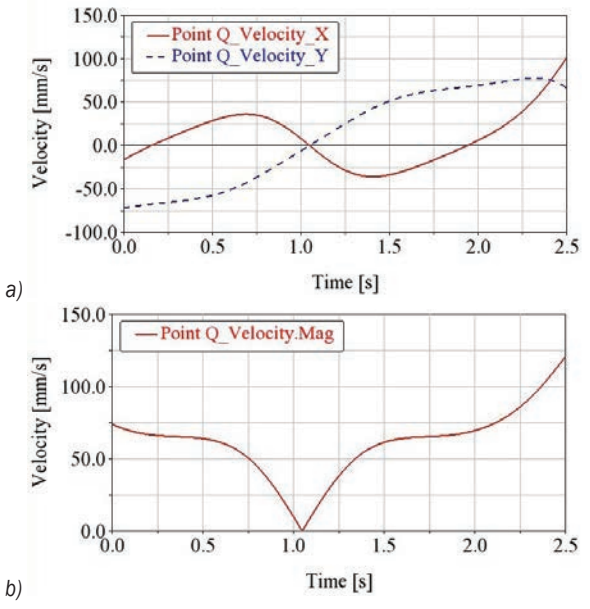

Fig. 24. *The diagram of velocity for point Q; a) the projections on the system axes, b) the magnitude*

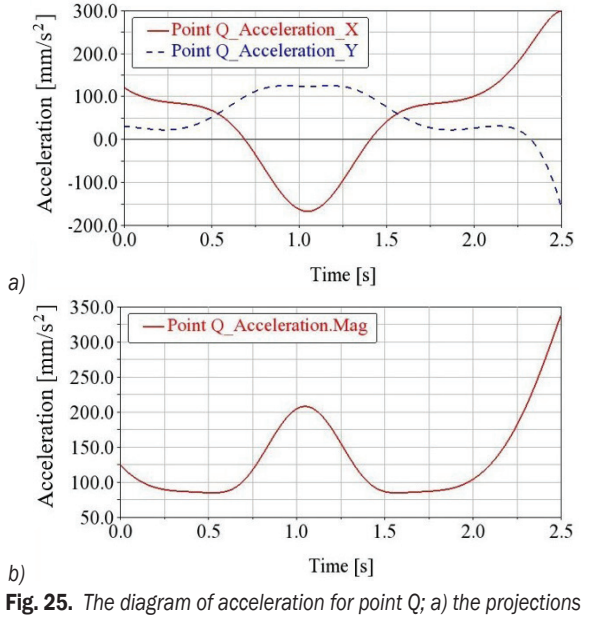

Fig. 25. *The diagram of acceleration for point Q; a) the projections on the system axes, and b) the magnitude*

2.2 Linear Direct Curve

According to the mechanism in Fig. 26, the point P has a translational motion, i.e., the direct curve is a

straight line, and the point Q plots the inverse curve. The element CP is fixed to the base and the element 7 is the driving element.

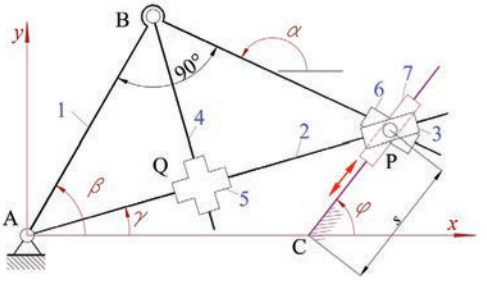

Fig. 26. *The kinematic scheme of the mechanism*

The lowest possible limit position of point P is at the intersection of the trajectory of point B with that of point P (Fig. 27).

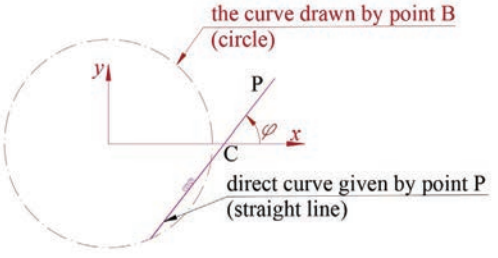

Fig. 27. *The limitation of the mechanism functioning*

In order to avoid the blockage in the operation of the mechanism (which is not caused by a change in the movement sense of the linear motor) the direction of the fixed element CP must not intersect the circular trajectory of point B.

Eqs. (22) and (23) provide the coordinates of P. For other points of the mechanism the equations are identical to those of the previously studied mechanism (Eqs. (4) to (9)).

$$x_P = x_C + S \cdot \cos\varphi, \tag{22}$$

$$y_P = y_C + S \cdot \sin\varphi. \tag{23}$$

For this mechanism, considering the same input data as those from paragraph 2.1 and $\varphi = 30$ degrees, the driving slide 7 can move on the CP guide under the abscissa axis of the reference system up to the limit point. A simulation was performed with the GWBASIC® software for an imposed stroke, $S = 100$ mm, in which the lower limit position of point P coincides with point C. The successive positions of the mechanism are shown in Fig. 28. A constant velocity has been considered for driving element 7, giving a variable velocity for point Q on the inverse curve.

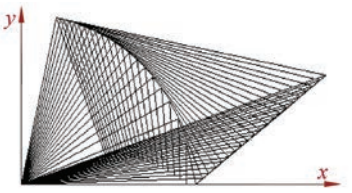

Fig. 28. *Successive positions of the mechanism*

The direct curve is plotted in Fig. 29 and the reverse curve in Fig. 30.

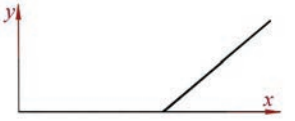

Fig. 29. *The direct curve*

Fig. 30. *The reverse curve*

The geometrical model of the mechanism obtained with the SolidWorks® software was imported into the ADAMS® software for simulation and kinematic analysis (Fig. 31).

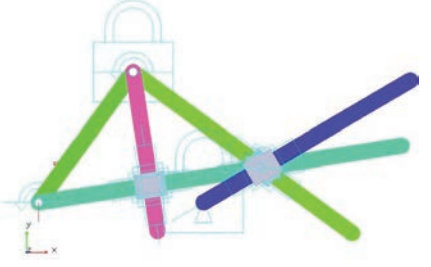

Fig. 31. *The model of the mechanism in the ADAMS® software*

A sinusoidal variation was set for the driving element 7 (Eq. (24), Fig. 32). The initial position of point P is 43 mm from C.

$$f\left(time\right) = 43 \cdot \sin\left(time\right). \tag{24}$$

Fig. 32. *Defining runtime function in the ADAMS® software*

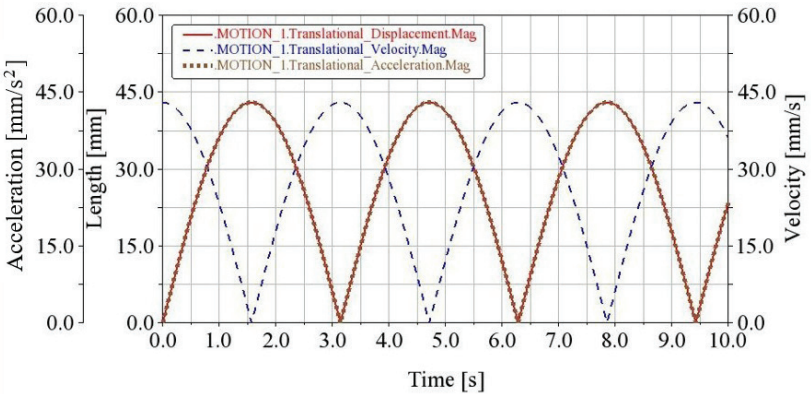

Fig. 33. *Kinematic diagrams for driving element*

The displacement [mm], the velocity [mm/s] and the acceleration [mm/s²] for driving element take values within the range of 0 to 43 (Fig. 33).

The trajectories of points P and Q were plotted during animation (Fig. 34) .

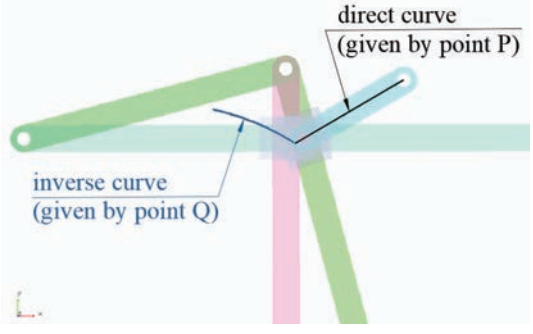

Fig. 34. *The curves drawn in the ADAMS® software*

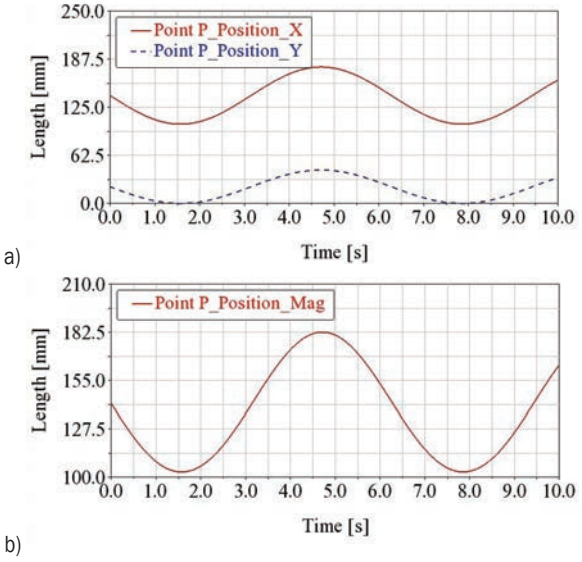

Fig. 35. *The diagram of coordinates for point P; a) the Cartesian coordinates, and b) the polar radius*

The law of P-point displacement has an inflection on both the direct and the return stroke at the middle of it.

Fig. 35 depicts the diagrams of the Cartesian coordinates and the polar radius of the point P as functions of time.

The maximum velocity has the value of 43 mm/s and the acceleration has the maximum value of 43 mm/s², in accordance with the law of motion imposed on the driving element (Figs. 36a nd 37) .

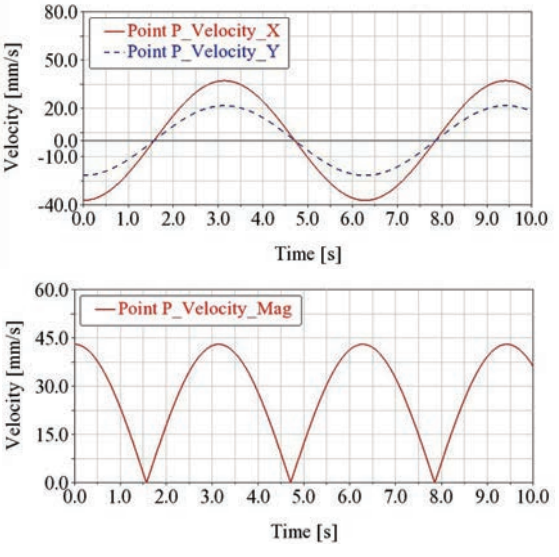

Fig. 36. *The diagram of velocity for point P; a) the projections on the system axes, and b) the magnitude*

The diagrams of the Cartesian coordinates and the magnitude of the point Q as functions of time are shown in Fig. 38

The point Q reaches the maximum speed value of 249 mm/s at the middle of the stroke (215 mm), after 17 s from the lower position of the slide (Fig. 39) .

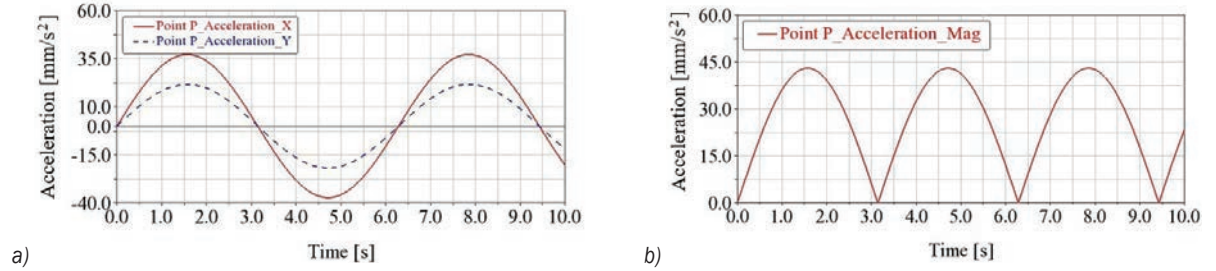

a) b)

Fig. 37. *The diagram of acceleration for point* P*; a) the projections on the system axes, and b) the magnitude*

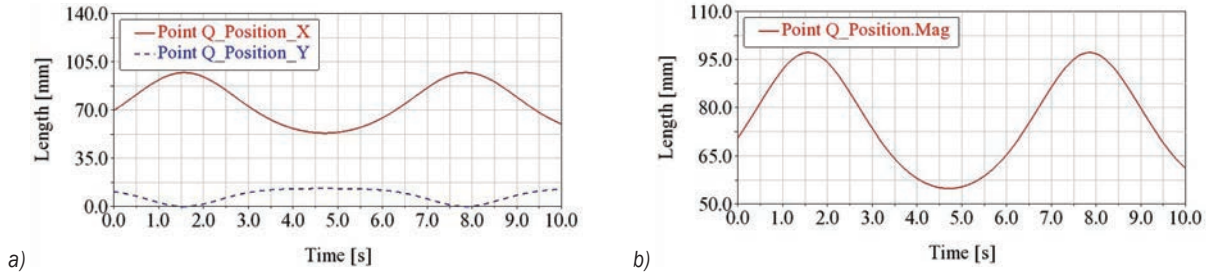

a) b)

Fig. 38. *The diagram of coordinates for point* Q*: a) the Cartesian coordinates, and b) the polar radius*

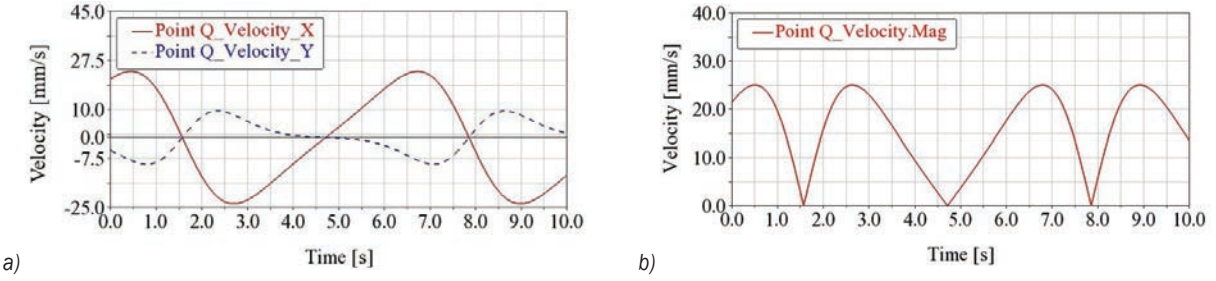

a) b)

Fig. 39. *The diagram of velocity for point Q: a) the projections on the system axes, and b) the magnitude*

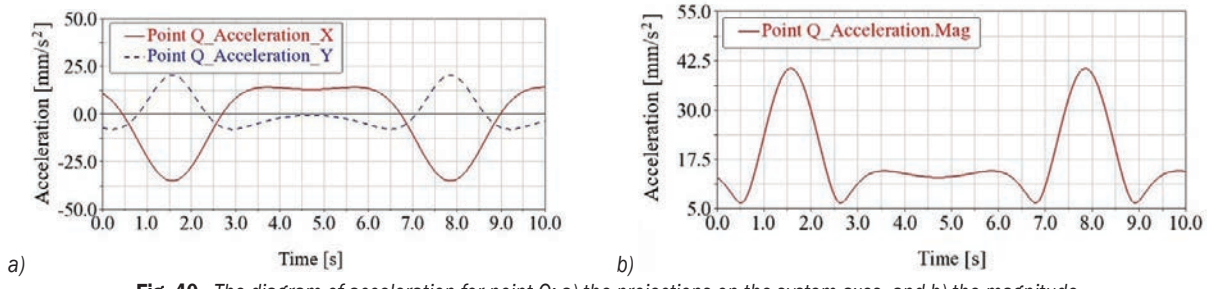

a) b)

Fig. 40. *The diagram of acceleration for point Q; a) the projections on the system axes, and b) the magnitude*

The acceleration has three local maxima (0.32 mm/s², 45 mm/s² and 45 mm/s²) on a double stroke (Fig. 40) .

2.3 Elliptical Direct Curve

The case when the direct curve of P is an ellipse has also been studied. An ellipsograph mechanism was taken into consideration (Fig. 41 ; the points on the GH connecting rod describe ellipses, if one of the slides is the driving element.

Artobolevsky's mechanism from Fig. 11 to which the ellipsograph mechanism is joined was considered so that the initial curve is an ellipse. The kinematic scheme for this adapted mechanism is given in Fig. 42.

The following dimensions were used for this mechanism: $x_F = 100$ mm, GH = 79 mm, GP = 36 mm,

AB = 100 mm. If the slide 8 is the driving element, the coordinate x_G at a given time is known.

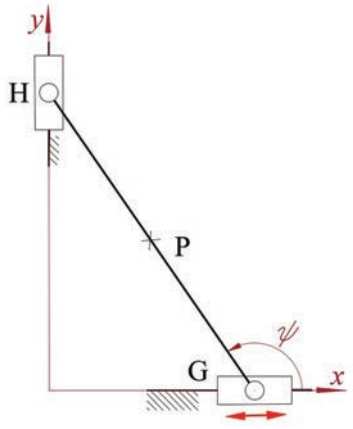

Fig. 41. *The ellipsograph mechanism*

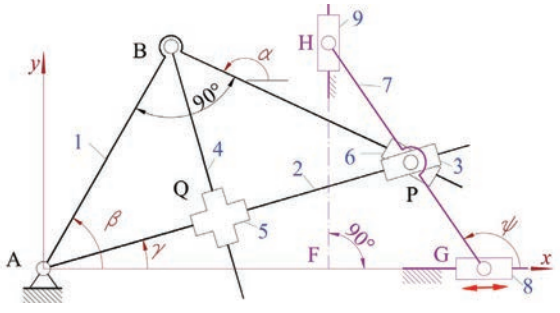

Fig. 42. *The kinematic scheme of the mechanism*

Eqs. (25) to (28) are useful for the calculus of Cartesian coordinates of H and P points.

$$x_H = x_G + GH\cos\psi = x_F = \text{const.}, \tag{25}$$

$$y_H = y_G + GH\sin\psi, \tag{26}$$

$$x_P = x_G + GP\cos\psi, \tag{27}$$

$$y_P = y_G + GP\sin\psi. \tag{28}$$

A simulation was performed with the GWBASIC® program, the driving element 8 having a constant velocity; the mechanism in one position is given in Fig. 43, and some successive positions of it are depicted in Fig. 44.

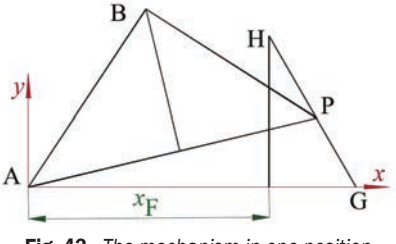

Fig. 43. *The mechanism in one position*

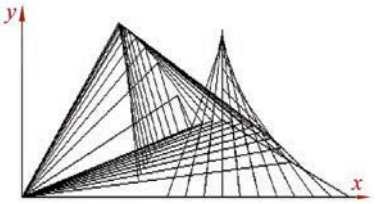

Fig. 44. *The mechanism in a few successive positions*

The curve drawn by point P during simulation is only a part of an ellipse (Fig. 45), being limited by the points of intersection P_1 and P_2, between the circle drawn by point B and the ellipse drawn by point P, due to the geometry of the mechanism (Fig. 46).

Fig. 45. *The curve drawn by point* P *(GWBASIC® program)*

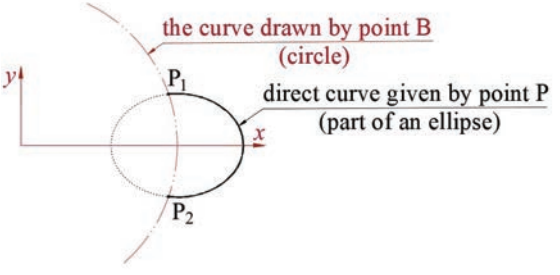

Fig. 46. *The limitation of the mechanism functioning*

The Cartesian coordinates of points P_1 and P_2 were determined with the Maple® software by solving Eq. (29).

$$\begin{cases} x^2 + y^2 = R^2 \\ \dfrac{(x-R)^2}{a^2} + \dfrac{y^2}{b^2} = 1 \end{cases}, \tag{29}$$

where R = AB = 100 mm, a = PH = 43 mm and b = PG = 36 mm.

The values of the coordinates of the locking points resulted as follows: $x_{P1} = x_{P2} = 93.4559$ mm, $y_{P1} = -y_{P2} = 35.5806$ mm.

To avoid the blockage in the operation of the mechanism, the abscissa of point F must be greater than the sum of the dimensions AB and HP. The inverse curve obtained during simulation is that of Fig. 47.

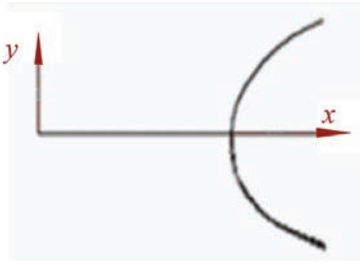

Fig. 47. *The inverse curve drawn by point Q (GWBASIC® software)*

The geometrical model of the mechanism was obtained with the SolidWorks® software and imported into the ADAMS® software for the kinematic analysis (Fig. 48). The starting position of the mechanism was considered in x_G = 137.79 mm and the corresponding coordinates of the point P are x_{P0} = 120.57 mm and y_{P0} = 31.613 mm (near to the point P_1).

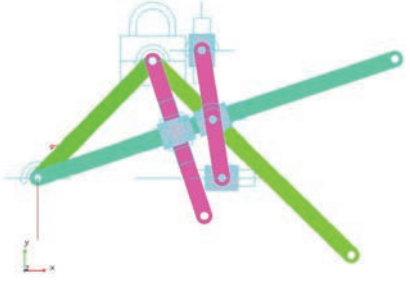

Fig. 48. *The model of the mechanism in the ADAMS® software*

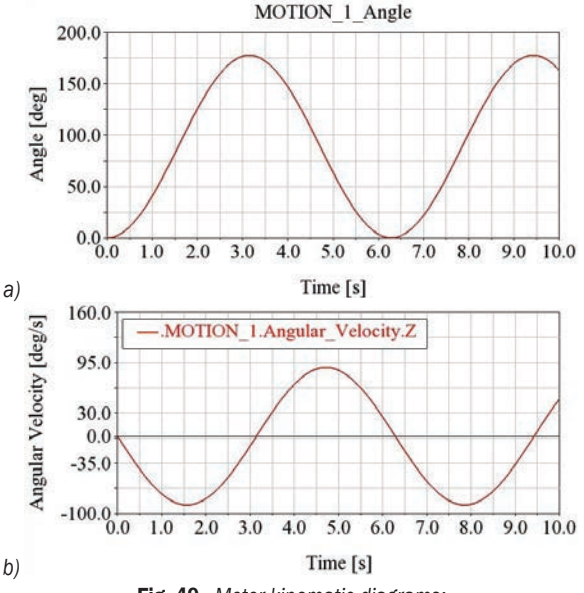

Fig. 49. *Motor kinematic diagrams; a) the angle, and b) angular velocity*

The engine from the G-rotation joint has the motion law given by Eq. 30. In the ADAMS® software the option "*velocity*" is selected.

$$f\left(time\right)=1.55\cdot\sin\left(time\right). \tag{30}$$

The maximum angular velocity of the engine is 89 deg/s (Fig. 49b) and the angular stroke of it is 178 degrees (Fig. 49a).

The Fig. 50 shows the elliptical curves generated by points P and Q using the ADAMS® software.

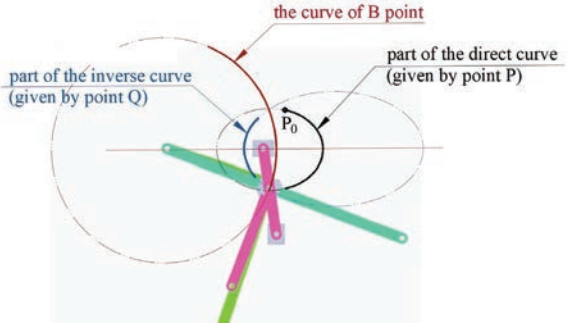

Fig. 50. *The curves drawn in the ADAMS® software*

The diagrams of the Cartesian coordinates and the polar radius of the point P as functions of time are shown in Fig. 51.

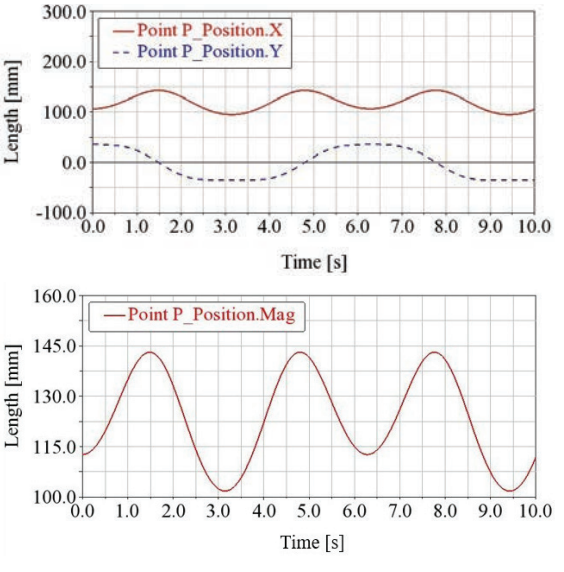

Fig. 51. *The diagram of coordinates for point P; a) the Cartesian coordinates, b) the polar radius*

For the selected 2×178 degrees double angular stroke of the motor, the point P will have an oscillating motion on an elliptical trajectory. When the point P moves clockwise on the ellipse (Fig. 52), the point Q moves in the trigonometric direction on its ellipse (Fig. 53).

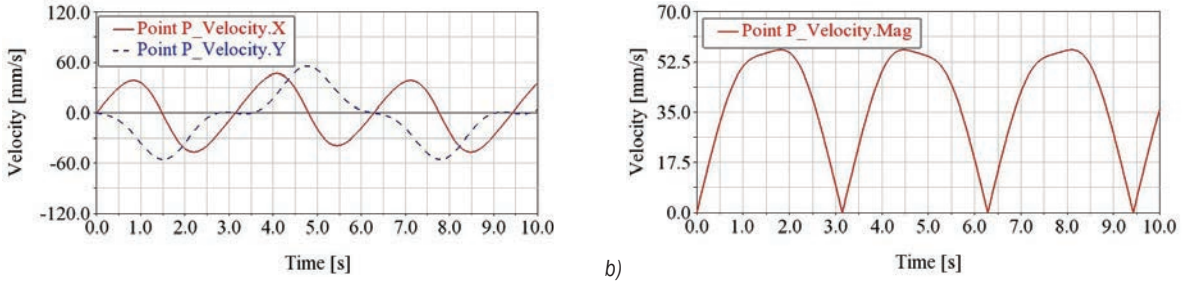

Fig. 52. *The diagram of velocity for point* P*; a) the projections on the system axes, and b) the magnitude*

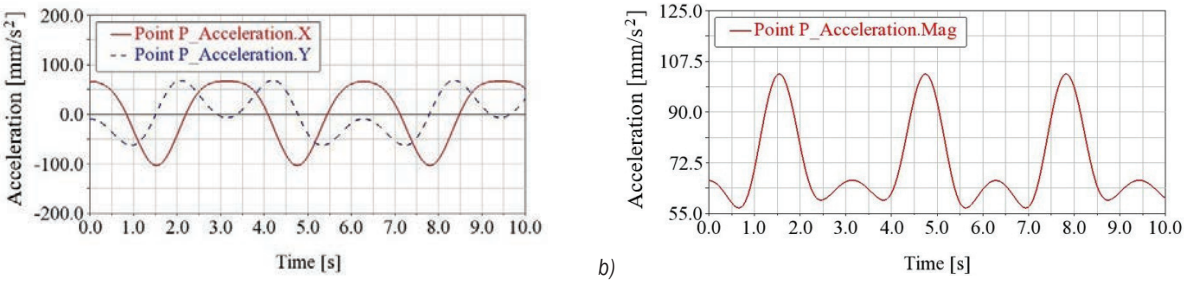

Fig. 53. *The diagram of acceleration for point* P*; a) the projections on the system axes, and b) the magnitude*

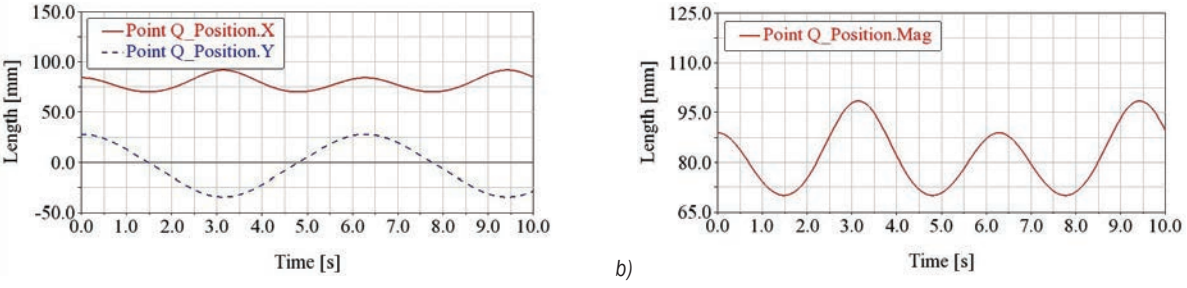

Fig. 54. *The diagram of coordinates for point* Q*; a) the Cartesian coordinates, and b) the polar radius*

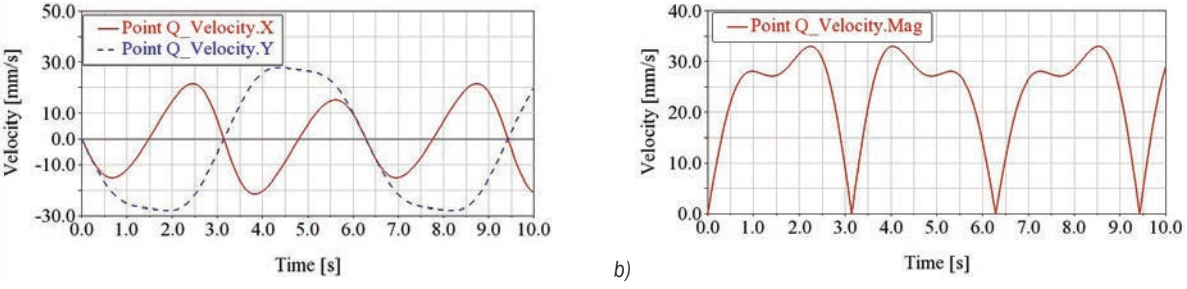

Fig. 55. *The diagram of velocity for point* Q*; a) the projections on the system axes, and b) the magnitude*

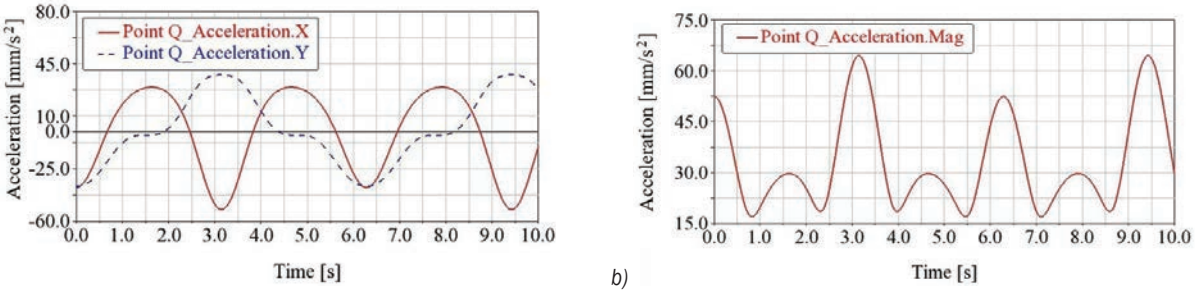

Fig. 56. *The diagram of acceleration for point* Q*; a) the projections on the system axes, and b) the magnitude*

The inverse curve drawn by the point Q is also an ellipse but the maximum velocity of point Q (Fig. 55) is slower than that of point P (33.2 mm/s and 35.5 mm/s, respectively) (Fig. 52) and the maximum acceleration of point Q also has lower values (56 mm/s² and 103.2 mm/s², respectively) (Fig. 56) than that of point P (Fig. 53).

2.4 Spiral direct curve

The case in which point P describes an Archimedes' spiral was also analysed. The proposed mechanism has the kinematic scheme given in Fig. 57. In order to have the point P drawing the Archimedes' spiral, two motors were used: one in rotation joint F and one in translation joint P (Fig. 57), with constant angular velocity and constant linear velocity respectively.

The equation of an Archimedes' spiral drawn by point P is $\rho = a \cdot \varphi$, where a is a constant and φ and ρ are their polar coordinates in relation to the fixed system xFy_1.

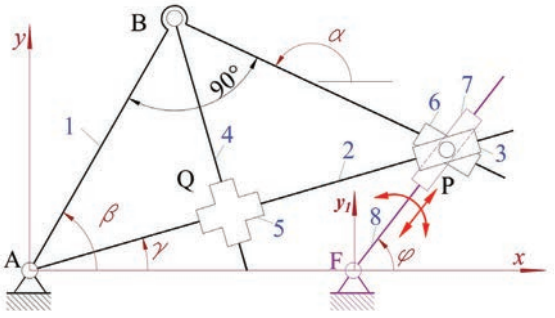

Fig. 57. *The kinematic scheme of the mechanism*

The following input data were considered for this mechanism: x_F = 100 mm, AB = 100 mm, a = 5 mm and φ = 0 to 4π.

The direct and inverse curve obtained with the GWBASIC® software are presented in Figs. 58 and 59.

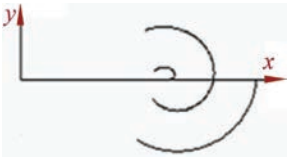

Fig. 58. *Divided Archimedes' spiral drawn by point P*

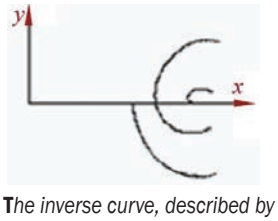

Fig. 59. *The inverse curve, described by point Q*

For the functioning of the mechanism on the three sub-intervals (Fig. 60), the element 8 must be positioned at one end of each divided curve.

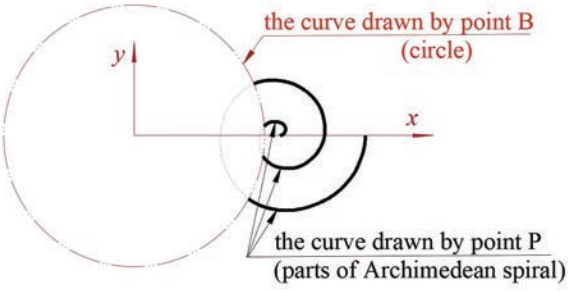

Fig. 60. *The limitation of the operating area*

The mechanism does not work in two sub-intervals and the limiting points are found at the intersection between the curve described by point B and that described by point P (Fig. 60).

The limitation of the operating area depends on the geometry of the mechanism and on the velocities of the two motors. If other values for the velocities of the motors are adopted, the pitch of the spiral will be changed. If the pitch is too large, the spiral drawn on the first 360 degrees will not intersect the circle generated by point B. For example, for the velocity of the linear motor of 30 mm/s and angular velocity of the rotary motor 0.6 rad/s, the constant of the Archimedes' spiral a = 50 and its pitch of 314.16 mm are obtained and the mechanism does not lock.

If one intends to keep the shape of a spiral that intersects the circle of B, the abscissa of point F must be increased, such as to avoid the functioning limitation. The geometrical model of the mechanism was obtained with the SolidWorks® software and imported into the ADAMS® software for the kinematic analysis (Fig. 61).

Two motors were placed in the ADAMS® software: one rotary in F joint and one linear in P-translation joint (Fig. 78).

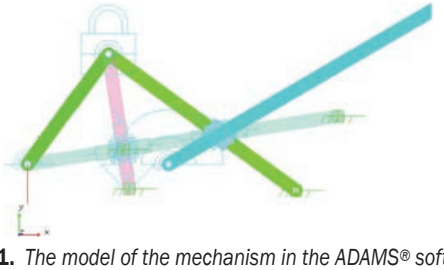

Fig. 61. *The model of the mechanism in the ADAMS® software*

In the case in which the point P goes on the direct curve in trigonometric direction with the angular

velocity of the driving element of 0.6 rad/s and the linear motor speed of 2 mm/s, the curves from Fig. 62 are obtained.

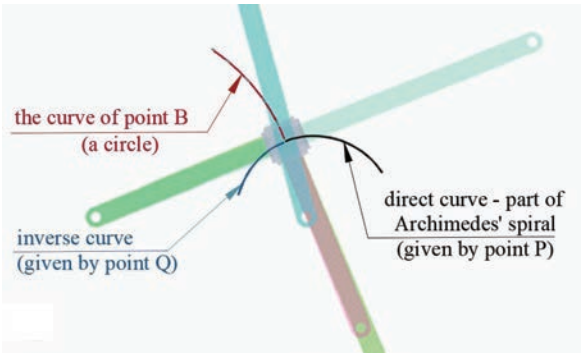

Fig. 62. *The case for trigonometric direction of* P *point motion*

Fig. 63 depicts the curves obtained when the point P goes on the direct curve in clockwise direction, with the angular velocity of the driving element of –0.6 rad/s and the linear motor speed of –2 mm/s.

The values of engine velocities determine the equation of the Archimedes' spiral (Eqs. (31) and (32)). a = 3.33 mm and the pitch of Archimedes' spiral equals 20.94 mm.

$$\rho = a \cdot \varphi, \tag{31}$$

$$\dot{\rho} = a \cdot \dot{\varphi}. \tag{32}$$

The position kinematic diagrams for point P are shown in Fig. 64 for this case.

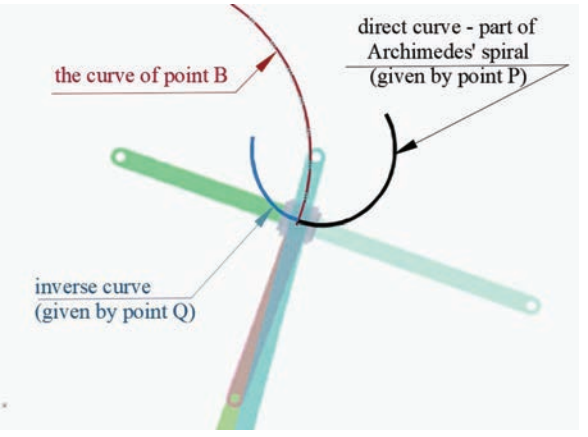

Fig. 63. *The case for the clockwise direction of* P *point motion*

During the functioning interval of 4 s, the slide 7 is moved with constant velocity by the linear motor towards the rotation joint C, but the velocity tangential component of the point P imposed by rotation motor decreases due to the decreasing of the radius, so that the absolute velocity diagram of the point is descending (Fig. 65a).

Although the slope of the velocity diagram is constant, the acceleration is variable (Fig. 65b) because the normal acceleration depends on the polar radius

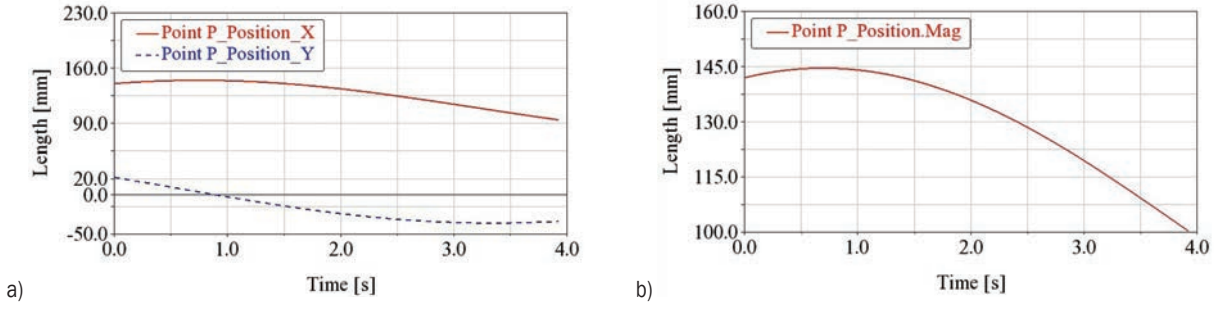

a) b)

Fig. 64. *The diagram of coordinates for point* P*; a) the Cartesian coordinate on* x_{Ay} *system, b) the polar radius*

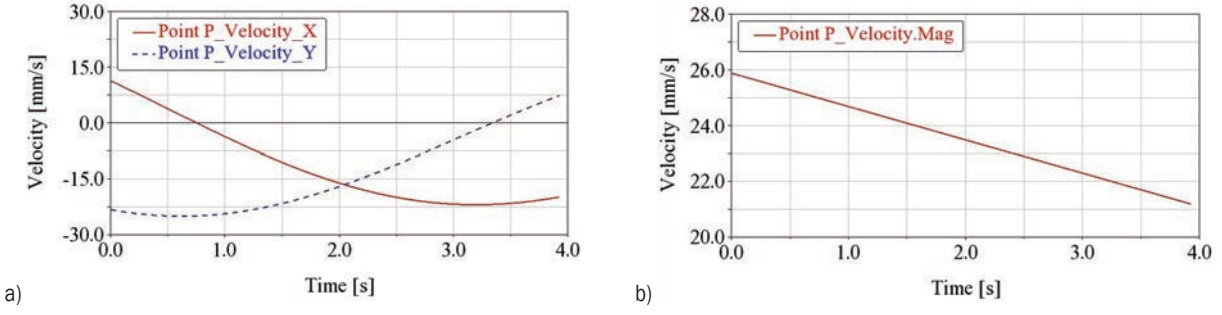

a) b)

Fig. 65. *The diagram of velocity for point* P*; a) the projections on the system axes, and b) the magnitude*

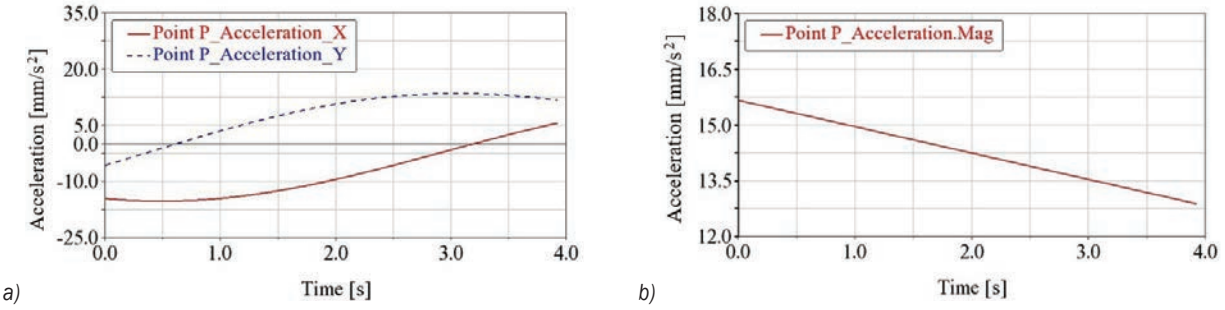

a) b)

Fig. 66. *The diagram of acceleration for point* P*; a) the projections on the system axes, and b) the magnitude*

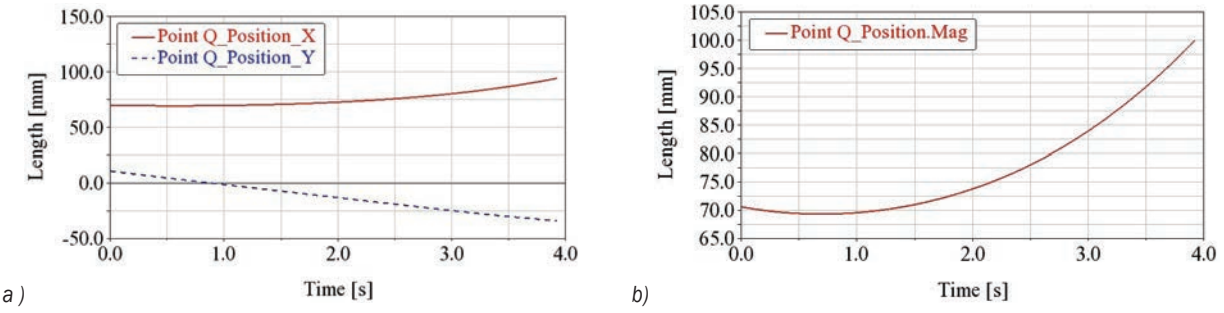

a) b)

Fig. 67. *The diagram of coordinates for point* Q*; a) the Cartesian coordinates, ad b) the magnitude*

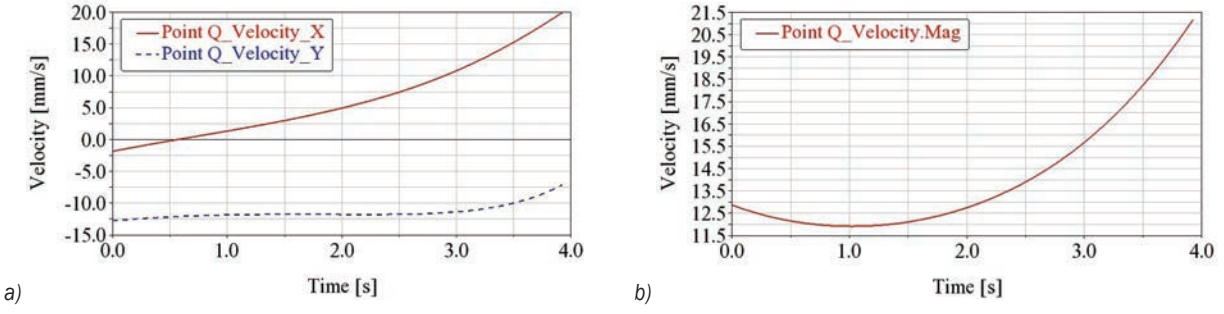

a) b)

Fig. 68. *The diagram of velocity for point* Q*; a) the projections on the system axes, b) the magnitude*

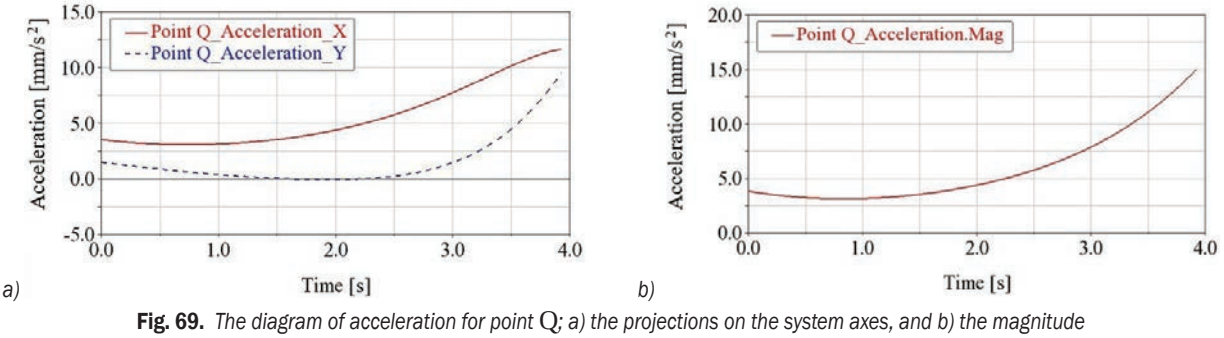

a) b)

Fig. 69. *The diagram of acceleration for point* Q*; a) the projections on the system axes, and b) the magnitude*

of the point P. In the initial position, the point P has the polar radius of 3 mm referring to the xFy_1 system and the normal acceleration is a^n = 15.48 mm/s², according to the kinematic diagram.

The animation and diagrams of the velocities reveal that the point P moves on the direct curve in a clockwise direction and the point Q goes in trigonometric direction on the inverse curve (Figs. 65 and 66).

While the velocity magnitude of the tracer point P of the direct curve is decreasing, that of the tracer point of the inverse curve is decreasing in the first phase and is increasing in the second phase to the value of 21 mm/s (Fig. 9).

The diagram of acceleration magnitude for point Q is shown in Fig. 10 and its maximum value is 5 mm/s^2 at the end of the interval.

3 CONCLUSIONS

This work has brought attention to the creation of new inversor mechanisms that draw exactly imposed curves and has analysed their functioning. We have established some applications for the inversor mechanisms in lifting-lowering systems, conveyor belts, machine tools, curve generation mechanisms, kinetic light art, and other industrial mechanisms.

A Crawford inversor mechanism has been analysed, and we have concluded that it is suitable for rapid placement/retraction movements in/from a given position of an object. It is also possible to perform optimization in order to coordinate the operating time.

Four new inversor mechanisms have been designed, starting from the structure of Artobolevsky's inversor mechanism, by adding kinematic chains that draw different direct curves (a circle, a straight line, an ellipse, and an Archimedean spiral).

Kinematic analysis of all these mechanisms was performed and the obtained inverse curves are in accordance with the information from **[3]**.

Following the results obtained for the proposed mechanisms, conclusions were drawn to avoid blockage in each particular studied case. The avoidance of the locking is achieved by modifying the geometry of the mechanisms, and for the case of the direct Archimedean spiral curve this can also be done by modifying the motion parameters of the motors.

We emphasise that the premises for a full motion study, including dynamic one, have been created for inversor mechanisms.

4 ACKNOWLEDGEMENTS

This research received no specific grant from any funding agency in the public, commercial, or not-for-profit sectors.

The authors declare that they have no conflict of interest.

5 REFERENCES

[1] Taimina, D. (2007). Historical mechanisms for drawing curves. Amy Shell-Gellasch, (ed.) *Hands on History: A Resource for Teaching Mathematics*, p. 89-104, Mathematical Association of America, **DOI:10.5948/UPO9780883859766.011**.

[2] Brix, T., Döring, U., Reeßing, M. (2011). Creating Present-Day Solutions from Historical Knowledge. *13th World Congress in Mechanism and Machine Science*, p. 1744-1751.

[3] Weisstein, E.W. (2020). Inverse Curve, from MathWorld - A Wolfram Web Resource. from *https://mathworld.wolfram.com/InverseCurve.html*, accessed on 2020-05-10.

[4] Steiner, J. (2020). Encyclopedia Britannica, no. 1911, from *https://en.wikisource.org/wiki/1911_Encyclop%C3%A6dia_Britannica/Steiner,_Jakob*, accessed on 2020-05-10.

[5] Artobolevsky, I.I. (1959). *Mechanism theory for solving planar curve problems*. Academy of Sciences of the USSR, Moscow. (In Russian).

[6] Tienari, O. (1980). *Reversing mechanism for the direction of rotation in a drilling apparatus*. Patent US4399876A, United States Patent Office, Washington.

[7] Artobolevsky, I. (1975). Mechanisms in Modern Engineering Design: A Handbook for Engineers, Designers and Inventors, from *https://archive.org/details/mechanism_in_modern_engineering_V1-lever_mechanism*, accessed on 2020-05-10.

[8] Bullough, W.A., Johnson, A.R., Makin, J., Tozer, R.C. (2001). ESF Clutch Driven Mechanisms and the ER Linear Inversor Motion a Demonstrator. Sulejman, A. (ed.) *Smart Structures*, vol. 429, Springer, Vienna, **DOI:10.1007/978-3-7091-2686-8_14**.

[9] Duca, C.D.; Buium, F., Pârăoaru, G. (2003). *Mechanisms*, Gh. Asachi, Iaşi. (In Romanian)

[10] Artobolevsky, I.I. (1971). *Mechanism in Modern Technology*. Vol. II., Nauka, Moscow. (In Russian)

[11] Tutunaru, D. (1969). *Planar Rectilinear Mechanisms and Inversor Mechanisms*. Tehnica, Bucharest. (In Romanian)

[12] Chalfin, N.L. (1961). *Phonograph Pickup Arm*. Patent 2977126A, United States Patent Office, Washington.

[13] Garrec, P. (1993). *Device for Transmitting Movement between a Solid and a Member, in Particular for a Robot Able to be Moved on Legs*. Patent 5219410 A, United States Patent Office, Washington.

[14] Kunzler, P.A., Schmitt, P., Poblano, R.D.V., Chan, B., Liang, P.A., Vairani, F.H., Kilian, A., Chin, R.C., Mitchell, W.J. (2011). *Wheel Embedded Suspension*. Patent 7938210B2, United States Patent Office, Washington.

[15] Nickstadt, G. (1974). *Gear Drive Reversing Mechanism*, Patent US3851537A, United States Patent Office, Washington.

[16] Shkolnik, N. (1984). *Walking Apparatus*. Patent US4462476A, United States Patent Office, Washington.

[17] Stephenson valve gear. Wikipedia, from *https://en.wikipedia.org/wiki/Stephenson_valve_gear*, accessed on 2020-05-10.

[18] Dijksman, E.A. (1994). True straight-line linkages having a rectilinear translating bar. Lenarčič, J., Ravani, B. (eds). *Advances in Robot Kinematics and Computational Geometry*, p. 411-420, Springer, Dordrecht, **DOI:10.1007/978-94-015-8348-0_41**.

[19] Evert, A., Dijksman (1993). A way to generalize Peaucellier's inversor. *The 6th IFToMM International Symposium on Linkages and Computer Aided Design Methods*, vol. 1, p. 73-82.

[20] Halicioglu, R., Dulger, L.C., Bozdana, A.T. (2014). Modelling and simulation based on Matlab/Simulink: A press mechanism. *2nd International Conference on Mathematical Modeling in Physical Sciences, Journal of Physics: Conference Series*, vol. 490, art. ID 012053, **DOI:10.1088/1742-6596/490/1/012053**.

[21] Tavoleri, C., Ottaviano, E., Ceccarelli, M. (2007). Design and problems of a new leg-wheel walking robot. *Advances in Climbing and Walking Robots. Proceedings of 10th International Conference*, p. 319-328, **DOI:10.1142/9789812770189_0038**.

[22] Simionescu, P.A; Tempea, I. (1999). Kinematic and kinetostatic simulation of a leg mechanism, *10th World Congress on Theory of Machines and Mechanisms*, p. 572-576.

[23] Halicioglu, R., Dulger, L.C., Bozdana, A.T. (2017). An automation system for data processing and motion generation. *International Artificial Intelligence and Data Processing Symposium*, **DOI:10.1109/IDAP.2017.8090294**.

[24] Nunez-Altamirano, D.A., Juarez-Campos, I., Márquez-Pérez, L., Flores-Díaz, O., Romero-Munoz, L. (2016). Dynamics of a novel robotic leg based on the Peaucellier - Lipkin mechanism on linear paths during the transfer phase. *Advances in Mechanical Engineering, Advances in Mechanical Engineering*, vol. 8, no. 7 p. 1-10, **DOI:10.1177/1687814016657046**.

[25] Huang, M. (2019). On dimension synthesis of Hart's inversor III straight-line mechanism as a precision robotic end-of-arm tool. *Proceedings of ASME International Mechanical Engineering Congress and Exposition, Volume 4: Dynamics, Vibration, and Control*, **DOI:10.1115/IMECE2019-11522**.

[26] Kawamoto, A. (2004). *Generation of Articulated Mechanisms by Optimization Techniques*. PhD thesis, Technical University of Denmark, Lyngby.

[27] Zhu, B., Zhang, X., Zhang, H., Liang, J., Zang, H., Li, H., Wang, R. (2020). Design of compliant mechanisms using continuum topology optimization: A review. *Mechanism and Machine Theory*, vol. 143, art. ID 103622, **DOI:10.1016/j.mechmachtheory.2019.103622**.

[28] Halicioglu, R., Jomartov, A., Kuatova, M. (2021). Optimum design and analysis of a novel planar eight-bar linkage mechanism. *Mechanics Based Design of Structures and Machines*, **DOI:10.1080/15397734.2021.1995410**.

[29] Tuleshov, A., Halicioglu, R., Shadymanova, A., Kuatova, M. (2021). Kinematic synthesis method and eccentricity effects of a Stephenson mechanism. *Mechanical Science*, no. 12, p. 1-8, **DOI:10.5194/ms-12-1-2021**.

[30] Ahrendt, M.H. (1944). A general method for the construction of a mechanical inversor. *Mathematics Teacher,* vol. 37, no. 2, p. 75-80, **DOI:10.5951/MT.37.2.0075**.

[31] Bryant, J., Sagwin, C. (2008). *How round is your circle? When engineering and mathematics meet.* Princeton University Press, Princeton.

[32] Juarez-Campos, I., Nunez-Altamirano, D., Marquez-Perez, L., Romero-Munoz, L., Juarez-Campos, B. (2018). Hexapod with legs based on Peaucellier-Lipkin mechanisms: A mathematical structure used in reconfiguration for path planning. *International Journal of Advanced Robotic Systems*, p. 1-18, **DOI:10.1177/1729881418795929**.

[33] Zhan, J.; Yang, K.; Huang, Z. (2014). Topological design of hinge-free compliant mechanisms using the node design variables methods. - In: Zhang, X., Liu, H., Chen, Z., Wang, N. (eds.) *Intelligent Robotics and Applications. Lecture Notes in Computer Science*, vol 8918. Springer, Cham, p. 567-575, **DOI:10.1007/978-3-319-13963-0_57**.

[34] Schoofs, I. (2020). Mesmerizing Slow Motion, from *https://ivoschoofs.com/project/just-because-you-are-a-character-doesnt-mean-you-have-character/*, accessed on 2020-05-10.

[35] Buckley, J., Huang, M.Z. (2011). A study on dimension synthesis for the peaucellier mechanism. *Proceedings of ASME International Mechanical Engineering Congress and Exposition*, **DOI:10.1115/IMECE2011-64278**.

[36] Crawford, W.R. (1936). The mechanical construction of the general conic section. *Engineer*, vol. 162, no. 4207.

[37] An Ingenious Reversing Mechanism for Machine Tools (1899). Scientific American, from *https://www.scientificamerican.com/article/an-ingenious-reversing-mechanism-fo/*, accessed on 2020-05-10.

[38] Gogu, G. (2005). Mobility of mechanisms: a critical review. *Mechanism and Machine Theory*, vol. 40, no. 9, p. 1068-1097, **DOI:10.1016/j.mechmachtheory.2004.12.014**.

Strojniški vestnik - Journal of Mechanical Engineering 69(2023)3-4, 119-134
DOI:10.5545/sv-jme.2022.266
Original Scientific Paper
Received for review: 2022-07-01
Received revised form: 2022-11-24
Accepted for publication: 2023-02-14

Influence Analysis and Performance Optimization of a Pneumatic Actuator Exhaust Utilization System

Qihui Yu[1,2,3] –·Fengqi Li[1]* – Xin Tan[1]

[1] Inner Mongolia University of Science & Technology, Department of Mechanical Engineering, China
[2] Beijing Key Laboratory, Pneumatic and Thermodynamic Energy Storage and Supply, China
[3] University of Nottingham, Department of Mechanical, Materials and Manufacturing Engineering, UK

Due to the loss of exhaust energy, the compressed air energy utilization efficiency in pneumatics system is low. To realize the recovery and utilization of cylinder compressed air, a new type of compressed air utilization system is proposed, and the composition and working principle of the system are introduced. According to the working process of the system, the mathematical model of the system is established by using equations such as energy equation and gas state equation. The model is simulated by MATLAB/Simulink tools, and the correctness of the mathematical model is verified by experiments. The mathematical models are converted into dimensionless models, and the main parameters affecting the system's operating characteristics are obtained through model simulation analysis. The influencing parameters are optimized by using the analytic hierarchy process and the grey correlation analysis method, and the exhaust utilization efficiency of the system is 34.7 % under the optimal parameter combination. To further utilize the compressed air expansion, the opening and closing time of the solenoid valve was controlled to study the energy-saving effect of the system. The study found that when the initial pressure of the compressed air supply tank was set to 0.5 MPa, 0.6 MPa, and 0.7 MPa, the maximum energy saving efficiency was 23.25 %, 24.99 %, and 26.12 %, respectively. When the volume of the compressed air supply tank is set to 0.8 L, 1 L, and 1.2 L, the maximum energy-saving efficiency is 30.01 %, 24.99 %, and 21.51 %, respectively. This paper provides a new technical scheme for compressed air recovery and reuse, as well as a theoretical basis for the control of subsequent compressed air utilization systems.

Keywords: pneumatic system, exhaust utilization, analysis, characteristic, energy saving

Highlights

- *An air exhaust utilization loop is proposed, which can recycle the air exhaust to realize energy savings.*
- *The speed of piston movement and the efficiency of exhaust gas utilization determine the performance of the system.*
- *The multi-objective parameters are optimized to keep the system stable and good performance.*
- *Controlling the on-off time of the solenoid valve can further improve the efficiency of gas utilization.*

0 INTRODUCTION

The pneumatic system has the characteristics of low-cost, high-strength ratio, convenient maintenance, cleanliness and environmental protection, and high safety [1] to [4]. However, compressed air is expensive to produce and is one of the most expensive energy carriers [5]. Research has found that the actual energy efficiency of some pneumatic systems is low, or even 80 % of the energy will be wasted in the form of heat or other energy in the worst case, which increases the application cost of pneumatic systems [6]. Developing and researching the energy savings of pneumatic systems are urgent tasks.

In recent years, some researchers have changed and optimized the structure of the pneumatic circuit to improve its energy efficiency. Du et al. [7] proposed a bridge-type energy-saving loop that fully utilizes the expansion energy to do work, and significantly improved the system energy efficiency by 60 % to 70 % through algorithm optimization control. After that, Du et al. [8] used a value to connect the two chambers of the cylinder to improve the bridge circuit and optimized the control through the finite element configuration method and the interior point method, which could achieve 55 % to 78 % of air energy saving and the cylinder runs more smoothly. Yang et al. [9] and [10] proposed a novel energy recovery booster valve (BVER) and studied its energy efficiency by introducing the concept of aerodynamics. Based on the thermodynamics of metamorphic compressed air, the energy efficiency evaluation and pressure response model of BVER is proposed, which increases the boost ratio by 15 % to 20 %, and the efficiency can be increased by 5 % to 10 % depending on the supply pressure. Endler et al. [11] added a quick-acting on-off valve to the circuit to reduce the impact of external load on compressed air consumption and proposed a compressed air energy-saving decision-making algorithm based on differential pressure and control signals. The research results show that compressed air consumption can be reduced by 17 % to 34 %. Shi et al. [12] and Shi and Cai [13] proposed an expansion energy booster, which cuts off the air supply before the piston moves to the end of the stroke and uses the air expansion to drive the remaining stroke to

*Corr. Author's Address: Inner Mongolia University of Science & Technology, Department of Mechanical Engineering, Baotou 014010, China, 380264335@qq.com

achieve energy savings. The SMC company proposes a product that applies the air-saving circuit. It cooperates with the cylinder through the valve and uses the compressed air in the exhaust chamber of the cylinder as the power source when the piston rod retracts to achieve the effect of energy saving, which reduces the air consumption by 35 % compared with the general circuit [14]. For the horizontal installation of the cylinder, Beater [15] adds a pressure-reducing valve to the circuit to reduce the consumption of compressed air by controlling the air supply pressure and shows that the use of this circuit can save 25 % of compressed air. Doll et al. [16] and Doll and Sawodny [17] took full advantage of the expansion energy by controlling five reversing valves, and the studies show that the circuit can save 38 % of the air under optimal conditions. Some scholars make full use of exhaust energy in the form of energy conversion. Cummins recovers energy and stores strain energy with a rubber inner bladder [18]. Luo et al. [19] adopt a closed-loop coordinated control strategy to convert exhaust energy into electrical energy for reuse by utilizing scroll expansion technology.

There are two ways to improve compressed air energy efficiency: changing the structure of the optimized pneumatic circuit and converting the energy of the compressed air. However, the former has a narrow application range and is difficult to control, and the latter has higher requirements on the conversion device and larger energy loss. In most conventional pneumatic circuits, the energy contained in the compressed air is rarely used efficiently. The method of recovering and utilizing compressed air is simple and easy to control and is an effective way to improve energy efficiency.

In some circuits for compressed air recovery and utilization, the two processes of recovery and utilization cannot be applied to the same scene, resulting in wasted compressed air energy. In view of the above problems, this paper proposes a pneumatic actuator exhaust utilization circuit and introduces the system composition and working principle. Secondly, the mathematical model of the system is established and an experimental platform is built, and the model is verified with experiments. Afterward, through a dimensionless model, the main parameters affecting the performance of the system are studied and optimized. Finally, by controlling the opening and closing time of the solenoid valve, the further utilization of the compressed air expansion energy is studied, which lays a good theoretical foundation for the next step to efficiently control the pneumatic system.

1 SYSTEM COMPOSITION AND WORKING PRINCIPLE

Fig. 1 shows the circuit diagram of the compressed air utilization system. It is mainly composed of the

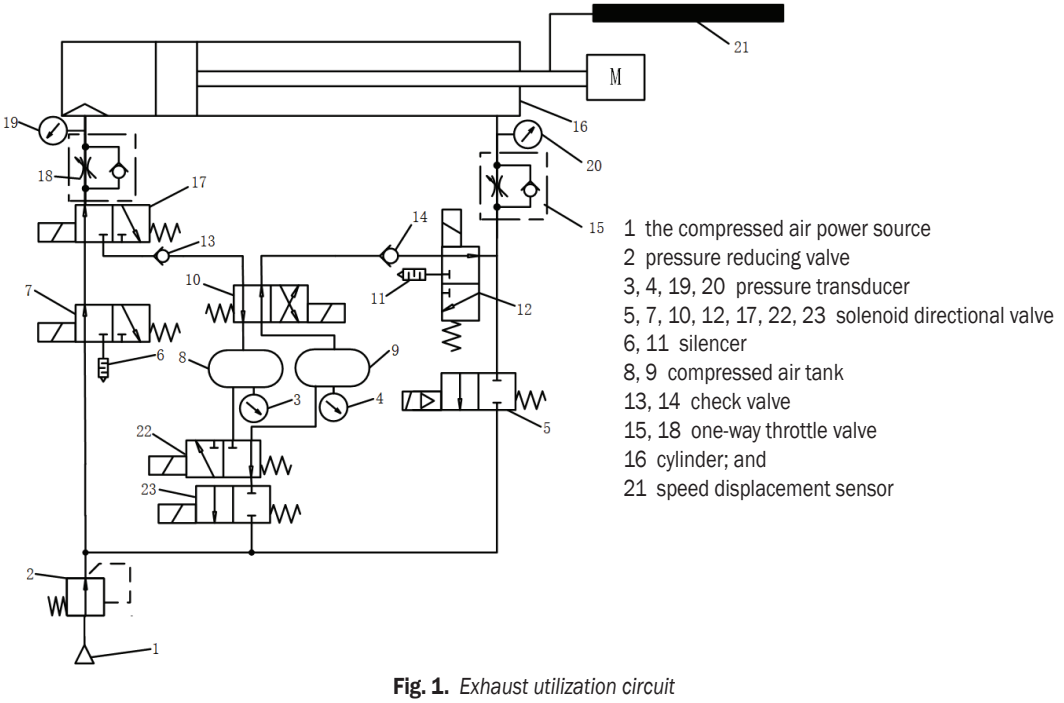

Fig. 1. *Exhaust utilization circuit*

compressed air source, cylinder, compressed air tank, directional valve, one-way valve, etc. The rod-less chamber of the cylinder is named chamber *a*, the rod chamber is named as chamber *b*, the compressed air tank connected with the chamber *a* is a recycle compressed air tank (*tank* 1) , and the compressed air tank connected with the chamber *b* is a compressed air supply tank (*tank* 2). The pressure of chamber *a*, chamber *b*, *tank* 1 and *tank* 2 are named by p_a, p_b, $p_{tank\ 1}$, $p_{tank\ 2}$. To study the influence of the relationship between the pressure in the compressed air tank and the cylinder chamber on the performance of the system, define the pressure ratio $\lambda_1 = p_a/p_{tank\ 1}$ as the recovery switching criterion, and $\lambda_2 = p_{tank\ 2}/p_b$ as the supply switching criterion. The principle of a pneumatic actuator exhaust utilization system is as follows.

When the piston rod is extended, the compressed air energy source 1 supplies compressed air to chamber *a*, the released compressed air is adjusted by valve 2, and flows into cylinder chamber *a* after passing through valve 7, value 17 and value 18 and drives the cylinder to the right, the compressed air in the chamber *b* is discharged into the environment through valve 5 and valve 12.

When the piston rod is retracted, *tank* 2 is used as an energy source to supply compressed air to chamber *b* through valve 4, valve 10, valve 12, and valve 15 when $p_{tank\ 2}/p_b > \lambda_2$. If $p_{tank\ 2}/p_b < \lambda_2$, the compressed air energy source 1 is adjusted by valve 2, and the compressed air is supplied to chamber *b* through valve 5 and *t* valve 15. If $p_a/p_{tank\ 1} > \lambda_1$, the compressed air in chamber *a* flows into the recovery compressed air tank through valve 8, valve 17, and valve 13. If $p_a/p_{tank\ 1} < \lambda_1$, Then the compressed air in chamber *a* is discharged into the environment through valve 8, valve 17, and value 7.

When the recovery process is completed, but the energy is not enough to drive the movement of the piston rod, compressed air energy source 1 is used to pressurize the compressed air tank through electromagnetic reversing valve 21 and value 22 to meet the requirements.

2 EXPERIMENTAL VERIFICATION OF MATHEMATICAL MODELS

2.1 Mathematical Models

To simplify the calculation, the following assumptions are proposed: (1) The compressed air in the loop follows the ideal compressed air law; (2) The compressed air source is a stable pressure source, there is no leakage in the system, and the effective area of the inlet and exhaust ports is the same; (3) The compressed air flows into a stable one-dimensional state; (4) The supply compressed air temperature is the same as the atmospheric temperature; (5) The initial pressure of *tank* 2 is a fixed value.

2.1.1 Energy Equation

Chambers *a* and *b* do not admit compressed air at the same time; according to [20], the energy equation of chambers *a* or *b* can be described as follows:

$$C_v m_i \frac{dT_i}{dt} = \left(S_i h_i + C_v G_i\right)\left(T_e - T_i\right) + RG_i T_i - p_i A_i u, \quad (1)$$

$$C_v m_i \frac{dT_i}{dt} = S_i h_i \left(T_e - T_i\right) + RG_i T_i - p_i A_i u, \quad (2)$$

where, C_v is the constant volume specific heat, [J/(kg·K)], m is compressed air mass, [kg], T is the temperature, [K], T_e is the atmospheric temperature, [K], S is the heat exchange area, [m^2], h is the heat exchange coefficient, [W/(m^{2}K)], R is the compressed air constant, [J/(kg·K)], G is the mass flow rate of the compressed air, [kg/s], p is the pressure, [MPa], A is the area, [m^2], and u is the speed of piston movement, [m/s]. Subscript I represents *a* or *b*.

The energy equation of tank can be described as follows [21]:

$$\frac{dT_j}{dt} = \frac{RT_j}{C_v p_j V_j}\left[G_j C_p T_u - G_j C_v T_j + h_j S_j \left(T_e - T_j\right)\right], \quad (3)$$

where, V is the volume, [m^3]. Subscript j represents *tank* 1or *tank* 2.

2.1.2 Mass Flow Equation

The mass flow equations of chambers *a*, *b*, *tank* 1 and *tank* 2 can be expressed as follows:

$$G_{i,j} = \begin{cases} \dfrac{A_e p_u D}{\sqrt{T_u}} & \dfrac{p_d}{p_u} \le b \\ \dfrac{A_e p_u B}{\sqrt{T_u}} \varphi\left(p_d, p_u\right) & \dfrac{p_d}{p_u} \le b \end{cases}, \quad (4)$$

where

$$\varphi(p_d, p_u) = \left(\frac{p_d}{p_u}\right)^{\frac{2}{k}} - \left(\frac{p_d}{p_u}\right)^{\frac{k+1}{k}}, \quad (5)$$

$$B = \sqrt{\frac{2K}{R(k-1)}}, \quad (6)$$

$$D = \left(\frac{2}{k+1}\right)^{\frac{1}{k-1}} \sqrt{\frac{2k}{R(k+1)}}, \quad (7)$$

where, p_d and p_u are the downstream and upstream pressures, respectively, [MPa], A_e is the effective area of the intake and exhaust ports, [m²], T_u is the upstream temperature, [K], k is the specific heat ratio, and b is the critical pressure ratio.

2.1.3 Dynamic Equation

The force diagram of the piston is shown in Fig. 2. The equation of motion of the piston can be obtained according to Newton's second law.

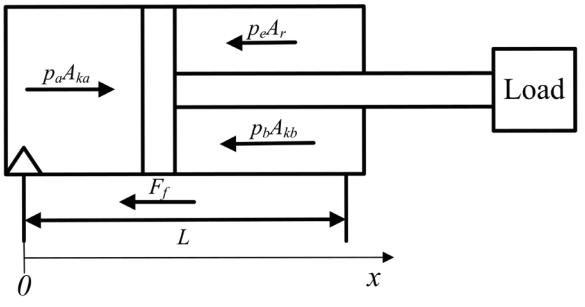

Fig. 2. *Movement direction and force diagram of piston*

The motion equation of the piston is shown in Eq. (8):

$$\frac{\mathrm{d}^2x}{\mathrm{d}t^2} = \begin{cases} \frac{1}{M}(p_aA_{ka} - p_bA_{kb} - p_eA_r - F_f) & x \neq n_a, L-n_b \\ 0 & x = n_a, L-n_b \end{cases}, \quad (8)$$

where, M is the mass of load, [kg], L is the cylinder stroke, [m], F_f is the friction, [N], A_{ki} is the effective area of the piston, [m²], p_e is atmospheric pressure, [MPa], A_r is the effective area of the piston rod, [m²]; n is the dead zone displacement, [m].

The friction force of the pneumatic system includes many factors. The composite model proposed by Canudas in [9] can comprehensively reflect the friction characteristics of the contact surface of the pneumatic system under lubrication conditions [22] and [23]. In this paper, the composite model described by Eq. (9) is used as the mathematical model of the friction force of the cylinder.

$$F_f = \begin{cases} \alpha \cdot u + \left[F_c + (F_s - F_c)e^{\left[-(u/u_s)^{\delta}\right]}\right]\mathrm{sgn}(u) & u \le u_e \\ \mu \cdot u & u > u_e \end{cases}, \quad (9)$$

where, α is the cylinder viscosity coefficient, [N/(m/s)], F_c is the coulomb friction force, [N], F_s is the maximum static friction force, [N], μ is the dynamic friction factor; u_s is the Stribeck velocity, [m/s], δ is an arbitrary index (0.5 to 2), and u_e is the critical speed, [m/s].

2.1.4 Equation of Compressed Air State

According to the pressure changes of the two chambers of the cylinder, the state equations of chambers a and b can be derived as:

$$\frac{\mathrm{d}p_i}{\mathrm{d}t} = \frac{1}{V_i}\left(RT_iG_i - p_iA_iu + \frac{p_iV_i}{T_i}\cdot\frac{\mathrm{d}T_i}{\mathrm{d}t}\right). \quad (10)$$

The equation of the state of the compressed air in the compressed air tank is expressed as follows [24]:

$$\frac{\mathrm{d}p_j}{\mathrm{d}t} = \frac{R}{C_vV_j}\left[G_jC_pT_u + h_jS_{hj}\left(T_e - T_j\right)\right], \quad (11)$$

where S_h is the surface area of the inner wall of the tank chamber, [m²].

2.1.5 Basic Parameters

The basic parameters are shown in Table 1, and the above mathematical model is constructed using MATLAB/Simulink. B is the value of process quantity in the simulation process.

Table 1. *Basic parameters of the system*

Parameter	Value	Parameter	Value	Parameter	Value
M, [kg]	5	$V_{tank\ 1}$, [L]	1	B	50
L, [mm]	200	$V_{tank\ 2}$, [L]	1	F_c, [N]	8
D, [mm]	63	C_v, [J/(kg·K)]	718	F_s, [N]	50
d, [mm]	20	C_p, [J/(kg·K)]	1005	T_e, [K]	293
p_s, [Pa]	600000	R, [J/(kg·K)]	287	P_0, [Pa]	600000
p_e, [Pa]	101300	b	0.5283		

2.2 Experimental Verification

In order to verify the correctness of the mathematical model, an experimental platform for exhaust utilization was built. The compressed air preparation unit consists of a regulator, a filter, and a lubrication control. Its main function is to reduce the pressure to a fixed value. Four pressure sensors are used to monitor the pressure in chamber a, chamber b, $tank\ 1$ and $tank\ 2$. Displacement sensors are used to monitor piston displacement. A force sensor is used to measure the output force of the pneumatic cylinder; an NI data acquisition card and computer are used to obtain experimental data.

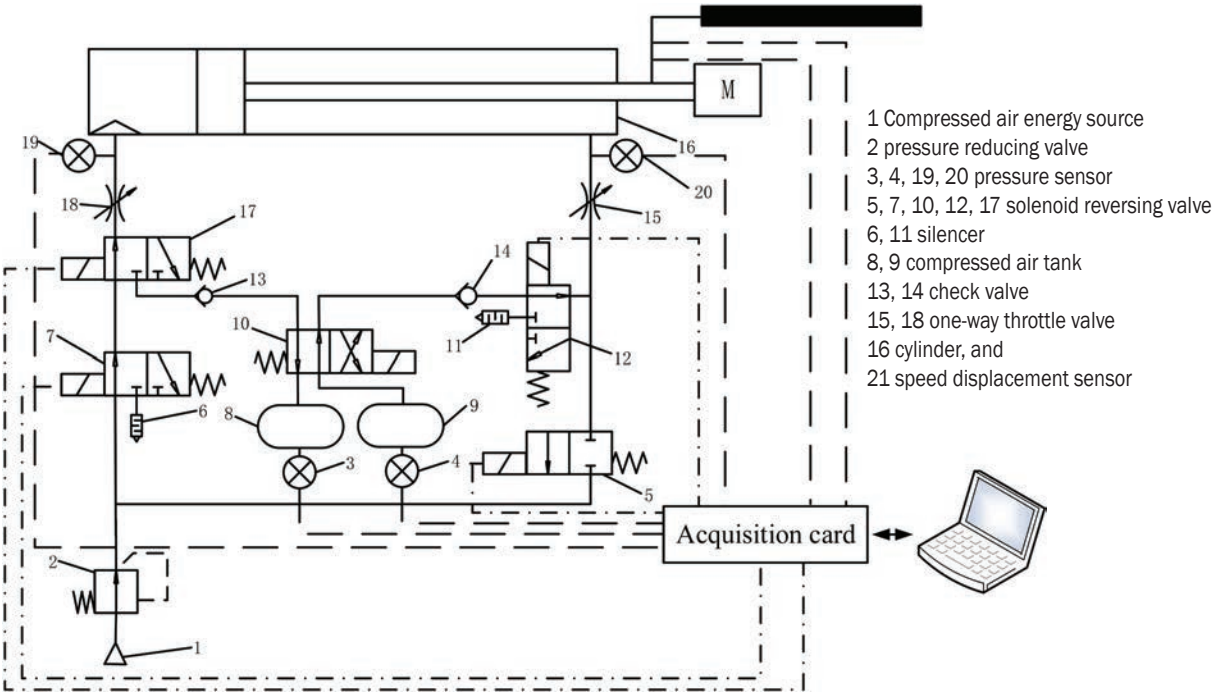

Fig. 3. *Schematic diagram of pneumatic system experiment*

The pressure sensor test range is 0 MPa to 1 MPa, and the force sensor test range is 3 N to 3000 N. The measurement accuracy of pressure, displacement, and force are, respectively 1 %, ±5 μm, and ±0.05 %. Therefore, the maximum absolute errors of pressure, displacement and force are 0.01 MPa, ±5 μm, and ±1.5 N, respectively.

The compressed air source should be turned on, and the pressure in *tank* 2 set to a fixed value through the regulator. The system uses LabVIEW to control and save the data and realize the return stroke of the cylinder by controlling the four solenoid valves.

Fig. 3 is the experimental schematic diagram of the system, and the experimental platform is shown in Fig. 4. Using the experimental platform, the experimental research on the compressed air utilization system is carried out. The compressed air source pressure is set to 0.6 MPa, the load mass is set to 5 kg. Fig. 5 shows the relationship between some parameters and time in the system.

The performance of the system will be shown by some parameters. Fig. 5 includes the piston displacement, velocity, chamber *a*, chamber *b*, and the changes of two tanks in simulation and experiment, which directly shows the performance of the system.

It can be seen from Fig. 5 that the experimental results and the various parameter curves in the simulation have the same trend of change, the pressure in chamber *b* rises first, and then decreases. As the pressure in chamber *a* decreases, the pressure in *tank* 1 first rises and then remains unchanged, and the pressure in *tank* 2 decreases first, remains unchanged in the middle, and finally decreases again.

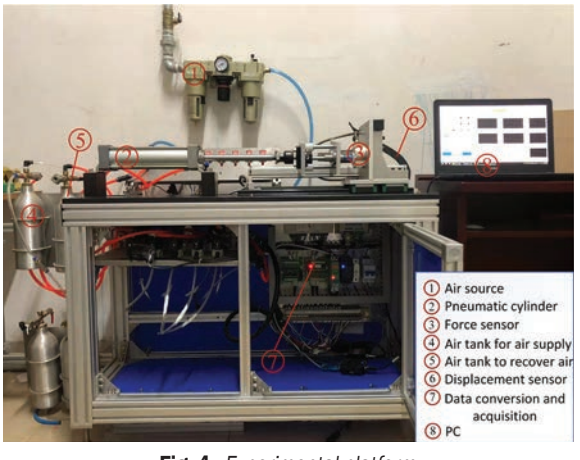

Fig. 4. *Experimental platform*

There are certain errors in the experimental and simulated values, but the maximum error is within 10 %. The reasons for the error in the analysis may be the estimation of parameters such as friction force in the simulation, the instability of the compressed air source pressure, the existence of compressed air leakage in

the pneumatic circuit, and the expansion energy of the compressed air in the cylinder is ignored. On the basis of previous studies [25], it can be known that the main cause of the error is the instability of gas source pressure. The purpose of this experiment is to explore the influence law of system performance through the general change trend of the curve. Therefore, the correctness of the model is verified by the comparison of the curve trend between simulation and experiment.

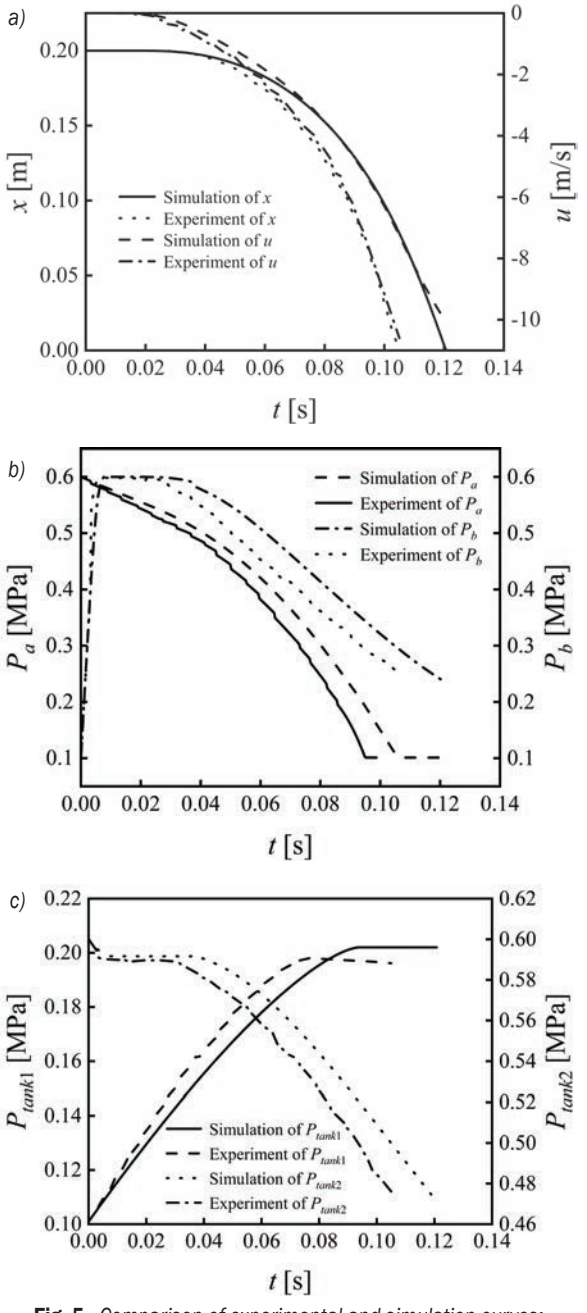

Fig. 5. *Comparison of experimental and simulation curves; a) displacement and velocity curve of piston, b) pressure curve of chamber a and b, and c) pressure curve of tank 1 and tank 2*

3 SIMULATION ANALYSIS OF DIMENSIONLESS MODELS

To understand the performance changes of the system more objectively, it is necessary to use the dimensionless method to eliminate physical units and study the characteristics of the system. To facilitate the research, the assumptions made in Section 2 also apply to this section. The reference values and the dimensionless variables are shown in Table 2. The basic mathematical model can be made dimensionless as described below.

Table 2. *Reference values and dimensionless variables*

Variable	Reference value	Dimensionless variable
P	p_s	$p^* = p/p_s$
T	$T_p = V_a/(A_e DR)$	$t^* = t/T_p$
G	$G_{max} = p_s A_e D/T_e$	$G^* = G/G_{max}$
T	T_e	$T^* = T/T_e$
X	L	$x^* = x/L$
A	A_{ka}	$A^* = A/A_{ka}$
V	V_a	$V^* = V/V_a$
M	$m_{max} = p_s V_a/(R\theta_0)$	$m^* = m/m_{max}$

3.1 Dimensionless Models

3.1.1 Dimensionless Energy Equation

When the compressed air is charged into chamber *a* or chamber *b*, its dimensionless energy equation can be expressed as follows:

$$m_i^* \frac{\mathrm{d}T_i^*}{\mathrm{d}t^*} = \left(\frac{S_i^* K_{ab}}{S_{\max}^*} + G_a^* \right)\left(1 - T_i^*\right) + \left(k-1\right)\left(G_i^* - p_i^* A_i^* u_i^*\right). \quad (12)$$

When the compressed air is discharged from chamber *a* or chamber *b*, its dimensionless energy equation can be expressed as follows:

$$m_i^* \frac{dT_i^*}{dt^*} = \frac{S_i^* K_{aa}}{S_{\max}^*}\left(1 - T_i^*\right) + \left(k-1\right)\left(p_i^* u_i^* - G_i^* T_i^*\right). \quad (13)$$

The dimensionless energy equation of the compressed air tank can be expressed as follows:

$$\frac{\mathrm{d}T_j^*}{\mathrm{d}t^*} = \frac{T_j^*}{p_j^*}\left[\left(k - T_j^*\right)G_j^* + K_{aj}\left(1 - T_j^*\right)\right], \quad (14)$$

where, K_a is the Kagawa coefficient [25], which represents the degree of heat transfer and is defined by Eqs. (15) and (16).

$$K_{ai} = \frac{T_p}{T_{hi}}, \tag{15}$$

$$K_{aj} = \frac{T_p}{T_{hj}}, \tag{16}$$

$$T_{hi} = \frac{C_v m}{S_{max} h_i}, \tag{17}$$

$$T_{hj} = \frac{C_v m_j}{S_j h_j}, \tag{18}$$

$$S_{max} = 2A_{ka} + 2L\sqrt{\pi A_{ka}}, \tag{19}$$

where, T_h is the thermal equilibrium time constant; T_p is the reference time constant; S_{max} is the maximum heat exchange area of the two chambers of the cylinder, [m²].

The dimensionless maximum heat exchange area of chamber *a* and *b* is expressed as follows:

$$S^*_{max} = \frac{S_{max}}{A_{ka}} = 2 + 2L\sqrt{\frac{\pi}{A_{ka}}}. \tag{21}$$

The dimensionless heat exchange area of the *tank* 1 and *tank* 2 is as follows:

$$S^*_j = \frac{S_j}{A_{ka}} = \frac{2A_j + 2L_j\sqrt{\pi A_j}}{A_{ka}}. \tag{22}$$

3.1.2 Dimensionless Mass Flow Equation

The dimensionless mass flow equation of chamber *a* or *b* is expressed as:

$$G^*_i = \begin{cases} \dfrac{p^*_u A^*_e}{\sqrt{T^*_u}} & \dfrac{p^*_d}{p^*_u} \le b \\ \dfrac{p^*_u B A^*_e}{D\sqrt{T^*_u}}\sqrt{\left(\dfrac{p^*_d}{p^*_u}\right)^{\frac{2}{k}} - \left(\dfrac{p^*_d}{p^*_u}\right)^{\frac{k+1}{k}}} & \dfrac{p^*_d}{p^*_u} \ge b \end{cases}. \tag{23}$$

The dimensionless mass flow equation of *tank* 1 is expressed as:

$$G^*_{tank1} = \begin{cases} 1 & p^*_{tank1} \le b \\ \sqrt{1 - \left(\dfrac{p^*_{tank1} - b}{1 - b}\right)} & p^*_{tank1} \ge b \end{cases}. \tag{24}$$

The dimensionless mass flow equation of *tank* 2 is expressed as:

$$G^*_{tank2} = \begin{cases} \dfrac{p^*_{tank2}}{\sqrt{T^*_{tank2}}} & p^*_{tank2} \le b \\ \dfrac{p^*_{tank2}}{\sqrt{T^*_{tank2}}}\sqrt{1 - \left(\dfrac{p^*_{tank2} - b}{1 - b}\right)} & p^*_{tank2} \ge b \end{cases}. \tag{25}$$

3.1.3 Dimensionless Motion Equation

The dimensionless motion equation of the piston is described as:

$$\frac{d^2 x^*}{d(t^*)^2} = \begin{cases} \left(\dfrac{1}{T^*_f}\right)^2 (A^*_{kb} p^*_b - p^*_a - p^*_e A^*_r - F^*_f) & x \ne 0, L \\ 0 & x = 0, L \end{cases}, \tag{26}$$

where, F^*_f is an estimated value that can be calculated by Eq. (27):

$$F^*_f = \begin{cases} F^*_s & u^* = 0 \\ F^*_c + C^* u^* & u^* \ne 0 \end{cases}, \tag{27}$$

where, C^* is the dimensionless viscous friction coefficient which can be described as follows:

$$F^*_s = \frac{F_s}{p_s A_{ka}}, \tag{28}$$

$$F^*_c = \frac{F_c}{p_s A_{ka}}, \tag{29}$$

$$C^* = \frac{C u_0}{p_s A_{ka}}, \tag{30}$$

where, u_0 is the reference speed, [m/s]; p_s is the compressed air source pressure, [MPa].

The dimensionless parameter T^*_f is defined by Eq. (32), and T^*_f corresponds to the *J* parameter used when selecting the cylinder.

$$T^*_f = \frac{T_f}{T_p}, \tag{31}$$

$$T_f = \sqrt{\frac{ML}{p_s A_{ka}}}. \tag{32}$$

The mathematical relationship between *J* parameter and T^*_f is shown below:

$$J = \left(\frac{1}{T^*_f}\right)^2. \tag{33}$$

3.1.4 Dimensionless Equation of State

According to the pressure changes of chamber *a* or *b*, dimensionless equation of state is expressed as follows:

$$\frac{dp_i^*}{dt^*} = \frac{G_i^* T_i^* - p_i^* A_i^* u_i^*}{V_i^*} + \frac{p_i^*}{T_i^*} \frac{dT_i^*}{dt^*}. \quad (34)$$

The equation of *tank* 1 is expressed as follows:

$$\frac{dp_{tank1}^*}{dt^*} = kG_{tank1}^* + K_{a3}\left(1 - T_{tank1}^*\right). \quad (35)$$

The equation of *tank* 2 is expressed as follows:

$$\frac{dp_{tank2}^*}{dt^*} = kG_{tank2}^* p_{tank2}^* \sqrt{T_{tank2}^*} + K_{a4}\left(1 - T_{tank2}^*\right). \quad (36)$$

3.2 Dimensionless Simulation Analysis

To explore the relationship between the dimensionless initial pressure of *tank* 2 and the utilization efficiency of compressed air, the ratio of the initial pressure p_0 of *tank* 2 to the compressed air source pressure p_s is defined as the dimensionless initial supply pressure of *tank* 2, which is expressed as $\beta^* = p_0/p_s$. Table 3 is the reference value of dimensionless parameters.

Based on the simulation program, the variation trend of each dimensionless physical quantity can be obtained by substituting parameters.

Fig. 6 shows the trend of dimensionless parameters over time. It can be seen from Fig. 6a that the piston does not move for an initial period of time. This is because the driving force of the driving chamber during this period is less than the sum of other resistances such as compressed air resistance and friction in the chamber *a*, and the piston is stationary. It can be seen from Fig. 6b that the pressure in chamber *b* first rises and then falls, because the friction force changes from static friction force to kinetic friction force after the piston moves, and the reduction of friction force accelerates the movement of the piston. At this time, the volume of chamber *b* increases, and the intake air volume is less than the increase in the volume of chamber *b*, the compressed air expands, and the pressure decreases. The pressure in chamber *b* does not rise again because the air supply time is short.

It can be seen from Fig. 6c that the pressure in *tank* 1 first increases and then remains unchanged. This is because the system does not meet the recovery criterion, the compressed air in chamber *a* is discharged into the atmosphere, the pressure in *tank* 1 remains unchanged. The pressure in *tank* 2 first decreases, then remains unchanged, and then decreases. This is because the system does not meet the air supply criterion, and the air supply from *tank* 2 is switched to the air supply. Fig. 6d shows the working condition of the recovery part and the pressure in *tank* 2 remains unchanged. Fig. 6e shows the specific working conditions of the gas supply part.

Table 3. *Dimensionless parameter reference value*

Dimensionless parameters	Symbol	Reference value
Dimensionless natural period	T_f^*	0.0663
Dimensionless static friction	F_s^*	0.0267
Dimensionless viscous friction coefficient	C^*	0.0153
Dimensionless piston area of chamber *b*	A_{kb}^*	0.8992
Dimensionless Coulomb friction	F_c^*	0.0043
Effective area of dimensionless compressed air inlet	A_{e2}^*	1
Kagawa coefficient of chamber *a*	K_{aa}	0.0563
Kagawa coefficient of chamber *b*	K_{ab}	0.0626
Dimensionless volume of *tank* 1	V_{tank1}^*	1.604
Dimensionless volume of *tank* 2	V_{tank2}^*	1.604
Recovery switching criterion	λ_1	1
Criteria for compressed air supply switching	λ_2	1
Dimensionless initial supply pressure of *tank* 2	β^*	1
Dimensionless air source pressure	β_s^*	1

4 PERFORMANCE RESEARCH AND PARAMETER OPTIMIZATION

To obtain main influence parameters on efficiency and speed, further research on its speed and efficiency characteristics is essential; it should select the parameters with the high degree of impact, optimize the main performance of the system, and obtain the parameter combination under the optimal conditions.

4.1 Performance Analysis

Piston velocity and exhaust utilization efficiency reflect the main performance of exhaust utilization system, so the parameters affecting piston velocity and exhaust utilization efficiency are studied as dimensionless.

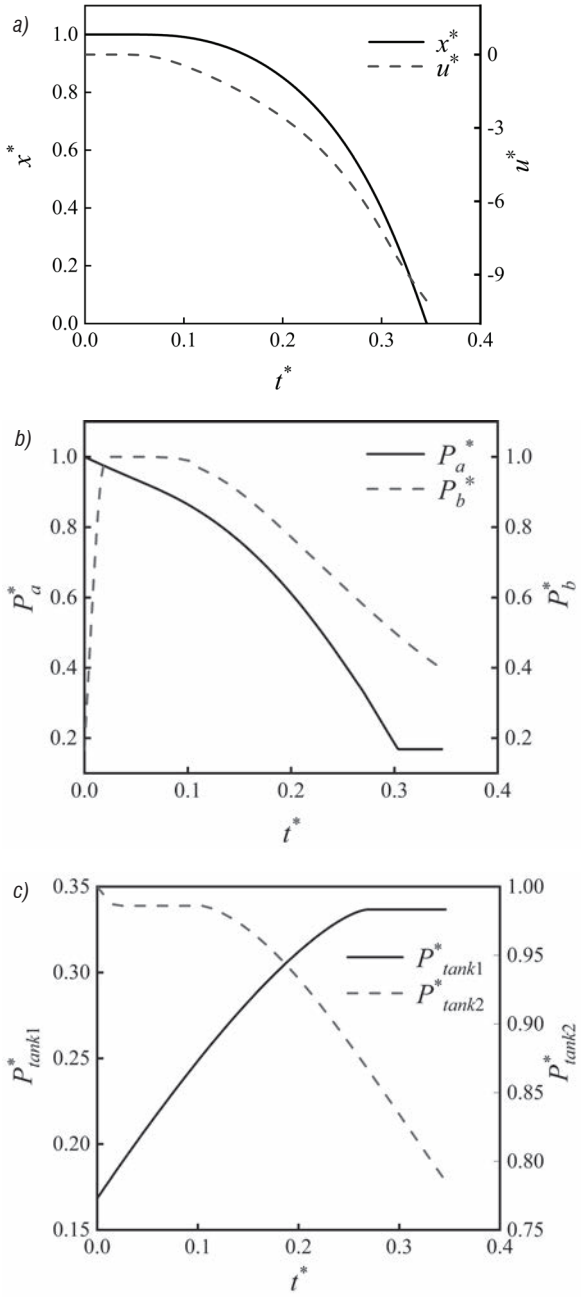

Fig. 6. *Simulation curve; a) displacement and velocity curve of piston, b) pressure curve of chamber a and b c) pressure curve of tank 1 and tank 1*

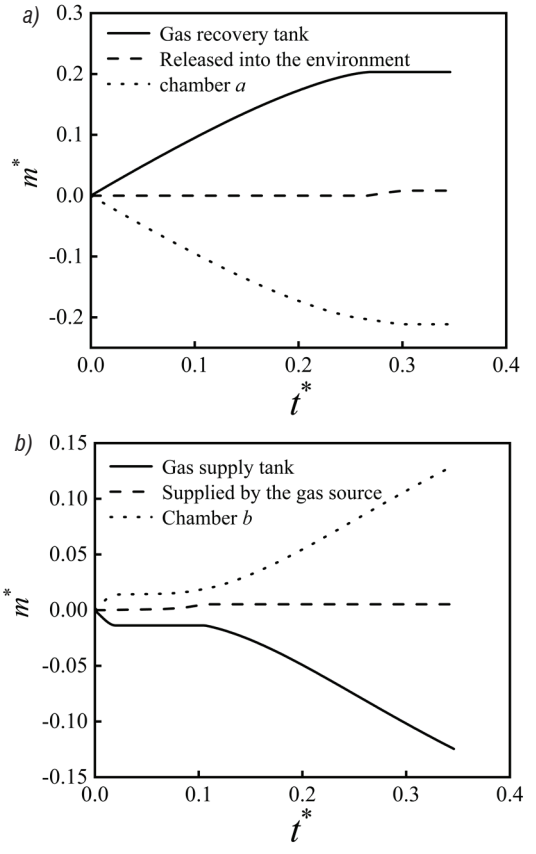

Fig. 7. *Change in compressed air mass; a) compressed air mass changes in the recovery part, b) compressed air mass changes in the supply part*

4.1.1 Dimensionless Speed Analysis

To facilitate the study of the influence of various dimensionless parameters on the speed characteristics of the piston, the dimensionless speed of the piston is defined as:

$$\overline{u^*} = \frac{\int_0^t u^* \mathrm{d}t}{t}. \tag{37}$$

The rate of change of dimensionless speed refers to the ratio of a parameter to the sum of the dimensionless average rate of change of all parameters. The sum of the dimensionless average speed change rate can be described as follows:

$$\begin{aligned}\overline{u}_{total-cg} = {} & \overline{u}_{T_f^*-cg} + \overline{u}_{F_s^*-cg} + \overline{u}_{C^*-cg} + \overline{u}_{A_{kb}^*-cg} + \overline{u}_{F_c^*-cg} \\ & + \overline{u}_{A_{e2}^*-cg} + \overline{u}_{K_{a1}-cg} + \overline{u}_{K_{a2}-cg} + \overline{u}_{V_{t1}^*-cg} + \overline{u}_{V_{t2}^*-cg} \\ & + \overline{u}_{\lambda_1-cg} + \overline{u}_{\lambda_2-cg} + \overline{u}_{\beta-cg} + \overline{u}_{\beta_s-cg}.\end{aligned} \tag{38}$$

It can be seen from Fig. 8 that u^* is mainly affected by T^*_f, A^*_{e2}, A^*_{kb}, β^*, and the rate of change of these parameters are respectively 23.57 %, 23.48 %, 36.42 %, and 7.88 %.

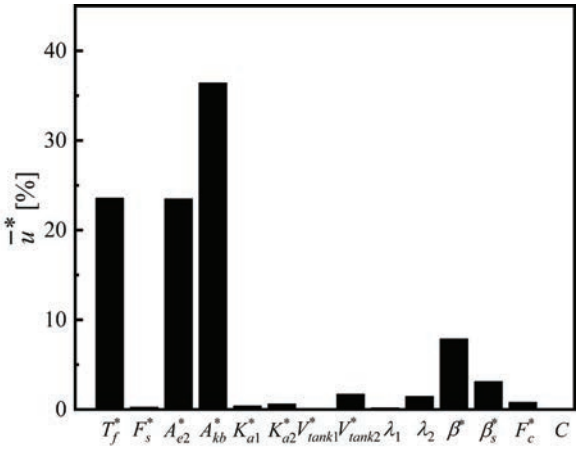

Fig. 8. *Rate of change of speed*

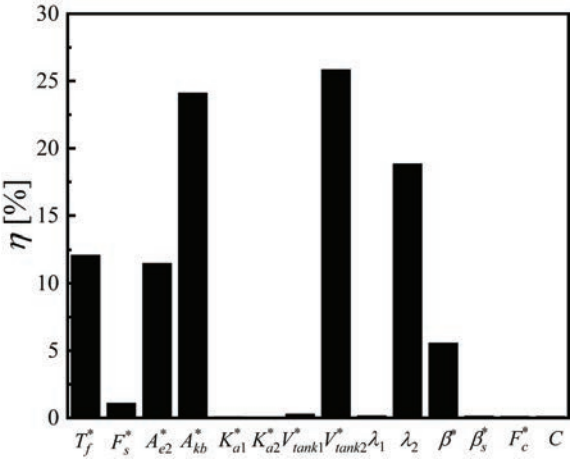

Fig. 9. *The rate of change of the dimensionless efficiency of each parameter*

4.1.2 Dimensionless Efficiency Analysis

At the initial moment of compressed air reuse, the pressure in the exhaust chamber of the cylinder can be approximated as the supply pressure. Because the temperature change in the pipeline is difficult to measure and the compressed air tank is large when the system is working, the change in the compressed air flow process is not considered, and only the enthalpy of the compressed air is considered. For the calculation of air volume and pressurized compressed air energy in standard state, please refer to the relevant literature [26] and [27].

The efficiency of compressed air utilization can be calculated by:

$$\eta = \frac{E_c^* - E_s^*}{E_c^*} \times 100\ \%, \tag{3}$$

where, E^*_c is the dimensionless energy at the beginning of the return trip, E^*_s is the dimensionless energy at the end of the return trip.

Through the model established by the above process, in the research process, the value of a single parameter is changed to obtain the influence rate of the change of each parameter on the compressed air utilization efficiency. In order to evaluate the characteristics of compressed air reuse efficiency more objectively, the dimensionless average efficiency is defined as follows:

$$\bar{\eta} = \frac{\int_0^t \eta dt}{t}. \tag{4}$$

The change rate of dimensionless efficiency refers to the ratio of a parameter to the sum of the dimensionless average efficiency change rates of all parameters. The sum of the dimensionless average efficiency change rate can be described as follows:

$$\begin{aligned}\bar{\eta}_{total-cg} = {} & \bar{\eta}_{T_f^*-cg} + \bar{\eta}_{F_s^*-cg} + \bar{\eta}_{C^*-cg} + \bar{\eta}_{A_{kb}^*-cg} + \bar{\eta}_{F_c^*-cg} \\ & + \bar{\eta}_{A_{e2}^*-cg} + \bar{\eta}_{K_{a1}-cg} + \bar{\eta}_{K_{a2}-cg} + \bar{\eta}_{V_{t1}^*-cg} + \bar{\eta}_{V_{t2}^*-cg} \\ & + \bar{\eta}_{\lambda_1-cg} + \bar{\eta}_{\lambda_2-cg} + \bar{\eta}_{\beta-cg} + \bar{\eta}_{\beta_s-cg}.\end{aligned} \tag{5}$$

Fig. 9 describes the change rate of the dimensionless efficiency of each parameter.

It can be seen from Fig. 9 that the compressed air utilization efficiency is mainly affected by V^*_{tank2}, A^*_{kb}, λ_2, T^*_f, and A^*_{e2}. The change rates of these parameters were 25.38 %, 24.41 %, 18.38 %, 12.1 %, and 11.49% .

4.2 Parameter Optimization

Optimizing the main parameters that affect the performance of the system can further improve the effect of energy saving. It can be seen from the above research that the dimensionless piston speed and compressed air utilization efficiency are mainly affected by T^*_f, A^*_{e2}, A^*_{kb}, λ_2, β^* and V^*_{tank2}. The orthogonal experiments should be designed in the optimization process, and the grey relational analysis method used to optimize the key parameters that affect the performance of the system.

The overall optimization objective function can be defined as follows:

$$f(x) = \alpha_1 u + \alpha_2 V_{\text{tank2}} + \alpha_3 \eta, \tag{12}$$

where, α_1 is the speed weighting factor, α_2 is the reused compressed air tank volume weighting factor, and α_3 is the reuse efficiency weighting factor.

There are three weighting factors in the objective function, and the importance of the three factors is different. The analytic hierarchy process can transform multi-objective and multi-criteria problems into multi-level single-objective problems, and the results are simpler and clearer. Here we choose the analytic hierarchy process to obtain the weighting factor. By dividing the importance of the factors, the weighting factors of the specific objective function as shown in Table 4 are obtained by calculation.

Therefore, the weighting factor of the objective function is $\alpha = (\alpha_1, \alpha_2, \alpha_3)^T = (0.5, 0.2, 0.3)^T$.

Table 4. *Objective function weighting factors*

Parameter	u	$V_{tak\ 2}$	η	$\sum_m \alpha_{mn}$	$\frac{\sum_m \alpha_{mn}}{\sum_n \sum_m \alpha_{mn}}$
u	1	5/2	5/3	31/6	0.5
$V_{tak\ 2}$	2/5	1	2/3	31/15	0.2
η	3/5	3/2	1	31/10	0.3
$\sum_n \sum_m \alpha_{mn}$				31/3	1

Table 5. *Parameter boundary value*

	Parameter					
Boundary value	T_f [s]	A_{e2} [mm²]	A_{kb} [mm²]	λ_2	β	$V_{tak\ 2}$ [L]
Lower boundary	0.0103	50.27	2626.37	0.8	0.4	0.8
Upper boundary	0.0326	176.72	3004.15	1.2	0.8	1.2

The most representative and smallest combination of all combinations of experimental factors is selected by orthogonal experiment method, and part of the experimental results is used to characterize all experimental conditions. When the value of $V_{tak\ 2}$ is set within 0.2 L from the initial value, the energy in *tak* 2 can meet the system requirements, and the compressed air recovery and utilization process will not be complicated. Values of λ_2 and β other than 0.2 from the initial value will have a greater impact on the speed of the piston, so λ_2 and β should be taken within 0.2 of the initial value. The upper and lower boundary values of T_f, A_{e2}, and A_{kb} are calculated according to the values of other parameters. Table 5 shows the upper and lower boundary values of each parameter.

Five values are selected for each of the six parameters, and the $L_{25}(5^6)$ orthogonal table is used to obtain the combination of parameters. The parameters' values are shown in Table 6

Table 6. *Parameters combinations*

No.	Parameter					
	T_f [s]	A_{e2} [mm²]	A_{kb} [mm²]	λ_2	β	$V_{tak\ 2}$ [L]
1	0.0103	50.27	2626.37	0.8	0.4	0.8
2	0.0103	95.00	2410.39	0.9	0.5	0.9
3	0.0103	113.10	2803.12	1	0.6	1
4	0.0103	153.94	2916.18	1.1	0.7	1.1
5	0.0103	176.72	3004.15	1.2	0.8	1.2
6	0.0146	50.27	2410.39	1	0.7	1.1
7	0.0146	95.00	2803.12	1.1	0.8	1.2
8	0.0146	113.10	2916.18	1.2	0.4	0.8
9	0.0146	153.94	3004.15	0.8	0.5	0.9
10	0.0146	176.72	2626.37	0.9	0.6	1
11	0.0207	50.27	2803.12	1.2	0.5	0.9
12	0.0207	95.00	2916.18	0.8	0.6	1
13	0.0207	113.10	3004.15	0.9	0.7	1.1
14	0.0207	153.94	2626.37	1	0.8	1.2
15	0.0207	176.72	2410.39	1.1	0.4	0.8
16	0.0292	50.27	2916.18	0.9	0.8	1.2
17	0.0292	95.00	3004.15	1	0.4	0.8
18	0.0292	113.10	2626.37	1.1	0.5	0.9
19	0.0292	153.94	2410.39	1.2	0.6	1
20	0.0292	176.72	2803.12	0.8	0.7	1.1
21	0.0326	50.27	3004.15	1.2	0.6	1
22	0.0326	95.00	2626.37	1.1	0.7	1.1
23	0.0326	113.10	2410.39	0.8	0.8	1.2
24	0.0326	153.94	2803.12	0.9	0.4	0.8
25	0.0326	176.72	2916.18	1	0.5	0.9

The parameters' combinations are substituted into the simulation model to obtain the value of each objective function, and the results are combined and calculated by the grey correlation degree method, and the value of the correlation degree is used to evaluate the pros and cons of these combinations, so as to obtain the optimal result. The corresponding parameter combinations are shown in Table 7 The optimal result is brought into the model simulation, and the single exhaust utilization efficiency of the system is 34%.

Table 7. *Optimized parameters*

Parameter					
T_f [s]	A_{e2} [mm²]	A_{kb} [mm²]	λ_2	β	$V_{tak\ 2}$ [L]
0.0292	176.72	2803.12	0.8	0.7	1.1

5 RESEARCH ON ENERGY-SAVING UTILIZATION OF EXPANSION ENERGY

In the above research process, only the transmission energy of the compressed air is used, while the

expansion energy of the compressed air is hardly used, which results in a waste of compressed air energy. To make use of the expansion of the compressed air, the opening and closing sequence of the solenoid valve is changed to control the air supply time to the chamber *b*, so that the air is sufficiently expanded to push the piston back. During the return process, the energy change of the pressurized compressed air in *tank* 2 and the speed of the piston are studied.

5.1 Solenoid Valve Working Status

Fig. 10 shows the value opening and closing sequence diagrams of the four solenoid valves under the basic operating conditions, where *u*1, *u*2, *u*3, and *u*4 are solenoid valve 7, solenoid valve 11, solenoid valve 12, a nd solenoid valve 5r espectively.

The 0 state in Fig. 10 indicates that the solenoid valve is de-energized and closed, and the 1 state indicates that the solenoid valve is energized and opened. In the actual working process, the solenoid valve does not act instantaneously when the solenoid valve is disconnected and closed; there is a 10 ms response time.

5.2 System Performance Analysis of Variable Initial Pressure of *tank* 2

The volume of *tank* 2 is 1 L, and the initial pressure of *tank* 2 is 0.5 MPa, 0.6 MPa, and 0.7 MPa, respectively, and cut off the compressed air supply of *tank* 2 to the chamber *b* at 0.06 s, 0.07 s, 0.08 s, 0.09 s and 0.1 s, respectively. The expansion of the compressed air in the chamber *b* can be utilized in the subsequent time. Fig. 11 shows the working conditions of the solenoid valve and the change of the pressure in *tank* 2 in different working conditions.

It can be seen from Fig. 12 that when the initial pressure of *tank* 2 is constant, the energy saving efficiency decreases with the increase of the time of cutting off *tank* 2, and when the time of cutting off *tank* 2 is fixed, the energy saving efficiency decreases with the increase of the initial pressure of *tank* 2. However, when the time of cutting off the *tank* 2 is 0.06 s, the energy saving efficiency increases with the increase of the initial pressure, and the maximum is 26.2 %. The reason may be that when the initial pressure of the *tank* 2 is large, the time of cutting off the *tank* 2 has a great influence on the energy saving efficiency.

It can be seen from Fig. 13 that when the initial pressure of *tank* 2 is constant, the average piston velocity increases with the increase of the time of cutting off *tank* 2, and when the time of cutting off *tank* 2 is fixed, the average velocity of piston increases with the increase of the initial pressure of *tank* 2. In the working process of the system, it is necessary to avoid cutting off the *tank* 2 too early to affect the normal operation of the system.

When the volume of *tank* 2 is 1 L, in order to improve the energy saving efficiency of the system and not make the piston speed too low affect the operation of the system, it is suggested that the time of cutting off *tank* 2 is 0.06 s to 0.08 s and the initial pressure of *tank* 2 is 0.6 MPa to 0.7 MPa.

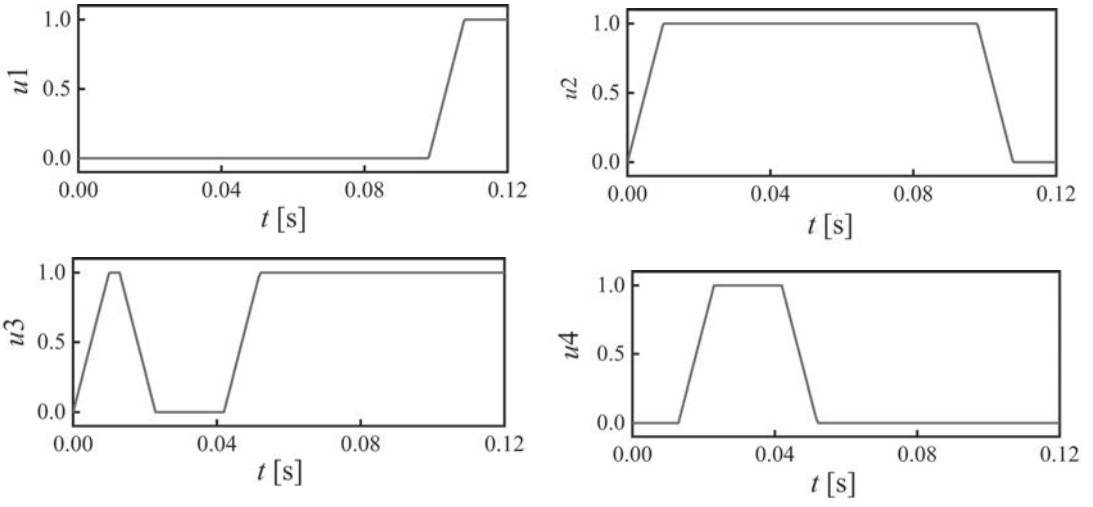

Fig. 10. *Working condition of solenoid valve*

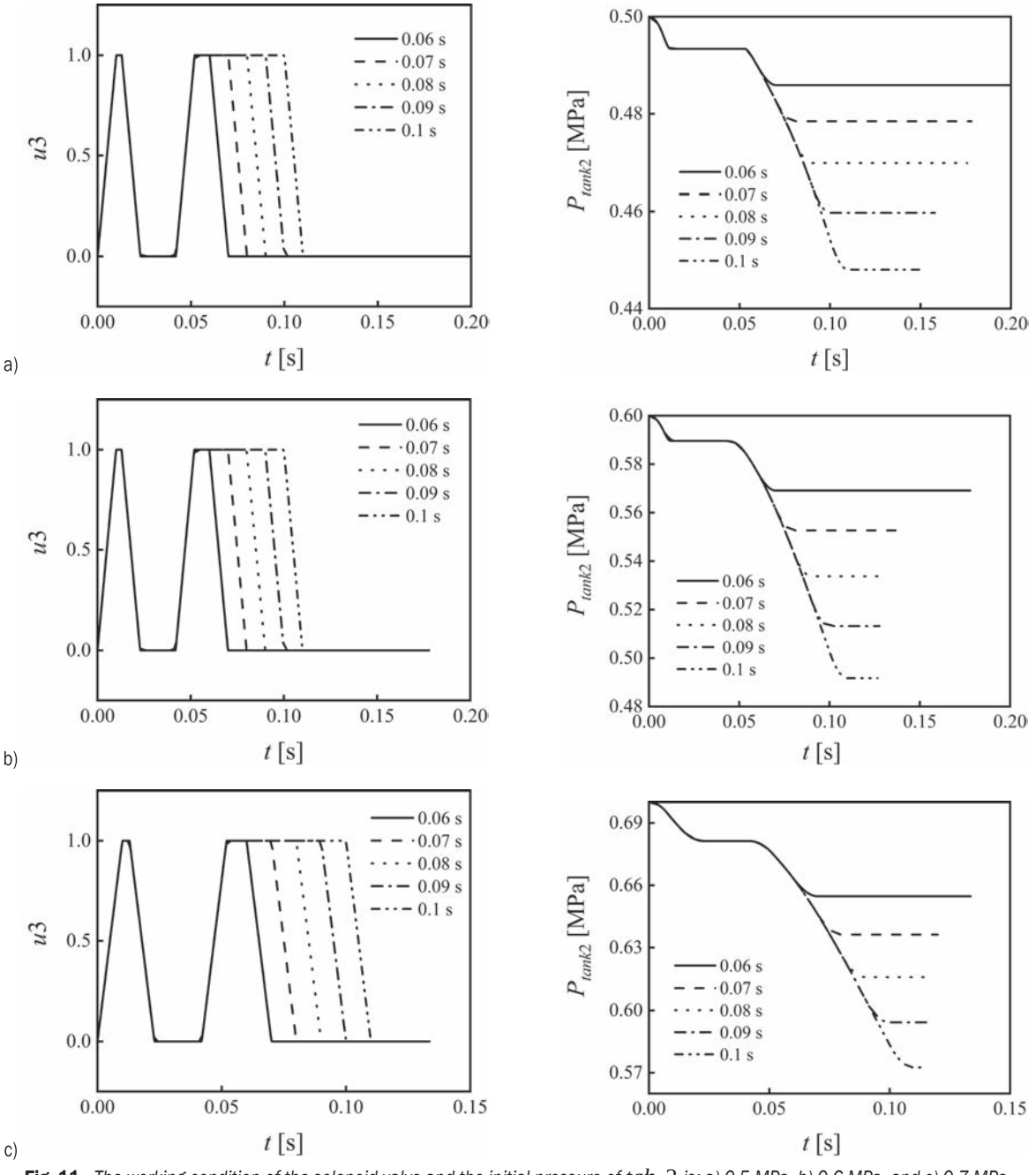

Fig. 11. *The working condition of the solenoid valve and the initial pressure of tank 2 is: a) 0.5 MPa, b) 0.6 MPa, and c) 0.7 MPa*

5.3 System Performance Analysis of Variable Volumes of *tank* 2

The initial pressure of *tank* 2 is 0.6 MPa, the volume of *tank* 2 is 0.8 L, 1 L, and 1.2 L, and cut off the compressed air supply of *tank* 2 to the chamber *b* at 0.06 s, 0.07 s, 0.08 s, 0.09 s and 0.1 s, respectively. The expansion of the compressed air in the chamber *b* can be utilized in the subsequent time. Fig. 14 shows the working conditions of the solenoid valve and the change of the pressure in *tank* 2 in different working conditions.

It can be seen from Fig. 15 that when the volume of *tank* 2 is constant, the energy saving efficiency decreases with the increase of the time of cutting off *tank* 2, and when the time of cutting off *tank* 2 is fixed,

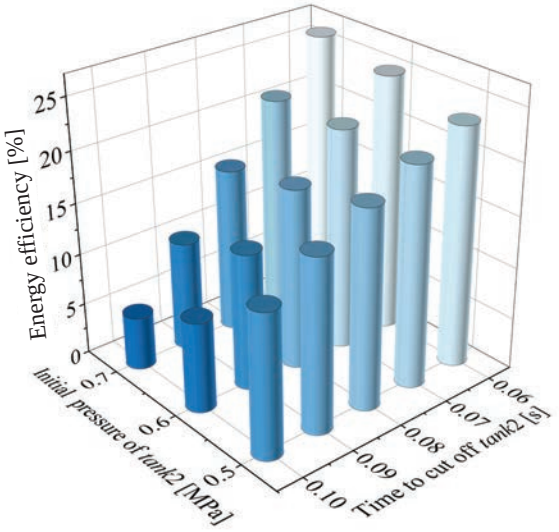

Fig. 12. *Energy efficiency*

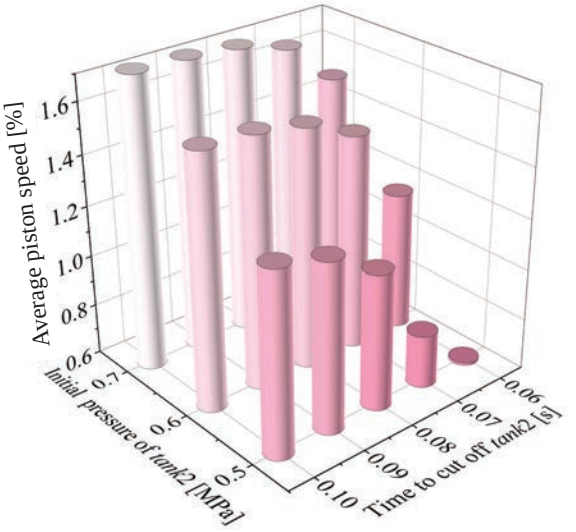

Fig. 13. *Piston average speed*

the average velocity of the piston decreases with the increase of the volume of *tank* 2.

It can be seen from Fig. 6 that when the volume of *tank* 2 is constant, the average piston velocity increases with the increase of the time of cutting off *tank* 2, and when the time of cutting off *tank* 2 is fixed, the average velocity of piston increases with the increase of *tank* 2 volume. This is because the increase in the volume of *tank* 2 leads to a decrease in pressure change, resulting in an increase in driving force.

When the initial pressure of *tank* 2 is 0.6 MPa, in order to improve the energy saving efficiency of the system and not make the piston speed too low affect the operation of the system, it is suggested that the time of cutting off *tank* 2 is 0.07 s to 0.08 s and the volume of *tank* 2 is 0.8 L to 1 L.

The difference in the compressed air supply time will make the expansion of the compressed air in the chamber *b* can be utilized to different degrees, but the piston speed will also be affected. The air supply time should be controlled to avoid the influence of the piston movement speed being too low on the system work.

6 CONCLUSION

To use the compressed air, this paper proposes a pneumatic actuator exhaust utilization system to return the compressed air to the compressed air tank and supply it under suitable conditions. The conclusions of this study are as follows:

1. A new exhaust utilization circuit is designed to recover and utilize compressed air.
2. The simulation results are in good agreement with the experimental results, which verifies the accuracy of the mathematical model of the system.
3. The operating characteristics of the system are mainly affected by the dimensionless parameters, such as natural period, effective piston area, chamber *b* area, initial of *tank* 2, volume of *tank* 2, and the criterion of compressed air supply switching.
4. Some parameters that have a greater impact on system characteristics are optimized. At the optimal parameters, the exhaust utilization efficiency of the system is 34.47%.
5. Expansion energy can be further utilized by controlling the air supply time. By controlling the air supply time, when the initial pressure of *tank* 2 is 0.5 MPa, 0.6 MPa, and 0.7 MPa, the maximum energy-saving efficiency is 23.25 %, 24.90 %, and 26.12 %. When the volume of *tank 2* is 0.8 L, 1 L, and 1.2 L, the maximum energy-saving efficiency is 30.01%, 24.90%, and 21.58%.

Overall, the compressed air utilization system can recover and utilize compressed air well. During the working process, the system parameters should be selected and optimized according to the specific work requirements. This paper provides a new technical solution for compressed air recovery and utilization and a theoretical basis for subsequent improvement of system control.

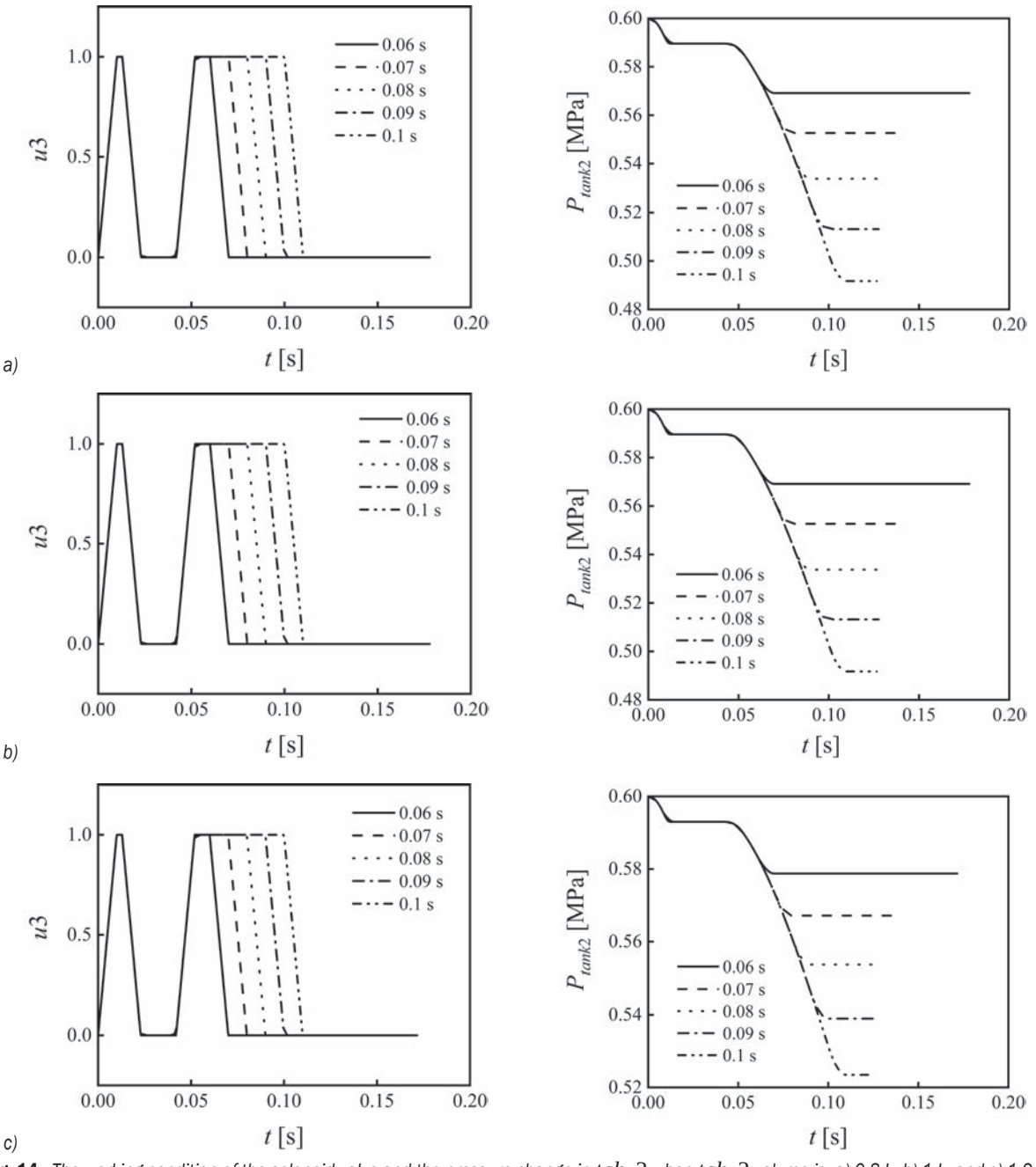

Fig. 14. *The working condition of the solenoid valve and the pressure change in tank 2 when tank 2 volume is: a) 0.8 L, b) 1 L, and c) 1.2 L*

7 ACKNOWLEDGEMENTS

The research work presented in this paper is financially supported by a Grant (2006[illegible] from the National Natural Science Foundation of China and the Beijing Outstanding Young Scientists Program (BJJWZYJH012019100021[illegible] .

8 REFERENCES

[1] Nazari, V., Surgenor, B. (2016). Improved position tracking performance of a pneumatic actuator using a fuzzy logic controller with velocity, system lag and friction compensation. *International Journal of Control, Automation and Systems*, vol. 14, p. 1376-1388, **DOI:10.1007/s12555-015-0202-0**.

[2] Wang, J., Pu, J., Moore, P. (1999). A practical control strategy for servo-pneumatic actuator systems. *Control Engineering Practice*, vol. 7, no. 12, p. 1483-1488, **DOI:10.1016/S0967-0661(99)00115-X**.

[3] Yusop. M.Y.M. (2006). *Energy Saving for Pneumatic Actuation Using Dynamic Model Prediction*. PhD Thesis. Cardiff University, Cardiff.

[4] Du, H., Xiong, W., Xu, C., Jiang, Z. (2018). Direct drive system based on small gas compressor. *Chinese Hydraulics and Pneumatics*, vol. 2, p. 52-56. (in Chinese)

[5] Krytikov, G., Strizhak, M., Strizhak, V. (2017). The synthesis of structure and parameters of energy efficient pneumatic actuator. Eastern-European *Journal of Enterprise Technologies*, vol. 1, no. 7(85), p. 38-44, **DOI:10.15587/1729-4061.2017.92833**.

[6] Cai, M., Kagawa, T. (2001). *Energy Consumption Assessment of Pneumatic Actuating Systems Including Compressor*.

[7] Du, H., Xiong, W., Jiang, Z., Li, Q., Wang, L. (2018). Energy efficiency control of pneumatic actuator systems through nonlinear dynamic optimization. *Journal of Cleaner Production*, vol. 184, p. 511-519, **DOI:10.1016/j.jclepro.2018.02.117**.

[8] Du, H., Hu, C., Xiong, W., Jiang, Z., Wang, L. (2020). Energy optimization of pneumatic actuating systems using expansion energy and exhaust recycling. *Journal of Cleaner Production*, vol. 254, art. ID 119983, **DOI:10.1016/j.jclepro.2020.119983**.

[9] Yang, F., Tadano, K., Li, G., Kagawa, T., Peng, J. (2016). Simulation on the characteristics of pneumatic booster valve with energy recovery. *Theory, Methodology, Tools and Applications for Modeling and Simulation of Complex Systems*. Springer, Singapore, p. 143-153, **DOI:10.1007/978-981-10-2669-0_16**.

[10] Yang, F., Tadano, K., Li, G., Kagawa, T. (2017). Analysis of the energy efficiency of a pneumatic booster regulator with energy recovery. *Applied Sciences*, vol. 7, no. 8, art. ID 816, **DOI:10.3390/app7080816**.

[11] Endler, L., De Negri, V.J., Castelan, E.B. (2015). Compressed air saving in symmetrical and asymmetrical pneumatic positioning systems. *Proceedings of the Institution of Mechanical Engineers, Part I: Journal of Systems and Control Engineering*, vol. 229, no. 10, p. 957-969, **DOI:10.1177/0959651815597819**.

[12] Shi, Y., Jia, G., Cai, M. Xu., W. (2015). Study on the dynamics of local pressure boosting pneumatic system. *Mathematical Problems in Engineering*, vol. 2015, art. ID 849047, **DOI:10.1155/2015/849047**.

[13] Shi, Y., Cai, M. (2012). Dimensionless study on outlet flow characteristics of an air-driven booster. *Journal of Zhejiang University SCIENCE A*, vol. 13, p. 481-490, **DOI:10.1631/jzus.A1100176**.

[14] Tong, Z. (2021). Advancing Pneumatic Technology and Industry. *Hydraulics Pneumatics & Seals*, vol. 41, no. 02, p. 98-109. (in Chinese)

[15] Beater, P. (2007). *Pneumatic Drives: System Design, Modelling and Control*. Springer, Berlin, **DOI:10.1007/978-3-540-69471-7**.

[16] Doll, M., Neumann, R., Sawodny, O. (2011). Energy efficient use of compressed air in pneumatic drive systems for motion tasks. *Proceedings of International Conference on Fluid Power and Mechatronics*, p. 340-345, **DOI:10.1109/FPM.2011.6045785**.

[17] Doll, M., Sawodny, O. (2010). Energy optimal open loop control of standard pneumatic cylinders. *7th International Fluid Power Conference*, Aachen, p. 259-270.

[18] Cummins, J.J., Barth, E.J., Adams, D.E. (2015). Modeling of a pneumatic strain energy accumulator for variable system configurations with quantified projections of energy efficiency increases. *Proceedings of the ASME/BATH Symposium on Fluid Power and Motion Control*, **DOI:10.1115/FPMC2015-9605**.

[19] Luo, X., Wang, J., Sun, H., Derby, J.W., Mangan, S.J. (2012). Study of a new strategy for pneumatic actuator system energy efficiency improvement via the scroll expander technology. *IEEE/ASME Transactions on Mechatronics*, vol. 18, no. 5, p. 1508-1518, **DOI:10.1109/TMECH.2012.2203920**.

[20] Cai, M. (2007). Theory and practice of modern deterministic techniques, Lecture 4: Energy of compressed gas. *Hydraulics Pneumatics and Seals*, vol. 5, p. 54-59. (in Chinese)

[21] Shi, Y., Cai, M. (2013). Dimensionless study on output flow characteristics of expansion energy used pneumatic pressure booster. *Journal of Dynamic Systems, Measurement, and Control*, vol. 135, no. 2, art. No. 021007, **DOI:10.1115/1.4007234**.

[22] Yu, Q., Cai, M., Shi, Y., Xu, Q. (2015). Optimization study on a single-cylinder compressed air engine. *Chinese Journal of Mechanical Engineering*, vol. 28, p. 1285-1292, **DOI:10.3901/CJME.2015.0520.072**.

[23] De Wit, C.C., Olsson, H., Astrom, K.J., Lischinsky, P. (1995). A new model for control of systems with friction. *IEEE Transactions on Automatic Control*, vol. 40, no. 3, p. 419-425, **DOI:10.1109/9.376053**.

[24] Harris, P., Nolan, S., O'Donnell, G.E. (2014). Energy optimization of pneumatic actuator systems in manufacturing. *Journal of Cleaner Production*, vol. 72, p. 35-45, **DOI:10.1016/j.jclepro.2014.03.011**.

[25] Yu, Q., Zhai, J., Wang, Q., Zhang, X., Tan, X. (2021). Experimental study of a new pneumatic actuating system using exhaust recycling. *Sustainability*, vol. 13, no. 4, art. ID 1645, **DOI:10.3390/su13041645**.

[26] Shi, Y., Cai, M. (2011). Working characteristics of two kinds of air-driven boosters. *Energy Conversion and Management*, vol. 52, no. 12, p. 3399-3407, **DOI:10.1016/j.enconman.2011.07.008**.

[27] Yu, Q., Hao, X., Tan, X. (2018). Performance analysis of an innovative kind of two-stage piston type expansion air engine. *Advances in Mechanical Engineering*, vol. 10, no. 5, art. ID 1687814018773860, **DOI:10.117/1687814018773860**.

Strojniški vestnik - Journal of Mechanical Engineering 69(2023)3-4, 135-154
DOI:10.5545/sv-jme.2022.239
Original Scientific Paper
Received for review: 2022-06-16
Received revised form: 2023-01-03
Accepted for publication: 2023-02-14

Effect of the Curvature Angle in a Conduit with an Adiabatic Cylinder over a Backward Facing Step on the Magnetohydrodynamic Behaviour in the Presence of a Nanofluid

Djamila Derbal[1]* – Mohamed Bouzit[1] – Abderrahim Mokhefi[2] – Fayçal Bouzit[1]
[1] University of Science and Technology of Oran, Faculty of Mechanical , Algeria
[2] Bechar University, Faculty of Sciences and Technology, Algeria

A backward facing duct are present in various industrial applications especially those focused on heat transfer. The flow through a curved backward facing duct especially in the presence of nanofluid presents complexities compared to a straight backward facing step (BFS) duct. Therefore, the present numerical study deals a nanofluid flow (Fe_3O_4-H_2O) forced convection in a curved backward facing duct. The objective of this investigation is to visualize at different curvature angles g (0°, 30°, 45°, 60°, 90°) imposed on the top wall of the duct, the effect of Hartmann number Ha (0, 50, 100), magnetic field inclination angle γ (0°, 60°, 90°), Reynolds number Re (10, 100, 200) and nanoparticle volume fraction φ (0 %, 0.05 %, 0.1 %). The dimensionless governing equations are solved using the multigrid finite element method. The results showed that the heat transfer was enhanced at the curved angle g = 90° for large Hartman numbers, thus, the average Nusselt number increased with a ratio of 240.74 % in the case of Hartmann number (Ha = 100).

Keywords: forced convection, backward-facing step, curved conduit, fixed cylinder, ferrofluid, finite element method, magnetohydrodynamic

Highlights

- *The discussion of magnetohydrodynamic behavior of laminar ferrofluid flow through a curved backward facing duct with a fixed cylinder is presented.*
- *The use of the horizontal magnetic field in the case of a curved geometry provide an enhancement of the heat transfer. Indeed, we note an increase of about 240 % in the heat transfer rate in case of important magnetic flux density.*
- *In the case of a curved backward facing duct, the presence of a vertical magnetic field has no effect on heat transfer.*
- *The increase in Reynolds number, Hartmann number and volume fraction of the nanoparticles enhance the heat transfer through a curved backward facing duct.*

0 INTRODUCTION

The sudden expansion geometry in a duct creates a separation and reattachment of the flow, as this expansion is a determining factor in the structure of the flow so the heat transfer is significantly affected. Thus, this geometry has a very important role in various engineering applications such as gas turbine engines, heat exchangers, combustion chambers, aircraft, and electronic devices and around buildings and many others. Indeed, it is receiving a lot of attention, so many studies focused on the separation and reattachment of the flow backward-facing step. For important Reynolds numbers Erturk **[1]** investigated a simulation of incompressible laminar steady flow in two dimensions (2D). In three-dimensional (3D), Lan et al. **[2]** presented in rectangular duct, a numerical study of laminar forced convection flow by means of a K-ε-ζ-f turbulence model. Iwai et al. **[3]** presented at little Reynolds number, the effect of the duct aspect ratio. An agreement of the numerical results with experimental results was revealed. Moreover, an increase of the Nusselt number near the sidewalls in the cases studied. Star et al. **[4]** developed for different Richardson number a reduced-order proper orthogonal decomposition (POD)-Galerkin simulation Reynolds-averaged Navier–Stokes (RANS) extended to low Prandtl number flow. In the fact, the buoyancy marks its influence on flow and heat transfer. In addition to a more accurate prediction of the flow behavior, the description of the fluid parameters as well as the identification of the rheological consequences are interesting. Kahine et al. **[5]** demonstrated the stabilizing impact of the shear thinning character of the fluid by numerical simulation compared to experimental data. To represent Newtonian fluids and the power law relationship between viscosity and shear rate, Mahmood et al. **[6]** analyzed the flow of Newtonian materials and a power law fluid representing the characteristics of shear thinning, thickening, with the finite element method. The control of turbulent flows can be realized using either

*Corr. Author's Address: University of Science and Technology of Oran, Faculty of Mechanical Eng., Maritime Science and Eng., Algeria, djamila.derbal@univ-usto.dz

external, stable or unstable forcing, and is of basic as well as practical interest [7]. Benard et al. [8] and Li et al. [9] studied the effect of periodic perturbations with an imposed frequency and amplitude on the evolution of vortices formed downstream of a backward facing step (BFS). For the little Reynolds number, Koide et al. [10] to enhance heat transfer; they provided a numerical simulation based on experimental data, behind a backward facing step, on the flow attachment in the transient regime. Tihon et al. [11] evaluated the effects of various control parameters on the periodic disturbance introduced in the flow. They presented an experimental approach, to examine the flow behavior in the backward flow step by means of the fluctuating wall shear rate downstream of the step, as well as the effect of the inlet flow pulses on the overall flows structure.

Heat transfer is the concern of many researches, so its improvement according to the process needs. A new method has been introduced to intensify the convective heat transfer, is to inject nanoparticles into the base fluid. In this regard, several recent researches have been carried out to show the effectiveness of using these nanoparticles in base fluids. The addition of nanoparticles in the base fluid marks their significant effect in different processes particularly those that concentrate on the thermal transfer [12] to [14]. Selimefendigil et al. [15] studied the effects of nanoparticles volume fraction, the inlet oscillation frequency and the Reynolds number on the fluid flow and thermal transfer features. They showed that the heat transfer is increased with the enhancement of the volume fraction of the nanoparticles, the Reynolds number and the frequency of the oscillation, experimentally, the degree of heat transfer flow over a backward-facing step duct increases as the volume concentration of the nanoparticles increases [16]. In order to observe clearly the effect of expanding rate, Togun et al. [17] introduces a numerical simulation of a turbulent and laminar heat transfer flow of nanofluid on a backward step, and various control parameters assumed. The results reveal that the angle of incidence of the vortex generators has significant effects on the heat transfer increase. Ahmed et al. [18] examined the forced convection heat transfer of a laminar fluid flow on a microscale BFS, the result indicates that the heat transfer is enhanced with a little increase in pressure drop in the case of a rectangular vortex generator (VG) wing with an angle of attack of θ° and a Reynolds number of . Abbassi and Nassrallah [19] analyzed the laminar flow of a viscous incompressible nanofluid through a backward-facing step duct under the effect of a magnetic field. They discussed the magneto hydrodynamic behavior under the effect of some control parameters. Furthermore, they demonstrated that the magnetic field significantly improves the heat transfer at high Prandtl numbers. Kumar and Dhiman [20] investigated for a particular Prandtl number and at different values of *Re* the forced convection characteristics of backward laminar flow in a two-dimensional channel. They discussed the effect of cylinder position on flow and heat transfer, an enhancement of the Nusselt number while using a circular cylinder compared to the case without a cylinder. Hussain et al. [21] we applied the Galerkin finite element method to compute the forced convective flow of a ferrofluid within a BFS containing a rotating cylinder with a fixed diameter, The magneto hydrodynamic behavior was analyzed assuming a wide range of control parameters namely Reynolds number, Hartmann number, magnetic field inclination angle and nanoparticle volume fraction. The effect of these parameters on the thermo magnetohydrodynamic (MHD) structure has been demonstrated. In addition, Selimefendigil and Öztop [22] presented the impact of these parameters on the flow and on the heat transfer in the case of mixed convection through a duct without cylinder. Mohammed et al. [23] investigated numerically, the effects on hydrodynamic and heat transfer of four different types of shapes that block the mixed convective of the laminar transient nanofluid flow through microscale BFS placed in a horizontal duct. Kherbeet et al. [24] showed the heat transfer characteristics reported experimentally and numerically on a laminar convective flow using a nanofluid with two nanoparticles types. It has been, shown that the Nusselt number increases and improves in the case of one nanofluid over the other. Lv et al. [25] in two-dimensional backward step flow, based on the analysis of several parameters, the flow characteristics are studied quantitatively using particle image velocimetry (PIV) while changing the Reynolds number and the weight nanofluid fraction. The mass and momentum transfer in the nanofluid improved, which leads to an improvement of the heat transfer. Amiri et al. [26] added an experimental study on the thermo-physical properties of egg nucleoplasmin (EggNP). The results indicate that a greater weight nanofluid concentration involves a faster rate of heat transfer on a backward facing step. Niemann and Fröhlich [27] in a turbulent mixed convective flow, they studied the buoyancy effect on the velocity field and on heat transfer is by comparing two simulations, one with the buoyancy term removed from the equations, and the other with a Richardson number of

0.338 The results contribute to the physical understanding of the effects of buoyancy on heat transfer in the considered regime. In addition, the data generated provides validation and improvement of turbulence models for turbulent heat transfer at low Prandtl numbers. To show the fin's impact on heat transfer. Boruah et al. [28] investigated the thermal-hydrodynamic properties and entropy creation for a mixed convective flow across a channel BFS with various baffle geometries. The results indicate that the wedge-shaped elliptical baffle arrangement in the duct BFS is an ideal design from the point of view of thermal-hydraulic efficiency and entropy generation. Thermal-hydrodynamic characteristics of fluids flowing through downward flowing duct in the presence of obstacles have received relatively little attention in the literature, despite the important effect that these obstacles can have on the flow structure and heat transfer [29]. Selimefendigil and Öztop [30] studied numerically the forced convection heat transfer over a backward facing step duct with a baffle on the top wall on a pulsating laminar flow. The effects of several important parameters were discussed, compared to a steady flow without baffle. They showed that in the case of a lower wall downstream of the enlargement, the presence of a deflector is not beneficial for the improvement of heat transfer. Selimefendigil and Öztop [31] studied numerically the laminar forced convection of a pulsed nanofluid flow over a BFS. They treated the effect of several control parameters and different geometrical factors namely: length and height of the bottom wall surface corrugation. The results show that the rate heat transfer increases with the inclusion of nanoparticles. Moreover, the rate of enhancement depends on the volume fraction of nanoparticles in the base fluid. Boruah et al. [32] demonstrated numerically a mixed convection flow of an incompressible non-Newtonian fluid across a channel BFS with a chicane. The results showed the impact of baffle location and nanoparticle diameter on the convective transfer. Furthermore, these results are beneficial for the design of a thermodynamic system capable of achieving maximum heat transfer with minimum irreversibility. Mohammed et al. [33] have numerically simulated a mixed convection flows of laminar and turbulent nanofluid on a backwards step. They analyzed the effect of geometrical parameters such as height, position of baffles, width and number of baffles analyzed. Heshmati et al. [34] presented the effect of several control parameters as well as deflectors with four different geometries. In addition, the effect of inclination and location was included. Due to the importance of thermal phenomena in curved ducts, several researches have been conducted in the literature. In order to give a detailed knowledge, to understand the complexity of non-isothermal flows, to prevent the phenomena of hydrodynamic instability that can occur, researchers have carried out work on non-isothermal flows to highlight these phenomena in this type of duct. Yanase et al. [35] proposed a numerical simulation of the convective non-isothermal heat transfer flow through a curved rectangular duct. The calculations performed by the spectral method for different Grashof numbers and Dean numbers. Several satisfactory results are obtained in terms of velocity and temperature. In addition, the convection remarkably enhanced from the hot wall to the fluid. Mondal et al. [36] studied numerically a convective heat transfer flow through a curved duct. Therefore, they treated the effect of Grashof number and aspect ratio on the thermo-hydrodynamic flow behavior over a wide temperature difference range applied to the cold inside and hot outside. Li et al. [37] presented a combination of experimental and numerical study to demonstrate the three-dimensional behavior of laminar flow in 210° curved rectangular ducts with three aspect ratios (*Ar*) and continuous curvature variation (*Cr*). The results show the complex changes in the formation, evolution of Dean vortices of different types. Furthermore, they demonstrated the effect of these control parameters on the instability of Dean vortices in the case of turbulent flow. Choi and Park [38] studied numerically the mixed convection flows through curved concentric annular ducts with constant wall temperature. The simulation was performed for different Dean numbers, different Grashof numbers and different radius ratios. Indeed, they presented the effect of these control parameters. Furthermore, they showed that for the Grashof number critical value, the average Nusselt number showed a strong dependence on the Dean number and the radius ratio. Chandratilleeke et al. [39] presented a numerical study to examine the development of recirculation zones and the appropriate heat transfer phenomenon that takes place from a laminar fluid flow through curved rectangular duct. In fact, they carefully analyzed the flow conditions leading to hydrodynamic instability and the generation of Dean vortices in curved duct, identifying the influences of the different control parameters. In addition, they examined the buoyancy force effect and secondary flow on the thermal process. Choi and Zhang [40] carried out a numerical simulation to evaluate the forced convection of a laminar flow of Al_2O_3 nanofluid through a curved duct. They found that the addition of Al_3O_2

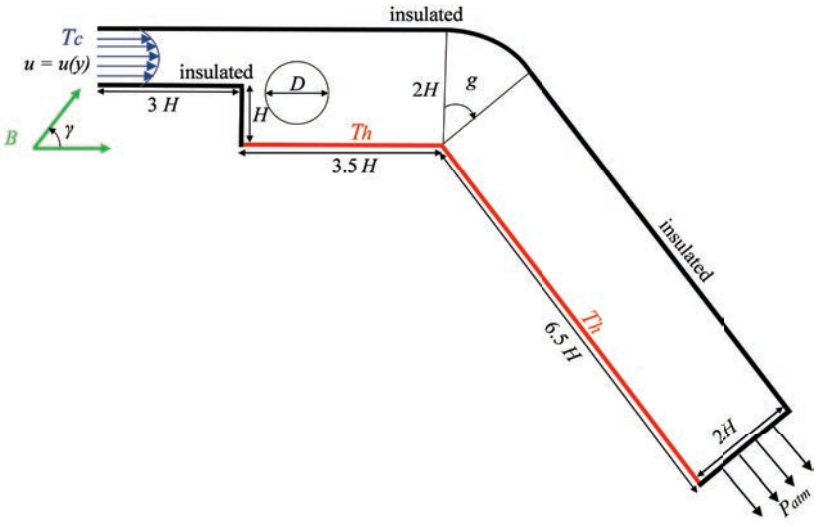

Fig. 1. *The physical configuration with the boundary conditions*

nanoparticles at low and increasing concentrations increases the average Nusselt number. Ajeel et al. [41] showed that different control parameters such as the corrugated shape of the curved duct, the installation of baffles with different geometric ratios as well as the hybridization of the nanoparticles positively affect the heat transfer.

The analysis of various previous works has shown that the thermo-magneto-hydrodynamic behavior in curved duct has not been widely studied especially the one with backward-facing step and in the presence of nanoparticles. In this regard, the objective of the present study is to provide a numerical simulation of a forced laminar convective flow, in the presence of Fe_3O_4 nanoparticles in the base fluid (water), through a curved backward-facing step duct containing a fixed adiabatic cylinder under an inclined magnetic field and using a single-phase nanofluid model. The finite element method was used to solve the equations governing the considered fluid flow. The influence of the curvature angle on the thermal and hydrodynamic structures was demonstrated for different values of the several control parameters.

1 GEOMETRIC DESCRIPTION

The physical study presentation, consists of a curved backward facing duct, containing a fixed cylinder of diameter D, centrally located at ($4H$, H), see (Fig. 1). In addition, an angle of curvature (g) is imposed on the duct and an external magnetic field has been imposed at an angle (γ). The expansion ratio is set to 2 and the step height is taken as H, halfway up the duct. The effects of viscous dissipation and Joule heating are not taken in to account the energy equation modelling. The induced magnetic field was assumed negligible. The ferrofluid at the inlet was considered cold and maintained at a temperature T_c, on the other hand, the bottom wall downstream of the step is maintained at a high temperature T_h and the other walls are maintained thermally adiabatic. The water and iron oxide thermo physical properties are presented in Table 1 The physical situation with boundary conditions is presented in Fig. 1

Table 1. *Thermophysical properties of water (H_2O) and iron oxide nanoparticles* [21]

Physical properties	Water (H_2O)	Nanoparticles (Fe_3O_4)
Density [kg·m^{-3}]	997.1	5,200.0
Specific heat [J·kg^{-1}·K^{-1}]	4,179	670.0
Thermal conductivity [W·m^{-1}·K^{-1}]	0.613	6.0000
Thermal expansion [K^{-1}] ($\times 10^{-5}$)	0.613	1.1800
Electrical conductivity [S·m^{-1}]	0.050	25,000

2 MATHEMATICAL MODEL

2.1 Governing Equations

$$\frac{\partial u}{\partial x}+\frac{\partial v}{\partial y}=0, \tag{1}$$

$$\rho_{ff}\left(u\frac{\partial u}{\partial x}+v\frac{\partial u}{\partial y}\right)=-\frac{\partial p}{\partial x}+\mu_{ff}\left(u\frac{\partial^2 u}{\partial x^2}+v\frac{\partial^2 u}{\partial y^2}\right)+\sigma_{ff}B_0^{\,2}\left(v\sin\gamma\cos\gamma-u\sin^2\gamma\right), \tag{2}$$

$$\rho_{ff}\left(u\frac{\partial v}{\partial x}+v\frac{\partial v}{\partial y}\right)=-\frac{\partial p}{\partial y}+\mu_{ff}\left(u\frac{\partial^2 v}{\partial x^2}+v\frac{\partial^2 v}{\partial y^2}\right)+\sigma_{ff}B_0^{\,2}\left(u\sin\gamma\cos\gamma-v\cos^2\gamma\right), \quad (3)$$

$$u\frac{\partial T}{\partial x}+v\frac{\partial T}{\partial y}=\alpha_{ff}\left(\frac{\partial^2 T}{\partial x^2}+\frac{\partial^2 T}{\partial y^2}\right). \quad (4)$$

The following equation present the stream function:

$$\frac{\partial \psi}{\partial x}=-v, \quad \frac{\partial \psi}{\partial y}=u. \quad (5)$$

2.2 Boundary conditions

For the numerical calculation of this study situation, the imposed boundary conditions are expressed as follows:

- Input condition: a parabolic velocity profile in the direction of the *x*-axis and a uniform cold temperature:

$$u=u(y), \quad v=0, \quad T=T_c. \quad (6)$$

- At the bottom wall downstream of the expansion: The conditions of no-slip velocity and uniform hot temperature:

$$u=v=0, \quad T=T_h. \quad (7)$$

- Outlet condition: The gradient of velocity and temperature in the normal direction (normal direction coincide with *x*-axis):

$$\frac{\partial u}{\partial n}=\frac{\partial v}{\partial n}=0, \quad \frac{\partial T}{\partial n}=0. \quad (8)$$

- The no-slip boundary conditions for the velocity are applied on the duct walls and on the cylinder contour and the adiabatic conditions for the temperature are imposed except for the bottom hot wall downstream of the expansion:

$$u=v=0, \quad \frac{\partial T}{\partial n}=0. \quad (9)$$

2.3 Dimensionless Governing Equations

To transform the set of partial differential equations into a dimensionless form, the following variables given in Table 2 were used. The boundary conditions used in the dimensionless form are summarized in Table 3. The thermo-physical properties of the ferrofluid are depend on the properties of the base fluid and the magnetic nanoparticles. Hence, the effective thermo-physical properties of the nanofluid are given above in Table 4.

Table 2. *The variables used to transform the system of partial differential equations in to dimensionless form*

$X=\frac{x}{H}$, $Y=\frac{y}{H}$	$U=\frac{u}{\overline{u}}$, $V=\frac{v}{\overline{u}}$	$P=\frac{p}{\rho_{ff}\overline{u}^2}$
$\theta=\frac{T-T_c}{T_h-T_c}$	$Pr=\frac{\nu_f}{\alpha_f}$, $Re=\frac{H\overline{u}}{\nu_f}$	$Ha=B_0H\sqrt{\frac{\sigma_{ff}}{u_{ff}}}$

The dimensionless equations governing the flow summarized as follows:

$$\frac{\partial U}{\partial X}+\frac{\partial V}{\partial X}=0, \quad (10)$$

$$U\frac{\partial U}{\partial X}+V\frac{\partial U}{\partial Y}=-\frac{\partial P}{\partial X}+\frac{1}{\mathrm{Re}}\frac{u_{ff}}{\rho_{ff}\nu_f}\left(\frac{\partial^2 U}{\partial X^2}+\frac{\partial^2 U}{\partial Y^2}\right)+\frac{\rho_f}{\rho_{ff}}\frac{\sigma_{ff}}{\sigma_f}\frac{Ha^2}{\mathrm{Re}}(V\sin\gamma\cos\gamma-U\sin^2\gamma), \quad (11)$$

$$U\frac{\partial V}{\partial X}+V\frac{\partial V}{\partial Y}=-\frac{\partial P}{\partial Y}+\frac{1}{\mathrm{Re}}\frac{u_{ff}}{\rho_{ff}\nu_f}\left(\frac{\partial^2 V}{\partial X^2}+\frac{\partial^2 V}{\partial Y^2}\right)+\frac{\rho_f}{\rho_{ff}}\frac{\sigma_{ff}}{\sigma_f}\frac{Ha^2}{\mathrm{Re}}(U\sin\gamma\cos\gamma-V\cos^2\gamma), \quad (12)$$

$$U\frac{\partial \theta}{\partial X}+V\frac{\partial \theta}{\partial Y}=\frac{1}{Re\,Pr}\frac{\alpha_{ff}}{\alpha_f}\left(\frac{\partial^2 \theta}{\partial X^2}+\frac{\partial^2 \theta}{\partial Y^2}\right). \quad (13)$$

The dimensionless equations stream function given as follows:

$$\frac{\partial \Psi}{\partial X}=-V, \quad \frac{\partial \Psi}{\partial Y}=U. \quad (14)$$

2.4 The Local and Nu_{ave} Number

A convective heat transfer occurred due to the difference temperature between the flowing nanofluid and the hot wall downstream of the expansion. This heat flow can be estimated using the Nusselt number. This local dimensionless number is defined as a thermal gradient over the heated surface. In effect, it gives a measure of the convective heat transfer that occurs on that surface.

Table 3. *Boundary conditions introduced in dimensionless form*

At the channel inlet:	$U = U(y), \quad V = 0, \quad \theta = 0, \quad \frac{\partial \Psi}{\partial Y} = 1$
At the downstream bottom wall:	$U = 0, \quad V = 0, \quad \theta = 1, \quad \frac{\partial \Psi}{\partial X} = 0$
At the channel outlet:	$\frac{\partial U}{\partial X} = \frac{\partial V}{\partial X} = \frac{\partial \theta}{\partial X} = 0, \quad \frac{\partial \Psi}{\partial Y} = U_S$
On the channel walls (except the bottom wall):	$U = V = \frac{\partial \theta}{\partial n} = 0, \quad \Psi = 0$
On the boundary of cylinder:	$U = V = 0, \quad \frac{\partial \theta}{\partial n} = 0, \quad \Psi = 0$

Table 4. *The effective thermo-physical characteristics of the nanofluid*

Density:	$\rho_{ff} = (1-\varphi)\rho_f + \varphi\rho_s$
Thermal diffusivity:	$\alpha_{ff} = \frac{K_{ff}}{(\rho c_p)_{ff}}$
Electrical conductivity:	$\sigma_{ff} = \sigma_f \left(1 + \frac{3(\sigma-1)\varphi}{(\sigma+2)-(\sigma-1)\varphi}\right), \sigma = \frac{\sigma_s}{\sigma_f}$
Specific heat:	$(\rho c_p)_{ff} = (1-\varphi)(\rho c_p)_f + \varphi(\rho c_p)_s$
Thermal expansion coefficient:	$(\rho\beta)_{ff} = (1-\varphi)(\rho\beta)_f + \varphi(\rho\beta)_s$
Thermal conductivity:	$\frac{k_{ff}}{k_f} = \frac{k_s + 2k_f - 2\varphi(k_f - k_p)}{k_s + 2k_f + \varphi(k_f - k_p)}$
Dynamic viscosity:	$\mu_{ff} = \frac{\mu_f}{(1-\varphi)^{2.5}}$

The local Nusselt number on the heated wall is defined as follows:

$$Nu = \frac{h_{ff} H}{k_f}, \tag{35}$$

where h_{ff} is the heat transfer coefficient represented as follows:

$$h_{ff} = \frac{q_w}{T_h - T_c}, \tag{36}$$

where q_w stands the heat flux on the heated wall given as follows:

$$q_w = -k_{ff} \frac{T_h - T_c}{H} \frac{\partial \theta}{\partial n}\bigg|_{L_1+\ell}. \tag{37}$$

We substitute Eq. (37) into Eq. (36) and Eq. (36) into Eq. (35); we will have the following result:

$$Nu = \frac{k_{ff}}{k_f} \frac{\partial \theta}{\partial n}. \tag{38}$$

The Nusselt number given by integrating the local Nusselt along the length of the hot wall as follows:

$$Nu_{ave} = \frac{1}{L_1 + l}\left(\int_0^{L_1} Nu \; dx + \int_0^{1} Nu \; dl\right), \tag{39}$$

where L_1 represent the horizontal length part hot wall, l represent the inclined length part hot wall.

3 VALIDATION CODE AND GRID INDEPENDENCE TEST

The general solving procedure focuses on numerical methods. The discretization of the governing equations consists in transforming the differential form of the governing systems Eqs. (10) to (14) into a discrete algebraic form that defines all unknowns at each point of a used grid. The finite element method based on Galerkin discretization is implemented to solve the present problems because of its flexibility for complex geometries through different types of meshes on the one hand, and the ease of introducing boundary conditions in the form of flows on the other hand. The application of the present method requires a rewriting of the governing equations in integral form. The weak formulation is used to include the boundary conditions. The numerical solution goes through the following steps: introduction of the mesh, approximation of the dependent functions, assembly and application of the boundary conditions and finally the solution of the global system of equations. The mesh adopted for the present study, shown in Fig. 2, has in its entirety a triangular shape. It is refined near the duct walls and near the cylinder circumference. However, an unstructured triangular mesh has been introduced in the rest of the duct. It should be noted that near the duct walls and near the cylinder circumference, a rectangular boundary layer mesh was used to ensure that the grid presentation is well aligned with the flow. In each node of the defined grid, to complete the computation in terms of iteration number, the convergence criterion used consists in stopping the calculation when the absolute difference between the old and the new values of the dependent variables, namely U, V, P and θ becomes less than 10^{-6}. If Ψ and n present respectively a dependent variable and iteration order, this criterion is established using the following formula:

$$\left|\frac{\Psi^{n+1}-\Psi^{n}}{\Psi^{n+1}}\right| \prec 10^{-6}. \quad (20)$$

The results obtained from the computational code should be independent of the grid form and not be modified by increasing the mesh elements number. Therefore, different grids were verified. Table 5 gives the evolution of the average Nusselt number, the dimensionless mean temperature and the dimensionless temperature for different numbers of mesh elements that were considered in the present simulation. The verification of the mesh was carried out for the case $g = 90°$ at $Pr = 6.2$, $Re = 300$, $Ha = 0$, $\gamma = 0°$, $\varphi = 0.05$, We have chosen to use a mesh corresponding to a number of elements equal to 44 01 beyond which there was no change in terms of average Nusselt number, mean and local dimensionless temperature. To confirm the accuracy of these numerical results, validation with other previous work is necessary. The numerical results of this work were compared with the numerical results of Hussain and Ahmed [18]. They numerically studied the forced convection of a laminar flow of a ferrofluid around a cylinder inside a backward facing step. Therefore, the isotherm forms obtained in the present work were compared with the results of the reference mentioned above, see Fig. 4, this comparison was done in the case of $Ha = 0$ and $Ha = 100$ for values of $Pr = 6.2$, $Re = 100$, $\gamma = 0°$ and $\varphi = 0.05$. In a further step, a comparison of the average Nusselt number as a function of the Hartmann number has also been plotted in Fig. 3 under the same conditions mentioned above. It is clear from these figures that the isotherms and the average Nusselt number are almost similar. Therefore, the results of this work show very good agreement with the reference Hussain and Ahmed [18].

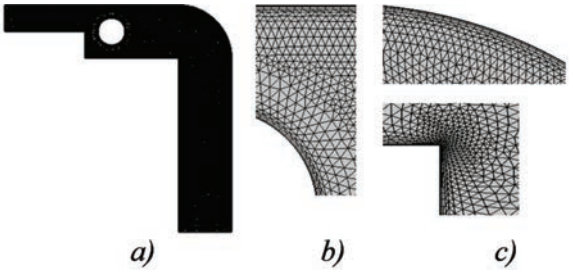

Fig. 2. *Mesh: a) inside the computational domain, b) zoom near the cylinder, and c) zoom near the curvature*

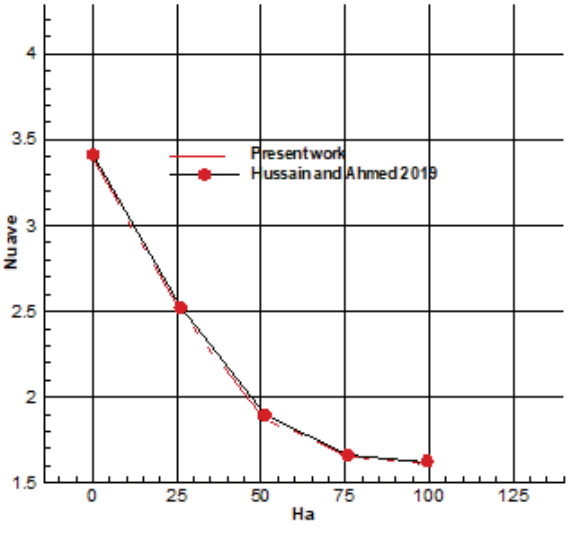

Fig. 3. *Comparison of the Nusselt average as a function of Ha of the present study with the reference Hussain and Ahmed [21]*

Table 5. *The average number of Nusselt and temperature for several numbers of elements*

Number of elements	17040	23713	31528	40401	50293	60970
Time of simulation [s]	17	25	30	50	55	78
Nu_{ave}	4.88585	4.89666	4.90630	4.92318	4.92170	4.92185
θ_{ave}	0.14977	0.15111	0.15257	0.15413	0.15424	0.15461
θ	0.05355	0.05361	0.05462	0.05530	0.05537	0.05534

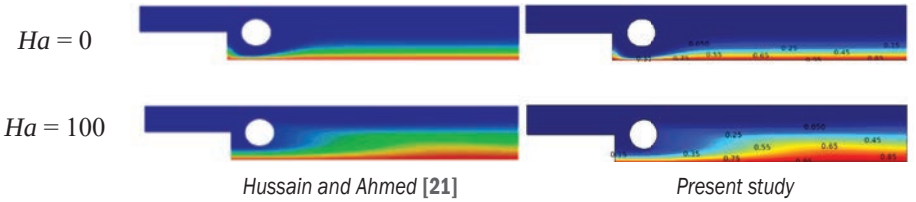

Fig. 4. *Comparison of the isotherms of the present study with the reference the reference Hussain and Ahmed [21]*

4 RESULTS AND DISCUSSIONS

In this section, the results of the numerical simulation of the nanofluid flow in a downward curved duct are shown. The isotherms, streamlines and average Nusselt number are presented for different values of Hartmann number *Ha* (0, 50, 100) , Reynolds number *Re* (100, 200, 300), nanoparticle volume fraction φ (0 %, 5 %, 1 %) and magnetic field inclination angle γ (0°, 30° , 90°). The simulation was based on demonstrating for each value of the curvature angle *g* (0°, 30°, 45° , 60° , 90°) the effect of these control parameters on the thermo hydrodynamic nanofluid behavior. In this study, water is the basic fluid in the formation of ferrofluid with *Pr* = 6.2. On the other hand, the presentation of the different profiles and graphs consists in setting the Reynolds number, the Hartmann number, the angle of inclination of the magnetic field and the volume fraction of the nanoparticles respectively to *Re* = 300, *Ha* = 50, γ = 0° and φ = 0.05 when the influence of one of them is highlighted.

4.1 Effect of Hartmann number

Fig. 5 gives the influence of the Hartmann number on the streamlines at different curvature angles. In the absence of the magnetic field for a straight geometry (*g* = 90°), an equilibrium between the pressure gradient and the centrifugal force is established downstream of the cylinder, so the action of the centrifugal and viscous forces simultaneously leads to the appearance of two counter-rotating vortices in the downstream part of the cylinder. Furthermore, by increasing

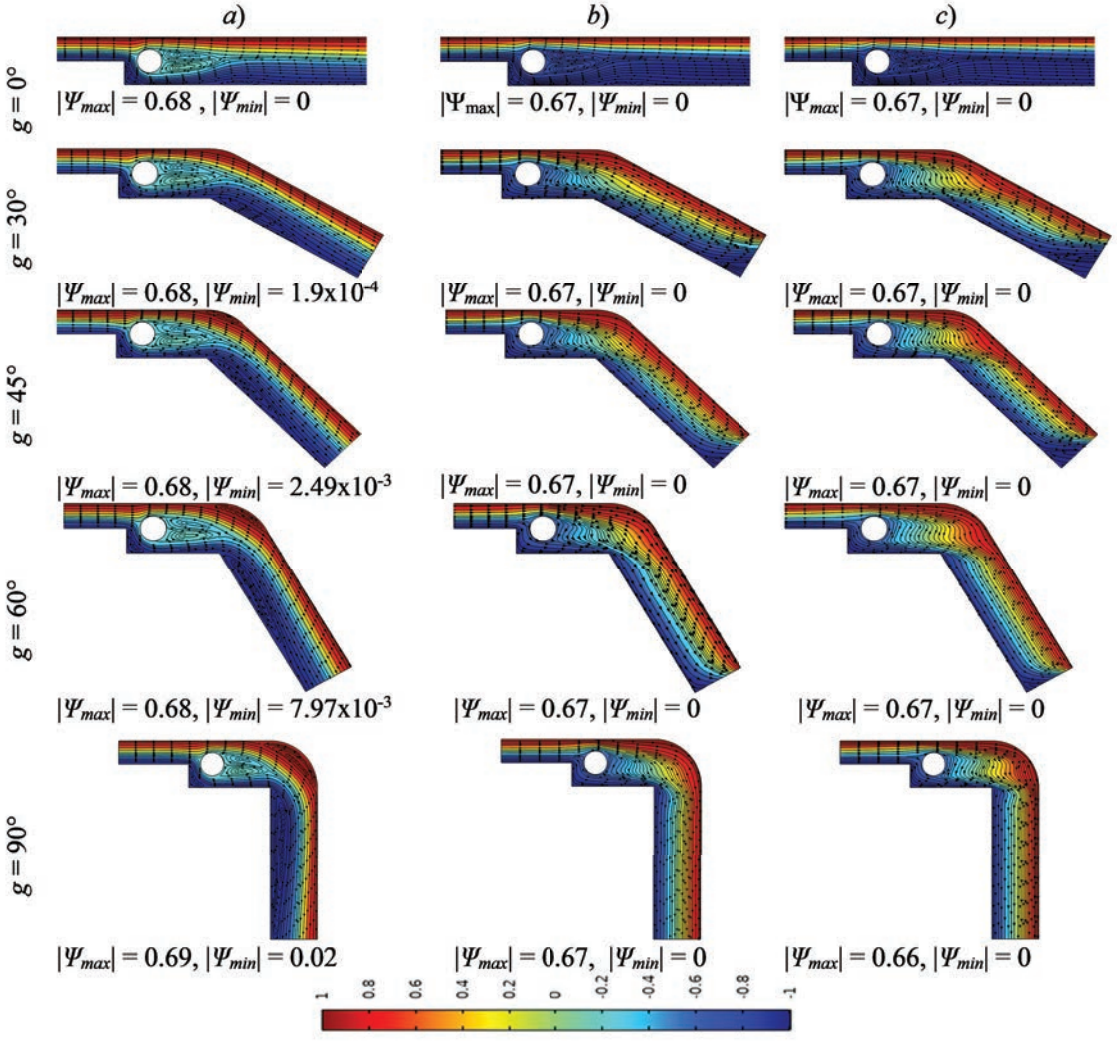

Fig. 5. *Streamlines at different angles of curvature (g) for a) Ha = 0, b Ha = 50, and c) Ha = 100, when Pr = 6.2.*

duct curvature angle g (30°, 45°, 60°) again in the absence of the magnetic field $Ha = 0$, we observe the formation of recirculation zones which are in this case dead zones, especially in the immediate vicinity of the curved hot wall, these vortices tend to widen by increasing the angle of curvature. As the magnetic field intensity increases from $Ha = 0$ to $Ha = 100$, these vortices disappear, favoring the contact of the ferrofluid with the hot wall. The increase in magnetic field intensity in the case of a straight duct ($g = 0°$) leads to an opposite impact to that of a curved duct. The mobility of nanoparticles in the duct decreases in terms of current function and velocity magnitude with increasing magnetic field in the case of a straight duct geometry ($g = 0°$), in contrast to a curved duct the flow intensifies with increasing Hartmann number. This behaviour is due to the Lorentz force, which obstructs the ferrofluid in the first case and drives it in the second case. The magneto hydrodynamic behaviour has an effect on the temperature contours as shown in Fig. 6 In fact, the intensity of forced convection increases as the Hartmann number increases from $Ha = 0$ (without magnetic field) to $Ha = 100$ in curved duct case g (30°, 45°, 60°, 90°). A reduction of the thermal boundary layer has been noted by virtue of the good heat transfer. Therefore the Nusselt number is better in straight curvature angle case $g = 90°$ on the one hand. On the other hand, in a straight duct case, the convection decreases by increasing the Hartmann number, the lines of the isotherms start to move towards the adiabatic wall at the top so the thermal boundary increases. Fig. 7 illustrates the effect of the curvature angle on the local Nusselt number along the hot wall in the case of Hartmann number values $Ha = 0$ and $Ha = 100$ respectively. It was found that in the absence of the magnetic field ($Ha = 0$), the local Nusselt number marks an increase in the initial part of the hot wall (just below the cylinder), so with the increase of the curvature angle it is found that the local Nusselt number decreases. Moreover in the case of a strong magnetic field ($Ha = 100$) the local Nusselt number shows an increase in the initial part of

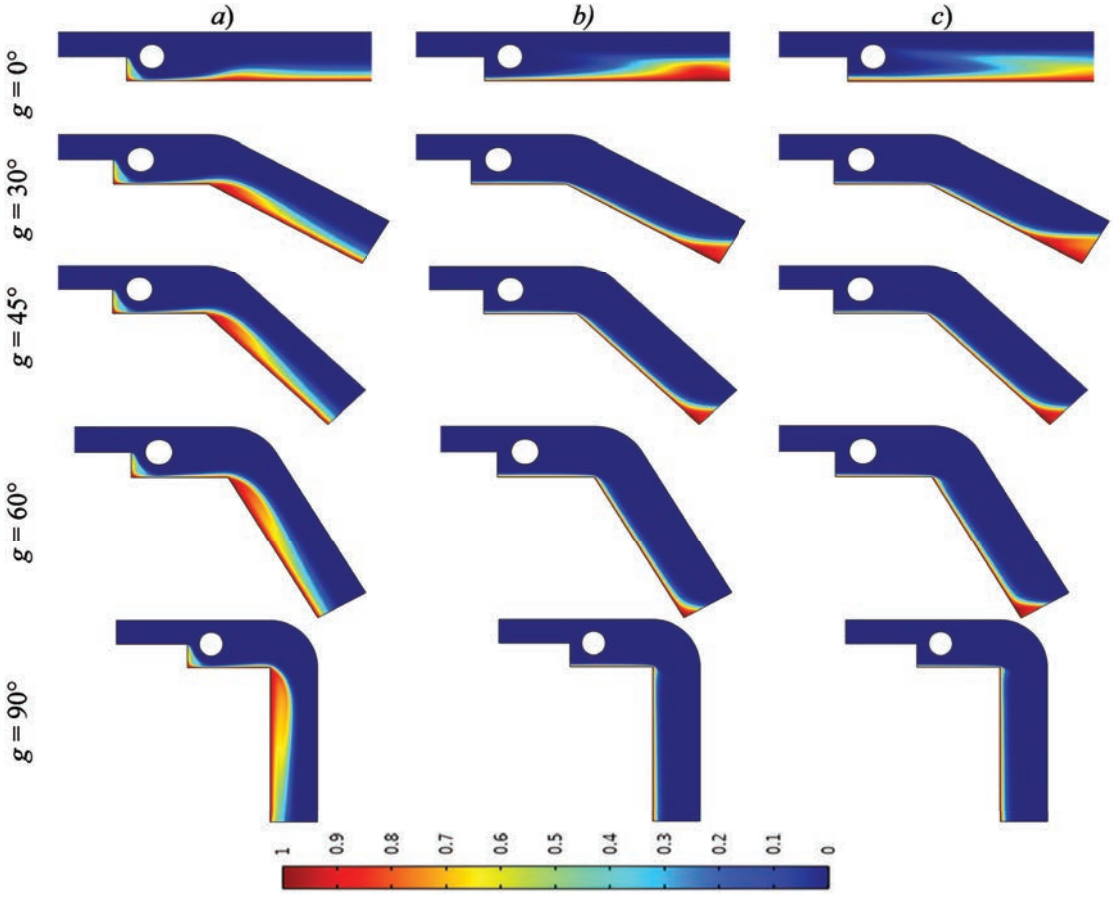

Fig. 6. *Isotherms at different angles of curvature (g) for a) Ha = 0, b Ha = 50, and c) Ha = 100*

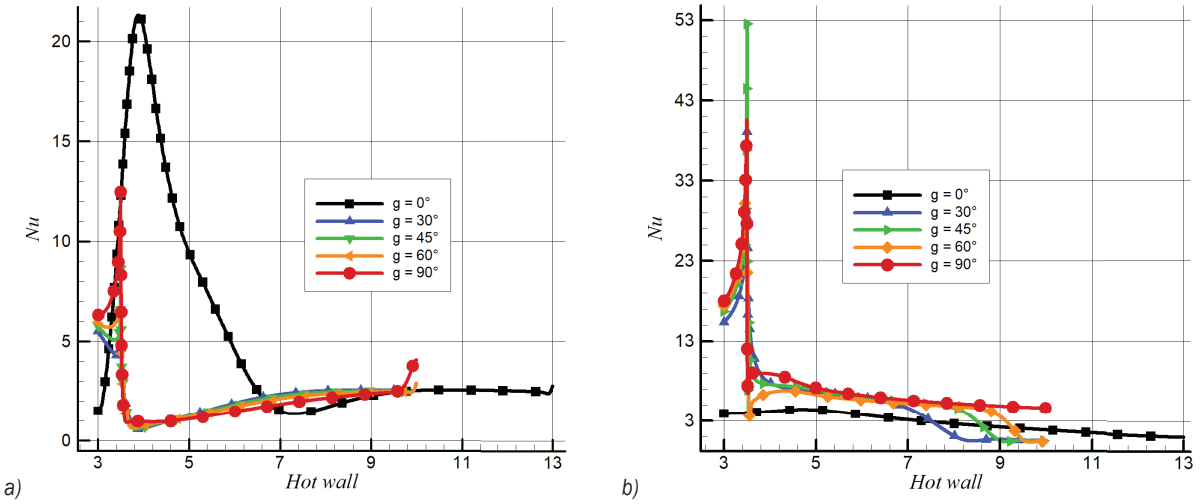

Fig. 7. *The effect of the curvature angle around the hot wall on local Nusselt: a) Ha = 0, and b) Ha = 100*

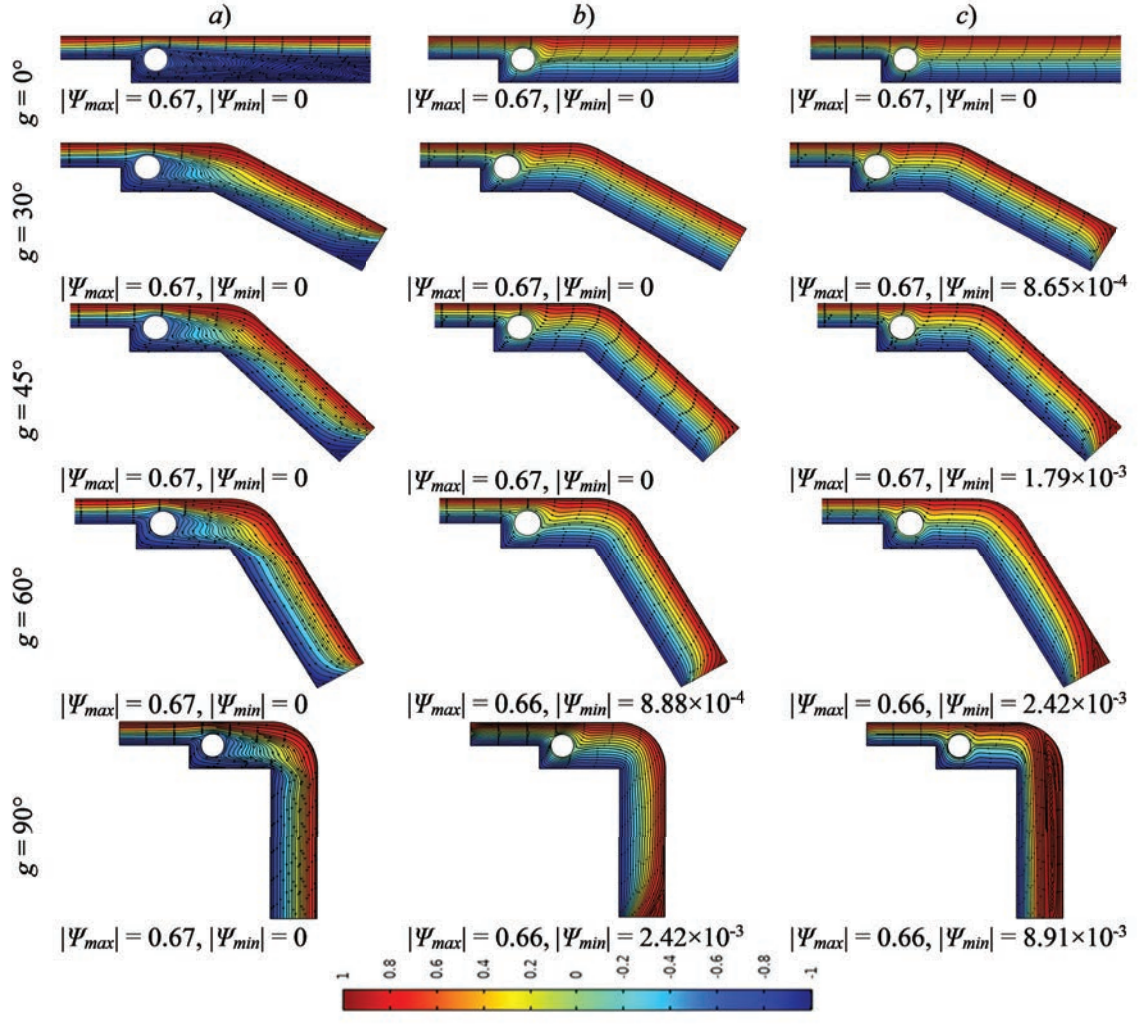

Fig. 8. *Streamlines at different angles of curvature (g) for: a) γ = 0°, b) γ = 60° , and c) γ = 90°*

the curvature hot wall part. Indeed the increase of the curvature angle leads to an improvement of the local Nusselt number in the curvature part.

This behavior is due to the Lorentz force that drives the flow in the curved part.

4.2 The Effect of the Inclination Angle of the Magnetic Field

Fig. 8 shows the hydrodynamic behavior of the nanofluid for different magnetic field inclination angles. It has been observed that in the case of straight duct ($g = 0°$), the ferrofluid flow is slow at the bottom of the cylinder at horizontal magnetic field ($\gamma = 0°$). Therefore by increasing the magnetic field inclination, the mobility of the nanoparticles increases to its maximum at the bottom in the vicinity of the cylinder near the hot wall at a vertical magnetic field ($\gamma = 90°$). Moreover, a mobility was noted in terms of current function in the curved part by increasing the duct curvature angle of g (30°, 3 , θ°) in the presence of a horizontal magnetic field. In contrast, in the presence of a vertical magnetic field and increasing the curvature angle, the current function lines are almost identical except in the case of curvature angle $g = 90°$, where the nanofluid flow marks a significant recirculation region at zero velocities in the immediate vicinity of the adiabatic wall. Physically this phenomenon is by virtue of the Lorenz force, which is driving as we increase the angle of inclination of the magnetic field from 0°, θ° to θ° where we note a strong flow in the case of a straight duct. On the other hand, the increase in the angle of inclination of the magnetic field directs this force in direction that obstructs the flow in the case of a curved for all angles of curvature. The isotherms presented in Fig. 9 show the thermal behavior, which is strongly influenced by the hydrodynamic state of the nanofluid under the

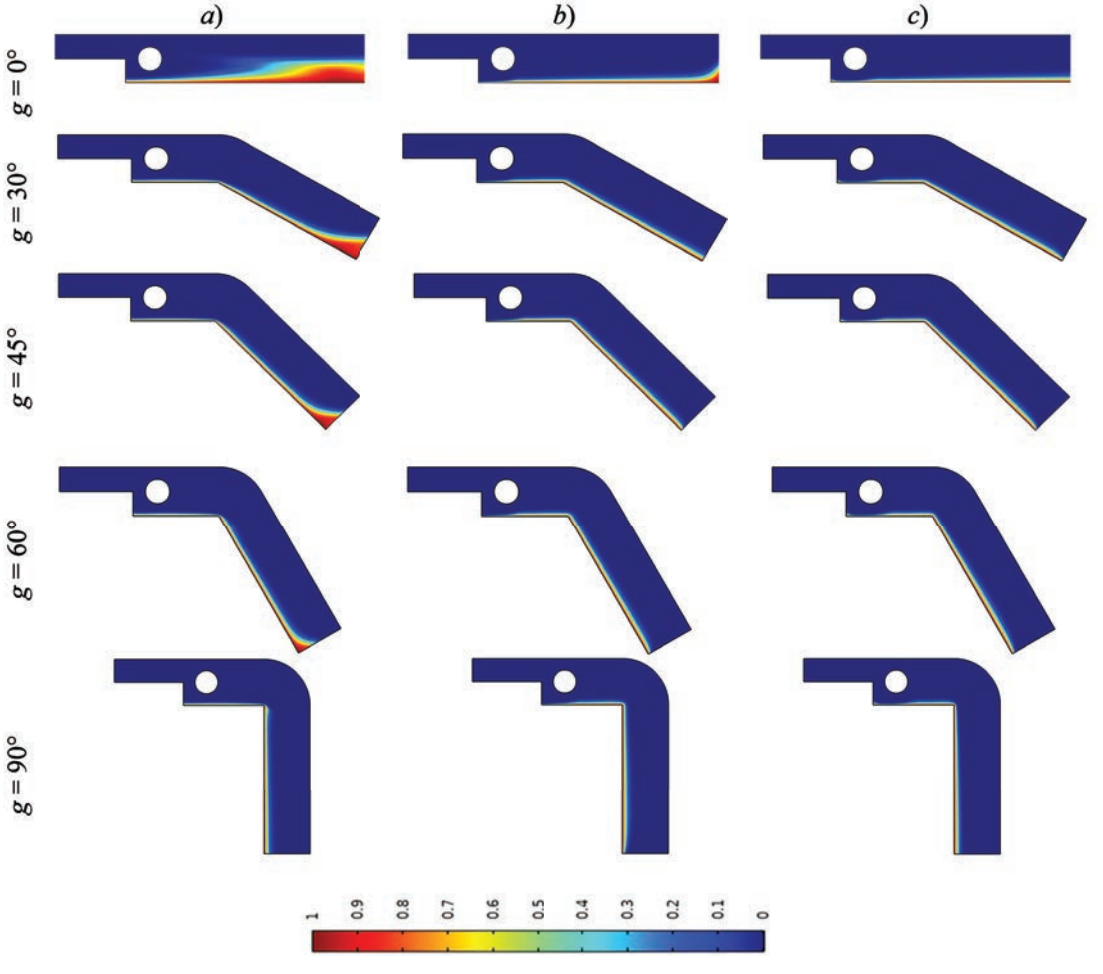

Fig. 9. *Isotherms at different angles of curvature (g) for: a) γ = 0°, b) γ = 60°, and c) γ = 90°*

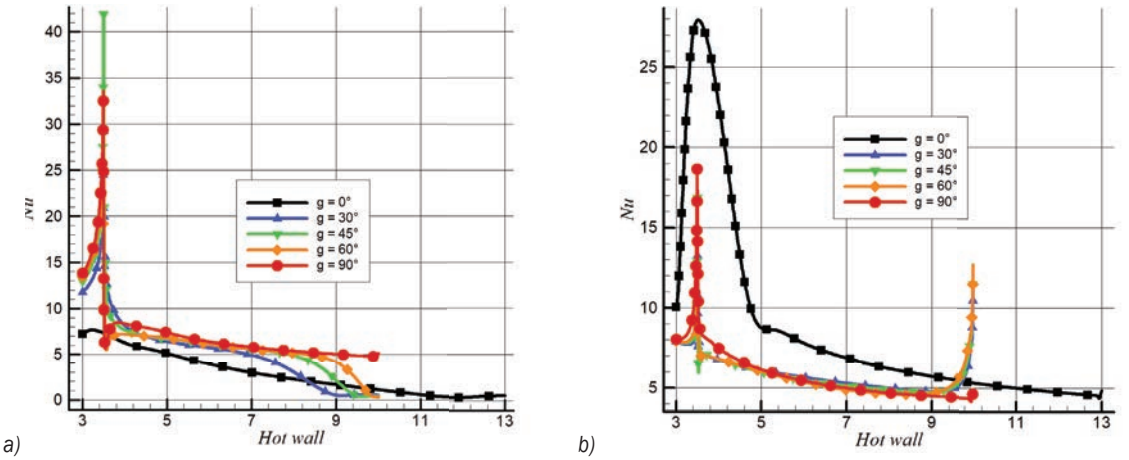

Fig. 10. *The effect of the curvature angle around the hot wall on local Nusselt number: a) at horizontal magnetic field (γ = 0°), and b) at a vertical magnetic field (γ = 90°)*

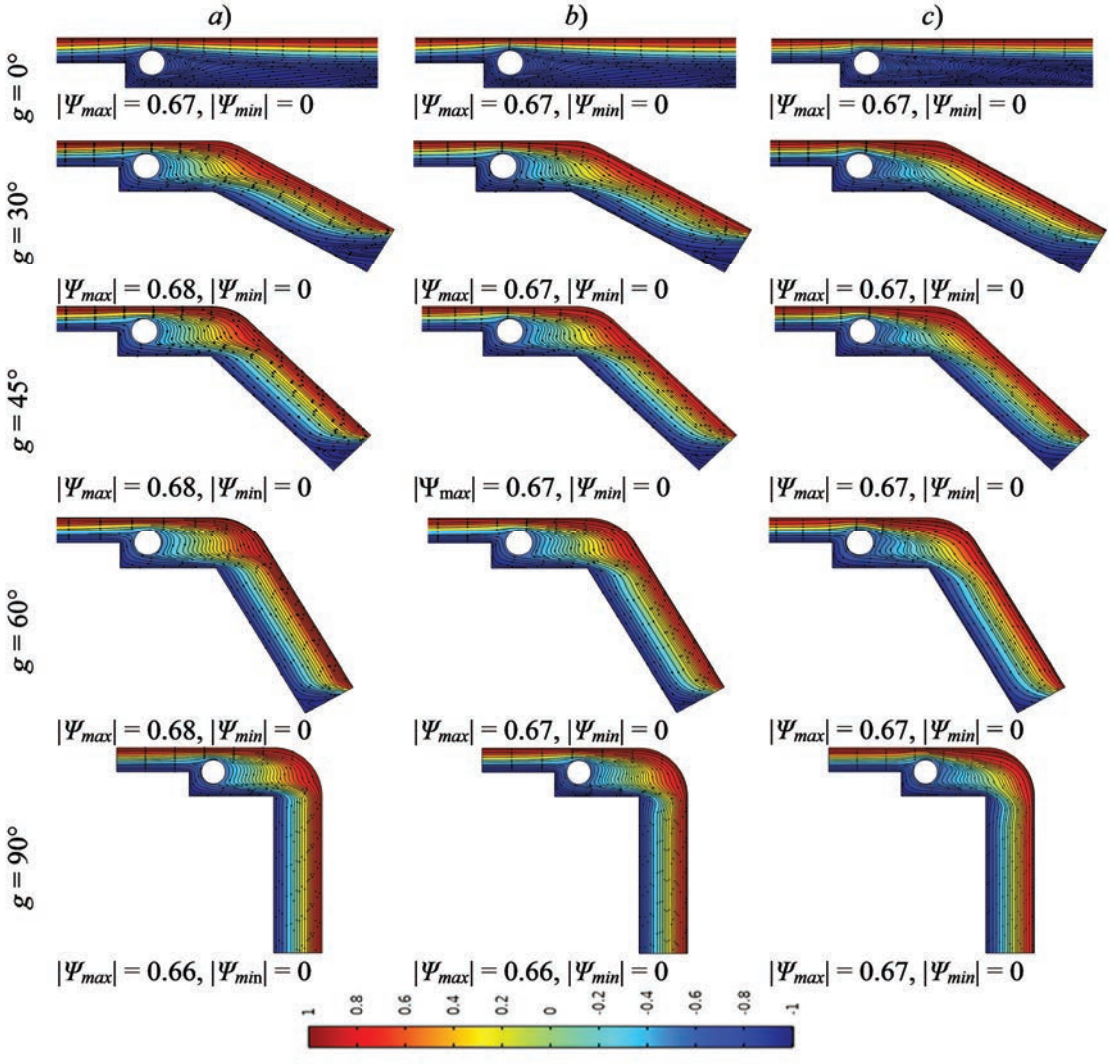

Fig. 11. *Streamlines at different angles of curvature (g) for: a) Re = 10, b) Re = 100, and c) Re = 300*

effect of the magnetic field inclination angle. In the case of a horizontal magnetic field, a decrease of the thermal layer is underlined in the case of a straight duct as the magnetic field inclination angle increases. Indeed, a reduced thermal layer corresponding to a good thermal convection is observed for a vertical magnetic field (γ = 90°). On the other hand, for a horizontal field by increasing the curvature angle, the thermal layer is reduced in the curved part due to the good thermal transfer. Moreover, by increasing the angle of curvature, the increase of the angle of inclination of the magnetic field has no effect on the heat transfer. Fig. 0 shows the variation of the local Nusselt number along the hot wall for the two values of inclination angle respectively γ = 0° and γ = 90°. We observe an improved local Nusselt number in the curved part in the case of a horizontal inclination angle (γ = 0°). On the other hand in the case of a vertical inclination angle (γ = 90°) the local Nusselt number in the curved part is practically the same by increasing the curvature angle and in the straight part, it increases relatively.

4.3 The Effect of Reynolds Number

Fig. 11 shows the influence of Reynolds number (or inertia) on the streamlines of the Fe_2O_3-water nanofluid flow in the downward curved duct. A significant increase in Reynolds number from a value of 0 to a value of 300, leads to significant changes in the hydrodynamic behavior of the nanofluid flow. In fact, in the case of a straight duct, the flow becomes more intensity as the Reynolds number increases, thus favoring the attachment of the nanofluid due to the enlarged duct type used. Furthermore, by increasing the curvature angle of the duct as well as the Reynolds number, the flow of the nanofluid becomes stronger where it marks its intensity at a curvature angle (g

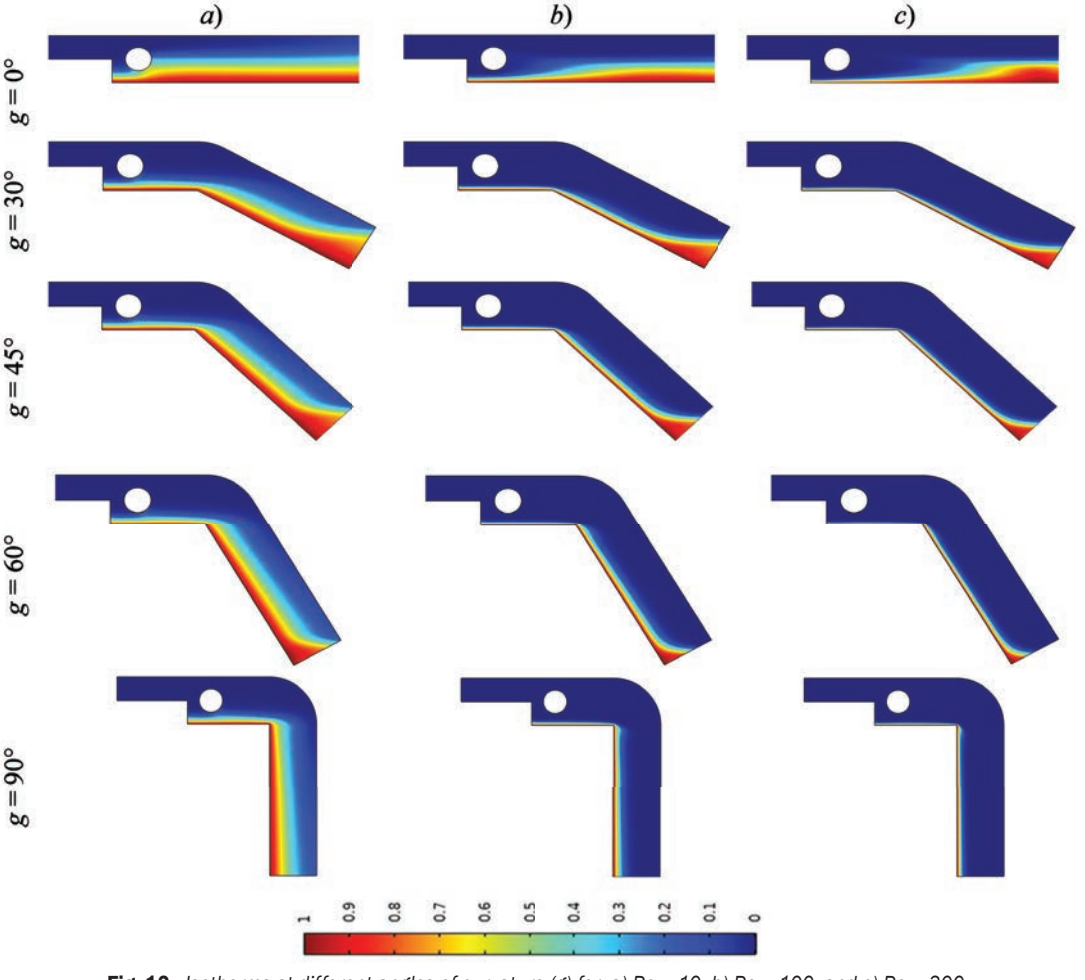

Fig. 12. *Isotherms at different angles of curvature (g) for: a) Re = 10, b) Re = 100, and c) Re = 300*

= 90°) thus favoring the attachment at a Reynolds number (Re = 300). This phenomenon is due on the one hand to the inertial forces which predominate the viscous forces as well as the Lorenz force when the Reynolds number increases in the case of a horizontal curvature angle (g = 0°). Moreover, by increasing the angle of curvature, the viscous forces and the Lorenz force carry away the flow next to the inertia forces, which increase with the increase of the Reynolds number. The thermal behavior is strongly influenced by the hydrodynamic state of the nanofluid under the effect of the inertia as shown in Fig. 12. Indeed the thermal band marks a decrease with the increase of the inertia in the case of a straight duct. On the other hand, we note a decrease of the thermal layer, which extends towards the hot wall increasingly by raising simultaneously the angle of curvature and the Reynolds number, reflecting an improved thermal transfer. Moreover, a significantly reduced thermal layer is mentioned in the case of a curvature angle (g = 90°) for a Reynolds number (Re = 300), by virtue of a good convection that took place in this situation.

4.4 Effect of Nanoparticle Concentration

Fig. 13 shows the streamline profiles for different curvature angles at different average nanoparticle concentrations φ (0, 0.05, 0.1).

It can be seen from this figure that there is no change in the streamline pattern by adding nanoparticles at different volume fractions to the base fluid. This is due on the one hand to the use of particles

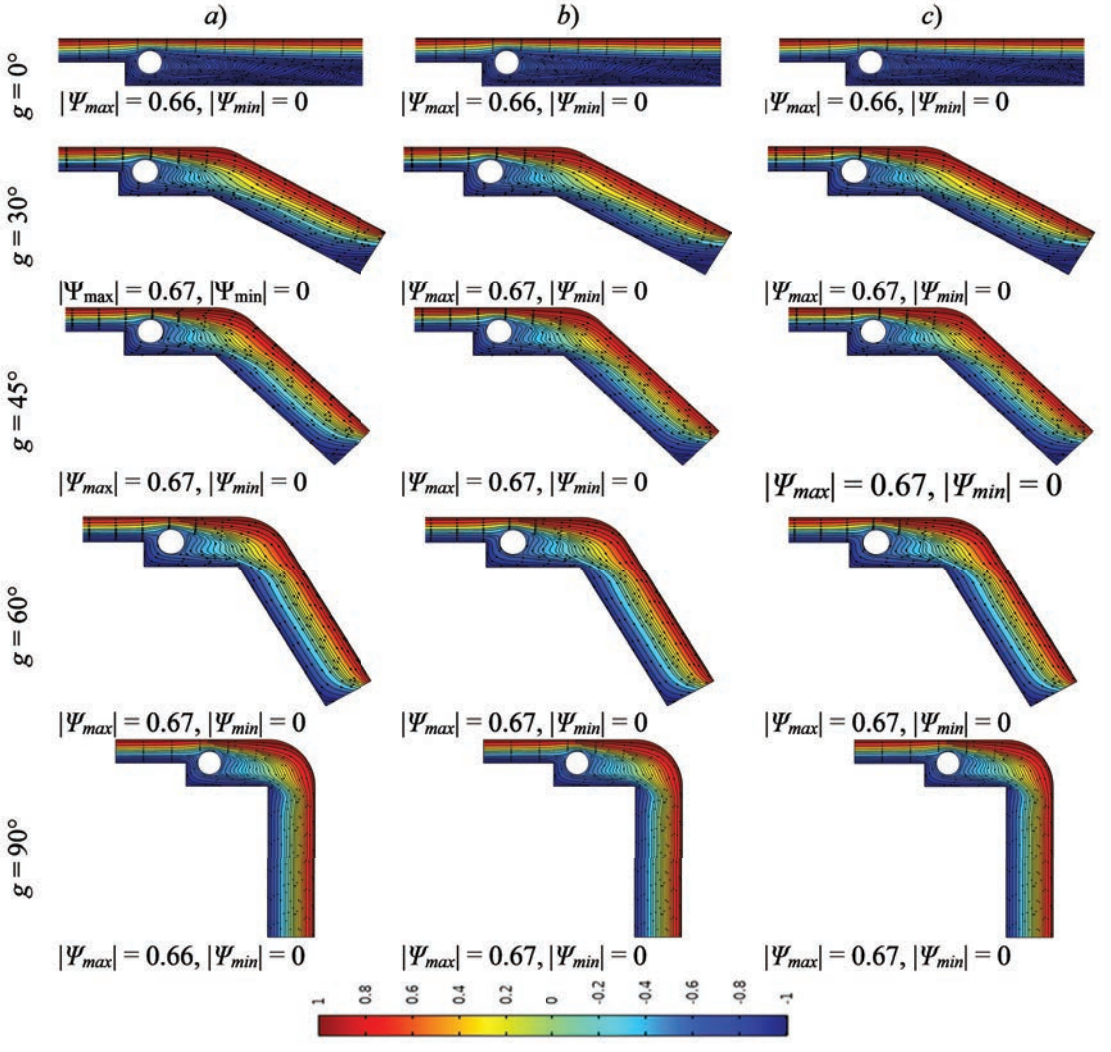

Fig. 13. *Streamlines at different angles of curvature (g) for: a) φ = 0, b) φ = 0.05, and c) φ = 0.1.*

of nanometric diameters at low concentrations. On the other hand, the injection of nanoparticles in applications related to heat transfer. In fact, the absence of buoyancy force based on the conditions of this study (forced convection) does not show the influence of the temperature formerly affected by the presence of nanoparticles on the hydrodynamic behavior. Indeed a weak influence of the viscosity and density on this behavior. From Fig. 14 it appears that the isotherms profiles show similarly no change. With the increase of the concentration of nanoparticles, the temperature increases in the middle of the duct in the straight part as well as the curved part. Indeed, a good increase is marked in the case of a curvature angle (g = 90°) and a nanoparticle concentration φ = 0.1, see Fig. 15. Effectively the increase of the temperature of the cold medium leads to a reduction in terms of thermal gradient.

4.5 Effect of Hartmann Number on Nusselt Number

The profiles of the average Nusselt number for different Hartmann numbers are shown in Fig. 16. Indeed at an angle of a horizontal magnetic field (γ = 0°), the Lorenz force obstructs the flow in the case of a straight duct (g = 0°) due to the perpendicularity between them.

Moreover, the increase of the magnetic field disfavors the forced convection, which explains the reduction of the mean Nusselt number by increasing the Hartmann number. In contrast, for a curved duct g (30°, 45°, 60°, 90°) the increase of the Hartmann

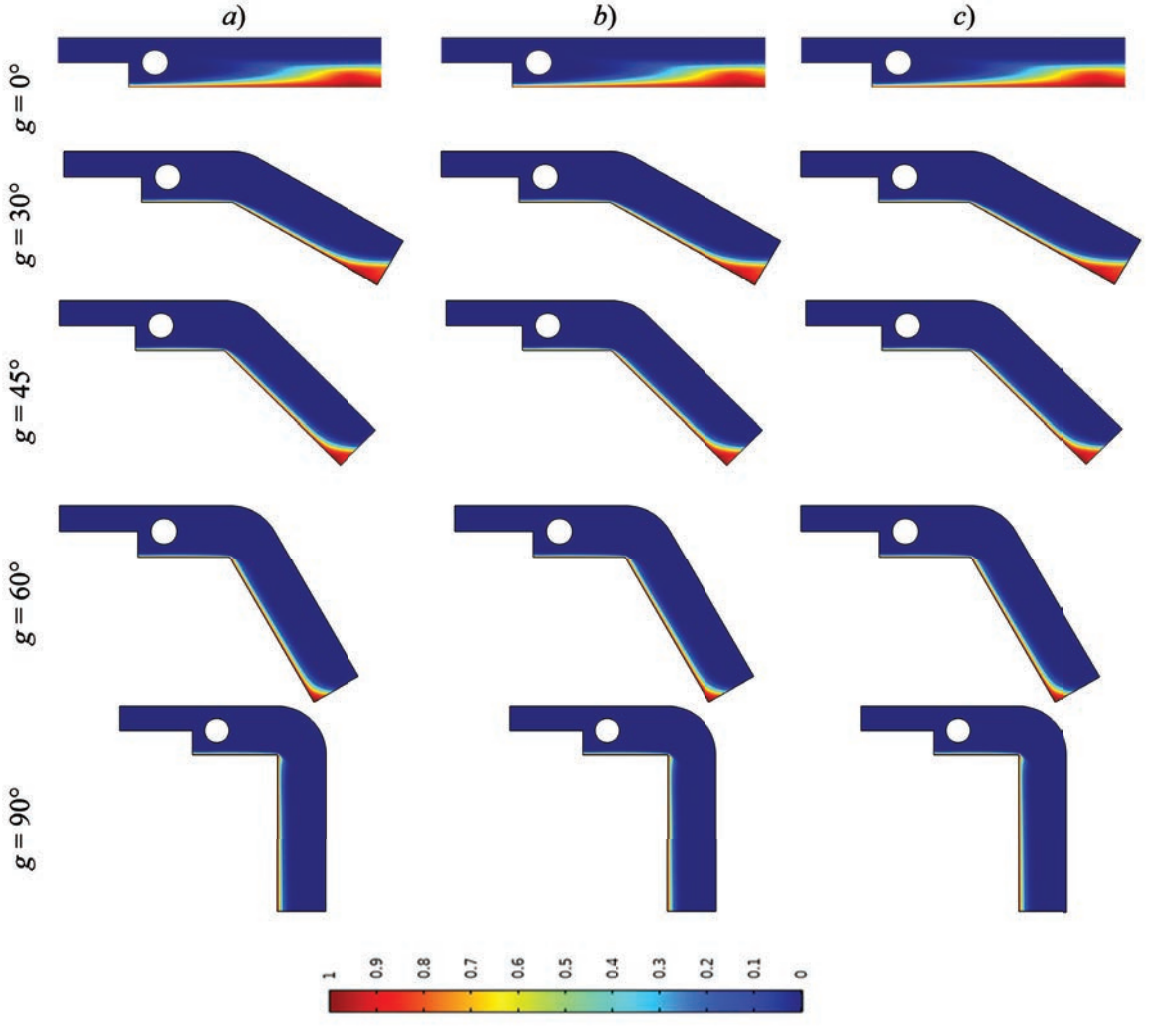

Fig. 14. *Isotherms at different angles of curvature (g) for: a) φ = 0, b) φ = 0.05, and c) φ = 0.1*

number as well as the curvature angle marks an increase of the average Nusselt number which achieves its maximum in the case of a curvature angle g = 90°. This behavior is in virtue of the magnetic force that drives the ferrofluid flow at latter case. Thus, a decrease of the thermal boundary layer was noted in this case. Overall the increase in the average heat transfer rate throughout the system reaches about 20.74 % when the Hartmann number increases from 0 to 100 at curvature angle g = 90°.

4.6 Effect of the Magnetic Field Inclination Angle on the Nusselt Number

Fig. 16 shows the average Nusselt number profiles at different curvature angles. It can be seen that the direction of the magnetic field significantly affects the average Nusselt number by increasing the curvature angle. Thus, an improvement of the average Nusselt number was noted with the increase of the magnetic field angle and the curvature angle except in the case of a vertical magnetic field (γ = 90°) where the increase of the curvature angle does not show any effect. This is in contrast to the case of a straight duct where the increase in the inclination of the magnetic field promotes heat transfer. Moreover, in the cases of curvature angles g (30°, 45°, 60°, 90°), the vertical magnetic field increases the average Nusselt number in the duct straight part and decreases it in its curved part.

Physically, this behavior is due to the Lorenz force that drives the flow in the first part. In the

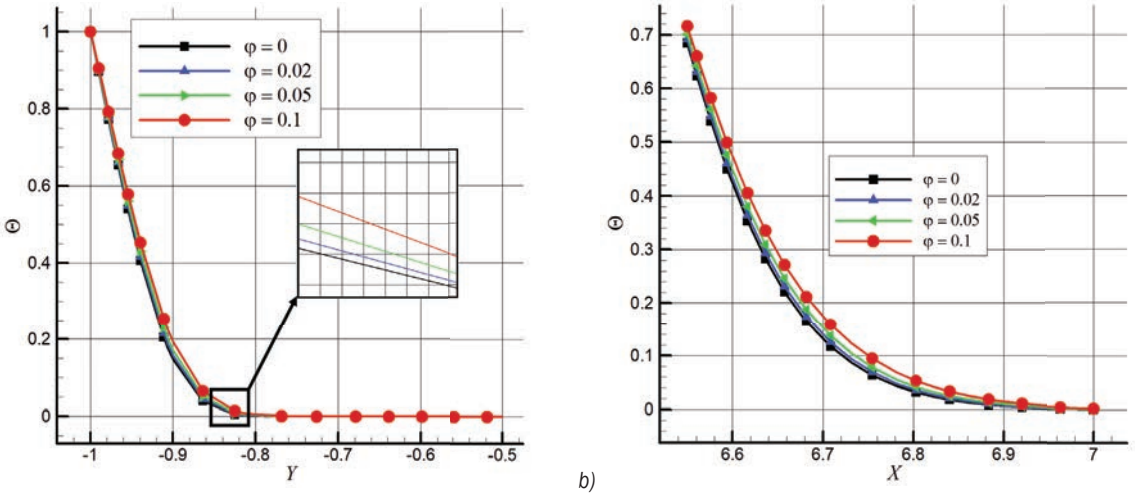

Fig. 15. *Dimensionless temperature component for different volume fractions (φ) at curvature angle (g = 90°) for: a) along the vertical line X = 5, Y = -1, and b) along the horizontal line X = 6.55, Y = -3*

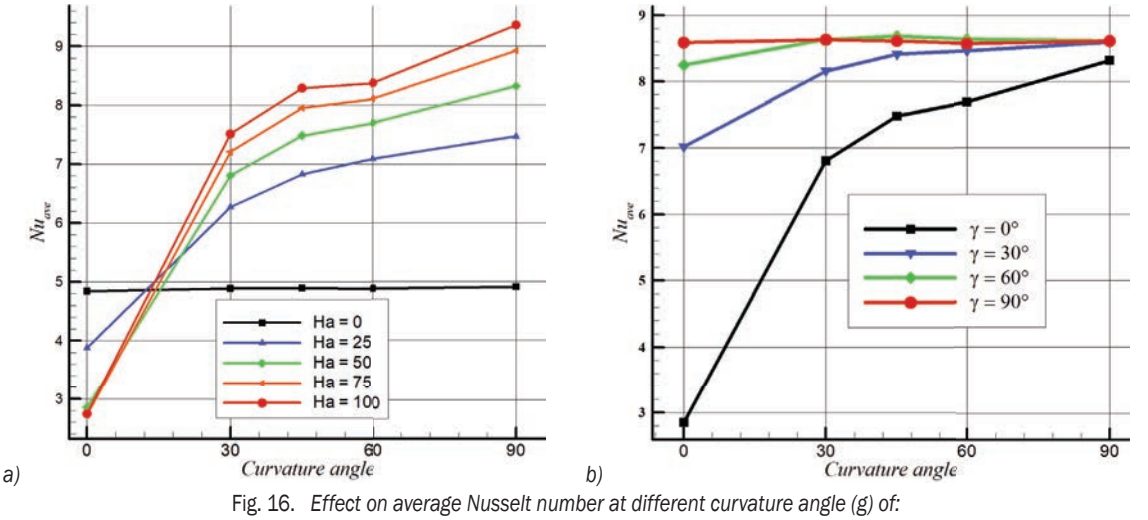

Fig. 16. *Effect on average Nusselt number at different curvature angle (g) of: a) Hartman number (Ha), and b) the magnetic field inclination (γ)*

second part, i.e. the curved part, as the curvature angle increases, the Lorenz force acts so that the ferrofluid moves away from the hot wall, thus disfavoring the thermal transfer. Indeed, on the one hand by increasing the curvature angle in the case of horizontal magnetic field, the heat transfer rate increase of 9 % has been noted at a curvature angle ($g = 90°$). On the other hand in the case of a vertical magnetic field the heat transfer is not significantly affected by the curvature angle increase, were we note the heat transfer rate increase of 0.31% at an angle of curvature ($g = 90°$).

4.7 Effect of Reynolds NUMBER on Nusselt Number

Fig. 17 shows the variation of the average Nusselt number with increasing Reynolds number. In the case of a straight duct the average Nusselt number increases with increasing Reynolds number. Indeed the forced convection is improved as the Reynolds number increases. This behavior is explained by the predominance of inertial forces over viscosity forces. Moreover, the convection is better at high Reynolds numbers in the case of a curved duct. This phenomenon is due to the viscosity forces, which are damped as the curvature angle increases. As a result, the average Nusselt number increases to its maximum for a Reynolds number value $Re = 300$ in the case of a right curvature angle ($g = 90°$).

Thus, the heat transfer is improved. Indeed, it was recorded an increase of the Nusselt number from the value of 0.9 to the value of 2.8 with an increase in the thermal rate of almost 248 % following an increase of the Reynolds number from 10 to 300 in the case of a straight duct. Furthermore, by increasing the curvature angle, it was found that the average Nusselt number increased from 1.9 to 8.32 with an increase in the heat transfer rate of 341.7 % at a curvature angle ($g = 90°$).

4.8 Effect of Nanoparticle Concentration on Nusselt Number

The variation of the heat exchange rate with the nanofluid use is an objective consideration for all applications including this type of heat transfer fluid. The average Nusselt number distribution shown in Fig. 16 obviously shows that the heat rate increases with increasing nanoparticle concentration and with increasing curvature angle. Moreover, an improvement in heat transfer at a curvature angle ($g = 90°$) of up to 12.5 % is recorded with the use of nanofluid with a concentration of 0.1 compared to the pure water.

5 CONCLUSIONS

In the present numerical study, the magnetohydrodynamic behavior of forced convection of a laminar Fe_3O_4-H_2O flow in a backward facing curved duct comprising a fixed cylinder has been investigated. The governing equations solved by the finite element method and wide control parameters ranges have been considered. Hence, the effects of Hartmann number, Reynolds number, magnetic field inclination angle and nanoparticle concentration on the thermo-magnetohydrodynamic nanofluid behavior

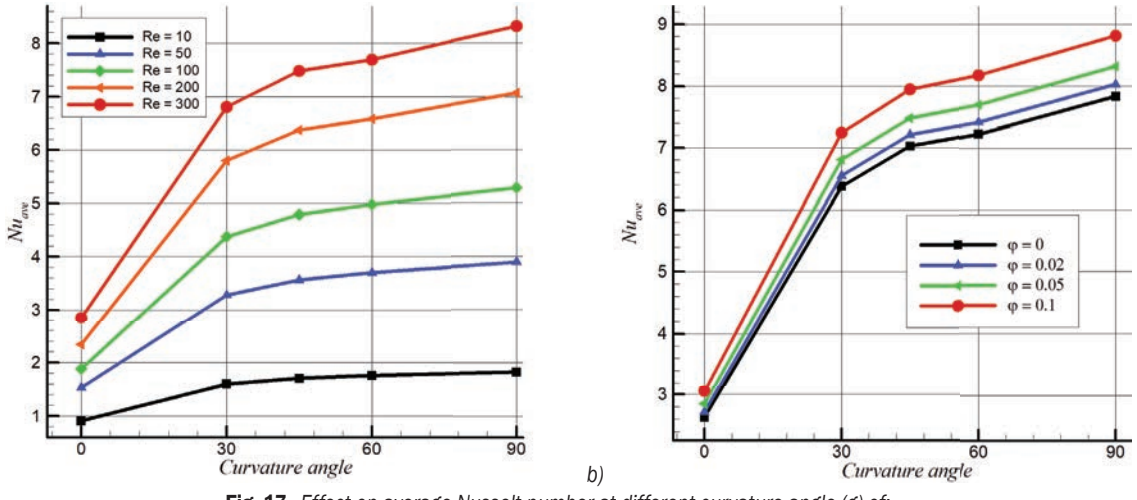

a) b)

Fig. 17. *Effect on average Nusselt number at different curvature angle (g) of: a) the Reynolds number (Re), and b) the nanoparticle volume fraction (φ)*

have been demonstrated. Through this study, the following essential points have been demonstrated:

- The increase in the Hartmann number slows down the ferrofluid flow within the straight duct with a backward facing step. However, this increase in the Hartmann number decreases the average Nusselt number in the straight duct case. On the other hand, the increase of the curvature angle as well as the magnetic field intensity favors the heat transfer. Therefore, the average Nusselt number improves by reaching its maximum value at the right curvature angle.
- The increase in the inclination angle degree of the magnetic field affects positively the heat transfer in the case of a straight duct with a backward facing step. Indeed this increase improves the average Nusselt number in this case. Moreover, the rise of the curvature angle as well as the magnetic field angle increases the convective heat transfer except for the straight magnetic field where the curvature angle shows no effect on the heat transfer.
- The increase in the Reynolds number leads to a significant enhancement of the convective heat transfer. In addition, with the increase of the curvature angle dampens the effect of viscous forces, thus, promoting heat transfer even more.
- The addition of Fe_3O_4 nanoparticles to pure water improves the heat transfer. In this case, the value of the average Nusselt number increases by almost 12.5 % compared to the pure water used. However, due to the low concentrations introduced, the nanofluid hydrodynamic was not largely affected due to low concentrations used.

7 NOMENCLATURE

Cp	specific heat [J·kg^{-1}·K^{-1}]
K	thermal conductivity [W·m^{-1}·K^{-1}]
Ha	Hartmann number
q	heat flux density [W·m^{-2}]
Re	Reynolds number
Nu_{ave}	average Nusselt number
Nu	local Nusselt number
Pr	Prandtl number
P	pressure [Pa]
P_{atm}	atmospheric pressure [Pa]
x, y	Cartesian coordinates [m]
X, Y	dimensionless coordinates
g	curvature angle [°]
H	step height
T	temperature [K]
T_c	cold temperature [K]
T_h	hot temperature [K]
u	velocity in x direction [m·s^{-1}]
v	velocity in y direction [m·s^{-1}]
V, U	Dimensionless velocity
$\bar{u}$	Vertical wall velocity [m·s^{-1}]

Greek symbols

α	thermal diffusivity [m^2·s^{-1}]
β	thermal expansion coefficient [K^{-1}]
θ	dimensionless local temperature
μ	dynamic viscosity [kg·m^{-1}·s^{-1}]
ρ	density [kg·m^{-3}]
σ	electrical conductivity [Ω^{-1}·m^{-1}]
γ	magnetic field inclination angle
φ	volume fraction
θ_{ave}	dimensionless average temperature

Subscripts:

s	solid
c	cold
f	base fluid
h	hot
ff	ferro-fluid
p	nanoparticles

8 REFERENCES

[1] Erturk, E. (2008). Numerical solutions of 2-D steady incompressible flow over a backward-facing step, Part I: High Reynolds number solutions. *Computers & Fluids*, vol. 37, no. 6, p. 633-655, **DOI:10.1016/j.compfluid.2007.09.003**.

[2] Lan, H., Armaly, B.F., Drallmeier, J.A. (2009). Three-dimensional simulation of turbulent forced convection in a duct with backward-facing step. *International Journal of Heat and Mass Transfer*, vol. 52, no. 7-8, p. 1690-1700, **DOI:10.1016/j.ijheatmasstransfer.2008.09.022.**

[3] Iwai, H., Nakabe, K., Suzuki, K. (2000). Flow and heat transfer characteristics of backward-facing step laminar flow in a rectangular duct. *International Journal of Heat and Mass Transfer*, vol. 43, no. 3, p. 457-471, **DOI:10.1016/S0017-9310(99)00140-4.**

[4] Star, S., Stabile, G., Rozza, G., Degroote, J. (2021). A POD-Galerkin reduced order model of a turbulent convective buoyant flow of sodium over a backward-facing step. *Applied Mathematical Modelling*, vol. 89, p. 486-503, **DOI:10.1016/j.apm.2020.07.029**.

[5] Kahine, K., Nguyen, V.T., Lebouché, M. (1997). Non-Newtonian Flow through Enlargements. *International Communications in Heat and Mass Transfer*, vol. 24, no. 8, p. 1103-1112, **DOI:10.1016/S0735-1933(97)00104-8**.

[6] Mahmood, R., Bilal, S., Majeed, A.H., Khan, I., Sherif, E.S.M. (2020). A comparative analysis of flow features of Newtonian and power law material: a New configuration. *Journal of Materials Research and Technology*, vol. 9, no. 2, p. 1978-1987, **DOI:10.1016/j.jmrt.2019.12.030**.

[7] Dejoan, A., Leschziner, M.A. (2004). Large eddy simulation of periodically perturbed separated flow over a backward-facing step. *International Journal of Heat and Fluid Flow*, vol. 25, no. 4, p. 581-592, **DOI:10.1016/j.ijheatfluidflow.2004.03.004**.

[8] Benard, N., Sujar-Garrido, P., Bonnet, J.P., Moreau, E. (2016). Control of the coherent structure dynamics downstream of a backward facing step by DBD plasma actuator. *International Journal of Heat and Fluid Flow*, vol. 61, p. 158-173, **DOI:10.1016/j.ijheatfluidflow.2016.04.009**.

[9] Li, Z.Y., Guo, S., Bai, H.L., Gao, N. (2019). Combined flow and heat transfer measurements of backward facing step flows under periodic perturbation. *International Journal of Heat and Mass Transfer*, vol. 130, p. 240-251, **DOI:10.1016/j.ijheatmasstransfer.2018.10.077**.

[10] Koide, Y., Sasaki, R., Kameya, Y., Motosuke, M. (2015). A burst wave-induced plasma actuator for controlling separated flow over a backward-facing step at low Reynolds numbers. *Experimental Thermal and Fluid Science*, vol. 66, p. 72-78, **DOI:10.1016/j.expthermflusci.2015.03.016**.

[11] Tihon, J., Pěnkavová, V., Pantzali, M. (2010). The effect of inlet pulsations on the backward - facing - step flow. *European Journal of Mechanics B/Fluids*, vol. 29, no. 3, p. 224-235, **DOI:10.1016/j.eurome-chflu.2010.02.001**.

[12] Mohamed, H., Camdali, U., Biyikoglu, A., Aktas, M. (2022). Enhancing the Performance of a Vapour Compression Refrigerator System Using R134a with a CuO/CeO2 Nano-refrigerant. *Strojniški vestnik - Journal of Mechanical Engineering*, vol. 68, no. 6, p. 395-410, **DOI:10.5545/sv-jme.2021.7454**.

[13] Al-Kouz, W. G., Kiwan, S., Alkhalidi, A., Sari, M. E., & Alshare, A. (2018). Numerical study of heat transfer enhancement for low-pressure flows in a square cavity with two fins attached to the hot wall using Al_2O_3-air nanofluid. *Strojniški vestnik-Journal of Mechanical Engineering*, vol. 64, no. 1, p. 26-36, **DOI:10.5545/sv-jme.2017.4989**.

[14] Taamneh, Y., & Bataineh, K. (2017). Mixed convection heat transfer in a square lid-driven cavity filled with Al_2O_3-water nanofluid. *Strojniski vestnik - Journal of Mechanical Engineering*, vol. 63, no. 6, p. 383-394, **DOI:10.5545/sv-jme.2017.4449**.

[15] Selimefendigil, F., Öztop, H.F. (2013). Identification of forced convection in pulsating flow at a backward facing step with a stationary cylinder subjected to nanofluid. *International Communications in Heat and Mass Transfer*, vol. 45, p. 111-121, **DOI:10.1016/j.icheatmasstransfer.2013.04.016**.

[16] Hilo, A.K., Iborra, A.A., Sultan, M.T.H., Hamid, M.F.A. (2020). Experimental study of nanofluids flow and heat transfer over a backward facing step channel. *Powder Technology*, vol. 372, p. 497-505, **DOI:10.1016/j.powtec.2020.06.013**.

[17] Togun, H., Safaei, M.R., Sadri, R., Kazi, S.N., Badarudin, A., Hooman, K., Sadeghinezhad, E. (2014). Numerical simulation of laminar to turbulent nanofluid flow and heat transfer over a backward-facing step. *Applied Mathematics and Computation*, vol. 239, p. 153-170, **DOI:10.1016/j.amc.2014.04.051**.

[18] Ahmed, H.E., Kherbeet, A.S., Ahmed, M.I., Salman, B.H. (2018). Heat transfer enhancement of microscale backward facing step channel by using turbulators. *International Journal of Heat and Mass Transfer*, vol. 126, p. 963-973, **DOI:10.1016/j.ijheatmasstransfer.2018.05.082**.

[19] Abbassi, H., Nassrallah, S.B. (2007). MHD flow and heat transfer in a backward-facing step. *International Communications in Heat and Mass Transfer*, vol. 34, no. 2, p. 231-237, **DOI:10.1016/j.icheatmasstransfer.2006.09.010**.

[20] Kumar, A., Dhiman, A.K. (2012). Effect of a circular cylinder on separated forced convection at a backward facing step. *International Journal of Thermal Sciences*, vol. 52, p. 176-185, **DOI:10.1016/j.ijthermalsci.2011.09.014**.

[21] Hussain, S., Ahmed, S.E. (2019). Unsteady MHD forced convection over a backward facing step including a rotating cylinder utilizing Fe304-water ferrofluid. *Journal of Magnetism and Magnetic Materials*, vol. 484, p. 356-366, **DOI:10.1016/j.jmmm.2019.04.040**.

[22] Selimefendigil, F., Öztop, H.F. (2015). Influence of inclination angle of magnetic field on mixed convection of nanofluid flow over a backward facing step and entropy generation. *Advanced powder Technology*, vol. 26, no. 6, p. 1663-1675, **DOI:10.1016/j.jmmm.2019.04.040**.

[23] Mohammed, H.A., Fathinia, F., Vuthaluru, H.B., Liu, S. (2019). CFD based investigations on the effects of blockage shapes on transient mixed convective nanofluid flow over a backward facing step. *Powder Technology*, vol. 346, p. 441-451, **DOI:10.1016/j.powtec.2019.02.002**.

[24] Kherbeet, A.S., Mohammed, H.A., Salman, B.H., Ahmed, H.E., Alawi, O.A. (2014). Experimental and numerical study of nanofluid flow and heat transfer over microscale backward-facing step. *International Journal of Heat and Mass Transfer*, vol. 79, p. 858-867, **DOI:10.1016/j.ijheatmasstransfer.2014.08.074**.

[25] Lv, J., Hu, C., Bai, M., Li, L., Shi, L., Gao, D. (2019). Visualization of SiO2-water nanofluid flow characteristics in backward-facing step using PIV. *Experimental Thermal and Fluid Science*, vol. 101, p. 151-159, **DOI:10.1016/j.expthermflusci.2018.10.013**.

[26] Amiri, A., Arzani, H.K., Kazi, S.N., Chew, B.T., Badarudin, A. (2016). Backward-facing step heat transfer of the turbulent regime for functionalized graphene nanoplatelets based water-ethylene glycol nanofluids. *International Journal of Heat and Mass Transfer*, vol. 97, p. 538-546, **DOI:10.1016/j.ijheatmasstransfer.2016.02.042**.

[27] Niemann, M., Fröhlich, J. (2016). Buoyancy-affected backward-facing step flow with heat transfer at low Prandtl number. *International Journal of Heat and Mass Transfer*, vol. 101, p. 1237-1250, **DOI:10.1016/j.ijheatmasstransfer.2016.05.137**.

[28] Boruah, M.P., Pati, S., Randive, P.R. (2019). Implication of fluid rheology on the hydrothermal and entropy generation characteristics for mixed convective flow in a backward facing step channel with baffle. *International Journal of Heat and Mass Transfer*, vol. 137, p. 138-160, **DOI:10.1016/j.ijheatmasstransfer.2019.03.094**.

[29] Selimefendigil, F., Öztop, H.F. (2013). Identification of forced convection in pulsating flow at a backward facing step with a stationary cylinder subjected to nanofluid. *International Communications in Heat and Mass Transfer*, vol. 45, p. 111-121, **DOI:10.1016/j.icheatmasstransfer.2013.04.016**.

[30] Selimefendigil, F., Öztop, H.F. (2013). Numerical analysis of laminar pulsating flow at a backward facing step with an upper

wall mounted adiabatic thin fin. *Computers & Fluids*, vol. 88, p. 93-107, **DOI:10.1016/j.compfluid.2013.08.013**.

[31] Selimefendigil, F., Öztop, H.F. (2017). Forced convection and thermal predictions of pulsating nanofluid flow over a backward facing step with a corrugated bottom wall. *International Journal of Heat and Mass Transfer*, vol. 110, p. 231-247, **DOI:10.1016/j.ijheatmasstransfer.2017.03.010**.

[32] Boruah, M.P., Randive, P.R., Pati, S. (2018). Hydrothermal performance and entropy generation analysis for mixed convective flows over a backward facing step channel with baffle. *International Journal of Heat and Mass Transfer*, vol. 125, p. 525- 542, **DOI:10.1016/j.ijheatmasstransfer.2018.04**.

[33] Mohammed, H.A., Alawi, O.A., Wahid, M.A. (2015). Mixed convective nanofluid flow in a channel having backward-facing step with a baffle. *Powder Technology*, vol. 275, p. 329-343, **DOI:10.1016/j.powtec.2014.09.046**.

[34] Heshmati, A., Mohammed, H.A., Darus, A.N. (2014). Mixed convection heat transfer of nanofluids over backward facing step having a slotted baffle. *Applied Mathematics and Computation*, vol. 240, p. 368-386, **DOI:10.1016/j.amc.2014.04.058**.

[35] Yanase, S.R.N.M., Mondal, R.N., Kaga, Y. (2005). Numerical study of non-isothermal flow with convective heat transfer in a curved rectangular duct. *International Journal of Thermal Sciences*, vol. 44, no. 11, p. 1047-1060, **DOI:10.1016/j.ijthermalsci.2005.03.013**.

[36] Mondal, R.N., Islam, M.S., Uddin, M.K. (2013). Unsteady solutions with convective heat transfer through a curved duct flow. *Procedia Engineering*, vol. 56, p. 141-148, **DOI:10.1016/j.proeng.2013.03.100**.

[37] Li, Y., Wang, X., Yuan, S., Tan, S.K. (2016). Flow development in curved rectangular ducts with continuously varying curvature. *Experimental Thermal and Fluid Science*, vol. 75, p. 1-15, **DOI:10.1016/j.expthermflusci.2016.01.012**.

[38] Choi, H.K., Park, S.O. (1994). Mixed convection flow in curved annular ducts. *International Journal of Heat and Mass Transfer*, vol. 37, no. 17, p. 2761-2769, **DOI:10.1016/0017-9310(94)90393-X**.

[39] Chandratilleke, T.T., Nadim, N., Narayanaswamy, R. (2012). Vortex structure-based analysis of laminar flow behaviour and thermal characteristics in curved ducts. *International Journal of Thermal Sciences*, vol. 59, p. 75-86, **DOI:10.1016/j.ijthermalsci.2012.04.014**.

[40] Choi, J., Zhang, Y. (2012). Numerical simulation of laminar forced convection heat transfer of Al203-water nanofluid in a pipe with return bend. *International Journal of Thermal Sciences*, vol. 55, p. 90-102, **DOI:10.1016/j.ijthermalsci.2011.12.017**.

[41] Ajeel, R.K., Sopian, K., Zulkifli, R., Fayyadh, S.N., Hilo, A.K. (2021). Assessment and analysis of binary hybrid nanofluid impact on new configurations for curved-corrugated channel. *Advanced Powder Technology*, vol. 32, no. 10, p. 3869-3884, **DOI:10.1016/j.apt.2021.08.041**.

Strojniški vestnik - Journal of Mechanical Engineering 69(2023)3-4, 155-168
DOI:10.5545/sv-jme.2022.303
Original Scientific Paper
Received for review: 2022-07-29
Received revised form: 2022-12-12
Accepted for publication: 2023-02-22

Impacts of Burnishing Variables on the Quality Indicators in a Single Diamond Burnishing Operation

Minh-Thai Le[1] – An-Le Van[2,*] – Trung-Thanh Nguyen[3]

[1]Le Quy Don Technical University, Faculty of Special Equipment, Vietnam
[2]Nguyen Tat Thanh University, Faculty of Engineering and Technology, Vietnam
[3]Le Quy Don Technical University, Faculty of Mechanical Engineering, Vietnam

Diamond burnishing is an effective solution to finish a surface. The purpose of the current work is to optimize parameter inputs, including the spindle speed (S), depth of penetration (D), feed rate (f), and diameter of tool-tip (DT) for improving the Vickers hardness (VH) and decreasing the average roughness (Ra) of a new diamond burnishing process. A set of burnishing experiments is executed under a new cooling lubrication system comprising the minimum quantity lubrication and double vortex tubes. The Bayesian regularized feed-forward neural network (BRFFNN) models of the performances are proposed in terms of the inputs. The criteria importance through the inter-criteria correlation (CRITIC) method and non-dominated sorting genetic algorithm based on the grid partitioning (NSGA-G) are applied to compute the weights of responses and find optimality. The optimal outcomes of the S, D, f, and DT were 370 rpm, 0.10 mm, 0.04 mm/rev, and 8 mm, respectively. The improvements in the Ra and VH were 40.7 % and 7.6 %, respectively, as compared to the original parameters. An effective approach combining the BRFFNN, CRITIC, and NSGA-G can be widely utilized to deal with complicated optimization problems. The optimizing results can be employed to enhance the surface properties of the burnished surface.

Keywords: single diamond burnishing; average roughness; Vickers hardness; Bayesian regularization; NSGA-G

Highlights

- *A new diamond burnishing operation combining the minimum quantity lubrication (MQL) system and vortex tubes was developed.*
- *Process parameters, including the spindle speed, depth of penetration, feed rate, and diameter of the tool tip were optimized.*
- *The average roughness and Vickers hardness of the burnished surface were enhanced.*
- *Optimal Bayesian regularized feed-forward neural network was proposed to present the non-linear data.*

0 INTRODUCTION

In industrial applications, the cost of lubricants accounts for 7 % to 17 % of the production expense. Moreover, the usage of the cutting fluid causes health risks and environmental problems; hence, the reduction or elimination of the lubricants is necessary. For this purpose, various cooling-lubrication (CL) approaches, including the minimum quantity lubrication (MQL), the Vortex tube (VT), and the cryogenic approach have been developed and utilized.

The deployment of the MQL system for different machining processes has attracted many researchers. Zaman and Dhar [1] stated that *Ra*, cutting force (*CF*), and cutting temperature (*CT*) were decreased by 53.8 %, 1.27 %, and 3.9 % at a proper parameter setting, respectively, for the MQL turning Ti6Al4V, in which the nozzle diameter, nozzle elevation angle (*A*), flow rate (*Q*), and air pressure were optimizing inputs. Tamang et al. [2] emphasized that the power consumption (*PC*), *Ra*, and tool wear (*TW*) of the MQL turning Inconel 825 were decreased by 66.5 %, 8.4 %, and 10.4 %, respectively, as compared to the dry condition. Moreover, the *Ra* of 0.94 µm, the *PC* of 5.4 kW, and the *TW* of 100.8 µm were obtained at the optimal condition. Zan et al. [3] stated that *CT*, *CF*, and acceleration were decreased by 150 ºC, 5.6 %, and 89 %, respectively using optimal values of the *Q*, nozzle distance (*N*), and *A* for the MQL milling Ti6Al4V. The *Ra* of 0.32 µm, the *CT* of 103.8 ºC, and the *CF* of 151 N for the MQL milling Inconel 718 were obtained by means of optimal parameters of the *S*, *f*, depth of cut (d), *Q*, and *A* [4]. Van and Nguyen [5] presented that the cylindricity, circularity, and average roughness of the MQL roller burnishing were reduced by 53.2 %, 53.8 %, and 72.9 %, respectively with the support of the optimal data of the nozzle diameter, *A*, *Q*, and air pressure. The maximum roughness and *VH* of the MQL roller burnishing were decreased by 17 % and 41 %, respectively using the ANN and PSO [6]. Sachin et al. [7] developed an MQL diamond-burnishing process, in which the optimal outcomes of the *Ra* and *VH* were 0.07 µm and 385 HV, respectively using the optimal data of the *S*, *f*, and burnishing force (f_b).

The VT has been widely utilized to enhance the technical performances of various machining processes. Mahapatro and Krishna [8] revealed that the *CT* and *Ra* of the VT-based turning Ti-6Al-4V were decreased by 35.6 % and 61 %, respectively,

*Corr. Author's Address: Nguyen Tat Thanh University, 300A Nguyen Tat Thanh, Ho Chi Minh, Vietnam, lvan@ntt.edu.vn

while the *CF* was increased by 8.6 %, as compared to the dry cutting. Singh et al. [9] emphasized that the VT caused 4 % to 6 % lower carbon emission for the turning Ti-3Al-2.5V in comparison with the dry condition. Gupta et al. [10] proposed an effective system VTMQL comprising the nitrogen, VT, and MQL to increase the machinability in the turning of AA 7075 T6 alloy, in which the *TW* and *Ra* were decreased by 18 % and 7% , respectively. Similarly, Mia et al. [11] revealed that the VTMQL caused reductions in the *TW* and *Ra* around 2 % and 3 %, respectively, for the precision turning of Al 6061 T6. The *CF* and *Ra* of the VTMQL-based drilling Hardox 500 steel were decreased by 36.8 % and 6.7 %, respectively, as compared to the MQL, while the *TW* decreased around 4.5 times in comparison with the dry condition [12].

The cryogenic method has been considered for different machining processes. Sharma et al. [13] stated that the *CF* of 49 N, the *CT* of 24.99 °C and the machining time of 3709 s were obtained at the optimal data for the cryogenic turning AISI D3 using the Taguchi method. The specific cutting energy (*SCE*), *Ra*, and *TW* for the cryogenic turning Ti-6Al-4V were decreased by 30.5 %, 22.8 %, and 4.3 %, respectively, as compared to the dry condition [14]. The *S* of 78 m/min, the *f* of 0.16 mm/rev, and SNMM tool insert could be applied to decrease the *Ra* (1.05 µm) and the *CF* (351 N) for the cryogenic turning Ti-6Al-4V [15]. The optimal values of the *S*, *f*, and f_b of the cryogenic diamond burnishing operation were 73 m/min, 0.08 mm/rev, and 60 N, respectively for decreasing the *Ra* and improving the *VH* [16]. Sachin et al. [17] stated that *Ra* of 0.2 µm and the *VH* of 398 HV for the diamond burnishing operation of the 17-4 hardened stainless could be obtained using optimal outcomes.

The diamond burnishing process is one of the finest finishing technologies, which has been widely executed on different surfaces for improving the properties and working functionalities [18] to [20]. Various CL methods, including cryogenic and MQL conditions, have been utilized in various diamond-burnishing operations. Unfortunately, the cryogenic approach requires an expensive investment, while the low cooling-lubrication impact is the greatest drawback of the MQL system when machining high- hardness steels due to the enormous amount of generated heat. Therefore, it is necessary to develop an efficient-economic cooling-lubrication approach that can effectively facilitate the diamond-burnishing process.

Additionally, the selection of optimal factors for improving the surface quality of the diamond burnishing under the impact of a new CL system is also an urgent demand.

In this paper, a new diamond burnishing operation comprising the MQL and double vortex tubes is

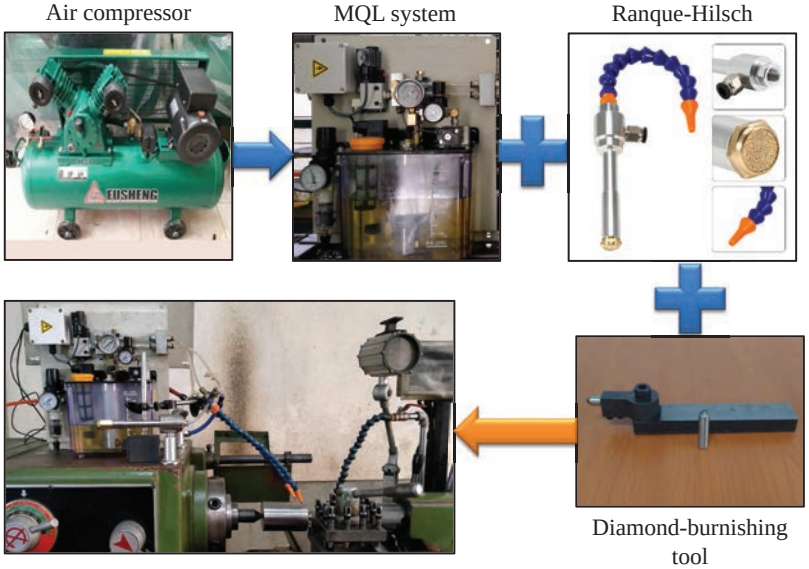

Fig. 1. *A new diamond-burnishing process*

first introduced. Then, we present the optimization approach and experiment. Next, the obtained results are discussed. Finally, conclusions are drawn, and future research is suggested.

1 NEW DIAMOND-BURNISHING PROCESS

The concept of the diamond burnishing operation with a new CL system is shown in Fig. 1 The compressed air is produced by the pneumatic pump and stored in the accumulator. The pressure value is detected and assigned using the pneumatic regulator valve. The lubricant is pumped by means of the electrical device, while the flow rate is adjusted using the frequency generator. The compressed air is transferred from the MQL system to the double vortex tubes for decreasing the working temperature. The cold mixture is produced and transferred into the burnishing regions.

Table 1. *Optimizing parameters of a new diamond burnishing process*

Symbol	Parameters	1	2	3
S	Spindle speed [rpm]	185	370	630
D	Depth of penetration [mm]	0.06	0.08	0.10
f	Feed rate [mm/rev]	0.04	0.06	0.08
DT	Tool-tip Diameter [mm]	6	8	10

2 OPTIMIZATION APPROACH

The burnishing parameters, including the spindle speed (S), depth of penetration (D), feed rate (f), and tool-tip diameter (DT) are presented in Table 1 The ranges of the S, D, and f are determined based on the characteristics of the machine tool, while the DT value is selected using the characteristics of the burnishing tool. Consequently, the optimizing issue is expressed as:

Minimize the Ra and maximize the VH.

Constraints: 150 rpm $\leq S \leq$ 630 rpm; 0.06 mm $\leq D \leq$ 0.10 mm; 0.04 mm/rev $\leq f \leq$ 0.08 mm/rev; 8 mm $\leq DT \leq$ 10 mm.

The optimizing approach is expressed in Fig. 2.

Step 1 The experimental data are observed using the Taguchi method.

The Ra value is calculated as:

$$Ra = \frac{\sum_{i=1}^{n} Ra_i}{n}, \tag{1}$$

where Ra_i denotes the average roughness at the i^{th} measured location.

The VH value is calculated as:

$$VH = \frac{\sum_{i=1}^{n} VH_i}{n}, \tag{2}$$

where VH_i is the Vickers hardness at the i^{th} position.

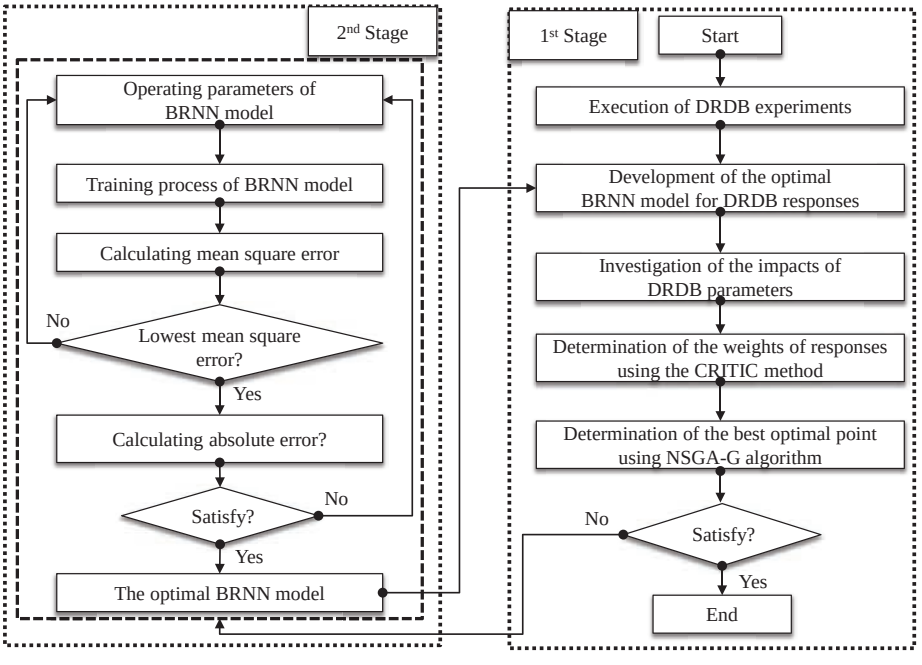

Fig. 2. *The optimizing procedure*

Step 2: The *Ra* and *VH* models are developed using the BRFFNN approach [21].

The input parameters are considered as probability density functions to the hidden layer, which is expressed as:

$$P = \frac{P(D|w,\beta,M)P(w|\alpha,M)}{P(D|\alpha,\beta,M)}, \quad (3)$$

where D and M presents the obtained data and the forward multi-layer perceptron, respectively. w and $P(w|\alpha,M)$ are the vector and prior knowledge of network weights, respectively. When the Gaussian function is employed, the likelihood-P $(D|w, \beta, M)$ is expressed as:

$$P(D|w,\beta,M) = \frac{1}{(\pi/\beta)^{n/2}} e^{-\beta d_d}, \quad (4)$$

where d_d is the sum of squared deviations for data.

The normalized factor P $(D|\alpha, \beta, M)$ is expressed as:

$$P(D|\alpha,\beta,M) = \frac{1}{(\pi/\alpha)^{N/2}} e^{-\alpha d_w}, \quad (5)$$

where d_w is the sum of squared errors for the weights.

The probability density function can be expressed as:

$$P = \frac{1}{Z_F(\alpha,\beta)} e^{-(\beta d_d + \alpha d_w)}. \quad (6)$$

The highest posterior probability density function causes maximum regularized objective function ($f = \beta d_d + \alpha d_w$).

To observe the optimal architecture of the BRFFNN model, the operating factors, including the number of neurons in each layer, performance function, transfer function, number of hidden layers, and learning functions are optimized and selected. The numerical experiments of each ANN model are executed to calculate the mean square error (*MSE*), which is expressed as:

$$MSE = \frac{1}{N}\sum_{i=1}^{N}\left(y_a - y_p\right)^2, \quad (7)$$

where y_a and y_p are the actual and predictive values, respectively. N denotes the number of testing points.

The best BRFFNN architecture is chosen with the lowest MSE value.

Step 3: The weights of the machining responses are calculated using the criteria importance through the intercriteria correlation (CRITIC) method.

The normalized burnishing response (x_{ij}) is computed as:

$$x_{ij} = \frac{x_{ij} - x_j^{word}}{x_j^{best} - x_j^{word}}. \quad (8)$$

The standard deviation (s_j) of each response is calculated as:

$$s_j = \sqrt{\frac{(\sum_{i=1}^{m} x_{ij} - x_m)^2}{m-1}}. \quad (9)$$

Determination of symmetric matrix of $n \times n$ with element r_{jk}, which is linear correlation coefficient between the vectors x_j and x_k.

Computation of measure of the conflict (I_j):

$$I_j = \sum_{k=1}^{m}(1 - r_{jk}). \quad (10)$$

Determination of the quantity of the information (C_j):

$$C_j = s_j \sum_{k=1}^{m}(1 - r_{jk}). \quad (11)$$

The computed (w_i) of burnishing response is calculated as:

$$w_i = \frac{C_j}{\sum_{k=1}^{n} C_j}. \quad (12)$$

Step 4: The optimal data of the burnishing parameters and responses are selected using the non-dominated sorting genetic algorithm based on the grid partitioning (NSGA-G) [22]. The operation steps of the NSGA-G are expressed in Fig. 3.

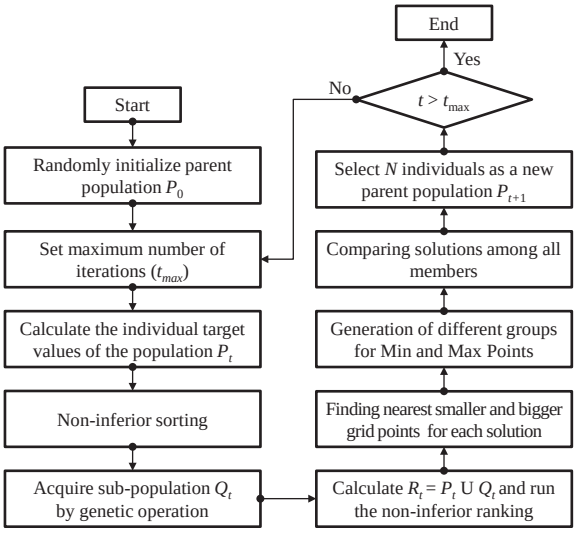

Fig. 3. *The working principle of the NSGA-G*

The random initialization of parent population: the parent population is executed based on the definition of the optimizing issue.

Non-dominance sorting of the parent population: the parent population (P) is divided into the number of the subsets (P_i), in which the subset P_{k+1} is dominated by the individual P_k. The individual P_i is expressed as:

$$P_i = \left\{ i / n_i, i \in \left\{ 1, 2, ..., N \right\} \right\}. \quad (13)$$

The population P_k is expressed as:

$$P_k = \left\{ \text{All individual} / n_i - \text{k}+1 \right\}, \quad (14)$$

where n_i is the number of individuals in the population for dominating generations.

The parent population with N size and offspring population with N members at t^{th} generation are produced with the aid of crossover and mutation operations.

Generation of different groups for Min and Max Points: the nearest smaller and bigger grid point for each solution were selected. The design space is divided into multi small groups.

Compare solutions in a group and selection of the best individual: The weak individuals are removed to form a new generation. The control loop is executed until the maximum number of generations is fit.

3 EXPERIMENTAL SETTING

The machining specimens having the round cylindrical shape are made from the hardened AISI 4340 steel. The length and diameter of each workpiece are 130 mm and 60 mm, respectively. The turning and grinding operations are applied to produce the external surface in each specimen. The average roughness and Vickers hardness of the pre-machined surface are approximately 2.46 µm and 420.6 HV, respectively.

The experiments are performed using a conventional turning machine. The dead and live centres are employed to hold the specimen (Fig. 4). The rotational motion of the workpiece is conducted by means of the friction between the machining sample and the dead centre.

A novel diamond-burnishing tool has been designed and fabricated to facilitate burnishing experiments, as shown in Fig. 5. Primary components are the shank, tool head, stem, diamond tip, positioning bolts, and adjusting screws. The stem having the diamond tip is tightly mounted in the tool head. The stem is replaced after each experiment to eliminate the impact of the tool wear. The hardness of 62 HRC and roughness of 0.05 µm are employed in the diamond tip.

The average roughness is computed from three different positions using the Mitutoyo SJ-301. The Vickers hardness is measured in three different points on the burnished surface using a Wilson Wolpert tester.

The representative values of the burnishing responses are presented in Fig. 5.

4 RESULTS AND DISCUSSIONS

4.1 Impacts of Process Parameters on the Ra and VH

Table 2 presents experimental data for the diamond burnishing operation.

Table 2. *Experimental data for a new diamond burnishing process*

	No.	*S*	*D*	*f*	*DT*	*Ra*	*VH*
Experimental data for developing the BRNN model	1	185	0.06	0.04	6	0.46	511.5
	2	370	0.06	0.06	6	0.42	478.3
	3	630	0.06	0.08	6	0.44	424.6
	4	370	0.06	0.04	8	0.31	488.8
	5	630	0.06	0.06	8	0.32	451.6
	6	185	0.06	0.08	8	0.54	480.2
	7	630	0.06	0.04	10	0.23	444.4
	8	185	0.06	0.06	10	0.42	484.8
	9	370	0.06	0.08	10	0.41	456.2
	10	370	0.08	0.04	6	0.27	497.7
	11	630	0.08	0.06	6	0.29	464.8
	12	185	0.08	0.08	6	0.54	474.3
	13	630	0.08	0.04	8	0.18	475.7
	14	185	0.08	0.06	8	0.41	496.6
	15	370	0.08	0.08	8	0.38	469.9
	16	185	0.08	0.04	10	0.29	485.1
	17	370	0.08	0.06	10	0.27	474.3
	18	630	0.08	0.08	10	0.33	446.8
	19	630	0.10	0.04	6	0.14	495.7
	20	185	0.10	0.06	6	0.39	497.3
	21	370	0.10	0.08	6	0.37	472.4
	22	185	0.10	0.04	8	0.26	503.8
	23	370	0.10	0.06	8	0.24	494.8
	24	630	0.10	0.08	8	0.29	470.9
	25	370	0.10	0.04	10	0.13	483.1
	26	630	0.10	0.06	10	0.18	475.7
	27	185	0.10	0.08	10	0.36	481.8
Experimental data for testing the precision of the BRNN model	28	185	0.06	0.05	7	0.46	505.4
	29	250	0.07	0.07	9	0.41	481.9
	30	250	0.09	0.05	7	0.32	501.3
	31	630	0.10	0.07	9	0.23	477.6
	32	370	0.07	0.06	10	0.31	470.5
	33	250	0.08	0.08	9	0.41	476.9
	34	185	0.06	0.05	9	0.41	496.3
	35	370	0.08	0.07	7	0.36	477.9
	36	370	0.06	0.06	8	0.37	479.4

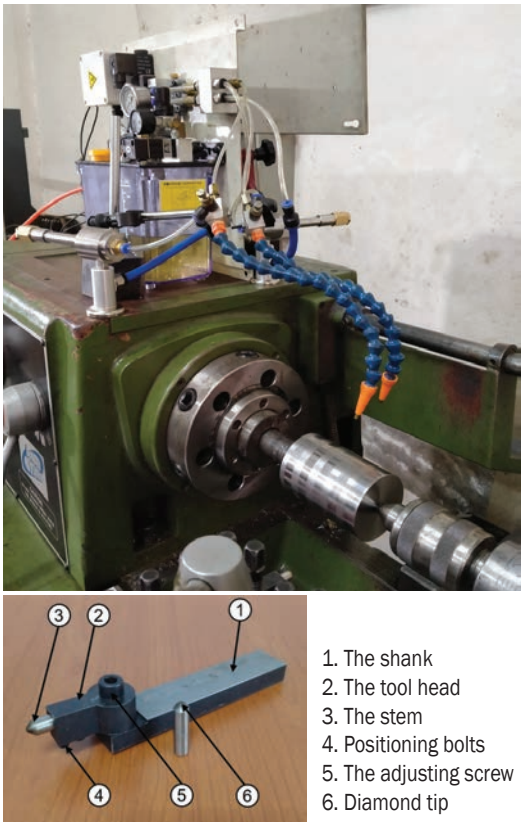

Fig. 4. *The experimental setting; a) burnishing experiment, and b) diamond burnishing tool*

As shown in Fig. 6, the *Ra* decreases (relatively around 34.8 %) with an increase in the *S* (from 80 rpm to 160 rpm). Higher *S* increases the engagement frequency between the diamond tip and the surface, which increases the number of burnishing traces. The irregularities of the pre- machined surface are easily deformed; thus, the *Ra* decreases. The machining temperature at the interfaces increases with an increased *S*, which reduces the hardness and strength of the workpiece; hence, the material is smoothly compressed. Therefore, a reduction in the *Ra* is obtained.

As shown in Fig. 6, an increase in the *D* (from 0.06 mm to 0.10 mm) leads to a reduction in the *Ra* (relatively around 30.4 %). Higher *D* increases the machining pressure on the surface to be machined, and the material is compressed. The pre-machined peaks are flattened, and the valleys are filled up; hence, the *Ra* significantly decreases.

As shown in Fig. 6 , an increase in the *f* (from 0.04 mm/rev to 0.08 mm/rev) increases the *Ra* (relatively around 24.4 %). An increased *f* causes a higher distance between the consecutive burnishing paths, which decreases the engagement frequency. The machining time available to process material decreases with an increased *f*; hence, the *Ra* increases.

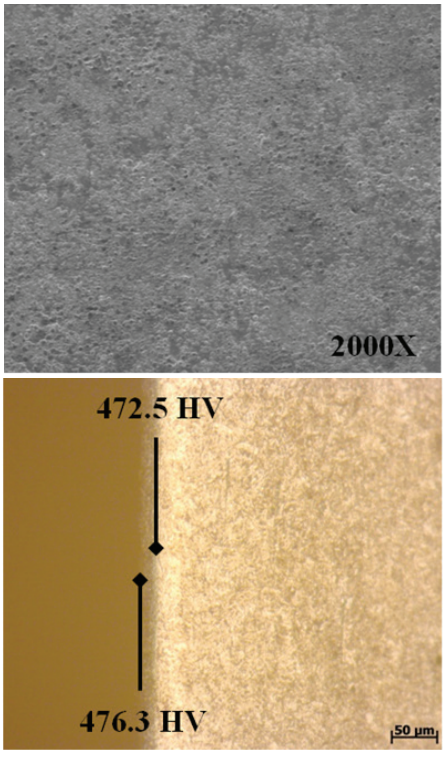

Fig. 5. *The representative values of a new diamond-burnishing process; a) the SEM image of the burnished surface at the experimental No. 11, and b) the Vickers hardness at the experimental No. 11*

As shown in Fig. 6, an increase in the *DT* (from 8 mm to 10 mm) decreases the *Ra* (relatively around 9.6 %). An increased *DT* causes a higher contact length between the tool tip and the specimen's surface. The pre-machined peaks are flattened, and the valleys are filled up; thus, the *Ra* significantly decreases.

Table 3. *Computed ANOVA results for the Ra*

Source	*S*	*MS*	*F* value	*p*-value
Model	0.209	0.015	41.916	< 0.0001
S	0.178	0.178	499.782	< 0.0001
D	0.164	0.164	458.560	< 0.0001
f	0.197	0.197	552.648	< 0.0001
DT	0.094	0.094	264.563	< 0.0001
Sf	0.013	0.013	35.166	0.0182
SDT	0.038	0.038	105.732	0.0091
S^2	0.103	0.103	288.085	< 0.0001
DT^2	0.015	0.015	42.619	0.0174
Residual	0.004	0.000		
Cor. total	0.213			
$R^2 = 0.9816$; Adjusted $R^2 = 0.9724$; Predicted $R^2 = 0.9682$				

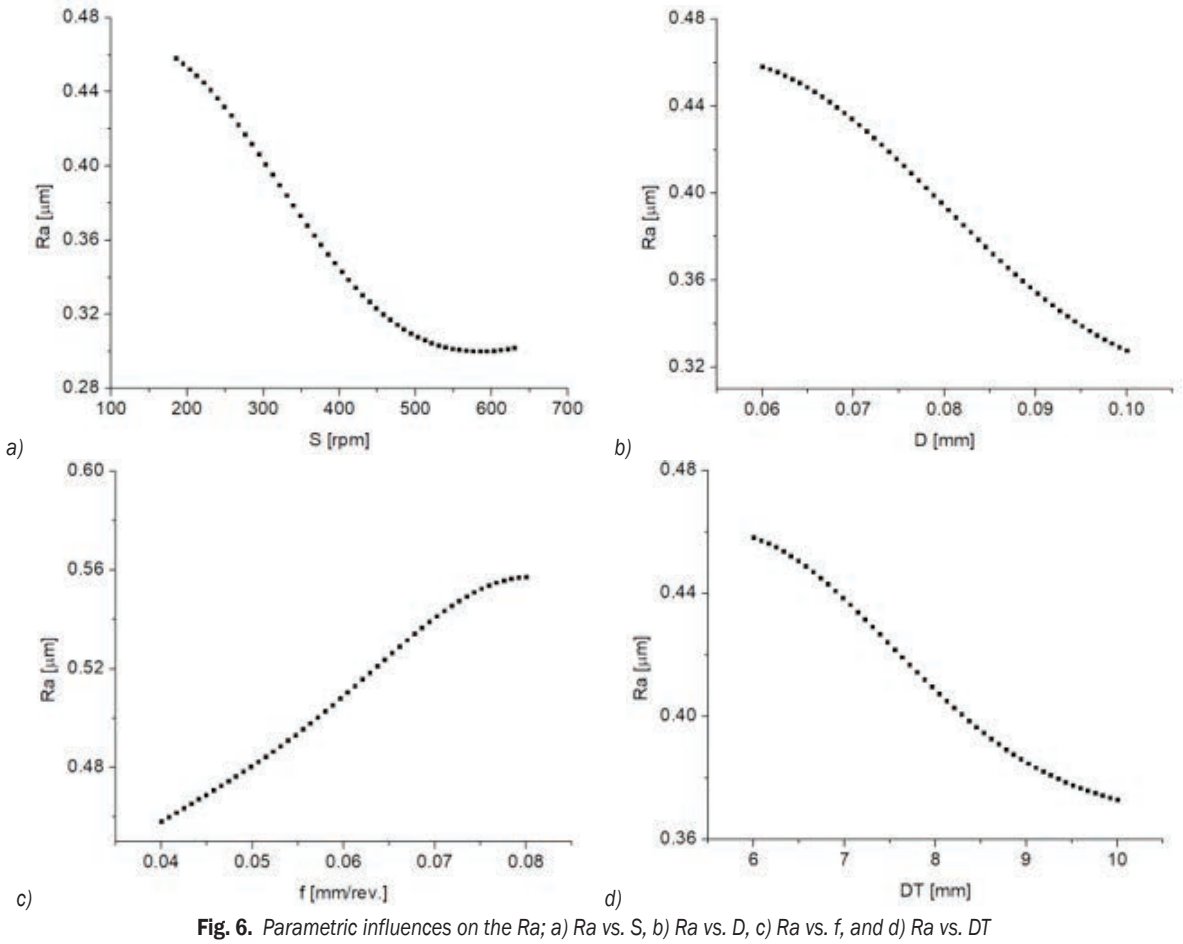

Fig. 6. *Parametric influences on the Ra; a) Ra vs. S, b) Ra vs. D, c) Ra vs. f, and d) Ra vs. DT*

The contribution of each factor on the *Ra* is shown in Table 3. Significant parameters are all single factors (*S*, *D*, *f*, and *DT*), interactive factors (*fS* and *SDT*), and quadratic factors (S^2 and DT^2). The contributions of the *S*, *D*, *f*, and *DT* are 21.49 %, 9.99 %, 23.73 %, and 11.36 %, respectively. The contributions of the *fS* and *SDT* are 15.15 % and 4.44 %, respectively. The contributions of the S^2 and DT^2 are 2.37 % and 1.83 %, respectively. The R^2 value of 0.98 indicates the *Ra* model is adequate.

As shown in Fig. 7a, the *VH* decreases (relatively around 12.3 %) with an increased *S* (from 105 rpm to 630 rpm). An increase in the *S* increases the engagement frequency, leading to higher machining temperature at the burnishing area; hence, the *VH* decreases.

As shown in Fig. 7b, an increased *D* (from 0.06 mm to 0.10 mm) leads to a higher *VH* (relatively around 2.5 %). An increased *D* increases the machining pressure on the surface to be machined.

The material is compressed and higher *VH* is obtained.

As shown in Fig. 7c, an increased higher *f* (from 0.04 mm/rev to 0.08 mm/rev) decreases the *VH* (relatively around 9.3 %). A higher *f* causes a low degree of plastic deformation due to higher distance among the consecutive traces; hence, the *VH* decreases.

As shown in Fig. 7d, an increased *DT* (from 6 mm to 10 mm) decreases the *VH* (relatively around 6.1 %). At a lower *DT*, higher burnishing pressure is produced due to the low contact area between the tool tip and surface to be machined. More material is compressed and the *VH* increases. When the *DT* increases, the burnishing pressure decreases; hence, the *VH* decreases.

The contribution of each factor on the Vickers hardness is shown in Table 4. Significant parameters are all single factors (*S*, *D*, *f*, and *DT*), interactive factors (*SD*, *fS*, *SDT*, *DDT*, and *fDT*), and quadratic factors (S^2, D^2, f^2, and DT^2). The contributions of the

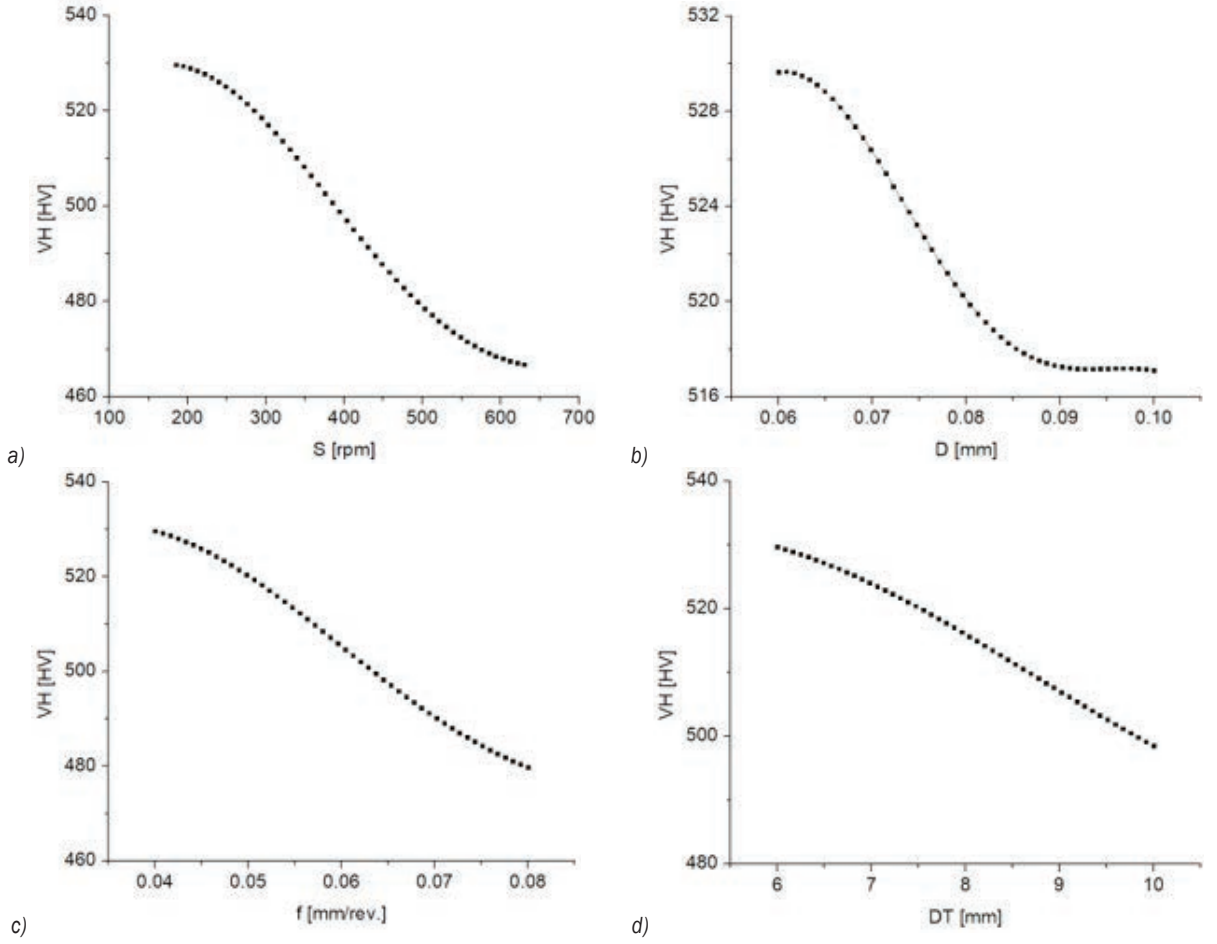

Fig. 7. *Parametric influences on the VH; a) VH vs. S, b) VH vs. D, c) VH vs. f, and d) VH vs. DT*

S, *D*, *f*, and *DT* are 35.95 %, 21.97 %, 6.31 %, and 8.37 %, respectively. The contributions of the *SD*, *Sf*, *SDT*, DDT, and *fDT* are 0.10 %, 1.25 %, 3.73 %, 1.18 %, and 1.19 %, respectively. The contributions of the S^2, D^2, f^2, and DT^2 are 2.82 %, 2.33 %, 4.44 %, and 5.38 %, respectively. The R^2 value of 0.9843 indicates the developed *VH* model is adequate.

4.2 Impacts of MQL Parameters on the Ra and VH

The ranges of the flow rate (*Q*), nozzle distance (*N*), and nozzle elevation angle (*A*) are selected based on the characteristics of the MQL system and confirmed with references [1], [3], and [5]. The Box-Benkhen design with two replications is applied to produce the experimental data in terms of saving trial costs and human efforts, as shown in Table 5

As shown in Fig. 8, when the *Q* relatively increases from 40 ml/h to 120 ml/h, the *Ra* is relatively decreased by 35.5 %. A higher *Q* increases the number

Table 4. *Computed ANOVA results for the VH*

Source	*S*	*MS*	*F* value	*p*-value
Model	7624.43	544.60	49.26	< 0.0001
S	1856.20	1856.20	167.90	< 0.0001
D	1216.86	1216.86	110.07	< 0.0001
f	1551.75	1551.75	140.36	< 0.0001
DT	834.39	834.39	75.47	< 0.0001
SD	951.41	951.41	86.06	0.0002
Sf	118.93	118.93	10.76	0.0014
SDT	356.78	356.78	32.27	0.0006
DDT	64.70	64.70	5.85	0.0012
fDT	159.84	159.84	14.46	< 0.0001
S^2	1064.63	1064.63	96.30	0.0011
D^2	173.16	173.16	15.66	0.0008
f^2	221.68	221.68	20.05	0.0005
DT^2	422.43	422.43	38.21	0.0004
Residual	521.37	521.37	47.16	
Cor. total	121.61	11.06		
$R^2 = 0.9843$; Adjusted $R^2 = 0.9752$; Predicted $R^2 = 0.9636$				

of oil droplets entering the burnishing zone, which enhances the cooling-lubrication efficiency. The friction at the interfaces decreases and the burnished surface is wetted and protected; hence, the *Ra* significantly decreases.

Table 5. *The impacts of MQL parameters on the Ra and VH*

No.	*Q* [ml/h]	*N* [mm]	*A* [deg]	*Ra* [μm]	*VH* [HV]
1	40	30	60	0.41	451.8
2	80	40	60	0.33	459.2
3	120	30	30	0.29	491.2
4	80	40	30	0.33	457.1
5	120	30	60	0.28	492.8
6	80	30	45	0.31	485.2
7	40	30	30	0.43	450.4
8	40	40	45	0.37	448.4
9	80	30	45	0.31	484.2
10	80	20	60	0.46	492.9
11	120	20	45	0.35	513.8
12	120	40	45	0.21	478.6
13	80	30	45	0.31	486.8
14	40	20	45	0.49	468.2
15	80	20	30	0.47	491.8

As shown in Fig. 8, when the *N* relatively increases from 20 mm to 40 mm, the *Ra* is relatively increased by 30.9 %. At a low distance, a high proportion of the mixture is effectively transferred into the burnishing zones, resulting in low friction at the interfaces. The cooling-lubrication efficiency improves; thus, the *Ra* decreases. When the distance increases, a low proportion of the mixture enters into the burnishing zones, resulting in a lower cooling-lubrication efficiency; hence, the *Ra* increases.

As shown in Fig. 8 , a higher *A* causes a reduced *Ra* value, while a further angle causes a negative impact. When the angle increases from 30 deg to 45 deg, the *Ra* is relatively decreased by 33.8 %. When the angle increases from 45 deg to 60 deg, the *Ra* is relatively increased by 21.9 %. An increased angle leads to a decreased *Ra* due to a reduction in friction with the aid of proper positions of nozzles. However, a further increased angle causes a higher frictional impact at the interfaces and the *Ra* slightly increases.

As shown in Fig. 9 , when the *Q* relatively increases from 40 ml/h to 120 ml/h, the *VH* is enhanced by 10.8 %. An increased *Q* leads to a higher amount of lubricant; thus, the burnished surface is wetted and protected. The friction at the interface decreases, leading to a reduction in the machining temperature. The diminishing of the residual stress is then prevented; thus, a higher *VH* is achieved.

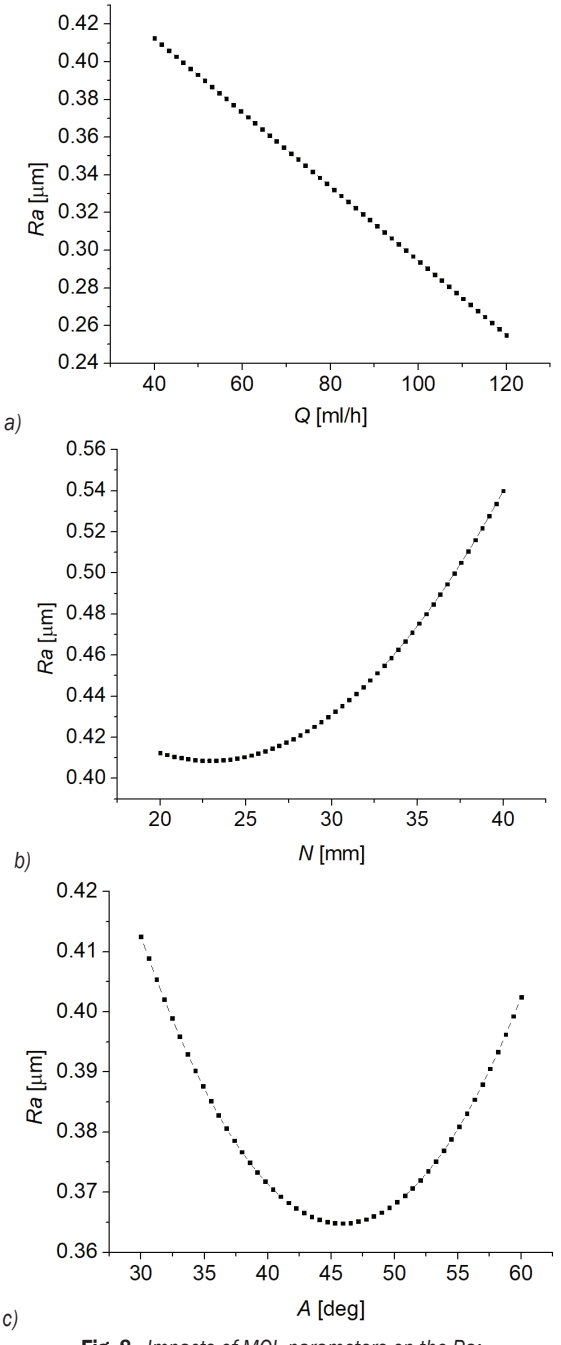

Fig. 8. *Impacts of MQL parameters on the Ra; a) Ra vs. Q, b) Ra vs. N, and c) Ra vs. A*

As shown in Fig. 9 when the *N* relatively increases from 20 mm to 40 mm, the *VH* is relatively decreased by 6.2 %. At a low distance, a higher amount of lubricant enters into the burnishing zone, which wets and protects the burnished surface. The machining temperature at the interfaces decreases, which diminishes the residual stress; hence, the *VH* enhances. At a low distance, the temperature at the

interfaces increases, leading to diminishing residual stress; hence, the *VH* decreases.

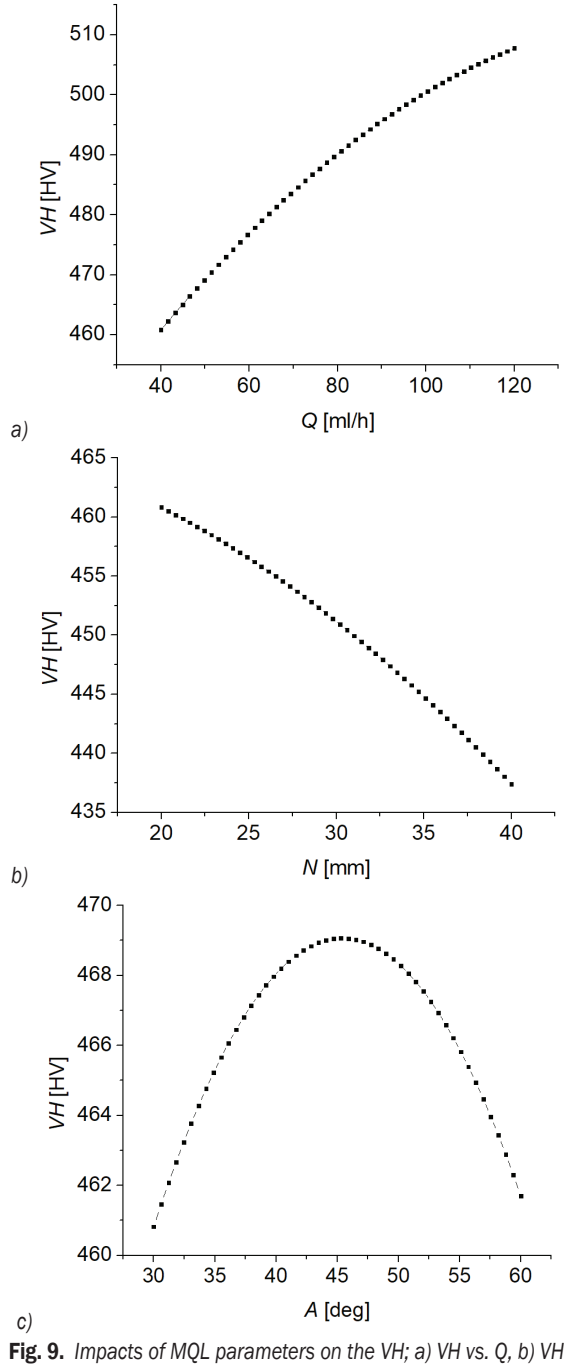

Fig. 9. *Impacts of MQL parameters on the VH; a) VH vs. Q, b) VH vs. N, and c) VH vs. A*

As shown in Fig. 9, the contradictory trends of the *VH* are observed under the variety of the elevation angle. When the angle increases from 30 deg to 45 deg, the *VH* is relatively improved by 17 %. When the elevation angle increases from 45 deg to 60 deg, the *VH* is relatively reduced by 15 %. An increased angle causes an accurate penetration of the mixture, leading to a reduction in the machining temperature; thus, a higher *VH* is obtained. A further increased angle leads to an improper cooling-lubrication efficiency, resulting in a higher burnishing temperature and the residual stress is relieved; hence, the *VH* decreases.

4.3 Optimal BRNN Model

The operating parameters of the BRFFNN model, including the *HN*, *PM*, *TF*, *HL*, and *LF* are shown in Table 6. The computational trials of the BRFFNN are performed based on the parameter combination entitled Taguchi L_{18}. The obtained results of the *MSE* values are shown in Table 7. As a result, the optimal data of the *HN*, *PM*, *TF*, *HL*, and *LF* are 19, MSEREG, logsig, 3, and LearnGDM, respectively. The schematic of the developed BRNN model is presented in Fig. 10.

To confirm the precision of the developed ANN model, the comparisons between the experimental and predictive results are conducted. Table 8 indicates the comparative values at different points. As a result, the computed deviations of the *Ra* and *VH* lie from -3.31 % to 4.85 % and -0.23 % to 0.56 %, respectively. The small errors revealed that the proposed models ensure the prediction accuracy.

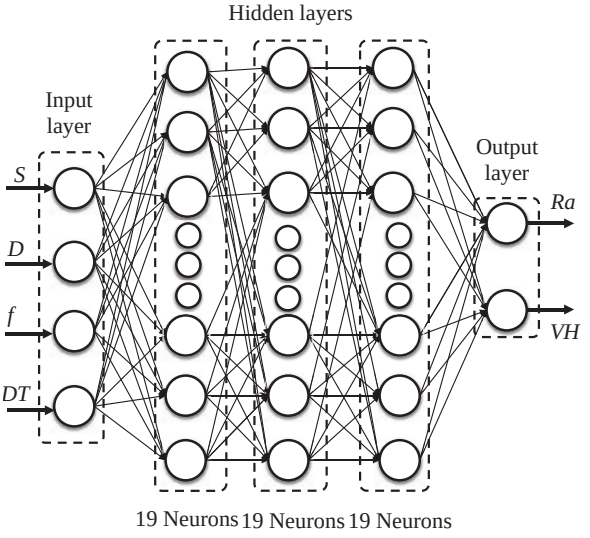

Fig. 10. *The schematic of the developed BRNN model*

The regression plots of the BRFFNN are depicted in Fig. 11, in which the *R* values of the training, testing, and all stages are 0.9946, 0.9832, and 0.9916, respectively. Consequently, the developed BRFFNN model can accurately approximate experimental data.

Table 6. *Operating parameters of the BRNN model*

Symbol	Parameters	Classifications
HN	Number of hidden neurons	15 to 20
PM	Performance function	Mean squared error: MSE; Mean squared error with regularization: MSEREG; Sum squared error: SSE
TF	Transfer function	Log sigmoid: logsig; Linear: purelin; Hyperbolic tangent sigmoid: tansig
HL	Number of hidden layers	1; 2; 3
LF	Learning function	Gradient descent with momentum weight and bias learning function: LearnGDM; Gradient descent weight and bias learning function: LearnGD

Table 7. *Computing the MSE values*

No.	*HN*	*PM*	*TF*	*HL*	*LF*	*MSE*
1	15	MSE	logsig	1	LearnGDM	0.004236
2	15	MSEREG	purelin	2	LearnGD	0.002298
3	15	SSE	tansig	3	LearnGDM	0.001948
4	16	MSE	logsig	2	LearnGD	0.001481
5	16	MSEREG	purelin	3	LearnGDM	0.000929
6	16	SSE	tansig	1	LearnGDM	0.001025
7	17	MSE	purelin	1	LearnGDM	0.000622
8	17	MSEREG	tansig	2	LearnGDM	0.00106
9	17	SSE	logsig	3	LearnGD	0.001016
10	18	MSE	tansig	3	LearnGD	0.001477
11	18	MSEREG	logsig	1	LearnGDM	0.000653
12	18	SSE	purelin	2	LearnGDM	0.006799
13	19	MSE	purelin	3	LearnGDM	0.000606
14	19	MSEREG	tansig	1	LearnGD	0.000632
15	19	SSE	logsig	2	LearnGDM	0.00066
16	20	MSE	tansig	2	LearnGDM	0.006992
17	20	MSEREG	logsig	3	LearnGDM	0.001112
18	20	SSE	purelin	1	LearnGD	0.007437

Table 8. *Investigation of the precision of the developed BRNN model*

No.	*Ra*			*VH*		
	Experiment	BRFFNN	Error [%]	Experiment	BRFFNN	Error [%]
28	0.46	0.47	-2.17	505.4	504.6	0.16
29	0.41	0.42	-2.44	481.9	480.6	0.27
30	0.32	0.33	-3.13	501.3	503.9	-0.52
31	0.23	0.22	4.35	477.6	479.9	-0.48
32	0.31	0.32	-3.23	470.5	468.4	0.45
33	0.41	0.42	-2.44	476.9	473.8	0.65
34	0.41	0.42	-2.44	496.3	498.7	-0.48
35	0.36	0.35	2.78	477.9	475.8	0.44

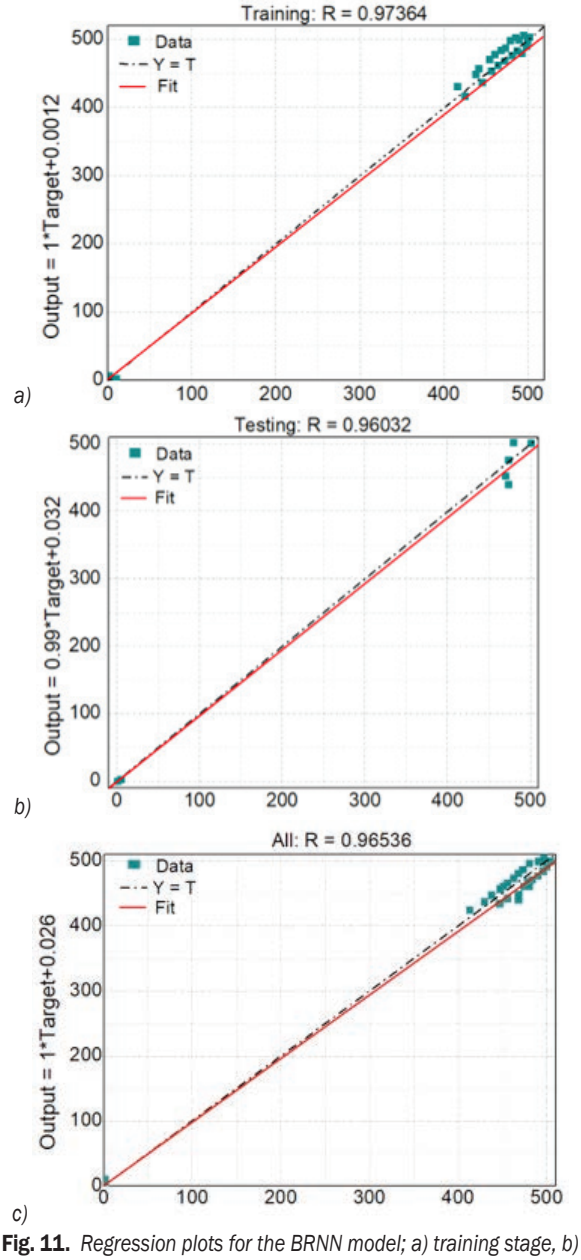

Fig. 11. *Regression plots for the BRNN model; a) training stage, b) testing stage, and c) all stages*

4.4 Optimizing outcomes

The computed weights of the *Ra* and *VH* are 0.53 and 0.47 respectively. To prove the effectiveness of the NSGA-G, the optimal data produced by NSGA-II are generated and compared. Fig. 12 presents the Pareto front produced by the NSGA-G. The computational times of the NSGA-G and NSGA-II are 60.8 s and 264 s, respectively. The number of feasible designs produced by the NSGA-G and NSGA-II are 101 points and 98 points, respectively. The optimal data

produced by the NSGA-G of the *S*, *D*, *f*, and *DT* were 370 rpm, 0.10 mm, 0.04 mm/rev, and 8 mm, respectively (Table 9). The optimal data produced by the NSGA-II of the *S*, *D*, *f*, and *DT* were 352 rpm, 0.10 mm, 0.04 mm/rev, and 7 mm, respectively. It can be stated that the NSGA-G provides a lower computational time, produces a higher number of feasible points, and better optimal results, as compared to the NSGA-II. Consequently, the *VH* is improved by 7.6 %, while the *Ra* is decreased by 40.7 % at the optimal solution, as compared to initial values.

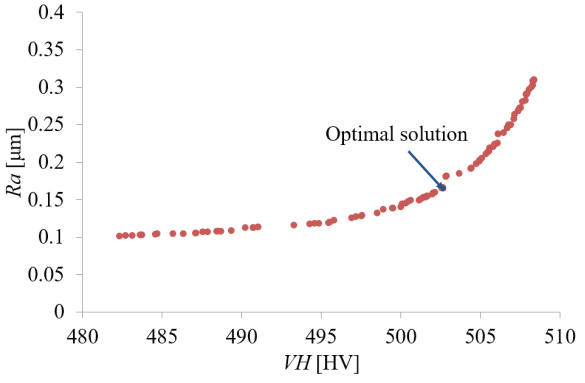

Fig. 12. *The Pareto front produced by the NSGA-G*

4.5 Scientific and Industrial Contributions

As a result, the average roughness and Vickers hardness of a new diamond burnishing process have been enhanced with the aid of optimum factors. The academic remarks are expressed as:

The proposed technique combining the ANN, CRITIC, and NSGA-G can be effectively utilized to find optimizing values of parameter inputs and responses for other diamond burnishing and machining processes.

The correlations developed by the BRFFNN approach can be applied to describe the complex data of the machining process.

The obtained data can be used in the practical diamond burnishing process to decrease the average roughness and enhance the Vickers hardness.

The industrial remarks are expressed as:

- A new diamond burnishing process comprising the MQL and double vortex tubes can be directly utilized in industrial applications for improving the surface properties of the external surface.
- The Pareto graphs can be applied to select optimal values of parameter inputs and responses for different burnishing aims.
- The CL efficiency of different machining operations (turning, milling, and grinding) can be enhanced with using the proposed system.
- The *Ra* and *VH* models developed BRFFNN approach can be precisely utilized to calculate the machining targets for different deployments.

4.6 Evaluation of the total diamond burnishing cost

The total diamond burnishing cost (*TDC*) is a summarization of the operation cost, lighting cost, depreciation cost, energy cost, tool cost, fluid cost, and cleaning cost. The *TDC* model is expressed as:

$$TDC = (C_o \times N_{db} \times \frac{t_{db}}{3600}) + (C_e \times P_{LT} \times \frac{t_{db}}{3600}) + (\frac{C_{mi} - C_{sv}) \times t_{db}}{M_l \times 3600}) + (\frac{C_e \times P_{db} \times t_{db}}{3600 \times \eta}) + (\frac{C_T \times t_{db}}{t_T}) + (F \times C_l \times 60 \times \frac{t_{db}}{3600}) + (C_c \times F \times \frac{t_h}{3600}), \quad (15)$$

where C_o, N_{db}, and t_{db} are the unit operator cost, the number of operators, and machining time, respectively. C_e and P_L are the unit energy cost and lighting power, respectively. C_{mi}, C_{sv}, and t_{db} are the initial cost, salvage value, and useful life, respectively. C_e, P_{db}, and η present the unit energy cost, power used in the machining time, and the working efficiency of the machine tool, respectively. C_T and T_T are the unit cost

Table 9. *Optimization results generated by the BRNN-CRITI-NSGAG*

Method	Optimization parameters				Responses	
	S [rpm]	*D* [mm]	*f* [mm/rev]	*DT* [mm]	*Ra* [μm]	*VH* [HV]
Initial values	630	0.06	0.04	6	0.27	467.2
NSGA-G	630	0.10	0.05	8	0.16	502.6
NSGA-II	352	0.10	0.04	7	0.18	497.2
Improvement [%]					40.7	7.6

and useful life of the diamond tool tip, respectively. C_l, F, and C_c present the unit cost, flow rate of the fluid, and the unit cost of the cleaning operation, respectively. Table 10 presents the experimental coefficients for the TDC model. The *TDC* value is decreased by 20 % at the selected optimality, as compared to the common values (Table 11).

Table 10. *The experimental coefficients for estimating total diamond burnishing cost*

C_o [USD/h]	N_w	C_{mu} [USD]	C_{sv} [USD]	M_l [h]	C_e [USD/kWh]
8.2	1	61500	4000	20000	0.14
C_T [USD]	t_T [s]	F [ml/h]	C_l [USD/l]	C_c [USD/l]	
13.8	3000	80	2	0.46	

Table 11. *The reduction in the total diamond burnishing cost*

Method	Optimization parameters				Cost
	S [rpm]	D [mm]	f [mm/rev]	DT [mm]	TDC [USD]
Common values	630	0.06	0.04	6	2.45
Optimal values	630	0.10	0.05	8	1.96
Reduction [%]					20.0

5 CONCLUSIONS

In this study, a new single diamond burnishing process was proposed and optimized to improve the Vickers hardness and decrease the average roughness. The parameter inputs were the *S*, *D*, *f*, and *DT*. The CRITIC method was applied to compute the weights, while the BRFFNN approach was utilized to develop the response model in terms of the optimizing factors. The obtained findings can be expressed as:

1. To enhance the Vickers hardness, the highest *DT* is applied, while the lowest values of the *S*, *f*, and *DT* are recommended. To decrease the average roughness, the highest values of the *S*, *D*, and *DT* are applied, while the lowest *f* is encouraged.
2. For the *Ra*, the *f* is named as the most effective parameter, followed by the *S*, *D*, and *DT*, respectively. For the *VH*, the *S* is named as the most effective parameter, followed by the *f*, *D*, and *DT*, respectively.
3. The optimal data of the *S*, *D*, *f*, and *DT* were 300 rpm, 0.10 mm, 0.04 mm/rev, and 8 mm, respectively. The *VH* was improved by 7.6 % while the *Ra* was decreased by 10.7 %. The total diamond burnishing cost could be decreased by 20 % at the optimal solution.
4. This investigation considered the average roughness and Vickers hardness of a new single diamond burnishing. Further work with more objectives, such as the wear rate, energy consumption, and grain size will be addressed.

6 REFERENCES

[1] Zaman, P.B., Dhar, N.R. (2020). Multi-objective optimization of double-jet MQL system parameters meant for enhancing the turning performance of Ti-6Al-4V Alloy. *Arabian Journal for Science and Engineering*, vol. 45, p. 9505-9526, **DOI:10.1007/s13369-020-04806-x**.

[2] Tamang, S.K., Chandrasekaran, M., Sahoo, A.K. (2018). Sustainable machining: an experimental investigation and optimization of machining Inconel 825 with dry and MQL approach. *Journal of the Brazilian Society of Mechanical Sciences and Engineering*, vol. 40, art. ID 374, **DOI:10.1007/s40430-018-1294-2**.

[3] Zan, Z., Guo, K., Sun, J., Wei, X., Tan, Y., Yang, B. (2021). Investigation of MQL parameters in milling of titanium alloy. *The International Journal of Advanced Manufacturing Technology*, vol. 116, p. 375-388, **DOI:10.1007/s00170-021-07441-4**.

[4] Sen, B., Mia, M., Mandal, U.K., Dutta, B., Mondal, S.P. (2019). Multi-objective optimization for MQL-assisted end milling operation: an intelligent hybrid strategy combining GEP and NTOPSIS. *Neural Computing & Applications*, vol. 31, p. 8693-8717, **DOI:10.1007/s00521-019-04450-z**.

[5] Van, A.L., Nguyen, T.T. (2022). Investigation and optimization of MQL system parameters in the roller-burnishing process of hardened steel. *Strojniški vestnik - Journal of Mechanical Engineering*, vol. 68, no. 3, p. 155-165, **DOI:10.5545/sv-jme.2021.7473**.

[6] Nguyen, T.T., Nguyen, T.A., Trinh, Q.H. Le, X.B., Pham, L.H., Le, X.H. (2022). Artificial neural network-based optimization of operating parameters for minimum quantity lubrication-assisted burnishing process in terms of surface characteristics. *Neural Computing & Applications*, vol. 34, p. 7005-7031, **DOI:10.1007/s00521-021-06834-6**.

[7] Sachin, B., Narendranath, S., Chakradhar, D (2019). Selection of optimal process parameters in sustainable diamond burnishing of 17-4 PH stainless steel. *Journal of the Brazilian Society of Mechanical Sciences and Engineering*, vol. 41, art. ID 219, **DOI:10.1007/s40430-019-1726-7**.

[8] Mahapatro, K., Krishna, P.V. (2022). Influence of flow parameters in the dual nozzle CO2-based vortex tube cooling system during turning of Ti-6Al-4V. *Proceedings of the Institution of Mechanical Engineers, Part C: Journal of Mechanical Engineering*, vol. 236, no. 9, **DOI:10.1177/09544062211057495**.

[9] Singh, R., Dureja, J.S., Dogra, M., Gupta, M.K., Jamil, M., Mia, M. (2020). Evaluating the sustainability pillars of energy and environment considering carbon emissions under machining ofTi-3Al-2.5V. *Sustainable Energy Technologies and Assessments*, vol. 42, art. ID 100806, **DOI:10.1016/j.seta.2020.100806**.

[10] Gupta, M.K., Mia, M., Singh, G., Pimenov, D.Y., Sarikaya, M., Sharma, V.S. (2019). Hybrid cooling-lubrication strategies to improve surface topography and tool wear in sustainable turning of Al 7075-T6 alloy. *The International Journal of Advanced Manufacturing Technology*, vol. 101, p. 55-69, **DOI:10.1007/s00170-018-2870-4**.

[11] Mia, M., Singh, G., Gupta, M.K., Sharma, V.S. (2018). Influence of Ranque-Hilsch vortex tube and nitrogen gas assisted MQL in precision turning of Al 6061-T6. *Precision Engineering*, vol. 53, p. 289-299, **DOI:10.1016/j.precisioneng.2018.04.011**.

[12] Duc, T.M., Long, T.T., Van Thanh, D. (2020). Evaluation of minimum quantity lubrication and minimum quantity cooling lubrication performance in hard drilling of Hardox 500 steel using Al2O3 nanofluid. *Advances in Mechanical Engineering*, vol 12, no. 2, p. 1-12, **DOI:10.1177/1687814019888404**.

[13] Sharma, A., Singh, R.C., Singari, R.M. (2020). Optimization of machining parameters during cryogenic turning of AISI D3 steel. *Sādhanā*, vol. 45, art. ID 124, **DOI:10.1007/s12046-020-01368-4**.

[14] Khan, M.A., Jaffery, S.H.I., Khan, M., Younas, M., Butt, S.I., Warsi, S.S. (2020). Multi-objective optimization of turning titanium-based alloy Ti-6Al-4V under dry, wet, and cryogenic conditions using gray relational analysis (GRA). *The International Journal of Advanced Manufacturing Technology*, vol. 106, p. 3897-3911, **DOI:10.1007/s00170-019-04913-6**.

[15] Mia, M., Khan, M.A., Dhar, N.R. (2017). Study of surface roughness and cutting forces using ANN, RSM, and ANOVA in turning of Ti-6Al-4V under cryogenic jets applied at flank and rake faces of coated WC tool. *The International Journal of Advanced Manufacturing Technology*, vol. 93, p. 975-991. **DOI:10.1007/s00170-017-0566-9**.

[16] Sachin, B., Narendranath, S., Chakradhar, D. (2018). Experimental evaluation of diamond burnishing for sustainable manufacturing. *Materials Research Expres*s, vol. 5, no. 10, art. ID 106514, **DOI:10.1088/2053-1591/aadb0a**.

[17] Sachin, B., Narendranath, S., Chakradhar, D. (2020). Application of desirability approach to optimize the control factors in cryogenic diamond burnishing. *Arabian Journal for Science and Engineering*, vol. 45, p. 1305-1317, **DOI:10.1007/s13369-019-04326-3**.

[18] Maximov, J.T., Duncheva, G.V., Anchev, A.P., Dunchev, V.P. (2020). Smoothing, deep, or mixed diamond burnishing of low-alloy steel components - optimization procedures. *The International Journal of Advanced Manufacturing Technology*, vol. 106, p. 1917-1929, **DOI:10.1007/s00170-019-04747-2**.

[19] Maximov, J.T., Duncheva, G.V., Anchev, A.P., Dunchev, V.P., Ichkova, M.D. (2020). Improvement in fatigue strength of 41Cr4 steel through slide diamond burnishing. *Journal of the Brazilian Society of Mechanical Sciences and Engineering*, vol. 42, art. ID 197, **DOI:10.1007/s40430-020-02276-8**.

[20] Duncheva, G.V., Maximov, J.T., Anchev, A.P., Dunchev, V.P., Agirov, Y.B. (2022). Multi-objective optimization of the internal diamond burnishing process. *Materials and Manufacturing Processes*, vol. 37, no. 4, p. 428-436, **DOI:10.1080/10426914.2021.1981937**.

[21] Milčić, D., Alsammarraie, A., Madić, M., Krstić, V., Milčić, M. (2021). Predictions of friction coefficient in hydrodynamic journal bearing using artificial neural networks. *Strojniški vestnik - Journal of Mechanical Engineering*, vol. 67, no. 9, p. 411-420, **DOI:10.5545/sv-jme.2021.7230**.

[22] Sivakumar, A., Bagath Singh, N., Sathiamurthi, P. Karthi Vinith, K.S. 3 (2021). Extremal-micro genetic algorithm model for time-cost optimization with optimal labour productivity. *Strojniški vestnik - Journal of Mechanical Engineering*, vol. 67, no. 12, p. 682-691, **DOI:10.5545/sv-jme.2021.7406**.

Strojniški vestnik - Journal of Mechanical Engineering 69(2023)3-4, 169-184
DOI:10.5545/sv-jme.2022.356
Original Scientific Paper
Received for review: 2022-09-05
Received revised form: 2023-01-12
Accepted for publication: 2023-02-10

Thermal Investigations on a CNC Lathe Fitted with a Dynamically Enhanced Steel-Reinforced Epoxy Granite Bed

Mula Venkata Ramana[1] *– Pudukarai Ramaswamy Thyla[1] – Subramanian Elango[2] – Chinnuraj Shanmugam[1]
[1]PSG College of Technology, Department of Mechanical Engineering, India
[2]Galaxy Machinery Pvt Ltd, India

Polymer concrete or epoxy granite is becoming more popular for beds, bases, and other structures of precision machine tools, owing to its excellent damping characteristics. To realize the same static rigidity as that of the cast-iron structures, steel-reinforced epoxy granite (SREG) structures are being used. The vast differences in the thermal properties of steel and epoxy granite (EG) are likely to cause higher magnitudes of thermal error. This work aims to investigate the thermal behaviour of a computerized numerical control (CNC) lathe built with a novel dynamically enhanced SREG bed and compare its performance with the lathe with a cast iron bed. Experimental and numerical investigations have been carried out under cross-feed (CF) drive idle running conditions to determine the TCP deformation. The results reveal that the thermal error in the CNC lathe with SREG bed is 1.68 times that of the lathe with cast iron (CI) bed at 20 °C and 1.8 times at 40 °C environmental temperature variation chamber (ETVC) conditions. It could be identified that the heat generated in the CF is conducted to the steel guideways embedded in the SREG bed, but further heat transfer to the EG portion of the bed is impeded, and hence the heat accumulation that occurs in the guideways leads to higher magnitude of the thermal error. The experimentally validated numerical model is used to extend the investigations to study the effect of the idle running of the longitudinal feed drive (LF) and combined cross and longitudinal feed drives, on the thermal behaviour of the lathe.

Keywords: precision machine tools, thermal error, steel reinforcement, epoxy granite

Highlights

- *The use of steel reinforcements in epoxy granite for machine tools is an innovative attempt to achieve the same stiffness as CI machine tool structures with enhanced damping characteristics.*
- *This research work aims to investigate the thermal error in a CNC lathe with an SREG bed and compare it with the thermal error in a CNC lathe with a CI bed.*
- *Thermal error in the CNC lathe with SREG bed is 1.68 times that of the lathe with CI bed at 20 °C and 1.8 times at 40 °C environmental temperature variation chamber (ETVC) conditions.*
- *A finite element model (FEM) has been developed, and the simulation results are well in agreement with the experimental results.*

0 INTRODUCTION

Machining accuracy is a crucial parameter in the development of precision machines. Since machine tool performance is governed by static, dynamic, and thermal stability, designers must contemplate these aspects at every stage of development [1] and [2]. Different materials with desired properties are used for various machine tool components. Cast iron (CI) is commonly used as a material for the base or bed since they are essential parts that hold all the other parts together and also can absorb shocks and vibrations [3] and [4]. Instead of CI, mineral castings such as tailor-made polymer concrete (PC) materials have gained popularity in recent years for use in high-performance and high-speed machine tools to ultra-precision machines and metrology applications due to their excellent damping characteristics [5] to [7].

Mineral castings are light in weight and require lower development and handling costs. A wide range of polymers and particulates have been used to develop custom-made polymer concrete for machine tool structures [8] and [9]. Epoxy granite (EG) is a type of tailor-made material that belongs to the polymer concrete group [10]. A suitable epoxy granite mix proportion can be chosen by optimizing several parameters, such as the type and content of the resin and filler, curing method, curing temperature, humidity, and, most importantly, the resin-to-filler ratio and matrix-to-aggregate ratio, which influence the characteristics of epoxy granite [11].

EG has a significantly high damping capacity due to the high viscoelasticity of the epoxy resin and a damping ratio that is seven to ten times that of conventional cast iron; however, it has a low modulus of elasticity [12]. EG is used as a machine tool structural material to improve dynamic performance by increasing stiffness with fibre addition, applying form design principles to structures, and embracing metal reinforcements [13] to [15]

Suh and Lee [16] developed a hybrid steel and polymer concrete bed, which was also incorporated

*Corr. Author's Address: 1PSG College of Technology, Department of Mechanical Engineering, India, venkataramana048@gmail.com

into a high-speed gantry-type milling machine. The dynamic performance revealed that the hybrid polymer concrete exhibited superior damping characteristics, with damping ratios ranging from (2.93 % to 5.9 %) when compared to existing case-iron beds with damping ratios ranging from (0.2 % to 0.3 %).

EG structures are capable of replacing existing CI structures for bed and base applications; In such cases, it is critical to maintain the footprints of the traditional CI bed to meet assembly requirements. Metal reinforcements are an alternative to making significant form design changes to enhance static stiffness whilst also meeting footprint requirements [17]. Chinnuraj et al. [17] presented the static and dynamic characteristics of a computerized numerical control (CNC) lathe with a CI bed and SREG bed. Experiments revealed that the dynamic performance of the lathe with an SREG bed improved considerably compared to that of the lathe with a CI bed.

Another advantage of EG is that its thermal conductivity is very low, which aids in maintaining thermal stability under different climatic conditions associated with environmental temperature variations [18] and [19]. However, it is vital to investigate the total machine tool's thermal behaviour and the thermal error under the influence of heat generated internally due to friction in bearings, guideways, and other moving assemblies. Thermal error accounts for 30 % to 70 % of the overall error in machine tools [20] and [21]. Although EG is thermally stable, since it is reinforced with steel whose thermal conductivity is much higher than that of EG, a bi-material effect can arise as the temperature of the machine tool rises and heat flows through the reinforcement in EG structures, resulting in thermal error.

Suh and Lee [22] investigated the thermal characteristics of steel and polymer composite sandwich structures for high-speed milling machines using finite element model (FEM) analysis and experiments to ensure that vertical column deformation was permissible given the allowable deformation for proper linear motor operation.

The objective of this work is to study the influence of the bi-material effect (different thermal properties) of steel and EG on the thermal behaviour of the lathe, in comparison to that of the lathe with the existing cast iron bed. In this work, investigations on the thermal behaviour of a CNC lathe built with an SREG bed have been carried out as a continuation of the static and dynamic investigations of this lathe presented by Chinnuraj et al. [17]. The thermal error associated with SREG structures must be investigated in order to obtain the full benefits of the thermally inert, high damping tailor-made EG material. Some feasible methods of reducing thermal error have prompted the use of EG material in precision machine tools. According to Tanabe and Takada [23], heat sources should be kept separated from polymer concrete structures in machine tools in order to reduce large thermal gradients.

Neugebauer et al. [24] reduced thermal error in a machine tool built with a mineral casting bed by isolating heat sources by providing a composite layer of different materials with different thermal expansion coefficients. Weidlich and Nestmann [25] studied thermal deformations in a polymer concrete bed caused by local temperature gradients and provided additional steel fixings in linear guideways to improve heat conduction; investigations into such a method revealed a 30 % reduction in deformation.

This paper presents the thermal behaviour of a CNC lathe fitted with a novel dynamically enhanced SREG bed in place of the conventional cast iron bed. Numerical models of the lathe with the original CI bed as well as the lathe with the newly proposed SREG bed have been developed and validated with experiments. The thermal conductivity of epoxy granite is nearly 1/30th of that of steel. When steel reinforcement is embedded inside epoxy granite, the vast differences in their thermal properties will contribute to high thermal contact resistance at the interface. To improve the accuracy of the numerical model, joint contact resistance has been incorporated between the steel reinforcement and epoxy granite by adopting the joint contact resistance proposed by Brahmi et al. [26]. To highlight the benefits of SREG structures for machine tools, brief insights on the static and dynamic analysis of lathe bed, Vertical Machining Centre (VMC) base, and VMC column have been explained in Section 2. Experimental investigations on the thermal behaviour of CNC lathe with CI and SREG beds have been presented in Section 3. The development and validation of the numerical model have been discussed in Section 4. The validated numerical model has been used to determine thermal error under the idle running of longitudinal feed drive and idle running of both cross and longitudinal feed drives, and conclusions have been made and presented in Sections 5 and 6, respectively.

1 LITERATURE REVIEW

Cutting forces induce twisting and bending of the machine tool structures; therefore, the machine tool bed/base/column must be rigid against both bending loads and twisting moments. This section

contains an overview of the literature on the use of steel reinforcement to obtain equal stiffness for EG machine tool structures.

Dunaj et al. [27] and [28] developed lightweight steel-polymer concrete frames that have a 239 % improvement in modal damping ratio and 8 % less weight than a steel frame for a vertical lathe to improve machining stability. The performance of a lathe with a steel-polymer concrete frame revealed that the static stiffness of the lathe steel support system is increased by 30 % and an 8 % (on average 5 %) reduction in relative tool-workpiece frequency response function amplitudes when compared to the steel variant.

Chinnuraj et al. [17], Venugopal et al. [29] and [30] carried out investigations on the application of SREG structures to CNC lathe and VMC. Static and dynamic investigations have revealed that the use of SREG structures in machine tools will enhance the static and dynamic performance of the machine. The authors developed numerical models of the structures and validated the same through experimental modal analysis; these validated models aid in the iterative design of steel reinforcements and the EG structure. Based on the numerical investigations, the best reinforcement design was chosen from among several proposed designs. SREG structures for CNC lathe and VMC with the best design configuration were fabricated and tested for static stability and modal frequencies. The results revealed that the SREG structures have higher stiffness and natural frequencies than the respective CI machine tool structures, with significantly lesser mass. The material properties of steel, cast iron, and EG are represented in Table 1

Table 1. *Machine tool structures material properties*

Property	Material		
	Steel	Cast iron	Epoxy granite [15]
Density, [kg/m³]	7800	7250	2300
Modulus of elasticity, [GPa]	210	110	30
Poisson's ratio	0.27	0.24	0.25
Compressive strength, [MPa]	250	600	110
Flexural strength, [MPa]	380	450	36
Damping ratio	0.0001	0.001	0.0176
Thermal conductivity, [W/(m·K)]	45 to 50	50	0.5 to 1.5
Thermal expansion coefficient, [°C]	$12x10^{-6}$	$6x10^{-6}$	$12x10^{-6}$
Heat capacity, [J/(kgK)]	460	460	700

The results of the static and dynamic analysis carried out on the SREG structures of the CNC lathe and VMC, with the finalized reinforcement configuration are presented in Table 2. Chinnuraj et al. [17] developed five design configurations for the steel reinforcement and developed the SREG bed with design configuration 5 among all designs, as shown in Fig. 1 which improved torsional stiffness, and provided a significant positive shift in natural frequencies and 22 % mass reduction as compared to CI bed. The torsional rigidity of the SREG bed was found to be 3.3 times that of the original CI bed. The developed SREG bed was fabricated, and the numerical model was validated by conducting static and modal testing.

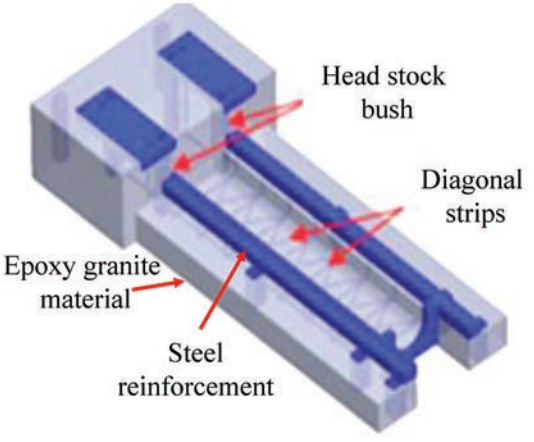

Fig. 1. *Steel-reinforced epoxy granite (SREG) bed*

Table 2 contains a review of the literature comparing the static dynamic characteristics of SREG or hybrid structures (steel and polymer concrete structures) to conventional structures.

Even though the static and dynamic characteristics of the SREG bed or hybrid structures have been proven to be superior to those of the original CI bed, the behaviour of the SREG bed to thermal loads needs to be investigated. There is a possibility of a bi-material thermal effect due to large changes in their operating conditions, ranging from extremely heavy loads encountered in rough machining cycles to extremely light loads encountered in finishing cycles. The results will aid in reconfiguring the reinforcement design to enhance heat transfer, thus reducing thermal error.

2 EXPERIMENTAL INVESTIGATIONS ON THE THERMAL BEHAVIOUR OF CNC LATHE WITH CI AND SREG BEDS

2.1 Experimental Procedure

As shown in Fig. 2, a CNC lathe was taken up for investigations on its thermal behaviour. The length

Table 2. *Static rigidity and modal parameters of CI and SREG structures*

Literature reference	Findings from static analysis			Findings from dynamic analysis				Mass of the developed structure [kg]		
	Parameter measured in developed structure	Parameter magnitude		First natural frequency [Hz]		Average damping ratio of structure		CI or Existing structure	SREG or hybrid structure	
		CI or Existing structure	SREG or hybrid PC	CI or Existing structure	SREG or hybrid PC	CI or Existing structure	SREG or hybrid PC		EG portion	Steel reinforcement
Chinnuraj et al. [17]	Torsional rigidity of the lathe with different beds [Nm/arc.s]	7.32	11.7	258	276	0.0007	0.004	110	67	19
Venugopal et al. [29]	Deformation along y-direction in VMC base [μm]	18.8	12.1	133	370	0.0013	0.005	890	1041	64
Venugopal et al. [30]	Deformation at the spindle nose in VMC column [μm]	76.8	75.2	92	89	0.001	0.004	660	542	161
Dunaj et al. [27] and [28]	Lightweight steel-concrete frame for vertical lathe	-	-	18.8	19.2	0.0008	0.002	1338	Variant 1: 1667 Variant 2: 1775 Variant 3: 1705	
Xu et al. [31]	Deformation of Steel-fibber Polymer Concrete (SFPC) lathe bed	0.21	0.41	143	165	0.003	0.04	-	-	-
Suh, J.D., Lee, D.G. [16]	Deformation of the machine tool bed under inertia and attraction forces [μm]	-	48.8	-	93	0.002 to 0.003	0.029 to 0.056	-	-	-
Chen, T.C. [32]	Z-axial static stiffness [N/μm]	330	286	98	240	0.0015	0.03	-	-	-

(L) and breadth or width (W) of the bed fitted in the lathe are 97 mm and 34 mm. The distance from the bed bottom to the top surface (H) is 405 mm. The dimensions of the machine tool are shown in Fig. 2. To provide the same information for measuring, pre-experiment adjustments, and corrections must be made precisely. The assumptions considered in this analysis are:

1. The effect of machining is not considered since a large amount of cutting liquid is required in the machining process; thermal deformation between the cutting tool and the parts being machined is ignored [33].
2. Since machining is not considered, the effect of chips is not factored.
3. The offset errors of the ball screws are already corrected by the controller parameters.
4. Since the experiments are carried out in a closed environment chamber, the environmental impact, such as magnetic field, humidity change, and vibration, is ignored since the primary objective of the research is to identify the discrepancy in CNC lathe performance with different beds.

Since TCP on the lathe turret is primarily associated with the moment of feed drives, the thermal behaviour of the feed drive has been considered separately to analyse its impact on the use of the SREG bed on TCP, which is prompted by the axis thermal growth of the feed drive. Methods for a systematic examination of the thermal behaviour of machine tools are provided by the International Organization for Standardization (ISO 230-3) [34].

The loading cycle considered for thermal analysis is three minutes running and one minute idle. The different machining operations carried out on the machine tool require fluctuating load cycles [33]. As per standards [34], the feed drive should run for 6 hours at the specified load cycle. The drive system's feed is to idle run at a maximum speed of 20 m/min for three minutes and stop for one minute. The load cycle is used to investigate the transient temperature variations in the machine structure as a result of intermittent and repeated machining circumstances.

Temperature sensors, RTD Pt100 as shown in Fig. 4 are used for temperature measurement by gluing them to different critical machine elements.

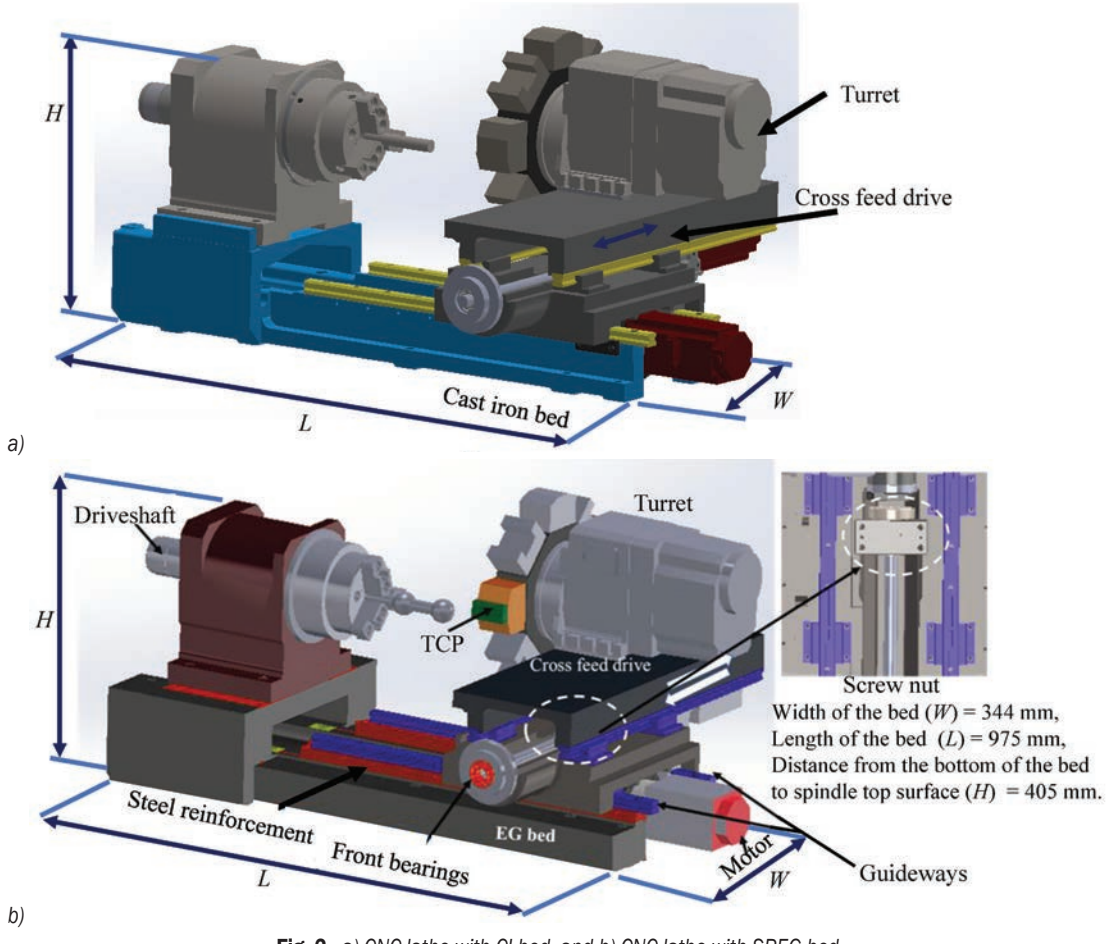

Fig. 2. *a) CNC lathe with CI bed, and b) CNC lathe with SREG bed*

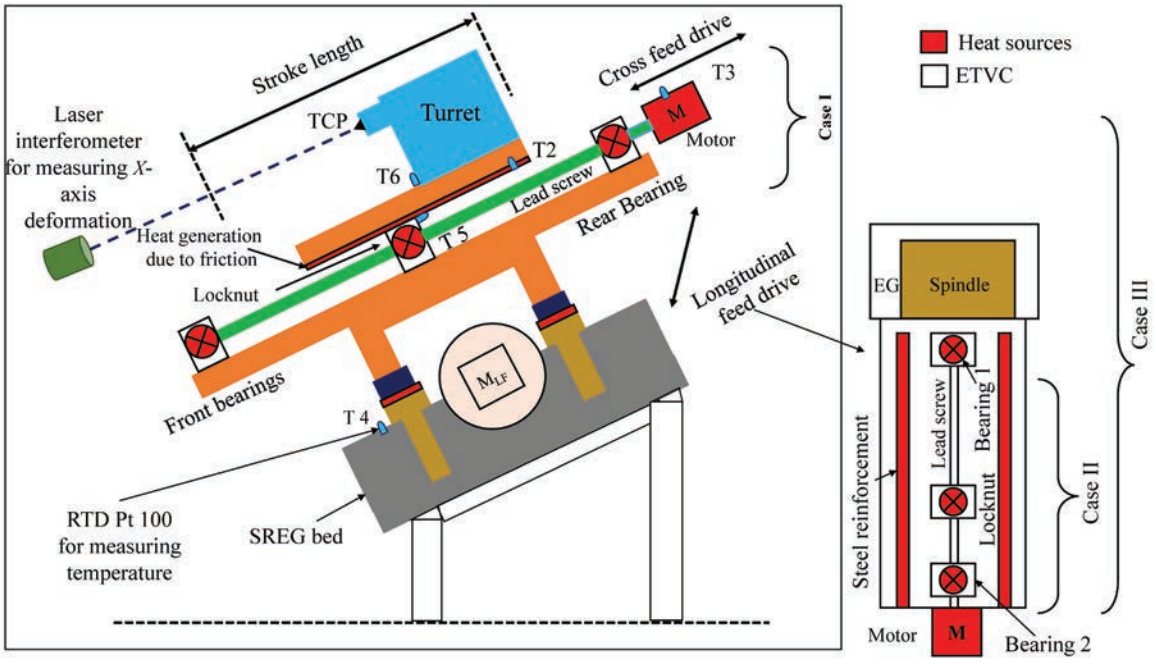

Fig. 3. *Schematic representation of experimental setup*

Since major heat sources are in motion during experimentation, a few sensors were mounted at critical locations, as shown in Table 3. A laser interferometer (Make: Renishaw XL80) is used to measure the x-axis thermal growth measurement. The XL-80 environmental compensation unit is attached to the sidewall surface of the machine tool casing as shown in Fig. 4 in order to minimize the influence of temperature and air pressure variation in laser interferometer measurement. The location of temperature and deformation sensors are represented in Fig. 3. Temperature data is collected every minute, and deformation is collected every 15 minutes by the data acquisition system (DAQ).

In order to make a meaningful comparative study of the effect of using the SREG bed against the CI bed in CNC lathe, the thermal deformation of structures arising due to ambient temperature variations has to be eliminated by conducting the experiments under identical controlled environments. Firstly, the experiments were carried out on the lathe, which was originally built with a cast iron bed, with the cross-feed drive idle running. Secondly, the studies were repeated on the lathe with a newly developed SREG bed instead of a cast iron bed as shown in Fig. 4.

The machine tool has two feed drives: cross feed (CF) drive and longitudinal feed (LF) drive. Since the standard testing procedure for the lathe with the original CI bed involves conducting experiments with the cross-feed drive idle running, the lathe with the SREG bed is also run with the cross-feed drive idle running. Experimental investigations were carried out at 20 °C and 40 °C, to simulate typical operating conditions, below and above room temperature. Firstly, the lathe with a CI bed is moved to an ETVC chamber and maintained at a temperature of 20 °C. The machine is allowed to soak and experiments are conducted by running the cross-feed drive with a loading cycle. Temperature and x-axis deformation of TCP at one fixed end are measured during the experiment. After the experiment under 20 °C ETVC conditions, the lathe is soaked at 40 °C and

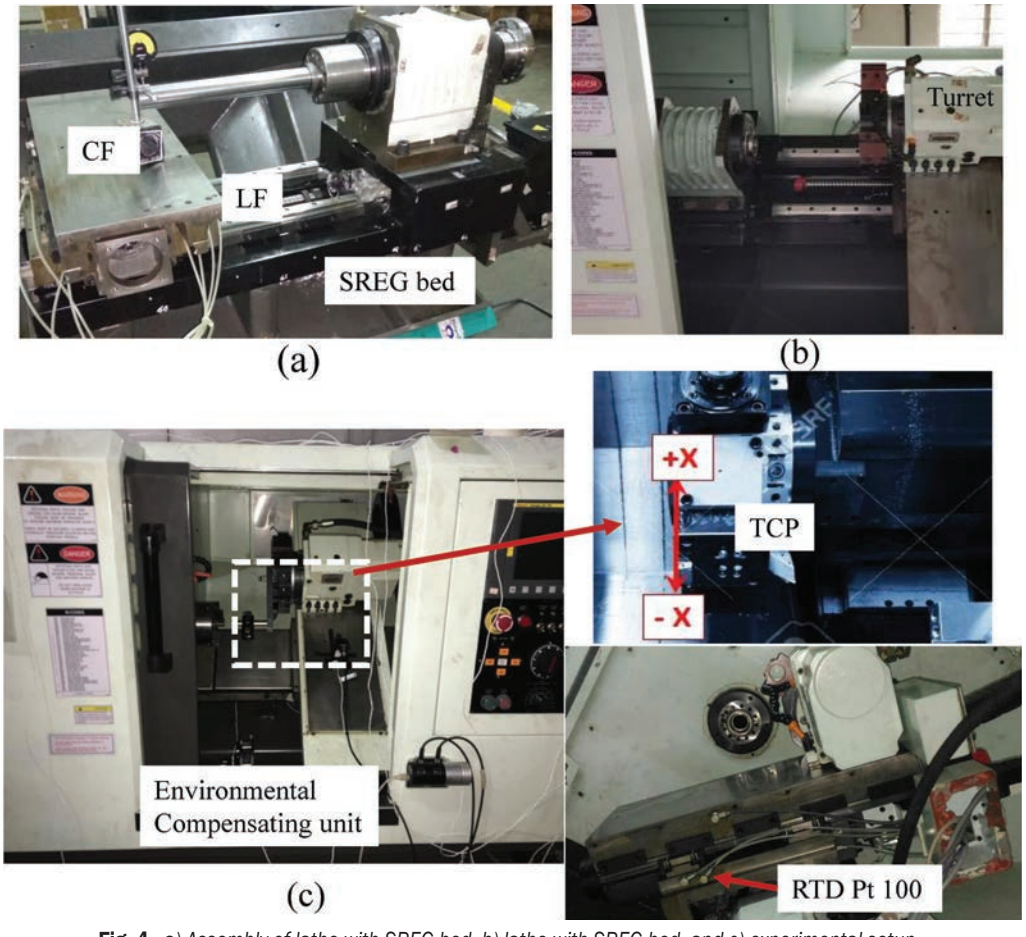

Fig. 4. *a) Assembly of lathe with SREG bed, b) lathe with SREG bed, and c) experimental setup*

the experiment was repeated. The CNC lathe is removed from the ETVC chamber, disassembled, and reassembled with an SREG bed. The experimental procedure is repeated on the CNC lathe with the SREG bed under both 20 °C and 40 °C ETVC conditions, similar to the lathe with the CI bed.

The soaking time required for the lathe with CI and SREG beds was found to be nearly the same, which is 4 hours for 20 °C and 7 hours for 40 °C environmental conditions. The heat from the heat sources is conducted to the surrounding structures, thus causing a thermal gradient in the machine tool structures. In such cases, the developed non-uniform temperatures could lead to expansion of structures resulting in thermal error. In Fig. 4, notations +X and -X refers to distances away from and towards the operator respectively.

2.2 Analysis of Thermal Behaviour under Cross-Feed Drive Idle Running

The temperature measured from experiments at various sensor locations glued on the lathe with the CI bed and the SREG bed at 20 °C and 40 °C is depicted in Figs. 5a and 6r espectively.

T1 represents the ambient temperature and the variation of the same is limited to 0.5 °C. Similarly, T2, T3, T4, T5, and T6 represent the temperatures at the LM block, drive motor, bed centre, ball screw housing, and turret. Since T2 and T3 represent the temperature in the vicinity of heat sources, they are found to be higher in magnitude in all the experiments.

Transient variation of X-axis thermal growth can be considered as a measure of thermal error. Transient variation of feed drive drifts in the lathe with a CI bed and SREG bed at 20 ºC and 40 ºC environment temperatures are analysed and the same is depicted

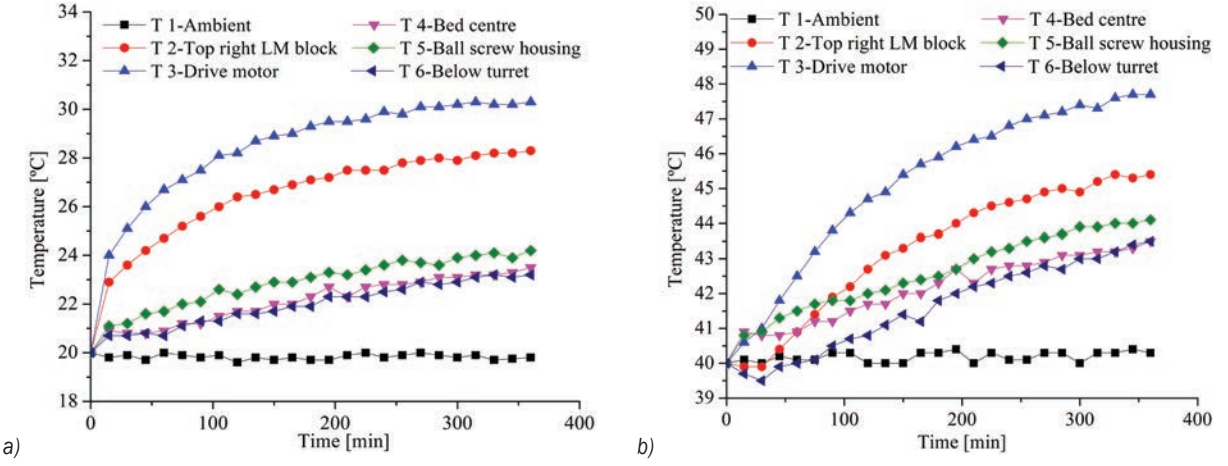

Fig. 5. *Transient variation of temperature in the lathe with CI bed at a) 20 ºC, and b) 40 ºC environment temperature*

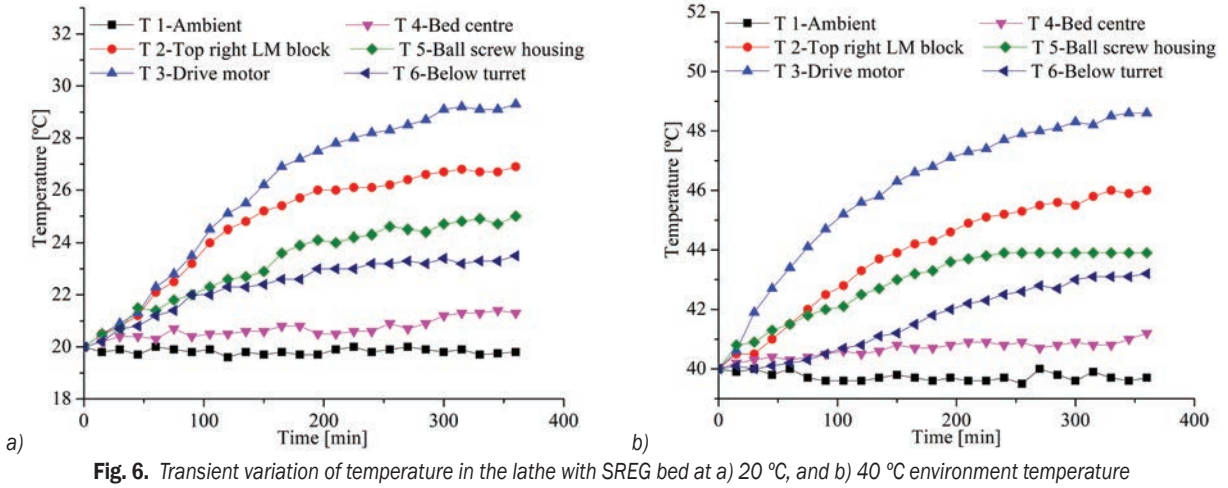

Fig. 6. *Transient variation of temperature in the lathe with SREG bed at a) 20 ºC, and b) 40 ºC environment temperature*

in Fig. 7 The trend of variation of the x-axis growth observed under 20 °C and 40 °C environment temperature conditions show the behaviour of the machine tool typically at temperatures below and above room temperature. Since the difference from 20 ºC to room temperature and 40 °C to room temperature is not similar, a slight difference with a similar trend in the opposite direction has been observed in the lathe with both the CI bed and SREG bed.

From Fig. 6 , at 20 °C from 0 min to 300 min, the temperature difference of 8 °C, and 11 °C, have been observed at T2, and T3, respectively. From Fig. 6, at 40 °C from 0 min to 300 min, the temperature difference of 7.5 °C, and 8 °C have been observed at T2, and T3, respectively. The change in temperatures of the structures is a higher magnitude of temperature difference observed at 20 °C than 40 °C, which refers to the rate of heat transfer being higher at 20 °C as compared to 40 °C. From the temperature profile, a maximum temperature difference has been observed in the drive motor and LM block locations in the first 120 min. From 120 min to 300 min, the rise in temperature is less which reflects a low-temperature difference. Therefore, the variation in *x*-axis thermal growth from 120 min to 300 min is low. The temperature of structures in the lathe with CI bed, from T2 to T6 reached steady-state reached after 120 min, whereas at 40 °C ETVC the steady-state has been identified after 300 min.

From Fig. 6, the temperature profile of the lathe with CI bed at 40 ºC, the temperature rises among T2 to T6 locations increased gradually. At 40 °C, the temperatures of the structures of the lathe with a CI bed are observed to be lesser than that in the lathe with an SREG bed. Therefore, the cumulative expansion of all structures in the lathe with CI bed at 40 °C will be lesser than the cumulative expansion of the corresponding structures of the lathe with SREG bed at 40 ºC. The results show that the temperature rise of the EG portion in the SREG bed is low owing to its very low thermal conductivity. A higher temperature rise has been observed in the lathe with SREG bed than that in the lathe with a CI bed, except in the bed itself. Figs. 7a and b compare the *x*-axis thermal growth in the CNC lathe with the CI bed at TCP to the *x*-axis thermal growth in the lathe with the SREG bed at 20 ºC ETCV and 40 ºC ETVC conditions, respectively. At 20 ºC chamber conditions, the thermal growth at TCP is in the negative direction (towards the operator), and the trend followed was identical to that reported by Ruijun et al. [35], and Xu et al. [36]. At 40 ºC chamber conditions, the thermal growth at TCP is in the positive direction (away from the operator), and the trend followed was identical to the observation in experiments conducted by Li et al. [37]. From Fig. 7 the *x*-axis growth in the lathe with the SREG bed is found to increase from 0 µm to 17 µm (towards the operator side) in the time span of 0 min to 60 min. Further, in the time span of 60 min to 225 min, the *x*-axis thermal growth is found to remain unaltered and then reversed from –8 µm to –43 µm in the time span of 225 min to 300 min. The start of the reverse trend is deemed as a sign of the development of re-initiation of unsteady-state due to non-uniform temperature.

From, Fig. 7a, at 20 ºC ETVC conditions the linear *x*-axis thermal growth at 300 min in the lathe with CI bed is limited to -8 µm, whereas for the lathe with the SREG bed, it is -43 µm. Due to more heat accumulation in the steel reinforcement, which is

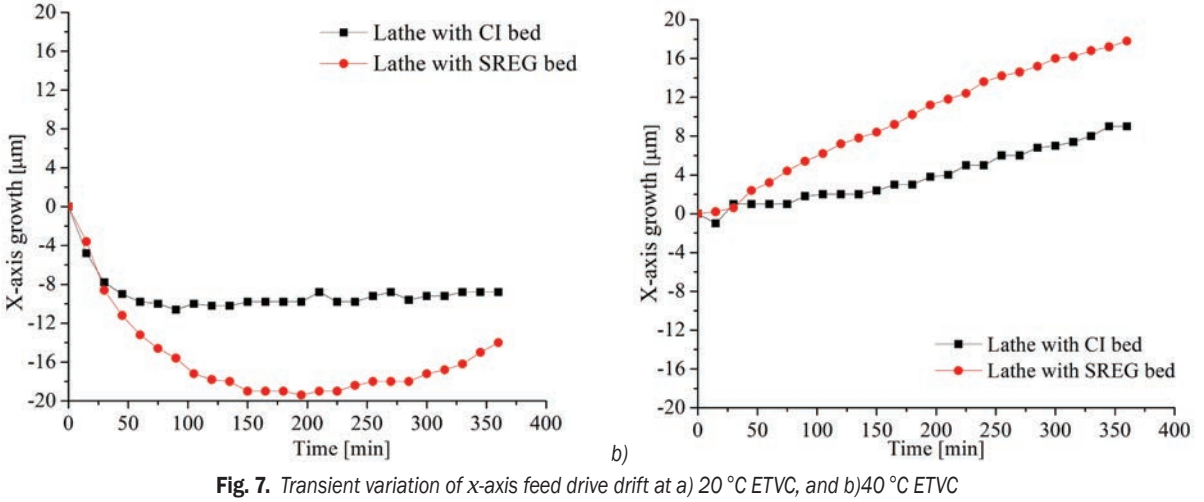

Fig. 7. *Transient variation of x-axis feed drive drift at a) 20 °C ETVC, and b)40 °C ETVC*

reflected as the temperature rises in the lathe with the SREG bed, more nonuniform temperature distribution leads to more thermal error than in the lathe with CI bed at 20 ºC.

From Fig. 7, the *x*-axis thermal growth in the lathe with CI bed from 0 min to 30 min gradually increased from 0 µm to 9 µm. Further, from 340 min to 360 min not much variation exists in the *x*-axis thermal growth. The *x*-axis thermal growth in the lathe with SREG bed from 0 min to 360 min gradually increased from 0 µm to 18 µm. The thermal error in the lathe with CI bed with the cross-feed drive idling as per the loading cycle is 9 µm. The experiments lasted for 360 min, as required by the standards, and the linearity for the *x*-axis thermal growth of both the lathe with CI bed and that with SREG bed at 40 ºC has not been observed in a time span of 0 min to 360 min. Finally, the linear axis growth at 360 min of idle run in the lathe with CI bed is limited to 9 µm, whereas in the lathe with SREG bed is 18 µm a time span of 0 min to 360 m in.

From the experiments, the lathe with the SREG bed exhibits 1.8 times higher thermal error at 20 ºC and 1.88 times higher at 40 ºC environment temperature than the thermal error in the lathe with CI bed. The higher thermal error in the lathe with the SREG bed is due to the more heat accumulation in the steel reinforcement. According to Weidlich and Nestmann [25], the thermal deformations in a machine tool with a polymer concrete bed is higher, and such deformations are reduced by improving heat conduction with the help of additional steel fixings. The measurements of temperature and deformations at required locations under different conditions and the analysis of the same are possible with a validated finite element modal. The development of the FEM is presented in Section 3.

3 DEVELOPMENT OF NUMERICAL MODEL FOR FEED DRIVE OF CNC LATHE WITH CI AND SREG BEDS

A numerical model is developed to investigate the thermal behaviour of the CNC lathes with a CI bed and SREG bed, under the influence of idle running of a cross-feed drive. The assumptions considered to perform the analysis are: 1) Internal heat generation is given as heat input for bearings and ball screw; 2) Heat flow is given as input for frictional heat generation in guideways; 3) Heat generated by air friction loss can be ignored because it is insignificant in comparison to other heat sources; 4) Small system structures such as nuts, holes, and so on are omitted; 5) Heat transfer through radiation is not considered; 6) On the bottom of the machine tool, no thermal deformation in the *x*, *y*, or *z* directions exist.

3.1 Modelling of Heat Sources with Analytical Heat Calculations

Since it is practically impossible to measure temperatures at locations of heat sources to serve as input data for numerical analysis, analytical models are used to estimate the generated heat and convection. The heat transfer mechanism from sources to other structures undergoes conduction, contact conduction, free convection, and forced convection. Fig. 8 represents the method of modelling heat for various heat sources with analytical equations. The heat sources are: 1) Heat produced due to the sliding of the carriage relative to the guide block; 2) Heat generated by the bearings; 3) Heat generated by the lock nut; 4) Feed drive motor electromagnetic heat losses. The model is considered to have an initial preload which is further considered as radial load (F_r) and axial load (F_a) on the angular contact bearing are 7834 N, and 600 N respectively. The feed rate is 20 m/min.

The torque and frictional heat due to friction in the bearings is calculated by the given Eq. (1) [38]:

$$H_b = 1.047 \times 10^{-4} n M_b, \tag{1}$$

where, M_b is total frictional torque acting on the bearing, and n is the shaft rotational speed, total frictional torque, $M_b = M_1 + M_1$. Here M_1 is load-related frictional torque and M_2 is viscosity-related frictional torque.

$$M_1 = f_1 F_b d_m, \tag{2}$$

where

$$\begin{aligned} f_1 &= 0.001\left(P_0 / C_0\right)^{0.33}, \\ F_b &= 1.4F_a - 0.1F_r, \\ P_0 &= 2.3F_r \tan\theta + F_a, \end{aligned} \tag{3}$$

$$M_2 = 10^{-7} f_0 V_0 n \left(\frac{2}{3} d_m^3\right), \quad \text{when} \quad v_0 n \geq 2000, \tag{4}$$

$$M_2 = 160 \times 10^{-7} f_0 d_m^3, \quad \text{when} \quad v_0 n \leq 2000. \tag{5}$$

In Eqs. (2), (4) and (5), the diameter of the pitch circle (d_m) of bearing is 33.5 mm, $f_0 = 2$ and $f_1 = 0.00043$ are the parameters related to the type, structure, force, and lubrication of bearings. Kinematic viscosity (v_0) of lubricant is 30 $\cdot 10^{-6}$ m^2/s, rotational speed (n) is 3000 rpm. The calculated internal heat generation in the bearing using Eqs. (4) and (5) is 3,21 $\cdot 10^6$ W/m^3.

The frictional heat generation between the moving nut and the ball screw is another important heat source. Eq. (6) [39] is used to calculate the heat developed by ball screw. The efficiency of the screw nut (η) is 9 %, the diameter of the screw nut (D_m) is 20 mm Parameters 1 (angle δ) and 2 (angle α) in Eq. (7) are 28º and 8.53º, respectively. Rotational speed (n) is 3000 rpm.

$$H_s = 0.01\pi n M_s, \quad (6$$

where M_s is total frictional torque of the ball screw system,

$$M_s = \frac{(1-\eta)W\tan(\alpha+\delta)D_m}{2}. \quad (7$$

From Eq. (6), the heat generation in screw nut (H_s) has been evaluated as 0,28.8 W/m3.

Heat generation in guideways can be evaluated using Eq. (8) [39]. The coefficient of friction (μ) is 0.2, the normal force acting on the guideway (F_g) is 0 N, and moving velocity (V) is 20 m/min.

$$H_g = \mu F_g V. \quad (8$$

From Eq. (8), heat generation in guideways (H_g) has been evaluated as 20 W. Motor heat losses are considered as 0 W, and the same is given as heat flow to the surface of the drive motor. For free convection around stationary surfaces, the convection coefficient (h) is considered as 0 W/(m^2·K) [19]. Average self-forced convection on rotary and reciprocating surfaces at the specified feed has been calculated as 35 W/(m^2·K) and 27 W/(m^2·K), respectively.

The heat transfer to the EG portion from reinforcement by considering joint contact resistance will be different in the condition without considering joint contact resistance, as depicted in Fig. 9. Hence, the joint contact resistance between steel reinforcement and epoxy granite structures has been evaluated and provided as joint contact conductance in the simulation. Contact conductance depends on the geometry, surface roughness, mean interface pressure, and joint temperature. Contact conductance is the inverse of thermal contact resistance developed in the joint. Eq. (2) is an analytical model developed by Bahrami et al. [26] for estimating the thermal contact resistance between metal and polymer and is considered in this work. Joint resistance is a summation of the thermal constriction/spreading resistance through the micro contacts (R_s) and bulk resistance of the polymer (R_b).

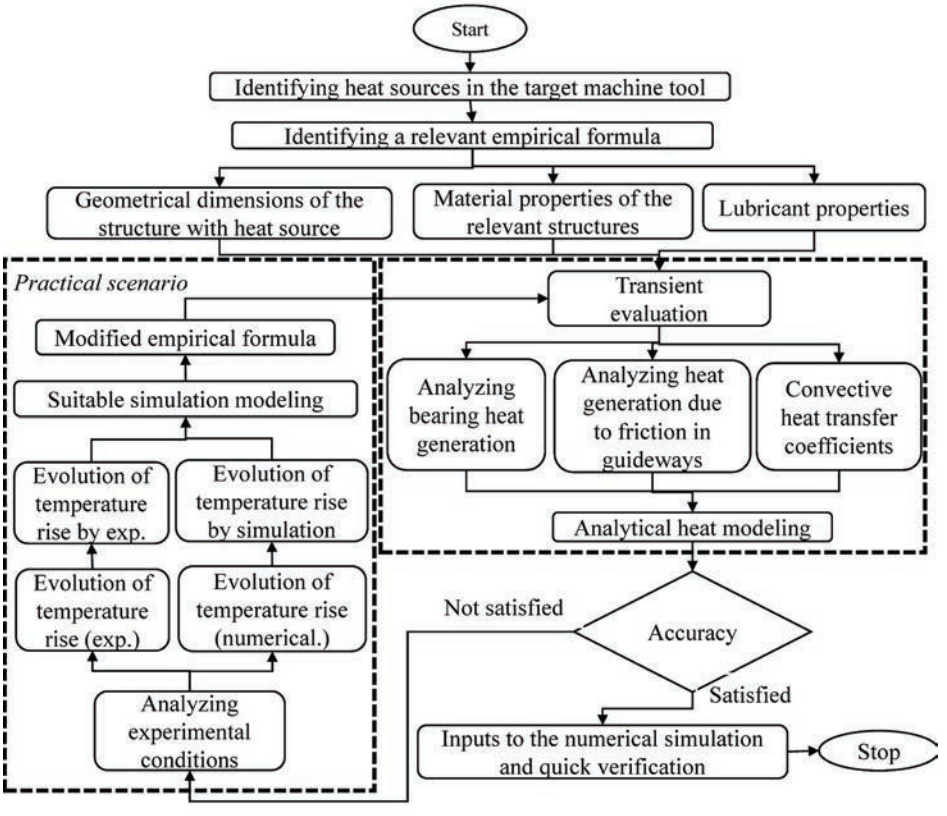

Fig. 8. *Methodology for heat generation modelling*

$$R_J = R_s + R_b, \tag{9}$$

$$R_S = \frac{0.565 H_m (\sigma / m)}{k_s F}, \tag{10}$$

$$R_b = \frac{\left(t_0 \left(1 - (P / E_P)\right)\right)}{\left(A_a k_p\right)}, \tag{11}$$

$$R_J = \frac{0.565 H_m (\sigma / m)}{k_s F} + \frac{\left(t_0 \left(1 - (P / E_P)\right)\right)}{\left(A_a k_p\right)}. \tag{12}$$

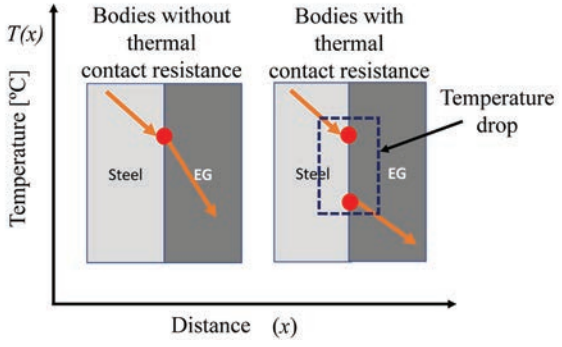

Fig. 9. *Heat transfer without and with thermal contact conductance*

Equivalent thermal conductivity of polymer and steel (k_s) is considered as:

$$K_s = \left(\left(2 k_m k_P\right) / \left(k_m + k_p\right)\right). \tag{13}$$

Polymer characteristics considered for epoxy are microhardness (H_m) is 0.5 GPa, combined surface roughness (σ) is 0.5 µm, surface asperities slope (m) is 0.4 µm/m, thermal conductivity of steel (k_m) is 60 W/(mK), minimum thickness of the polymer throughout the reinforcement (t_0) is 5 mm. Contact pressure (P) is 0.1 MPa, modulus of elasticity of the polymer (E_p) is 20 GPa. Thermal conductivity of the polymer (K_p) is 1.5 W/(mK). From the analytical Eq. (12) , the joint contact resistance is estimated as 12.5 $(m^2 \cdot K)/W$, and the joint contact conductance value, which is the inverse of joint contact resistance, is found to be 0.08 $W/(m^2 \cdot K)$.

Boundary conditions are applied to the lathe model in transient thermal analysis in ANSYS workbench. Later, for thermo-mechanical analysis, transient thermal analysis is coupled with static structural analysis. In experiments, throughout a 6 h time span, the temperature and *x*-axis thermal growth for the lathe have been collected. Similarly, for numerical transient analysis, total time span of 21,600 s (6 hours) was considered, and heat input values were provided at locations of heat sources as per the loading cycle.

3.2 Numerical Thermal Investigations on CI and SREG CNC Lathe

A 3D Solid model of CNC lathe has been used for performing transient thermal finite element analysis (FEA) at 20 °C and 40 °C environmental temperatures for CNC lathe with CI and SREG beds.

Figs. 10a and b represent 3D meshed models of the lathe with SREG bed and lathe with CI bed, respectively. Other than the bed, which used the tetrahedron mesh method, the remaining structures used the hex dominant mesh method. A mesh convergence analysis was conducted to establish the optimal mesh size for the finite element model. The study concluded that a mesh size of 10 mm was sufficient to produce accurate results and was therefore selected as the refined mesh size to ensure the reliability of the model. During analysis, calculated heat values were provided at the heat source locations in FE model. Convection (free air circulation) has been applied at the exposed boundaries. Figs. 10c and e depict the temperature distribution, Fig. 10d and f depicts the deformation under idle running of the cross-feed drive for lathe with CI and SREG beds at 20 ºC, ETVC condition. The differences in temperature of various structures are responsible for deformation. The cumulative deformation of all

Table 3. *Temperature comparison at sensor locations: experimental vs. numerical results*

	Sensor location	Lathe with CI bed at 20 ºC			Lathe with SREG bed at 20 ºC			Lathe with CI bed at 40 ºC			Lathe with SREG bed at 40 ºC		
		Exp.	FEA	% dev	Exp.	FEA	% dev	Exp.	FEA	% dev	Exp.	FEA	% dev
T 1	Ambient temperature	20	20	0	20	20	0	40	40	0	40	40	0
T 2	Top right LM block	24	25	4.2	26	27	3.8	43.5	46	1.2	46	48	4.3
T 3	Drive motor	29	29.2	0.6	32	33.3	4.1	48	51	6.2	49	52	6.1
T 4	Bed centre	23	22.5	2.2	22	21.5	2.3	43.5	43	1.2	42	41.5	1.2
T 5	Ball screw housing	24	25	4.2	25	26	4	44	45	2.3	44	45	2.3
T 6	Below turret	22	24	9.1	24	24.5	2.1	42	45	2.4	43.5	45.5	4.6

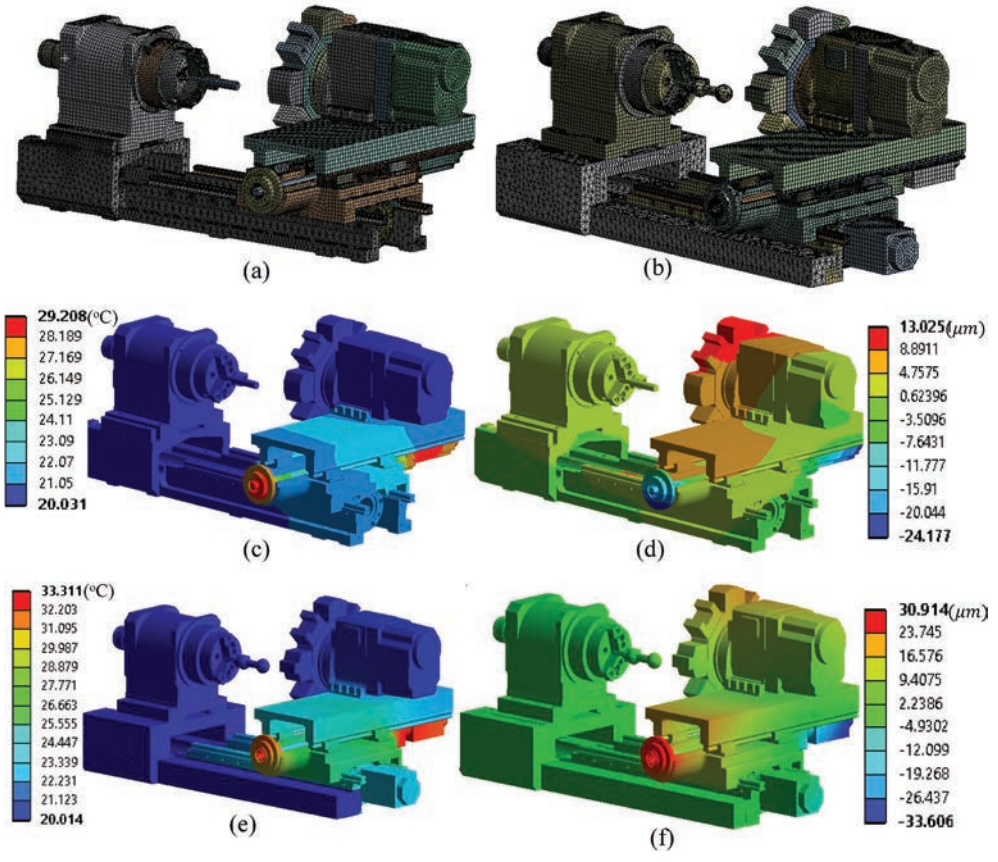

Fig. 10. *a) 3D mesh model of lathe with CI bed, b) 3D mesh model of lathe with SREG bed, c) temperature distribution in lathe with CI bed, d) deformation of the lathe with CI, e) temperature distribution of lathe with SREG bed, and f) deformation of lathe with SREG bed (under cross feed-drive idle running at 20 °C)*

Table 4. *Deformation comparison at sensor locations: experimental vs. numerical results*

Chamber temperature [°C]	Deformation measurement location	Deformation in lathe with CI bed [μm]			Deformation in lathe with SREG bed [μm]		
		Exp.	FEA	Deviation [%]	Exp.	FEA	Deviation [%]
20	TCP	8.8	9.5	7.9	14.8	16	8.1
40	TCP	9	9.4	4.5	17	17.2	3.4

structures is responsible for deformation at the TCP. Lead screws of both longitudinal and cross feed drives have significant temperature rises since they are nearer to the heat sources. The rise in temperature in all structures except the bed in the lathe with SREG bed is higher than the lathe with CI bed.

The effect of resistance causes a temperature rise in all locations, but in the case of the SREG bed, the temperature is less because of its lower thermal conductivity Although there is not much temperature rise at TCP, the deformation at various structures causes a considerable deformation at TCP. The major structures contributing to TCP deformation are saddle, cross slide, bearing hub, bearings, cross feed drive guideways, and turret. The temperature obtained from the different sensor locations in the experiment and temperature from same locations obtained from FEA are compared in Table 3. Deformation (x-axis growth at TCP) from experiments and FEA are compared in Table 4 Results from the FE analysis and experiments have been consolidated in Tables 3 and 4

There is a good correlation between the results, and the numerical model developed is deemed validated. The validated simulation FEM model can be used for further analysis. The temperature and deformation in the lathe with CI bed and SREG bed from the simulations results are depicted in Fig. 10. Below the cross-feed drive bearing hub, saddle, structures in LF and the SREG bed are stationary.

Structures above the cross-feed drive (i.e., cross rail, turret, etc.) are subjected to motion.

These moving structures dissipate more heat due to self-forced convection. Therefore, the surface temperature of the top structure is less due to more heat dissipation. The temperature in the structures below the cross-feed drive is higher due to more heat conduction from nearby heat sources and less heat dissipation from these stationary structures. Even though the bottom structures experience higher temperature rise, they are constrained from expanding; the higher thermal growth of the top structures can be attributed to their free expansion at the top.

The transient state temperature and the thermal expansion from simulations at different locations are depicted in the Fig. 11 The total heat generated at the left and right bearings is the same but for the temperature of the right bearing is much higher than that of the left bearings because the right bearing is near the motor.

From Fig. 11 it is observed that the temperatures of the bed and steel reinforcement are not continuous and there are temperature drops due to thermal contact

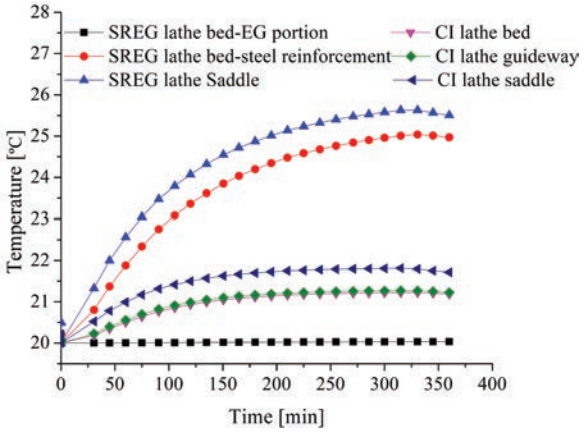

Fig. 11. *Temperature profile of structures in lathe with CI bed and SREG bed at 20 °C*

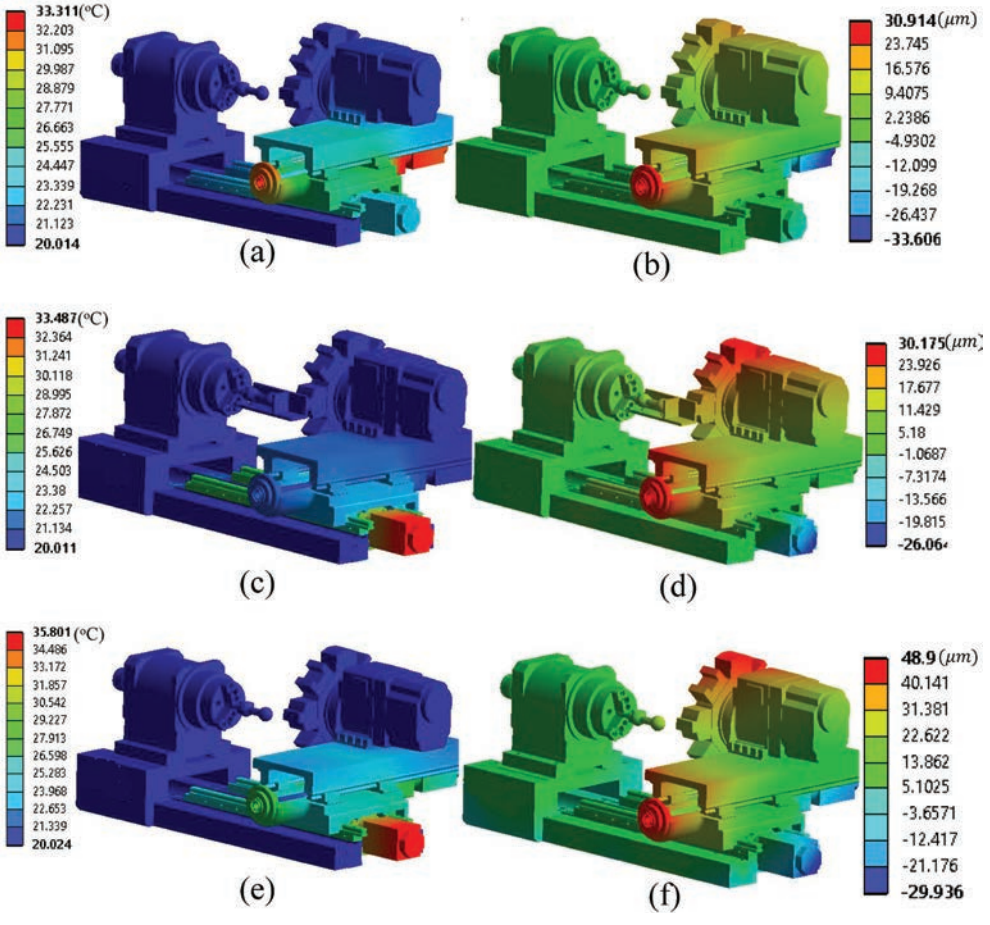

Fig. 12. *Temperature distribution in lathe with SREG bed under 20 °C a) -Case-1, c) -Case-2, and e) Case-3; Deformation plot of lathe with SREG bed under 20 °C ETVC b) Case-1, d) Case-2, and f) Case-3*

resistance. This can be attributed the high thermal contact resistance, which can also be referred to as low thermal contact conductance between steel reinforcement and EG. The motor deforms along the negative direction since it is exposed to convection and is free to expand in other directions, overhanging due to self-weight. Each of the two transits per period (one while moving downwards, one while moving upwards) leads to an increase in temperature, followed by a more gradual decrease due to heat diffusion.

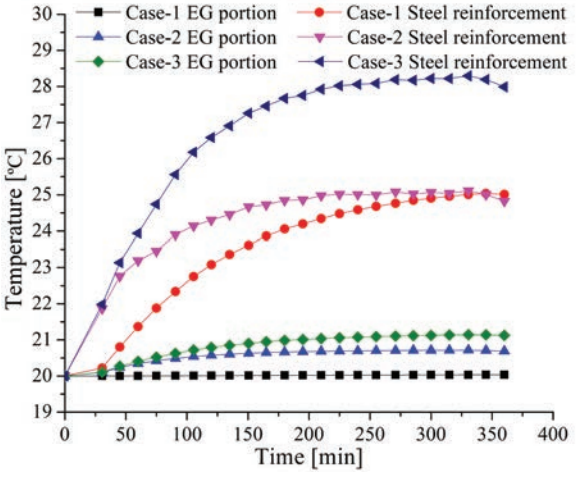

Fig. 13. *Transient temperature profile for EG and steel reinforcement in Case-1, Case-2 and Case-3*

Motor temperatures in the lathe with SREG bed are 3 ºC higher than the temperature at the same location in the lathe with CI bed. The steel reinforcement and EG structures are bonded together during fabrication, the heat flow from the top structures to the bed is not possible due to the difference in thermal characteristics of both materials. Consequently, a large temperature difference in bed and reinforcement has been observed. In the SREG bed, the EG portion and steel reinforcement are bonded together, and the reinforcement is provided to the bottom end of the bed. The temperature rise and expansion of EG in SREG bed are low, but it can be seen from the simulation result that the deformation of the EG is more than that of the CI bed which is due to expansion of corresponding bonded steel reinforcement.

4 NUMERICAL SIMULATIONS UNDER IDLE RUNNING OF LONGITUDINAL FEED DRIVE AND BOTH FEED DRIVES

A combination of machining operations associated with feed and depth of cut will be responsible for a moment of both longitudinal and cross feed drives.

Therefore, the validated numerical model is used to analyse the thermal behaviour of the lathe with SREG bed under idle conditions of the longitudinal feed drive (Case-2) and both longitudinal and cross feed drives (Case-3). From temperatures and deformation of structures as shown in Fig. 12, it is clear that there is a more heat accumulation in steel reinforcement, which lead to higher thermal error in Case-2 and Case-3 as compared to Case-1. In Case-1, the heat generated in the cross-feed drive flows towards the structures above as well as below the drive, thus resulting in gradual increase in temperature of the steel reinforcement. In Case-2, since the heat sources are nearer to the SREG bed, due to more accumulation of heat in one side heat can flow from bottom to top. Therefore, a higher slope exists in the temperature profile of steel reinforcement at the beginning, as shown in Fig. 13. Similarly, in Case-3, one-sided heat flow from bottom to the top exists but with the same self-forced convection area as in Case-2.

From Fig. 13, it can be noted that the temperature of steel reinforcement in Case-3 is higher than that in Case-1 and Case-2. Idle running of LF will lead to more heat accumulation in the steel reinforcement than in Case-1, but after three hours, the temperature has been found to attain a steady state. No significant temperature rise was observed in EG in all the cases. Simultaneous idle running of both CF and LF has been found to result in a thermal error of 33 µm which is 1.4 times higher than the thermal error in Case-2, and 1.9 times higher than that in Case-1. A similar trend has been observed in simulation results of feed drive with SREG bed at 40 ºC. From temperatures and deformation of structures, it is clear that there is more heat accumulation in steel reinforcement, which leads to higher thermal error in Case-2 and Case-3 as compared to Case-1.

5 CONCLUSIONS

Steel-reinforced epoxy granite structures have gained popularity due to their high damping characteristics and stiffness that is comparable or superior to that offered by CI structures. A systematic approach for thermal analysis of a CNC lathe with CI and SREG bed in closed ETVC conditions at 20 ºC and 40 ºC is presented in this article. The results reveal that the lathe with SREG bed exhibits a thermal error which is 1.68 times that of the lathe with CI bed at 20 ºC and 1.8 times at 40 ºC ETVC conditions. Furthermore, a thermo-mechanical FE model of the machine was developed. There was a high level of agreement when

the measured and simulated results were compared. Thermal analysis of the CNC lathe with the SREG bed reveals that it is more susceptible to thermal error than cast iron machines due to the accumulation of heat in steel reinforcement, which can be attributed to the low thermal conductivity of the surrounding epoxy granite portion. As a result, the thermal deformation of the steel structure in the bed is larger, and thus leads to higher thermal error. Simulation results revel that idle running of LF develop 13 times than thermal error in idle running of CF. Idle running of both CF and LF develop 19 and 14 times than thermal error under idle running of CF and LF, respectively. This research initiative will make it feasible to apply strategies for thermal error reduction to machine tools with SREG structures.

6 ACKNOWLEDGMENTS

The authors acknowledge M/s Galaxy Machinery, India, Pvt Ltd, for the support and technical contributions. Authors' sincere thanks to AICTE-New Delhi, for providing fellowship through NDF program (National Doctoral Fellowship). The authors are sincerely thankful to PSG College of Technology-Coimbatore, for providing constant support in this research work. The authors wish to acknowledge the Advanced Machine Tool Testing Facility (AMTTF) for providing a thermal chamber to perform experiments.

7 FUNDING

The authors gratefully acknowledge the financial support for this research work by the Office of the Principal Scientific Adviser to the Government of India [Project sanction no. F.No.: Prn.SA/DRDP/MT/2001(G)].

8 REFERENCES

[1] Ni, Y. Liu, X., Zhang, B., Zhang, Z., Li, J. (2018). Geometric error measurement and identification for rotational axes of a five-axis CNC machine tool. *Strojniški vestnik - Journal of Mechanical Engineering*, vol. 64, no. 5, p. 290-302, **DOI:10.5545/sv-jme.2017.4581**.

[2] Selvakumar, M., Venugopal, P.R., Velayudhan, G. (2022). Optimization of a tuned mass damper location for enhanced chatter suppression in thin-wall milling. *Strojniški vestnik - Journal of Mechanical Engineering*, vol. 68, no. 5, p. 339-349, **DOI:10.5545/sv-jme.2022.4**.

[3] Kępczak, N., Pawłowski, W., Kaczmarek, L. (2015). Cast iron and mineral cast applied for machine tool bed - dynamic behavior analysis. *Archives of Metallurgy and Materials*, vol. 60, no. 2, p. 1023-1029, **DOI:10.1515/amm-2015-0254**.

[4] Saljé, E., Gerloff, H., Meyer, J. (1988). Comparison of machine tool elements made of polymer concrete and cast iron. *CIRP Annals*, vol. 37, no. 1, p. 381-384, **DOI:10.1016/S0007-8506(07)61659-X**.

[5] Bedi, R., Chandra, R.. Singh, S.P. (2013). Mechanical properties of polymer concrete. *Journal of Composites*, vol. 2013, art. ID 948745, **DOI:10.1155/2013/948745**.

[6] Haddad, H., al Kobaisi, M. (2012). Optimization of the polymer concrete used for manufacturing bases for precision tool machines. *Composites Part B: Engineering*, vol. 43, no. 8, p. 3061-3068, **DOI:10.1016/j.compositesb.2012.05.003**.

[7] Mula V.R., Thyla, P.R., Mahendrakumar, N., Praveena, K. (2021). Selection of resin and aggregates for particulate polymer concrete machine tool structures-A review. *Materials Today: Proceedings*, vol. 46, p. 8621-8628, **DOI:10.1016/j.matpr.2021.03.595**.

[8] Mahendrakumar, N., Thyla, P.R., Mohanram, P.V., Kumaran, C.R., Jayachandresh, J. (2019). Study on static and dynamic characteristics of nettle-polyester composite micro lathe bed. *Proceedings of the Institution of Mechanical Engineers, Part L: Journal of Materials: Design and Applications*, vol. 233, no. 2, p. 141-155, **DOI:10.1177/1464420716663568**.

[9] Möhring, H.-C., Brecher, C., Abele, E., Fleischer, J., Bleicher, F. (2015). Materials in machine tool structures. *CIRP Annals*, vol. 64, no. 2, p. 725-748, **DOI:10.1016/j.cirp.2015.05.005**.

[10] Mahdi, F., Abbas, H., Khan, A.A. (2013). Flexural, shear and bond strength of polymer concrete utilizing recycled resin obtained from post consumer PET bottles. *Construction and Building Materials*, vol. 44, p. 798-811, **DOI:10.1016/j.conbuildmat.2013.03.081**.

[11] Ferdous, W., Manalo, A., Wong, H.S., Abousnina, R., AlAjarmeh, O.S., Zhuge, Y., Schubel, P. (2020). Optimal design for epoxy polymer concrete based on mechanical properties and durability aspects. *Construction and Building Materials*, vol. 232, **DOI:10.1016/j.conbuildmat.2019.117229**.

[12] Bajgirani, A.G., Moghadam, S., Arbab, A., Vatankhah, H. (2016). The mechanical characteristics of polymer concrete using polyester resin. *Journal of Fundamental and Applied Sciences*, vol. 8, no. 3, p. 571-578, **DOI:10.4314/jfas.v8i3s.238**.

[13] D'Mello, J., D'Souza, A.G., Gowda, S.H., Pinto, D. (2019). Experimental investigation of compression, flexural strength and damping behaviour of granite particulate epoxy matrix composite. *AIP Conference Proceedings*, vol. 2080, **DOI:10.1063/1.5092895**.

[14] Selvakumar, A., Mohanram, P. (2013). Evaluation of mechanical characteristics for mineral cast materials with varying resin content. *Journal of Engineering and Technology*, vol. 3, no. 1, p. 52, **DOI:10.4103/0976-8580.107102**.

[15] Xu, P., Yu, Yh (2008). Research on steel-fibber polymer concrete machine tool structure. *Journal of Coal Science and Engineering (China)*, vol. 14, p. 689-692, **DOI:10.1007/s12404-008-0444-z**.

[16] Suh, J.D., D. G. Lee, D.G. (2008). Design and manufacture of hybrid polymer concrete bed for high-speed CNC milling

machine. *International Journal of Mechanics and Materials in Design*, vol. 4, p. 113-121, **DOI:10.1007/s10999-007-9033-3**.

[17] Chinnuraj S.,Thyla, P.R., Elango, S., Venugopal, P.R., Mohanram, P.V., Nataraj, M., Mohanraj, S., Manojkumar, K.N., Ayyasamy, S. (2020). Static and dynamic behavior of steel-reinforced epoxy granite CNC lathe bed using finite element analysis. *Proceedings of the Institution of Mechanical Engineers, Part L: Journal of Materials: Design and Applications*, vol. 234, no. 4, p. 595-609, **DOI:10.1177/1464420720904606**.

[18] Mayr, J., Jedrzejewski, J., Uhlmann, E., Donmez, M.A., Knapp, W., Härtig, F., Wendt, K., Moriwaki, T., Shore, P., Schmitt, R., Brecher, C., Würz, T., Wegener, K. (2012). Thermal issues in machine tools. *CIRP Annals*, vol. 61, no. 2, p. 771-791, **DOI:10.1016/j.cirp.2012.05.008**.

[19] Selvakumar, A., Mohanram, P.V. (2013). Evaluation of effective thermal conductivity for mineral cast structural materials using steady-state and transient methods. *Journal of Testing and Evaluation*, vol. 41, no. 4, p. 1-7, **DOI:10.1520/JTE20120216**.

[20] Bryan, J. (1990). International status of thermal error research. *CIRP Annals*, vol. 39, no. 2, p. 645-656, **DOI:10.1016/S0007-8506(07)63001-7**.

[21] Prabhu Raja, V., Thirumalaimuthukumaran, M., Thyla, P.R., Shyam Kirthi, S. (2019). A strategy for minimization of thermal error in headstock assembly of CNC lathe. *Machining Science and Technology*, vol. 23, no. 1, p. 57-78, **DOI:10.1080/10910344.2018.1466328**.

[22] Suh, J.D., Lee, D.G. (2004). Thermal characteristics of composite sandwich structures for machine tool moving body applications. *Composite Structure*, vol. 66, no. 1-4, p. 429-438, **DOI:10.1016/j.compstruct.2004.04.065**.

[23] Tanabe, I., Takada, K. (1994). Thermal deformation of machine tool structures using resin concrete : Thermal behaviour of concrete bed of machine tool in fluctuating ambient temperature," *JSME International Journal. Ser. C, Dynamics, Control, Robotics, Design and Manufacturing*, vol. 37, no. 2, p. 384-389, **DOI:10.1299/jsmec1993.37.384**.

[24] Neugebauer, R., Neugebauer, R., Drossel, W.-G., Ihlenfeldt, S., Al, E. (2012). Inherent thermal error compensation of machine tool structures with grated meneral casting, p. Art. 12053, 5, **https://publica.fraunhofer.de/handle/publica/377838**.

[25] Weidlich, D., Nestmann, S. (2001). Kompaktführungen an Mineralgussgestellen. *Werkstatt und Betrieb*, no. 7-8, p. 120-123, **https://publica.fraunhofer.de/handle/publica/199233**

[26] Bahrami, M., Yovanovich, M.M., Marotta, E.E. (2006). Thermal joint resistance of polymer-metal rough interfaces. *Journal of Electronic Packaging, Transactions of the ASME*, vol. 128, no. 1, p. 23-28, **DOI:10.1115/1.2159005**.

[27] Dunaj, P., Powałka, B., Berczyński, S., Chodźko, M., Okulik, T. (2020). Increasing lathe machining stability by using a composite steel-polymer concrete frame. *CIRP Journal of Manufacturing Science and Technology*, vol. 31, p. 1-13, **DOI:10.1016/j.cirpj.2020.09.009**.

[28] Dunaj, P., Dolata, M., Tomaszewski, J., Majda, P. (2022). Static stiffness design of vertical lathe with steel-polymer concrete frame. *International Journal of Advanced Manufacturing Technology*, vol. 121, no. 1-2, p. 1149-1160, **DOI:10.1007/s00170-022-09391-x**.

[29] Venugopal, P.R.,Dhanabal. P., Thyla, P.R., Mohanraj, S., Nataraj, M., Ramu, M, Sonawane, H. (2020). Design and analysis of epoxy granite vertical machining centre base for improved static and dynamic characteristics. *Proceedings of the Institution of Mechanical Engineers, Part L: Journal of Materials: Design and Applications*, vol. 234, no. 3, p. 481-495, **DOI:10.1177/1464420719890892**.

[30] Venugopal, P.R., Kalayarasan, M., Thyla, P.R., Mohanraj, P.V., Nataraj, M., Mohanraj, S., Sonawane.H. (2019). Structural investigation of steel-reinforced epoxy granite machine tool column by finite element analysis. *Proceedings of the Institution of Mechanical Engineers, Part L: Journal of Materials: Design and Applications*, vol. 233, no. 11, p. 2267-2279, **DOI:10.1177/1464420719840592**.

[31] Xu, P., Yu, Y.-H. (2008). Research on steel-fibber polymer concrete machine tool structure. *Journal of Coal Science and Engineering (China)*, vol. 14, p. 689-692, **DOI:10.1007/s12404-008-0444-z**.

[32] Chen, T.-C., Chen, Y.-J. Hung, M.-H., Hung, J.-P. (2016). Design analysis of machine tool structure with artificial granite material. *Advances in Mechanical Engineering*, vol. 8, no. 7, p. 1-14, **DOI:10.1177/1687814016656533**.

[33] Shi, H., Ma, C., Yang, J., Zhao, L., Mei, X., Gong, G. (2015). Investigation into effect of thermal expansion on thermally induced error of ball screw feed drive system of precision machine tools. *International Journal of Machine Tools and Manufacture*, vol. 97, p. 60-71, **DOI:10.1016/j.ijmachtools.2015.07.003**.

[34] ISO 230-3:2007. *Test Code for Machine Tools Part 3: Determination of Thermal Effects*. International Organisation for Standardization, Geneva.

[35] Ruijun, L., Wenhua, Y., Zhang, H.H., Qifan, Y. (2012). The thermal error optimization models for CNC machine tools. *International Journal of Advanced Manufacturing Technology*, vol. 63, p. 1167-1176, **DOI:10.1007/s00170-012-3978-6**.

[36] Xu, Z.Z., Liu, X.J., Kim, H.K., Shin, J.H., Lyu, S.K. (2011). Thermal error forecast and performance evaluation for an air-cooling ball screw system. *International Journal of Machine Tools and Manufacture*, vol. 51, no. 7-8, p. 605-611, **DOI:10.1016/j.ijmachtools.2011.04.001**.

[37] Li, Y., Zhao, W., Wu, W., Lu, B., Chen, Y. (2014). Thermal error modeling of the spindle based on multiple variables for the precision machine tool. *International Journal of Advanced Manufacturing Technology*, vol. 72, p. 1415-1427, **DOI:10.1007/s00170-014-5744-4**.

[38] Babu, S.R., Raja, V.P., Thyla, P.R., Thirumalaimuthukumaran, M. (2014). Prediction of transient thermo-mechanical behavior of the headstock assembly of a CNC lathe. *International Journal of Advanced Manufacturing Technology*, vol. 74, no. 1-4, p. 17-24, **DOI:10.1007/s00170-014-5916-2**.

[39] Min, X., Jiang, S. (2011). A thermal model of a ball screw feed drive system for a machine tool. *Proceedings of the Institution of Mechanical Engineers, Part C: Journal of Mechanical Engineering Science*, vol. 225, no. 1, pp. 186-193, **DOI:10.1177/09544062JMES2148**.

Strojniški vestnik - Journal of Mechanical Engineering 69(2023)3-4, 185-195
DOI:10.5545/sv-jme.2022.359
Original Scientific Paper
Received for review: 2022-10-05
Received revised form: 2022-12-05
Accepted for publication: 2023-02-10

Design of a Self-Folding Composite Variable-Diameter Wheel Structure based on 4D Printing Technology

Wencai Zhang[1] – Zhenghao Ge[1] – Duanling Li[2,*]

[1] Shaanxi University of Science and Technology, College of Mechanical and Electrical Engineering, China
[2] Beijing University of Posts and Telecommunications, School of Automation, China

The conventional variable-diameter wheel's complex control system and structure seriously affect its mobility and dependability in unstructured terrain. Based on 4-dimensional (4D) printing technology, this work proposes a self-folding composite variable-diameter wheel consisting of a self-folding structure and an outer hub that can self-adjust the wheel diameter under thermal stimulation, avoiding the drawbacks of conventional structures. The structure integrates the control system and variable-diameter mechanical structure using 4D printing. The design and construction of the self-folding structures are introduced, and the mathematical model and design parameters for self-folding motion are obtained using kinematic analysis. Based on the above research and material properties analysis, a programmable morphing structural design and morphing influence investigation based on manufacturing parameters are carried out for the self-folding rod that controls the contraction of this structure. The digital model and prototype have been developed to verify the feasibility of the design and the correctness of the theoretical analysis and to realize the self-adjusting wheel diameter under thermal stimulation.

Keywords: self-folding, smart materials, 4D printing, variable-diameter wheel

Highlights

- *A conventional variable-diameter wheel's complex structure is simplified using 4D printing technology to integrate the control system and the variable-diameter mechanical structure.*
- *A conventional variable-diameter wheel's complex control system is simplified using smart materials to control wheel diameter changes under external thermal stimulation.*
- *Conventional mechanical structure design, smart materials, and fabrication are integrated via 4D printing. The single mechanical structure design extends to a programmable morphing structure design.*

0 INTRODUCTION

Robots have been increasingly used in aerospace, industrial production, geological exploration, and other fields. When carrying out the design of robots (except fixed-position robots), the traveling mechanism, as the crucial system for performing tasks, is mainly wheeled traveling device, legged traveling device, crawler traveling device, or composite traveling device [1] to [3]. Wheeled traveling devices are widely used because of their adaptability, reliable operation, and easy control. However, with the expanding scope of human research, engineering, and habitat, complex and harsh application scenarios require wheeled mechanisms with enhanced environmental adaptability [4]. Therefore, the variable-diameter wheel, which changes the diameter to cope with different terrain changes and improves the passing capability, has been created [5] to [7]. Commonly variable-diameter wheels can be divided according to their deformation modes: inflatable and mechanical [8] to [9]. Among these, the mechanical type gained the attention of many scholars because of its simple design concept, high stiffness, and good movement efficiency [10] to [12]. Mechanical variable-diameter wheels typically necessitate integrating both the control system and the variable-diameter mechanical structure to switch between different environments to improve passing capability. However, these mechanical structures are often less reliable and more difficult to control due to their complex structures and control systems [13] to [15]. As a result, variable-diameter wheels must retain their original powerful passing capability while maintaining a simple structure with low control complexity and improved reliability. This urgent issue must be addressed.

The emergence of smart materials and 4-dimensional (4D) printing technology provides a new idea for the design of variable-diameter wheels. By changing smart materials' distribution and geometric parameters, combining 4D printing technology with conventional mechanical structure design methods creates a structure with a controlled self-driven deformation or transformation function under predetermined structural excitation conditions. The single mechanical structure design extends to a programmable morphing structure design. Applying this new idea will effectively circumvent the defects of the conventional variable-diameter wheel. This work's main contributions are listed as follows:

*Corr. Author's Address: Shaanxi University of Science & Technology, Weiyang District, Xi'an, China, liduanlini@163.com

1 Based on 4D printing technology, this work proposes a novel self-folding composite variable-diameter wheel structure. The structure comprises a self-folding structure and an outer hub.
2. Based on mechanical structure design methods and principles, kinematic analysis introduces to obtain a mathematical model of self-folding motion.
3. The structural design based on programmable morphing and research of morphing influence based on manufacturing parameters is conducted for the self-folding rod to control the contraction of this structure.
4 Constructed simulations and experiments achieve the drivable self-adjustment of the wheel size ratio under predetermined thermal stimuli.

1 DESIGN OF A SELF-FOLDING COMPOSITE VARIABLE-DIAMETER WHEEL STRUCTURE

This section consists of three parts. First, it gives the general design concept and operation mode of the self-folding composite variable-diameter wheel structure. Second, it introduces the composition of the core self-folding structure that attains the wheel diameter change function. Finally, there are discussions on the design differences between self-folding and conventional mechanical structures.

A self-folding composite variable-diameter wheel structure with thermally stimulated deformation response property is designed (see Fig. 1a). The structure consists of a self-folding structure (see Fig. 1c) and an outer hub (see Fig. 1b), prepared with a high-precision 3D printer.

Usually ($T<T_g$), the self-folding structure unfolds and works as a moving wheel. At that moment, the wheel diameter reaches its maximum value. Applying an external thermal stimulus ($T>T_g$), the self-folding structure contracts along the track and into the outer hub and uses the outer hub as a moving wheel. At this moment, the wheel diameter reaches its minimum value (see Fig. 1d).

The response of the self-folding structure to external thermal stimulus is crucial to attaining the change in wheel diameter. For this purpose, the self-folding structure consisting of a self-folding rod and an angulated scissor rod is designed (see Fig. 2). When an external thermal stimulus is applied, the self-folding rod changed from an unfolded state to a folded state according to the pre-programmed design and drives the angulated scissor rod to contract the entire structure during the traveling process (see Fig. 1d).

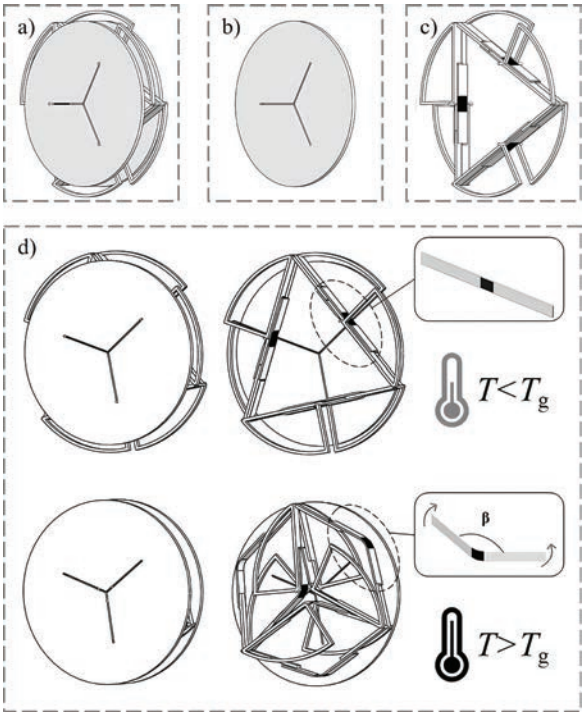

Fig. 1. *Schematic; a) self-folding composite variable-diameter wheel structure, b) outer hub, c) self-folding structure, and d) structural contraction process*

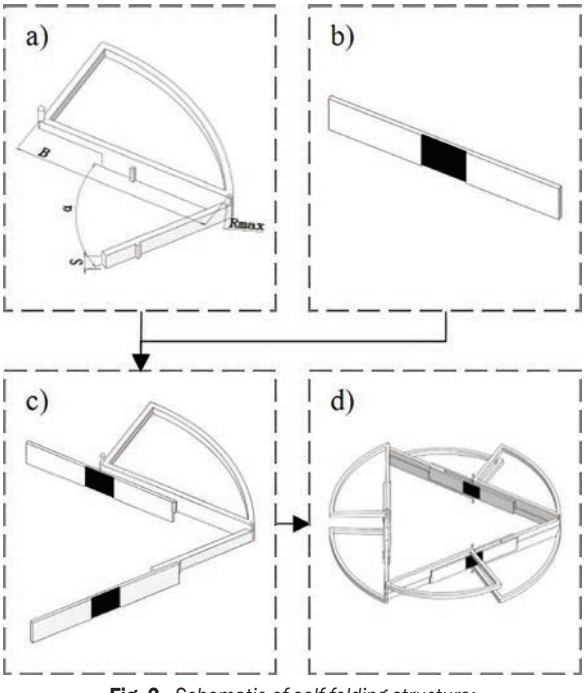

Fig. 2. *Schematic of self-folding structure; a) angulated scissor rod, b) self-folding rod, c) assembly structure, and d) self-folding structure*

Because of the distinct features of controlled structural transformation in response to predetermined

thermal stimuli, the critical structural design parameters and mathematical model required for deformation control need to be deduced in order to investigate the deformation control relationship between the angulated scissor rod and the self-folding rod. However, the conventional mechanical structure design method cannot be used as a single basis for this research, which aims to lay part of the foundation for the next advancement of conventional structural design to programmable morphing structural design.

2 ANALYSES OF SELF-FOLDING STRUCTURE

This section contains two subsections. First, there are analyses of the self-folding structure's design methods and structural principles. Second, kinematic analysis is carried out to obtain the equation and structural design parameters for drivable self-folding motion.

2.1 Design Method and Structural Principle

Two angulated scissor rods (*dp* and *ba)* and two self-folding rods (*tpq* and *uaj*) are extracted from the self-folding composite variable-diameter wheel structure to establish a rectangular coordinate system (see Fig. 3a).

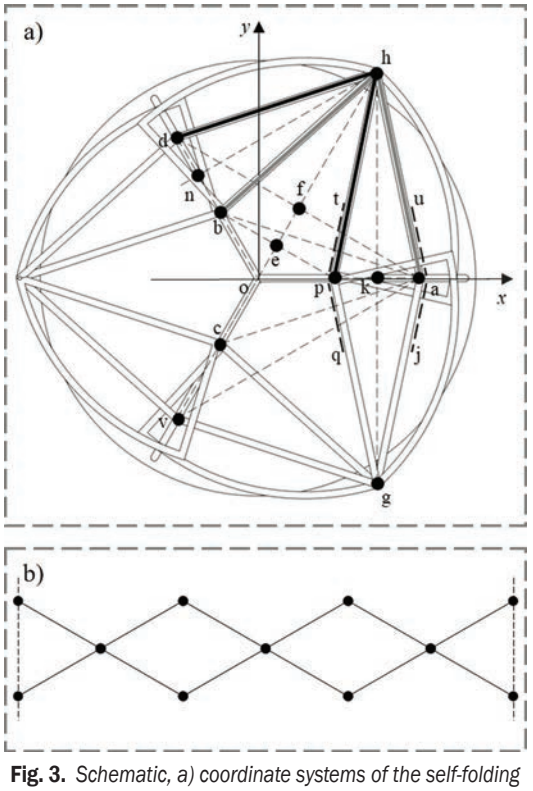

Fig. 3. *Schematic, a) coordinate systems of the self-folding structure, b) structured expansion kinetic chain*

The perpendicular lines are made through point *h* to line *b* and the *x*-axis, with the intersection points *n* and *k*. The top angle α and the length *B* of *dp* and *ba* are manufacturing parameters (see Fig. 2a) whose values are constants. We can prove the following:

$$\because \angle dpa = \angle bha = \alpha$$
$$\because \angle bpa \text{ is the common angle}$$
$$\therefore \angle dpb = \angle dpa - \angle bpa = \angle bha - \angle bpa = \angle pha$$
$$\because dp = ba = ph = ah$$
$$\therefore \triangle dpb \text{ and } \triangle pha \text{ are congruent isosceles triangles}$$

$$\because \text{The lines } hn \text{ and } kh \text{ are the perpendicular bisector of } \triangle dpb \text{ and } \triangle pha$$
$$\therefore \triangle dpn = \triangle hpb = \triangle phk = \triangle kha$$

$$\because \angle dpn = \angle hpb = \angle phk = \angle kha$$
$$\therefore 2\angle hpb + \angle bpa = 2\angle phk + \angle bhp = \alpha$$
$$\therefore \angle hpb + \angle bpa + \angle phk = \alpha$$
$$\because \angle ohp + \angle okh + \angle hko + \angle nok = 2\pi$$
$$\because \angle ohp = \angle okh = \pi/2$$
$$\therefore \angle nok = \angle doa = \pi - \alpha$$

Let α be

$$\alpha = \pi - \frac{2\pi}{m}, \quad (m = k + 3 \wedge k \in Z), \tag{1}$$

where *m* is the number of rod groups required to construct the self-folding structure, there are 2*m* self-folding rods and 2*m* angulated scissor rods.

The above proof concludes that the angle in a circular segment (such as $\angle dca$) corresponding to each group of angulated scissor rods is always constant. Its value is only related to the number of rod groups m. The value of m also determines the top angle α of the angulated scissor rods. Thus, using m rod groups, a ring-shaped self-folding structure can be constructed. The specific construction method is as follows (see Figs. 2 and 3): hinges connect the angulated scissor rods at the top angles *h* and *g*. The self-folding rods are bonded at the limit blocks *t*, *v*, *u*, and *j*. By analogy, a self-folding structure can be constructed consisting of m rod groups. The purpose of the limit blocks is to prevent uneven force or collision interference between the self-folding rods and the angulated scissor rods due to the inaccurate positioning of the bond.

In this work, the value of *m* for the designed self-folding structure is set to 3. The structure is expanded into a plane kinetic chain along the line connecting point *p* and point *a* (see Fig. 3b). Applying the loop connectivity matrix (LCM) [16], we know that:

$$\mathbf{R}_{\mathbf{LCM}}=\begin{bmatrix}1 & 1 & 0 & 0\\ 0 & 1 & 1 & 0\\ 0 & 0 & \ddots & 1\\ 0 & 0 & 0 & m\end{bmatrix}, \tag{2}$$

Let F is the degree of freedom. According to Eq. (2):

$$F=1+1-1+1-1+1-1=1.$$

From the above calculations, we conclude that the self-folding structure has single degrees of freedom.

The previous paragraph analyses the self-folding structure's design methods and structural principles. On this basis, this structure's contraction change process is explained (see Fig. 4).

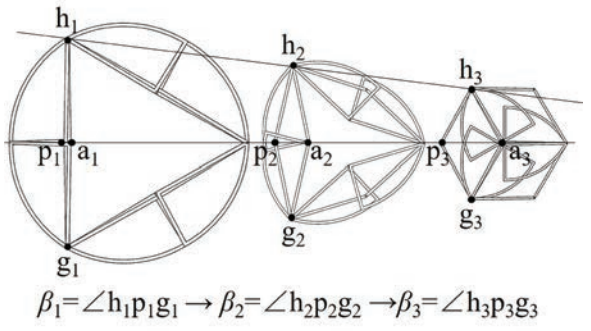

Fig. 4. *Contraction process of the self-folding structure*

The self-folding rod folded under external thermal stimulation, and the folding angle change process is $\beta_1 \rightarrow \beta_2 \rightarrow \beta_3$. The self-folding rod midpoint *p* and *a* move along the line *pa*, which drives the angulated scissor rod between the hinge point *h* along the path of the connecting line h_1h_3 movement. The diagonal *pa* changes throughout the process. One large and one small circle in different states are formed by connecting a series of diagonal endpoints *h* in the unfolded state to a series of diagonal endpoints *a* in the folded state, which obtains structural contraction changes.

2.2 Kinematic Analysis

The angles *hpg* and *hag* are defined as folding angle β (see Fig. 4). The angulated scissor rod length is defined as *B* (see Fig. 2a).

In the triangle *hda*, let angle *hpa* is the *Z*, the length of the line *ad* is (see Fig. 3):

$$ad=2B\cos\angle ahd=2B\cos\left(Z-\frac{\alpha}{2}\right). \tag{3}$$

In the triangle *da*,

$$ad^2=od^2+oa^2-2od\cdot oa\cdot\cos(\pi-\alpha). \tag{4}$$

When the folding angle reaches a minimum value, the structure is contracted. Let $R_{\min}$ be the minimum circumcircle radius. Let $\beta_{\min}$ be the minimum folding angle. In the triangle *da*, it can be seen that $R_{\min}$ is equal to *ao* and *od*, bringing Eq. (3) into Eq. (4); we know that:

$$ad^2=R_{\min}^2+R_{\min}^2-2R^2{}_{\min}\cos(\pi-\alpha),$$
$$ad=2B\cos\left(Z_{\min}-\frac{\alpha}{2}\right).$$

Let Eq. (3) equal Eq. (4), and we can solve the following:

$$4B^2\cos\left(Z_{\min}-\frac{\alpha}{2}\right)=2R^2{}_{\min}(1+\cos\alpha). \tag{5}$$

According to Eq. (5), we can solve the following:

$$R_{\min}=B\cos\left(Z_{\min}-\frac{\alpha}{2}\right)\cos^{-1}\frac{\alpha}{2}, \tag{6}$$

$$Z_{\min}=\arccos\left(\frac{R_{\min}}{B}\cos\frac{\alpha}{2}\right)+\frac{\alpha}{2}. \tag{7}$$

Combined with Fig. 4, it can be seen that R_{min} is equal to *B*. Bringing Eq. (7), we can solve the following:

$$Z_{\min}=\frac{\alpha}{2}+\frac{\alpha}{2}=\pi-\frac{2\pi}{m}, \tag{8}$$

$$\beta_{\min}=2Z_{\min}=2\pi-\frac{4\pi}{m}. \tag{9}$$

When the folding angle reaches a maximum value, the structure is unfolded. Let $R_{\max}$ be the maximum circumcircle radius. Let $\beta_{\max}$ be the maximum folding angle. In the triangle *oha*, it can be seen that $R_{\max}$ is equal to *oh*; we know that:

$$R_{\max}=B\sin^{-1}\left(Z_{\max}-\frac{\alpha}{2}\right). \tag{10}$$

Combined with Fig. 4, it can be seen that angle *haf* is equal to angle *foa*, and we can solve the following:

$$Z_{\max}-\frac{\alpha}{2}=\frac{\pi-\alpha}{2}=\frac{\pi}{2}. \tag{11}$$

$$\beta_{\max}=2Z_{\max}=\pi. \tag{12}$$

Let χ be the structural contraction ratio, bringing Eq. (6) and Eq. (10), and we can solve the following:

$$\chi = \frac{R_{\min}}{R_{\max}} = \sin\left(\frac{\pi}{m}\right). \quad (13)$$

From the above calculations, we conclude that the m value determines the structure's construction, contraction process, and contraction ratio. As a result, the crucial structural design parameter required for deformation control is m. Taking the structure with an m value equal to 3 as an example, the contraction ratio χ of this structure is about 0.866 and its folding angle β varies from 60 ° to 120 °.

3 PROGRAMMABLE MORPHING RESEARCH OF SELF-FOLDING RODS

In this section, we research the programmable morphing of the self-folding structure after obtaining the design method and structural principle. The self-folding rod is a component with an integrated motion actuator and driver. It is the core part that controls the contraction of the self-folding structure.

This section contains three subsections. First, it tests the thermo-mechanical properties of the materials required to manufacture the self-folding rod. Second, it researches programmable morphing based on various materials' structural design and thermo-mechanical properties. Finally, it researches the influence of folding morphing based on the adjustment of manufacturing parameters.

3.1 Characterization of Material Properties

The manufacturing and control of self-folding rods can utilize the thermo-mechanical properties of different materials. In addition, heat stimulation is used as a means of structure activation in this work. Therefore, material property tests are conducted to characterize the material's thermo-mechanical properties and provide a relevant basis for subsequent research.

Four commercial elastomer materials are selected, thermoplastic polyurethane (TPU) (Dake, Shenzhen, China), and one shape memory polymer material, polylactic acid (PLA) (Raise Premium, Shanghai, China). The dynamic thermo-mechanical properties of these five materials are analysed using a dynamic thermo-mechanical analyser (DMA-Q800, New Castle, United States), selected tensile mode. The practical test length of the PLA and TPU printed filaments is 10 mm, and the diameter is 1.75 mm. The test loading temperature range is 25 °C to 90 °C. The accuracy of the temperature loading is ±0.2 °C. The temperature rise rate is controlled by 2 °C/min during the test. The dynamic axial stretching rate is 1 Hz. The dynamic thermo-mechanical analyser (DMA) test results (see Fig. 5) included the changes in the storage modulus G and dissipation factor angle Tan δ with temperature T. The T_i, T_g, and T_h of PLA are 46 °C, 60.2 °C, and 73.3 °C, respectively. The G values for PLA corresponding to the three temperatures are 2849 MPa, 1328 MPa, and 6.73 MPa. The subscripts i, g, and h represent the beginning, transition, and end of PLA's glass transition phase. Similarly, the DMA test results for TPU show that the T_g of TPU is below room temperature, and G values of TPU decrease slowly with increasing temperature.

3.2 Structural Design Based on Programmable Morphing

The self-folding rod drives the whole structure to produce contraction by bending. Therefore, this section discusses how to program the self-folding rod to produce bending by structural design.

A self-folding rod structure based on thermal stimulus-response is designed. The structure is manufactured using a fused deposition modelling (FDM) dual-nozzle printer (Raise E2, Shanghai, China) utilizing TPU and PLA material (see Fig.

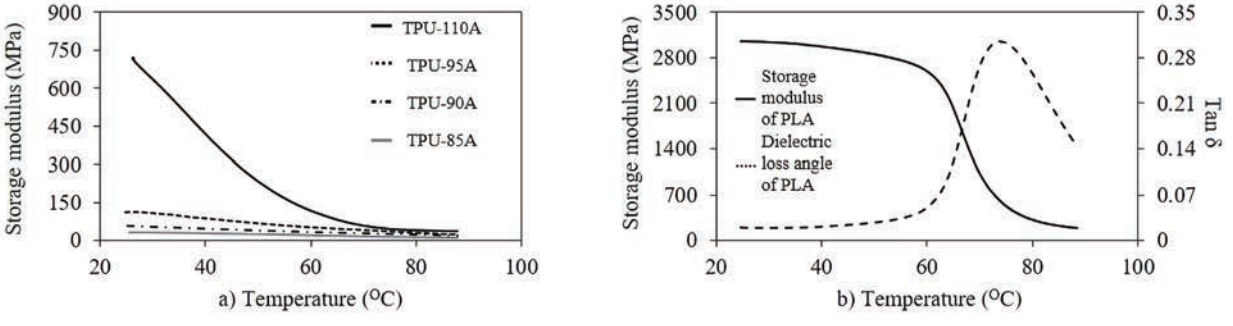

Fig. 5. *DMA test results, a) storage modulus of TPU, b) storage modulus and dissipation factor angle of PLA*

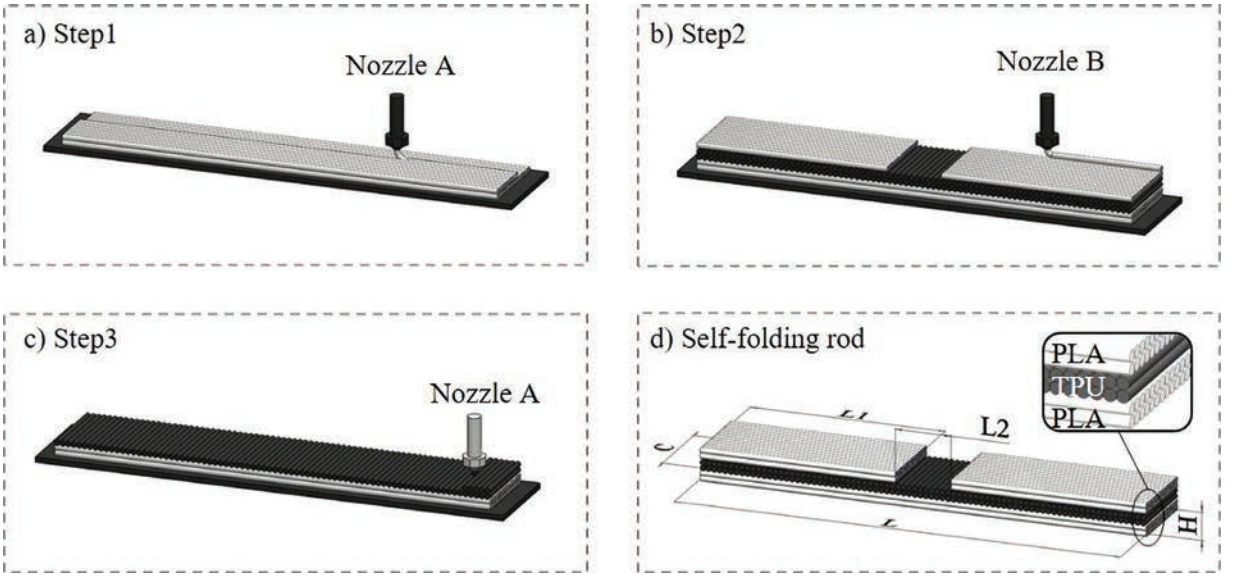

Fig. 6. *Schematic of the manufacturing process of the self-folding rod; a) nozzle A print the first layer, b) nozzle B prints the second layer, c) nozzle A print the second layer, and d) self-folding rod*

6. The structure consists of 6 layers, 4 of which are continuous and 2 of which are split. The separation layers are designed to control the deformed part's width and compensate for the edge bending generated by the PLA layer.

First, we explain the principle of the morphing produced by the self-folding rod. Heating and squeezing the PLA filament during the printing process cause the polymer chains to stretch and align in the direction of that path and subsequently generate stress. They are stored in the printed material due to the constraining effect of the printing platform or previous layer. They are fixed layer by layer as the printing process cools. When the PLA layers are removed from the printer and reheated above its glass transition temperature T_g, the PLA layer shortens along the printing direction and expands slightly along the other two directions. Thus, the PLA drives the structure to produce morphing.

Second, we explain how the structural design can program the self-folding rod to produce bending. PLA layers with unidirectional filling patterns exhibit anisotropic deformation behaviour, resulting in more significant anisotropic behaviours than PLA layers with multidirectional filling patterns [17] and [18]. For this reason, all PLA layers in this work are always printed in the same orientation. However, only single-layer PLA structures are used, which can produce unpredictable flexural-torsional deformations. The DMA test finds that the glass transition temperature of TPU is generally lower than room temperature. The TPU elastic modulus is relatively stable over the T_h temperature range from room temperature to PLA, and it is assumed that it cannot contract; it can only bend and slightly elongate. Using these properties, PLA and TPU are combined in layers to form a combination structure. TPU converts the unpredictable flex-torsion of PLA into bending. Although the TPU plays a restricted role in the structure, its filling patterns also affect the morphing. The experimental results reveal that when the filling patterns of the TPU layers are perpendicular to the PLA layers, and there is no separation layer, the structure exhibited the best bending (see Fig. 7).

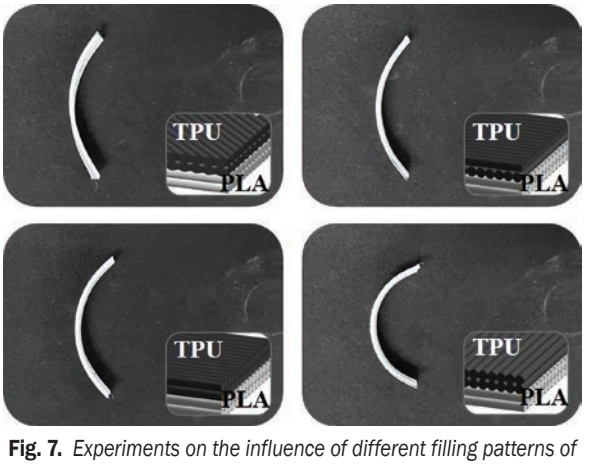

Fig. 7. *Experiments on the influence of different filling patterns of TPU layer on bending deformation*

3.3 Morphing Influence based on Manufacturing Parameters

After the self-folding rod bends by structural design to meet the required folding angle β and driving of the self-folding structure as much as possible, this section discusses the morphing influence of the self-folding rod under different manufacturing parameters. The previous discussion shows that releasing stored prestress in the PLA layer and the TPU layer's restriction controls the self-folding rod's bending. Therefore, if the morphing influence of the self-folding rod is obtained, it is necessary to research the effect of the restricted capability of the TPU or the prestress storage capability of the PLA on the change of the folding angle β.

First, the restricted capability of the TPU is discussed. Four self-folding rods are printed and experimented with using four TPU materials. Hot water is chosen as the activation medium for the experiments to ensure a uniform, accurate and fast heat application on the samples [21]. The glass transition temperature T_g of the PLA material selected from Fig. 5, and the printing speed are 30 mm/s. The temperature setting of the water bath device (LICHEN-HH4 Shanghai, China) is kept constant. All samples are kept in water for the experiments, and heating stops when they no longer exhibit visual signs of deformation. The printing parameters, sample size, and experimental parameters are shown in Table 2.

Experiments find that TPU materials with higher storage modulus are more resistant to structural bending. Therefore, the high storage modulus of the TPU material causes a weak self-folding rod drive and a large folding angle β (see Fig. 8). According to another experimental result in the literature [19] to [20], the lower the percentage of hard polymer segments supporting TPU materials, the more difficult it is to print them. After considering the printing quality and material properties, this work chose a single TPU-90A material to print the self-folding rod.

Table 2. *Self-folding rod of sample structure size, printing, and experimental parameters*

Structure size [mm]	H	C	$L2$	$L1$	L
	1.2	10	10	45	100
Printing parameters	Layer height [mm]				0.2
	Infill amount [%]				100
	Extrusion width [mm]				0.4
	Nozzle diameter [mm]				0.4
	Printing platform temperature [°C]				30
	PLA Printing temperature [°C]				235
	TPU Printing temperature [°C]				200
Experimental parameters	Activation medium				Water
	Water bath temperature [°C]				68
	Water bath time [s]				≥180

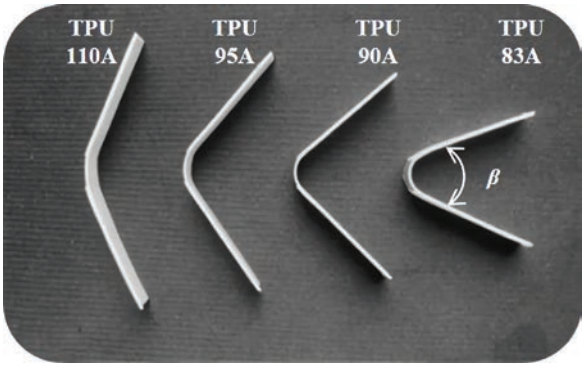

Fig. 8. *Experiment on the influence of TPU layer restriction capability on the change of folding angle β*

Second, the prestress storage capability of the PLA is discussed. The print speed adjustment causes different stretching of the PLA material during the extrusion process, resulting in different residual

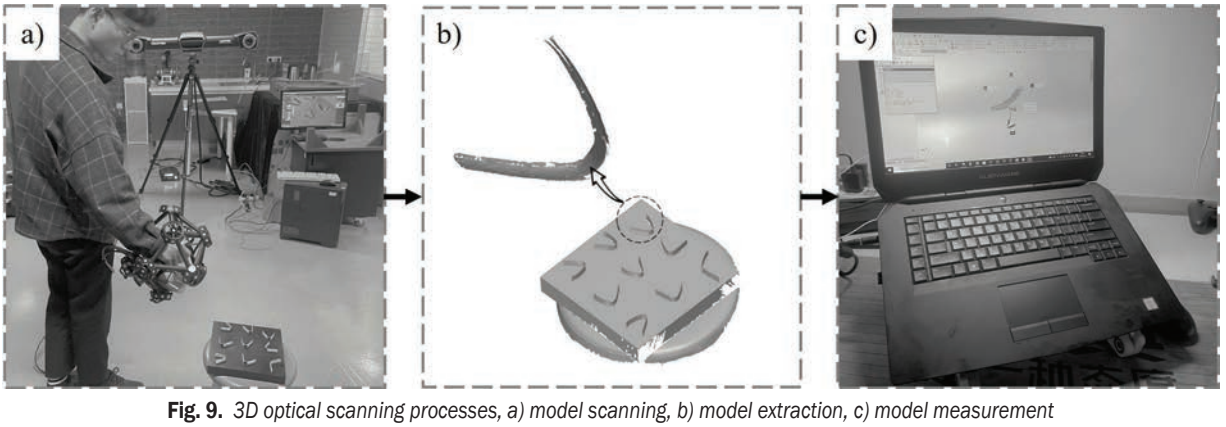

Fig. 9. *3D optical scanning processes, a) model scanning, b) model extraction, c) model measurement*

stresses stored in the material. For each group of five samples, PLA layers were printed at 60 mm/s and 30 mm/s, and TPU layers at 30 mm/s. The other parameters were the same as those shown in Table 2, except for adjusting the PLA printing speed. The experimental method was the same as described before.

An optical 3D scanner (MetraSCAN 3D, Lévis, Canada) was used to measure the folding angle β after deformation for each experiment group, aiming to assess the experimental results more accurately and quantitatively. The samples are removed from the constant temperature water bath, cooled to room temperature, and placed on a scanning test bench to capture the surface shape. The collected data are combined to create a 3D model for quantitative deformation assessment (see Fig. 9).

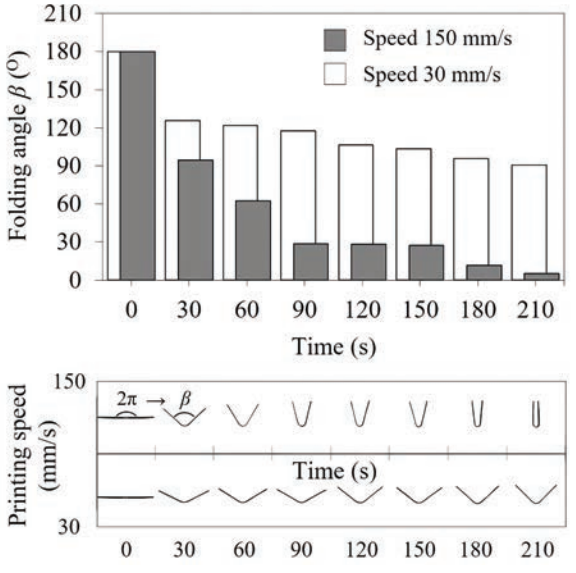

Fig. 10. *Experiment on the influence of PLA layer prestress storage capability on the change of folding angle β*

The average measured results of the folding angle β are shown in Fig. 10. The experimental results indicate the following:

1. Printing PLA materials at faster print speeds allow for more significant stretching polymer chain during extrusion. This approach allows the self-folding rod to maintain higher residual stresses, resulting in a broader range of folding angle variations and stronger drive capability.
2. The folding angle of the self-folding rod gradually decreases as the water bath time increases. Throughout the process, the bending is most evident in the first minute. After three minutes, the self-folding rods no longer produce significant bending, keeping their folding angle stable. Therefore, the folding capability of the self-folding rod continuously decreases with the increased water bath time.

4 MANUFACTURE AND EXPERIMENTS OF THE SELF-FOLDING COMPOSITE VARIABLE-DIAMETER WHEEL STRUCTURE

This section contains two subsections. The self-folding composite variable-diameter wheel structure with an *m* value of 3 is named the M3 structure. First, the M3 structure's manufacturing is discussed, and there are simulations of the design's viability. Second, it creates the prototype and verifies the feasibility of the M3 structural design analysis and self-adjusting wheel diameter under thermal stimulation through experiments.

4.1 Manufacture of Self-Folding Composite Variable-diameter Wheel Structure

The self-folding composite variable-diameter wheel structure is rapid-prototyped using a 3D printer. The M3 structure is constructed with 6 angulated scissor rods, 6 self-folding rods, and 2 outer hubs.

The manufacturing process needs to be described because it contains the drivable self-adjustment of the self-folding structure. The M3 structure's folding angle β variation ranges between 60 ° and 120 °. According to the experimental results provided in the

Table 3. *Manufacturing parameters of the self-folding rods*

Structure parameters	Height, H [mm]	Width, C [mm]	Separation layer width, $L1$ [mm]	Separation layer spacing distance, $L2$ [mm]	Length, L [mm]
	1.2	10	45	10	100

Printing parameters	Number of rod groups, m	Range of folding angle variation of 150 mm/s printing, B [°]	Range of folding angle variation for M3 structure, B [°]	PLA layer printing		TPU layer printing		Printing platform temperature, [°C]
				speed [mm/s]	temperature [°C]	speed [mm/s]	temperature [°C]	
	3	[180°, 5°]	[180°, 120°]	150	235	30	200	30

previous section, the self-folding rod at either of the two printing speeds can meet the design requirements of the M3 structure for the range of folding angle variations. However, in this work, a printing speed parameter of 60 mm/s is used to manufacture the self-folding rod and drive the deformation of the M3 structure to ensure that the structure obtains a significant driving force. The specific manufacturing parameters are shown in Table 3.

The angulated scissor rod and outer hub are 3D printed using a common high-temperature resistant polycarbonate material (Raise Premium, Shanghai, China). The angulated scissor rod's length B is first determined. Eq. (1) is then used to calculate the top angle α of the angulated scissor rod based on the value of m. Eq. (6) and Eq. (8) are used to calculate the radius of the theoretical unfolding and contraction of the circumcircle based on the above two parameters. Because of the thickness K limitation (see Fig. 2a), the structure does not reach the theoretical state. As a result, the radius can be increased appropriately based on the actual situation to determine the appropriate circumcircle unfolding and contraction radius. The actual circumcircle unfolding radius determines the value of R_{max} in the manufacturing of the angulated scissor rod (see Fig. 2a), and the actual circumcircle contraction radius determines the value of R_{min} in the manufacturing of the external hub. The specific manufacturing parameters of the angulated scissor rod and the outer hub in this work are shown in Table 4.

By the above manufacturing parameters, a digital M3 structure model is established, and the drivable self-adjustment of the wheel during travel is verified using Solidworks Motion. The gravitational load is 9806.65 mm/s², indicated by the green arrow. The outer hub with a rotational speed is 5 r/min, indicated by the red arrow. The ground material is chosen to be the same polycarbonate material as the outer hub, with a friction coefficient of 0.29 between each other [22]. A simplified constant force replaces the self-folding rod drive force for ease of calculation with a value of 0.5 N [23], which loads on the surface where the angulated scissor rods bond to the self-folding rods, indicated by the blue arrow. The simulation results indicate that the structure with the above designs can achieve self-folding of the wheel during travel (see Fig. 11).

4.2 Experiments of Self-Folding Composite Variable-diameter Wheel Structure

The M3 structure is manufactured according to the above parameters. The experimental verification conditions and parameter settings are consistent with previous experiments. The experimental contraction procedure is shown in Fig. 12.

Before thermal stimulation, the self-folding rod is flat, and the folding angle β reaches its maximum value. The self-folding structure unfolds in the outer hub, moving under normal wheel diameter conditions. At this moment, the circumcircle diameter of the M3

Table 4. *Manufacturing parameters of the angulated scissor rods and outer hub*

Structure parameters	Number of rod groups m	Top angle α [°]	Circumcircle radius				Side length B [mm]	Thickness K [mm]	Width S [mm]
			Theoretical value		Actual value				
			R_{min} [mm]	R_{max} [mm]	R_{min} [mm]	R_{max} [mm]			
	3	60	60	69.282	62	70	60	3	5

Printing parameters	Printing platform temperature [ºC]	Printing speed [mm/s]	Layer height [mm]	Infill amount	Extrusion width [mm]	Printing temperature [°C]
	110	60	0.2	15%	0.4	235

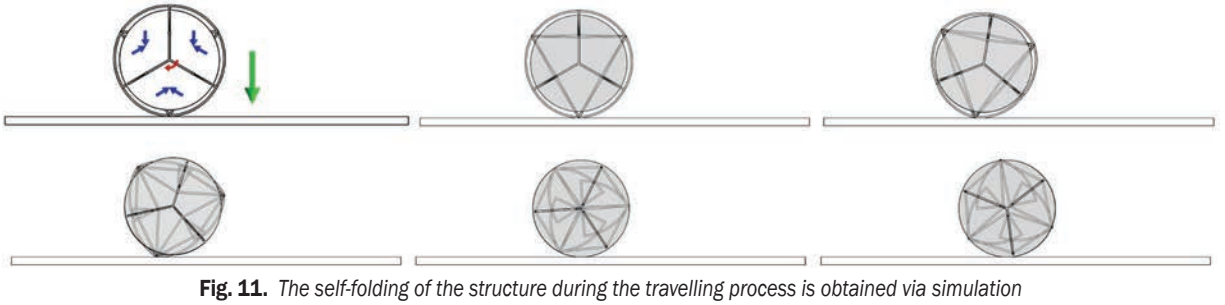

Fig. 11. *The self-folding of the structure during the travelling process is obtained via simulation*

structure is 40 mm (see Fig. 12a). After thermal stimulation, the self-folding rod is controllable bending, and the folding angle β reaches its minimum value. The self-folding structure moves along the outer hub track and into it.

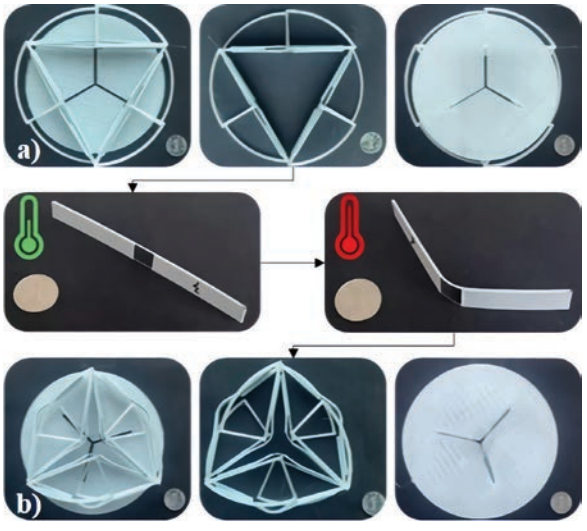

Fig. 12. *Experiments of the self-folding composite variable-diameter wheel structure*

The outer hub is used to achieve movement under contracting wheel diameter conditions. At this moment, the circumcircle diameter of the M3 structure is 124 mm (see Fig. 12 b). The experimental results demonstrate that the structure can realize the self-adjusting wheel diameter under the predetermined thermal stimulation according to the set deformation control method.

5 DISCUSSION AND CONCLUSIONS

Based on 4D printing technology, we have designed a novel self-folding composite variable-diameter wheel structure. Unlike the conventional variable-diameter wheel, its novel self-folding structure combines a control system and a variable-diameter mechanical structure into one. Under predetermined thermal stimulation, the wheel diameter self-adjustment function is activated. Furthermore, we use digital prototype simulations and principle prototype experiments to validate the correctness and feasibility of the design method, theoretical analysis, and deformation control methods.

The design integrates conventional mechanical structure design, smart materials, and manufacture via 4D printing technology. A single mechanical structure design extends to a programmable morphing structure design. Compared to a conventional variable-diameter wheel, the self-folding composite variable-diameter wheel structure designed using this new idea has less structural complexity and control difficulty.

The limitations of realistic application scenarios need to be considered. The self-folding rod within the prototype needs to be redesigned to enable bi-directional self-folding characteristics. The driving force of the self-folding rod must be redesigned to obtain bi-directional self-adjustment of the wheel diameter. The prototype should be tested in unstructured terrain and data collected on speed, time, and centrifugal force to determine parameters such as driving speed.

6 ACKNOWLEDGEMENTS

This work is funded by the National Natural Science Foundation of China (Grant No. 51809 , Beijing Natural Science Foundations (Grant No.3212009 and No.L222038 , and Beijing Municipal Key Laboratory of Space-ground Interconnection and Convergence of China.

7 REFERENCES

[1] Fu, H.X., Li, X.M., Wang, X., Ku, L.Y., Xiao, Z. (2022). Thermal mechanical coupling analysis of a flexible spoke non-pneumatic tire. *Strojniški vestnik - Journal of Mechanical Engineering*, vol. 68, no. 3, p. 143-154, **DOI:10.5545/sv-jme.2021.7401**.

[2] Duan, X., Huang, Q., Li, K. (2015). Design and motion characteristics analysis of small wheel-track-leg composite robot. *Journal of Mechanical Engineering*, vol. 41, no. 8, p. 108-114, **DOI:10.3321/j.issn:0577-6686.2005.08.018**.

[3] Li, Y., Ge, S., Zhu, Hua., Liu, J. (2010). Mechanism and overrunning capability of four-tracked dual-swing arm robot. *Robotics*, vol. 32, no. 2, p. 157-165, **DOI:10.1007/s11771-013-1460-8**.

[4] Jia, Y., Sun, Z., Zheng Y., Li, H., Tao, Z., Zhang, T., Tian, He. (2020). Overview on development of planetary rover technology. *Journal of Deep Space Exploration*, vol. 7, no. 5, p. 419-427, **DOI:10.15982/j.issn.2096-9287.2020.20200031**. (in Chinese)

[5] Lee, D.Y., Kim, S.R., Kim, J.S. (2017). Origami wheel transformer: a variable-diameter wheel drive robot using an origami structure. *Soft Robotics*, vol. 4, no. 2, p. 163-180, **DOI:10.1089/soro.2016.0038**.

[6] Wang, W., Zhang, Z.B., Gao, B.W. (2020). Control of tracking of two-wheeled differential spherical mobile robot. *Journal of Measurement Science and Instrumentation*, vol. 11, no. 3, p. 276-283, **DOI:10.2991/jrnal.2014.1.1.3**.

[7] Ma, N., Li, D.Y., He, W.,Deng, Y., Li, J., Gao, Y., Bao, H., Zhang, H., Xu, X., Liu, Y., Wu, Z., Chen, L. (2021). Future vehicles: interactive wheeled robots. *Science China Information Sciences*, vol. 64, art. ID 156101, **DOI:10.1007/s11432-020-3171-4**.

[8] Zhang, Z.Z., Lv, J.G., Song, B., Guo, S.Y., Gao, F. (2014). Analysis and prospect of non-pneumatic tire technology. *Tire Industry*, vol. 34, no. 9, p. 523-527.

[9] Lee, D.Y., Kim, J.K., Sohn, C.Y., Heo, J.M., Cho, K.J. (2021). High-load capacity origami transformable wheel. *Science Robotics*, vol. 6, no. 53, art. ID abe0201, **DOI:10.1126/scirobotics.abe0201**.

[10] Zhao, Y.Q., Huang, C., Jiang, C. (2013). Modeling and pass ability study of a new mechanical elastic wheel. *China Mechanical Engineering*, vol. 24, no. 6, p. 724-729.

[11] Wang, W., Zhao, Y.G, Jiang, C., Wu, J. (2013). Analysis of mechanical transfer characteristics of a new mechanical elastic wheel. *Journal of Jiangsu University (Natural Science Edition)*, vol. 34, no. 3, p. 261-266, **DOI:10.3969/j.issn.1671-7775.2013.03.003**.

[12] Zang, L.G., Zhao, Y.G., Li, B., Wang, J., Du, X.B. (2014). Analysis of mechanical elastic wheels to improve tire wear resistance and grip. *Journal of Agricultural Engineering*, vol. 30, no. 12, p. 256-263, **DOI:10.3969/j.issn.1002-6819.2014.12.007**.

[13] Park, H.S., Sitti, M. (2009). Compliant footpad design analysis for a bio-inspired quadruped amphibious robot. *2009 IEEE-RSJ International Conference on Intelligent Robots and Systems*, p. 645-651, **DOI:10.1109/IROS.2009.5354680**.

[14] Xie, X.L., Gao, F., Huang, C., Zeng, W. (2017). Design and development of a new transformable wheel used in amphibious all-terrain vehicles (A-ATV). *Journal of Terramechanics*, vol. 69, p. 45-61, **DOI:10.1016/j.jterra.2016.11.001**.

[15] Yin, X.Y., Wang, C.W., XIE, G.M. (2012). A salamander-like amphibious robot system and control design. *2012 IEEE International Conference on Mechatronics and Automation*, p. 956-961, **DOI:10.1109/ICMA.2012.6283272**.

[16] Liu, T., Yu, C.H. (1996). Identification and classification of multi-degree-of-freedom and multi-loop mechanisms. *Journal of Mechanical Design*, vol. 117, no. 1, p. 104-111, **DOI:10.1115/1.2826092**.

[17] van Manen, T., Janbaz, S., Zadpoor, A.A. (2017). Programming 2D/3D shape-shifting with hobbyist 3D printers. *Materials Horizons*, vol. 6, no. 4, p. 1064-1069, **DOI:10.1039/c7mh00269f**.

[18] Kačergis, L., Mitkus, R., Sinapius, M. (2019). Influence of fused deposition modeling process parameters on the transformation of 4D printed morphing structures. *Smart Materials and Structures*, vol. 28, art. ID 105042, **DOI:1088/1361-665X/ab3d18**.

[19] Qi, H.J., Boyce, M.C. (2005). Stress-strain behavior of thermoplastic polyurethanes. *Mechanics of Materials*, vol. 37, no. 8, p. 817-839, **DOI:10.1016/j.mechmat.2004.08.001**.

[20] Kim, K., Park, J., Suh, J.H., Kim, M., Jeong, Y., Park, I. (2017). 3D printing of multiaxial force sensors using carbon nanotube (CNT)/thermoplastic polyurethane (TPU) filaments. *Sensors and Actuators A: Physical*, vol. 263, p. 493-500, **DOI:10.1016/j.sna.2017.07.020**.

[21] Hu, G., Damanpack, A.R., Bodaghi, M., Liao, W.H. (2017). Increasing dimension of structures by 4D printing shape memory polymers via fused deposition modeling. *Smart Materials and Structures*, vol. 26, art. ID 125023, **DOI:10.1088/1361-665X/aa95ec**.

[22] Rubin, A., Gauthier, C., Schirrer, R. (2012). The friction coefficient on polycarbonate as a function of the contact pressure and nanoscale roughness. *Polymer Physics*, vol. 50, no. 8, p. 580-588, **DOI:10.1002/polb.23046**.

[23] Yang, L. (2021). *Shape Memory Behaviors of 4D Printed Angle-Ply Laminated and Rectangular Braided Preforms and Their Composites*. Donghua University, Shanghai.

Vsebina

Strojniški vestnik - Journal of Mechanical Engineering
letnik 69, (2023), številka 3-4
Ljubljana, marec-april 2023
ISSN 0039-2480

Izhaja mesečno

Razširjeni povzetki (extended abstracts)

Strojniški vestnik - Journal of Mechanical Engineering 69(2023)3-4, SI 11

Prejeto v recenzijo: 2022-11-18
Prejeto popravljeno: 2023-01-23
Odobreno za objavo: 2023-03-06

Vpliv enostavne/sestavljene jamičaste teksture na vibracije in hrup zaradi trenja pri valjčnih aksialnih ležajih

Yueyong Wang[2] – Yimin Zhang[2,*] – Yibing Wang[2] – Risheng Long[1]
[1]Inštitut za zanesljivost opreme, Univerza za kemijsko tehnologijo v Shenyangu, Kitajska
[2]Šola za strojništvo, Tehniška univerza v Shenyangu, Kitajska

Za izboljšanje zanesljivosti in obstojnosti valjčnih aksialnih ležajev (VAL) je bil preučen vpliv enostavne/sestavljene jamičaste strukture na tribološke lastnosti ležajev ter na vibracije in hrupnost ležajev zaradi trenja.

Sestavljena jamičasta struktura na gredni podložki je bila ustvarjena z laserskim označevalnikom. Torna sila, vibracijski pospeški in hrup ležajev so bili izmerjeni na univerzalnem preizkuševališču za trenje in obrabo. Analizirane so bile razlike glede trenja, obrabe, vibracij in hrupnosti med površinami z enostavno/sestavljeno jamičasto teksturo in neteksturiranimi površinami.

Preizkusi torne obrabe, vibracij in hrupnosti ležajev so bili opravljeni na univerzalnem preizkuševališču (MMW-1a, Kitajska) s pomočjo večfunkcijskega sistema za merjenje vibracij in hrupa. Preizkuševališče je vključevalo sistem za preizkušanje trenja in obrabe, zajem signalov, analizator idr. za sinhroni zajem signalov trenja, vibracij in hrupa med preizkusom.

Parametri preizkuševališča: sila vzdolžne obremenitve (2600±100 N), vrtilna hitrost (250 vrt/min) in čas preizkusa (11.000 s). Gredna podložka je bila pred vsakim preizkusom najprej stehtana na elektronski tehtnici (točnost 0,1 mg, ponovljivost 0,01 mg). Na jamičasto teksturirano površino je bilo nanesenih 10 mg komercialnega maziva. Vsi preizkusi trenja, obrabe, vibracij in hrupnosti so bili zaradi doslednosti opravljeni po zgornjih korakih. Med preizkusi ni bilo dodano mazalno olje.

Potek torne sile pri VAL je mogoče razdeliti v tri faze. Za stacionarno fazo v pogojih omejenega mazanja (pribl. prvih 4000 s) je značilno kopičenje mazalnega olja v jamicah. V fazi iniciacije in razvoja napak (4000 s do 8000 s) prihaja do delnega drobljenja kontaktne površine, v jamicah pa se nabirajo najlonski prah od obrabe in delci. V fazi rasti napak (8000 s do 11000 s) se poslabša lokalno drobljenje, mazalnega olja postopoma zmanjka in občasno prihaja do mletja na suho.

Izgube zaradi obrabe pri ležajih z enostavno/sestavljeno teksturo so bile znatno manjše in nižje kot pri skupini ležajev z neteksturirano površino. Izguba zaradi obrabe pri skupini G02 je znašala 3,38 mg, kar je najmanj med vsemi preizkušenimi ležaji. Izguba zaradi obrabe pri skupinah G03 in G06 je bila srednje velika ter je znašala 3,9 mg oz. 4,9 mg. Izguba zaradi obrabe pri skupini G07 je znašala 8,08 mg, enako kot pri neteksturirani skupini G08 z izgubo 8,36 mg.

Pri povečanem hrupu so bile frekvence torne sile, signala zvočnega tlaka in signala vibracijskega pospeška približno enake (1500 Hz). Torna sila je tesno povezana z vibracijami in hrupom.

Hrup in vibracije so povezani z nihanji trenja, ki nastanejo zaradi mikroskopskih nepravilnosti na obrabnih površinah, kot so brazde in sloji abradiranih delcev. Enostavne/sestavljene teksturirane kontaktne površine s pravilno geometrijo lažje ujamejo delce od obrabe v jamice. Enostavne in sestavljene jamice tako pomagajo pri zmanjševanju nepravilnosti in hrupa.

Delovna obremenitev ležajev je v večini primerov razmeroma velika. Opravljena je bila primerjava trenja in obrabe za ležaje s teksturiranimi in neteksturiranimi površinami v enakih pogojih (testna obremenitev = 2600 N). Preizkusi trenja in obrabe pod večjimi obremenitvami so bili opravljeni po poznejši nadgradnji opreme.

Enostavne/sestavljene teksturirane površine imajo potencial za absorbiranje vibracij in zmanjšanje hrupnosti. Učinkovito zatirajo samovzbujene vibracije v sistemu tornih parov VAL ter tako zmanjšujejo stopnjo vibracij in hrupa pri teh ležajih.

Ključne besede: valjčni aksialni ležaj, enostavna/sestavljena teksturirana površina, torna sila, obraba, vibracije in hrup zaradi trenja

*Naslov avtorja za dopisovanje: Inštitut za zanesljivost opreme, Univerza za kemijsko tehnologijo v Shenyangu, Shenyang, Kitajska, zhangyimin@syuct.edu.cn

Strojniški vestnik - Journal of Mechanical Engineering 69(2023)3-4, SI 12

Prejeto v recenzijo: 2022-10-02
Prejeto popravljeno: 2023-01-19
Odobreno za objavo: 2023-02-14

Inverzne krivulje - raziskava dveh mehanizmov inverzorjev

Alina Duta[1]* – Iulian Popescu[2] – Ionut Daniel Geonea[1] – Simona-Mariana Cretu[1] – Ludmila Sass[1] – Dragos-Laurentiu Popa[1]

[1] Univerza v Craiovi, Fakulteta za mehaniko, Romunija
[2] Tehniška akademija, Romunija

Raziskovalno področje, ki ga obravnava pričujoči članek, so mehanizmi za generiranje inverznih krivulj.

Mehanizmi inverzorji se uporabljajo v sistemih za dvigovanje in spuščanje, transportnih trakovih, obdelovalnih strojih, vzmetenju električnih koles, hodečih in plezajočih robotih, mehanizmih za generiranje krivulj, prijemalnih rokah, v kinetični svetlobni umetnosti in pri drugih industrijskih mehanizmih. Mehanizmi inverzorji za točno vodenje po premočrtnih ali krožnih poteh imajo to prednost, da nimajo vodil v območju generiranih krivulj.

Zgodovinsko znanje na področju mehanizmov in strojegradnje je neizčrpen vir navdiha za nove tehnične izume.

Vse večje zanimanje za mehanizme inverzorje nas je motiviralo, da smo se lotili tega področja in predlagali variante mehanizmov na podlagi Artobolevskyjevega inverzorja v pogojih blokiranja zaradi pomanjkanja novejših aplikacij inverzorjev, ki bi risali druge krivulje kot premice. Artobolevskyjev inverzor je bil ustvarjen po modelu Crawfordovega inverzorja.

Crawfordov inverzor je bil najprej strukturno in kinematično analiziran s programom ADAMS® za določene dimenzije. Določene so bile vršne vrednosti hitrosti in pospeškov sledilne točke na inverzni krivulji. Te vrednosti so primerne za hitro premikanje objekta v dani položaj oz. umikanje iz njega. Možna je tudi optimizacija za koordiniranje časa delovanja.

S programom ADAMS® sta bili opravljeni kinematična analiza in simulacija štirih inverzorjev, izpeljanih iz Artobolevskyjevega mehanizma, ki rišejo različne začetne krivulje (krožnico, premico, elipso in Arhimedovo spiralo). Zapisali smo enačbe za računanje položaja točk, potrebnih za realizacijo geometrijskega modela v programu ADAMS® s pomočjo metode vektorskih kontur, formule za razdaljo med dvema točkama in specifične enačbe inverznih krivulj. Inverzne krivulje so bile generirane za omejene delovne pogoje zaradi geometrijskih dimenzij in kinematičnih parametrov. Za vse predlagane modele je bila privzeta specifična geometrija. Predstavljeni so vzroki za blokiranje mehanizmov med delovanjem in pogoji za njihovo odpravo. Do blokade je v vseh primerih prišlo zaradi sekanja med direktno krivuljo in krožno trajektorijo, ki jo opisuje točka elementa z vrtilnim gibanjem s konstantnim θ- stopinjskim kotom. Pri direktni krivulji v obliki Arhimedove spirale se je blokiranju mogoče izogniti tako s prilagoditvijo geometrije mehanizma kakor tudi s spremembo parametrov gibanja motorjev. Pridobljene so bile zvezne funkcije hitrosti in pospeševanja.

Poudariti je treba, da so bili ustvarjeni pogoji za celovito študijo gibanja mehanizmov inverzorjev, vključno s študijo dinamike. Ob upoštevanju vse večjega zanimanja raziskovalcev za razvoj aplikacij z mehanizmi inverzorji ter za povečanje nabora ravninskih in prostorskih mehanizmov se izkazuje potreba po ustvarjanju novih mehanizmov, podobnih mehanizmom iz pričujočega članka, ter po analizi njihovega delovanja.

Ključne besede: mehanizem inverzor, zgodovinski mehanizmi, kinematična analiza, položaji blokiranja, računalniška simulacija, program ADAMS®

*Naslov avtorja za dopisovanje: Univerza v Craiovi, Fakulteta za mehaniko, Craiova, 200512, Romunija, alina.duta@edu.ucv.ro

Strojniški vestnik - Journal of Mechanical Engineering 69(2023)3-4, SI 13

Prejeto v recenzijo: 2022-07-01
Prejeto popravljeno: 2022-11-24
Odobreno za objavo: 2023-02-14

Analiza vplivov in optimizacija delovanja sistema za izkoriščanje energije pri odzračevanju pnevmatskih aktuatorjev

Qihui Yu[2,3] – Fengqi Li[1]* – X in Tan[1]

[1] Znanstveno-tehniška univerza Notranje Mongolije, Oddelek za strojništvo, Kitajska
[2] Državni laboratorij v Pekingu za pnevmatsko in termodinamično shranjevanje energije in oskrbo z energijo, Kitajska
[3] Univerza v Nottinghamu, Oddelek za strojništvo, materiale in proizvodni inženiring, Združeno kraljestvo

Izkoristek cilindrov kot najbolj razširjenih aktuatorjev je ključnega pomena za učinkovitost pnevmatskih sistemov. Pri odzračevanju tradicionalnih pogonskih cilindrov se plin iz delovne komore izpušča v ozračje, izkoristek energije pa je posledično slab. V članku je predstavljen predlog krogotoka za izkoriščanje energije izpuščenega zraka, ki lahko izboljša izkoristek pnevmatskih pogonskih sistemov. Glavni cilj je določitev glavnih parametrov, ki vplivajo na delovne lastnosti pnevmatskega aktuatorja s krogotokom za izkoriščanje energije pri odzračevanju. Z ortogonalno analizo in analitičnim hierarhičnim procesom so bile določene optimalne vrednosti glavnih vplivnih parametrov. Cilji optimizacije so bili učinkovitost rabe energije izpuščenega zraka, hitrost gibanja bata in prostornina rezervoarja za dovod plina. Teoretični rezultati so bili nato potrjeni še eksperimentalno. Za dodaten izkoristek energije pri ekspanziji je bilo preučeno tudi časovno krmiljenje odpiranja in zapiranja elektromagnetnega ventila. Energija izpuščenega plina se reciklira in ponovno uporabi za prihranek pri energiji. Članek obravnava naslednje raziskovalne vsebine:

(1) Predstavljen je predlog strategije in sistema za rekuperacijo in izkoriščanje energije zraka, izpuščenega iz pnevmatskih cilindrov. Opredeljen je matematični model sistema. Postavljeno je bilo preizkuševališče za potrditev simulacijskega modela in preučitev dinamičnih lastnosti krogotoka za izkoriščanje energije izpuščenega plina v realnih pogojih.
(2) Matematični modeli so bili pretvorjeni v brezdimenzijske modele, iz katerih so bili pridobljeni glavni parametri, ki vplivajo na delovne karakteristike sistema. Stopnja izkoristka energije izpuščenega zraka pri optimalni kombinaciji parametrov znaša 34,4% .
(3) Za izboljšanje omenjene stopnje izkoristka je bilo določeno zaporedje odpiranja in zapiranja elektromagnetnega ventila in preučene so bile lastnosti gibanja ter učinkovitost izkoriščanja energije pri različnih časovnih zaporedjih odpiranja in zapiranja elektromagnetnega ventila, različnih začetnih dovodnih tlakih plina in različnih prostorninah plinskega rezervoarja.

Predstavljene inovacije:

(1) Predstavljen je predlog novega tipa sistema za rekuperacijo in izkoriščanje energije stisnjenega zraka v pnevmatskih cilindrih;
(2) Vplivni parametri so bili optimizirani z analitičnim hierarhičnim procesom in s sivo korelacijsko analizo;
(3) Energija ekspanzije je bila še dodatno izkoriščena s krmiljenjem časa dovoda zraka.

Članek predstavlja novo tehnično rešitev za rekuperacijo in izkoriščanje energije stisnjenega zraka.

V prihodnjih študijah bo preučena strategija za krmiljenje odpiranja in zapiranja elektromagnetnih ventilov, ki bo še dodatno izboljšala izkoristek energije stisnjenega zraka.

Ključne besede: pnevmatski sistem, izkoriščanje energije izpuščenega zraka, učinkovitost varčevanja z energijo, analitična hierarhija, metoda sive korelacijske analize, energija ekspanzije

*Naslov avtorja za dopisovanje: Znanstveno-tehniška univerza Notranje Mongolije, Oddelek za strojništvo, Baotou 014010, Kitajska, 380264335@qq.com

Strojniški vestnik - Journal of Mechanical Engineering 69(2023)3-4, SI 14

Prejeto v recenzijo: 2022-06-16
Prejeto popravljeno: 2023-01-03
Odobreno za objavo: 2023-02-14

Vpliv kota ukrivljenosti v kanalu z adiabatnim valjem nad nazaj obrnjeno stopnico na magnetohidrodinamično obnašanje ob prisotnosti nanofluida

Djamila Derbal[1]* – Mohamed Bouzit[1] – Abderrahim Mokhefi[2] – Fayçal Bouzit[1]
[1] Univerza za znanost in tehnologijo v Oranu, Alžirija
[2] Univerza Bechar, Fakulteta za znanost in tehnologijo, Alžirija

Cilj te študije je numerično simulirati prisilni laminarni konvektivni tok ob prisotnosti nanodelcev Fe_3O_4 v osnovni tekočini (voda) skozi ukrivljen kanal z nazaj obrnjeno stopnico, ki vsebuje fiksni adiabatni valj, pod nagnjenim magnetnim poljem in z uporabo enofaznega modela nanofluida. Za reševanje enačb, ki urejajo tok obravnavane tekočine, je bila uporabljena metoda končnih elementov. Vpliv kota ukrivljenosti na toplotne in hidrodinamične strukture je bil prikazan za različne vrednosti več kontrolnih parametrov. Tako so bili dokazani vplivi Hartmannovega števila, Reynoldsovega števila, kota nagiba magnetnega polja in koncentracije nanodelcev na termo-magnetnohidrodinamično obnašanje nanofluida. Splošni postopek reševanja je osredotočen na numerične metode. Diskretizacija vladajočih enačb je sestavljena iz pretvorbe diferencialne oblike vladajočih sistemov v diskretno algebrsko obliko, ki opredeljuje vse neznanke v vsaki točki uporabljene mreže. Metoda končnih elementov, ki temelji na Galerkinovi diskretizaciji, se uporablja za reševanje sedanjih problemov zaradi njene prilagodljivosti za kompleksne geometrije z različnimi vrstami mrež na eni strani in enostavnosti uvajanja robnih pogojev v obliki tokov na drugi strani. Uporaba te metode zahteva prepisovanje enačb v integralni obliki. Za vključitev robnih pogojev se uporablja šibka formulacija.

Numerična rešitev poteka v naslednjih korakih: uvedba mreže, aproksimacija odvisnih funkcij, sestava in uporaba robnih pogojev ter končno reševanje globalnega sistema enačb. Mreža, uporabljena za to študijo, ima v celoti trikotno obliko, ki je ob stenah kanala in ob obodu valja izboljšana, da se zagotovi, da je postavitev mreže dobro usklajena s tokom. V preostalem delu kanala pa je bila uvedena nestrukturirana trikotna mreža.

S to študijo so bile dokazane različne točke:

- Povečanje Hartmannovega števila upočasni pretok ferrofluida v ravnem kanalu z nazaj obrnjenim korakom. Vendar pa to povečanje Hartmannovega števila zmanjša povprečno Nusseltovo število v primeru ravnega kanala. Po drugi strani pa povečanje kota ukrivljenosti in intenzivnosti magnetnega polja pospešuje prenos toplote. Zato se povprečno Nusseltovo število izboljša in doseže največjo vrednost pri pravem kotu ukrivljenosti.
- Povečanje stopnje naklonskega kota magnetnega polja pozitivno vpliva na prenos toplote v primeru ravnega kanala z nazaj obrnjeno stopnico. To povečanje dejansko izboljša povprečno Nusseltovo število v tem primeru. Poleg tega naraščanje kota ukrivljenosti kot tudi kota magnetnega polja povečuje konvektivni prenos toplote, razen pri ravnem magnetnem polju, kjer kot ukrivljenosti ne vpliva na prenos toplote.
- Povečanje Reynoldsovega števila povzroči znatno povečanje konvekcijskega prenosa toplote. Poleg tega se s povečanjem kota ukrivljenosti ublaži učinek viskoznih sil, kar še bolj pospeši prenos toplote.
- Dodatek nanodelcev Fe_3O_4 čisti vodi izboljša prenos toplote. V tem primeru se vrednost povprečnega Nusseltovega števila poveča za skoraj 12,5 % v primerjavi z uporabljeno čisto vodo. Vendar pa zaradi nizkih koncentracij, ki so bile vnesene, hidrodinamika nanoproizvoda ni imela velikega vpliva na uporabljene nizke koncentracije.

Ključne besede: prisilna konvekcija, nazaj obrnjen korak, ukrivljen kanal, nepremični valj, ferrofluid, metoda končnih elementov, magnetohidrodinamika

*Naslov avtorja za dopisovanje: Univerza za znanost in tehnologijo v Oranu, Fakulteta za strojništvo, Alžirija, djamila.derbal@univ-usto.dz

Strojniški vestnik - Journal of Mechanical Engineering 69(2023)3-4, SI 15

Prejeto v recenzijo: 2022-07-29
Prejeto popravljeno: 2022-12-12
Odobreno za objavo: 2023-02-22

Vpliv parametrov obdelave na kazalnike kakovosti pri finem poliranju z enim diamantom

Minh-Thai Le[1] – An-Le Van[2,*] – Trung-Thanh Nguyen[3]

[1] Tehniška univerza Le Quy Don, Fakulteta za specialno opremo, Vietnam
[1] Univerza Nguyen Tat Thanh, Tehniška fakulteta, Vietnam
[2] Tehniška univerza Le Quy Don, Fakulteta za strojništvo, Vietnam

Cilj pričujočega dela je optimizacija vhodnih parametrov hitrosti vretena, globine penetracije, podajanja in premera konice orodja za izboljšanje trdote po Vickersu in zmanjšanje povprečne hrapavosti pri novem procesu diamantnega finega poliranja.

Pri operacijah diamantnega finega poliranja se uporabljajo različni načini hlajenja in mazanja, vključno s kriogenim odrezavanjem in mazanjem z minimalno količino maziva (MQL). Kriogeni pristop je žal povezan z dragimi naložbami, medtem ko je največja slabost sistema MQL pri obdelavi jekel visoke trdote, kjer nastaja velika količina toplote, majhna učinkovitost hlajenja in mazanja. Pomembna je tudi izbira optimalnih dejavnikov za izboljšanje kakovosti površin po diamantnem finem poliranju pri uporabi novega hladilno-mazalnega sistema.

Za vhode so predlagani modeli usmerjenih nevronskih mrež z Bayesovo regularizacijo. Za izračun teže odgovorov in iskanje optimuma sta bila uporabljena metoda CRITIC in genetski algoritem z nedominantnim razvrščanjem na podlagi razdelitve mreže.

Izboljšanje povprečne hrapavosti in trdote po Vickersu znaša 40,7 % oz. 7,6 %.

Pristop s kombinacijo nevronske mreže, metode CRITIC in genetskega algoritma z nedominantnim razvrščanjem je uporaben za različne zahtevne optimizacijske probleme. Rezultate optimizacije je mogoče uporabiti za izboljševanje lastnosti fino poliranih površin.

V pričujoči študiji sta bili obravnavani povprečna hrapavost in trdota po Vickersu pri finem poliranju z enim diamantom. V prihodnje bodo obravnavani tudi dejavniki kot so hitrost obrabe, raba energije in velikost zrn.

Predlagano tehniko je mogoče uporabiti tudi za optimizacijo vhodnih parametrov in odgovorov pri drugih procesih diamantnega finega poliranja in obdelave.

Korelacije je mogoče uporabiti za opis kompleksnih podatkov v zvezi s procesom obdelave.

Pridobljeni podatki so uporabni v praktičnih procesih diamantnega finega poliranja za zmanjšanje povprečne hrapavosti ter izboljšanje trdote po Vickersu.

Novi proces diamantnega finega poliranja z MQL in dvojnimi vrtinčnimi cevmi bo neposredno uporaben za izboljševanje lastnosti zunanjih površin v industriji.

Razvite modele je mogoče uporabiti za natančen izračun ciljev obdelave.

Ključne besede: fino poliranje z enim diamantom, povprečna hrapavost, trdota po Vickersu, Bayesova regularizacija, NSGA-G, umetne nevronske mreže, optimumi

*Naslov avtorja za dopisovanje: Univerza Nguyen Tat Thanh, Tehniška fakulteta, 300A Nguyen Tat Thanh, Ho Chi Minh, Vietnam, lvan@ntt.edu.vn

Strojniški vestnik - Journal of Mechanical Engineering 69(2023)3-4, SI 16

Prejeto v recenzijo: 2022-09-05
Prejeto popravljeno: 2023-01-12
Odobreno za objavo: 2023-02-10

Raziskava toplotnih lastnosti CNC-stružnice z dinamično izboljšano posteljo iz epoksi granita, ojačenega z jeklom

Mula Venkata Ramana[1] *– P udukarai Ramaswamy Thyla[1] – Elango Subramanian[2] – Shanmugam Chinnuraj[1]
[1]Tehniški kolidž PSG, Oddelek za strojništvo, Indija
[2] Galaxy Machinery Pvt Ltd, Indija

Polimerni beton oz. epoksi granit se zaradi svojih odličnih dušilnih lastnosti vse bolj uveljavlja pri izdelavi postelj, okvirjev in drugih delov preciznih obdelovalnih strojev. Za doseganje statične togosti, ki je primerljiva s togostjo litoželeznih konstrukcij, se uporabljajo konstrukcije iz epoksi granita, ojačenega z jeklom (SREG). Velike razlike v toplotnih lastnostih jekla in epoksi granita (EG) pa lahko povzročijo tudi povečanje napak pri obdelavi zaradi toplotnih vplivov. V članku so preučene toplotne lastnosti CNC-stružnice, zgrajene z novo dinamično izboljšano posteljo SREG. Podana je primerjava njene zmogljivosti s stružnico s posteljo iz litega železa. Za določitev deformacije v središču orodja (TCP) je bila opravljena eksperimentalna in numerična raziskava v pogojih prostega teka pogona prečnega podajanja (CF).

Lega TCP na revolverju stružnice je povezana predvsem z momentom pogonov za podajanje, zato so bile toplotne lastnosti teh pogonov oz. temperaturni raztezki osi pogonov obravnavani posebej. Metoda za sistematično obravnavo toplotnih lastnosti obdelovalnih strojev je določena v standardu ISO 230-3 z obremenitvenim ciklom, ki ga sestavljajo tri minute delovanja in minuta mirovanja ter se ponavlja 6 ur. Pogonski sistem tri minute izvaja podajanje z največjo hitrostjo 20 m/min brez obremenitve in se nato ustavi za eno minuto. Z obremenitvenim ciklom se analizirajo temperaturni prehodni pojavi v konstrukciji stroja zaradi občasnih oz. ponavljajočih se razmer med obdelavo. Za temperaturne meritve so bila uporabljena temperaturna tipala RTD Pt100, za meritev temperaturnih raztezkov po osi x pa laserski interferometer Renishaw XL80. Podatki o temperaturi so bili shranjeni vsako minuto, podatki o deformacijah pa vsakih 5 m inut s sistemom za zajem podatkov (DAQ).

Rezultati eksperimentov v temperaturni komori (ETVC) so razkrili, da je termična napaka pri CNC-stružnici s posteljo SREG 1,68-krat večja kot pri stružnici s posteljo iz litega železa pri 20 °C in 1,8-krat večja pri 40 °C. Ugotovljeno je bilo, da se toplota, ki nastaja v prečnem pogonu, prevaja na jeklena vodila v postelji SREG, nadaljnji prenos toplote v epoksi-granitni del postelje pa je oviran. Akumulacija toplote v vodilih tako povzroči večjo termično napako. Razvit je bil tudi termomehanski model stroja po metodi končnih elementov. Analitični modeli za oceno generirane toplote in konvekcije so bili uporabljeni kot vhodni podatki za numerično analizo. Rezultati meritev se ujemajo s simulacijami. Eksperimentalno validirani numerični model odpira možnosti preučitve vpliva prostega teka vzdolžnega pogona (LF) ter kombiniranega delovanja pogonov CF in LF na toplotne lastnosti stružnice. Glede na rezultate simulacij je termična napaka pri prostem teku LF 1,3-krat večja od termične napake pri prostem teku CF. Ko sta pogona CF in LF delovala hkrati v prostem teku, je bila termična napaka za 1,9- (CF) oz. 1,4-krat (LF) večja.

Pričujoče delo bo v pomoč raziskovalcem pri razumevanju toplotnih lastnosti obdelovalnih strojev, pri katerih so nekateri deli iz konvencionalnih materialov zamenjani z deli iz alternativnih materialov kot je epoksi granit, ojačen z jeklom. Lahko bo tudi izhodišče za uvajanje primernih metod za preprečevanje termičnih napak.

Ključne besede: precizni obdelovalni stroji, termična napaka, jeklena ojačitev, epoksi granit, temperaturni raztezki, polimerni beton, postelja stružnice, dušenje

*Naslov avtorja za dopisovanje: Tehniški kolidž PSG, Oddelek za strojništvo, Indija, venkataramana048@gmail.com

Strojniški vestnik - Journal of Mechanical Engineering 69(2023)3-4, SI 17

Prejeto v recenzijo: 2022-10-05
Prejeto popravljeno: 2022-12-05
Odobreno za objavo: 2023-02-10

Konstruiranje samozložljivega kolesa variabilnega premera na podlagi tehnologije 4D-tiska

Wencai Zhang[1] – Zhenghao Ge[1] – Duanling Li[2,*]

[1] Znanstveno-tehniška univerza v Shaanxiju, Kolidž za strojništvo in elektrotehniko, Kitajska
[2] Univerza za pošto in telekomunikacije, Šola za avtomatizacijo, Kitajska

Krmilni sistem in konstrukcija konvencionalnih koles variabilnega premera znatno krnita njihovo mobilnost in zanesljivost pri vožnji po nestrukturiranem terenu. S prihodom pametnih materialov in tehnologije 4D-tiska so se pojavile tudi nove rešitve za omenjeni problem. S spremembo razporeditve in geometrijskih parametrov pametnih materialov ter s povezovanjem tehnologije 4D-tiska s tradicionalnim konstruiranjem je mogoče izdelati konstrukcije, ki pri vnaprej določenih pogojih vzbujanja same nadzorujejo deformacijo oz. transformacijo. Statične mehanske konstrukcije je tako mogoče nadgraditi v smeri programirljive preoblikovalnosti. Z opisanim konceptom se je mogoče izogniti pomanjkljivostim konvencionalnih koles spremenljivega premera.

V pričujočem članku je predstavljen predlog samozložljivega kompozitnega kolesa variabilnega premera, izdelanega s tehniko 4D-tiska ter sestavljenega iz samozložljive konstrukcije in zunanjega pesta, ki omogoča samodejno prilagajanje premera pod vplivom temperaturnih nihanj ter tako odpravlja pomanjkljivosti konvencionalnih konstrukcij. Kolo vključuje krmilni sistem in mehansko konstrukcijo variabilnega premera. Predstavljeni sta zasnova in zgradba samozložljivih konstrukcij, s kinematično analizo pa so določeni matematični model in konstrukcijski parametri samodejnega zlaganja. Na podlagi omenjenih študij in analiz lastnosti materiala je bila opravljena raziskava programirljive preoblikovalne konstrukcije in vpliva izdelovalnih parametrov samozložljive palice, ki uravnava zlaganje konstrukcije. Razvita sta bila digitalni model in prototip za preverjanje uporabnosti konstrukcije, validacijo teoretičnih analiz in izvedbo kolesa, ki omogoča samodejno nastavljanje premera pod vplivom temperaturnih sprememb.

Glavni prispevki študije so:

1. Predlog nove konstrukcije kompozitnega samozložljivega kolesa z variabilnim premerom, izdelanega s pomočjo tehnike 4D-tiska. Kolo je zgrajeno iz samozložljive konstrukcije in zunanjega pesta.
2. Kinematična analiza na podlagi metod in načel snovanja mehanskih konstrukcij za določitev matematičnega modela samodejnega zlaganja.
3. Konstruiranje na podlagi programirljivega preoblikovanja ter raziskava vpliva izdelovalnih parametrov za samozložljivo palico, ki uravnava zlaganje konstrukcije.
4. Načrtovanje simulacij in eksperimentov za doseganje samodejnega prilagajanja premera kolesa pod vplivom vnaprej določenih temperaturnih sprememb.

V prihodnjih raziskavah bodo morale biti zajete tudi omejitve v realnih delovnih scenarijih, ki so osredotočene na dve področji:

1. Preoblikovanje samozložljive palice za dvosmerno zlaganje ter izboljšanje pogonske sile za doseganje dvosmernega prilagajanja velikosti kolesa.
2. Izvedba eksperimentov na nestrukturiranem terenu za zajem podatkov o hitrosti, času in centrifugalni sili, s katerimi bo mogoče optimizirati parametre kot je hitrost vožnje.

Ključne besede: samodejno zlaganje, pametni materiali, 4D-tisk, kolo variabilnega premera

*Naslov avtorja za dopisovanje: Znanstveno-tehniška univerza v Shaanxiju, Kolidž za strojništvo in elektrotehniko, Weiyang District, Xi'an, Kitajska, liduanlini@163.com

Guide for Authors

All manuscripts must be in English. Pages should be numbered sequentially. The manuscript should be composed in accordance with the Article Template given above. The suggested length of contributions is 10 to 20 pages. Longer contributions will only be accepted if authors provide justification in a cover letter. For full instructions see the Information for Authors section on the journal's website: http://en.sv-jme.eu .

SUBMISSION:

Submission to SV-JME is made with the implicit understanding that neither the manuscript nor the essence of its content has been published previously either in whole or in part and that it is not being considered for publication elsewhere. All the listed authors should have agreed on the content and the corresponding (submitting) author is responsible for having ensured that this agreement has been reached. The acceptance of an article is based entirely on its scientific merit, as judged by peer review. Scientific articles comprising simulations only will not be accepted for publication; simulations must be accompanied by experimental results carried out to confirm or deny the accuracy of the simulation. Every manuscript submitted to the SV-JME undergoes a peer-review process.

The authors are kindly invited to submit the paper through our web site: http://ojs.sv-jme.eu. The Author is able to track the submission through the editorial process - as well as participate in the copyediting and proofreading of submissions accepted for publication - by logging in, and using the username and password provided.

SUBMISSION CONTENT:

The typical submission material consists of:

- A **manuscript** (A PDF file, with title, all authors with affiliations, abstract, keywords, highlights, inserted figures and tables and references),
- Supplementary files:
  - a **manuscript** in a WORD file format
  - a **cover letter** (please see instructions for composing the cover letter)
  - a ZIP file containing **figures** in high resolution in one of the graphical formats (please see instructions for preparing the figure files)
  - possible **appendicies** (optional), cover materials, video materials, etc.

Incomplete or improperly prepared submissions will be rejected with explanatory comments provided. In this case we will kindly ask the authors to carefully read the Information for Authors and to resubmit their manuscripts taking into consideration our comments.

COVER LETTER INSTRUCTIONS:

Please add a **cover letter** stating the following information about the submitted paper:

1. Paper **title**, list of **authors** and their **affiliations**. **One** corresponding author should be provided.
2. **Type of paper**: original scientific paper (1.01), review scientific paper (1.02) or short scientific paper (1.03).
3. A **declaration** that neither the manuscript nor the essence of its content has been published in whole or in part previously and that it is not being considered for publication elsewhere.
4. State the **value of the paper** or its practical, theoretical and scientific implications. What is new in the paper with respect to the state-of-the-art in the published papers? Do not repeat the content of your abstract for this purpose.
5. We kindly ask you to suggest at least two **reviewers** for your paper and give us their names, their full affiliation and contact information, and their scientific research interest. The suggested reviewers should have at least two relevant references (with an impact factor) to the scientific field concerned; they should not be from the same country as the authors and should have no close connection with the authors.

FORMAT OF THE MANUSCRIPT:

The manuscript should be composed in accordance with the Article Template. The manuscript should be written in the following format:

- A **Title** that adequately describes the content of the manuscript.
- A list of **Authors** and their **affiliations**.
- An **Abstract** that should not exceed 250 words. The Abstract should state the principal objectives and the scope of the investigation, as well as the methodology employed. It should summarize the results and state the principal conclusions.
- 4 to 6 significant **key words** should follow the abstract to aid indexing.
- 4 to 6 **highlights;** a short collection of bullet points that convey the core findings and provide readers with a quick textual overview of the article. These four to six bullet points should describe the essence of the research (e.g. results or conclusions) and highlight what is distinctive about it.
- An **Introduction** that should provide a review of recent literature and sufficient background information to allow the results of the article to be understood and evaluated.
- A **Methods** section detailing the theoretical or experimental methods used.
- An **Experimental section** that should provide details of the experimental set-up and the methods used to obtain the results.
- A **Results** section that should clearly and concisely present the data, using figures and tables where appropriate.
- A **Discussion** section that should describe the relationships and generalizations shown by the results and discuss the significance of the results, making comparisons with previously published work. (It may be appropriate to combine the Results and Discussion sections into a single section to improve clarity.)
- A **Conclusions** section that should present one or more conclusions drawn from the results and subsequent discussion and should not duplicate the Abstract.
- **Acknowledgement** (optional) of collaboration or preparation assistance may be included. Please note the source of funding for the research.
- **Nomenclature** (optional). Papers with many symbols should have a nomenclature that defines all symbols with units, inserted above the references. If one is used, it must contain all the symbols used in the manuscript and the definitions should not be repeated in the text. In all cases, identify the symbols used if they are not widely recognized in the profession. Define acronyms in the text, not in the nomenclature.
- **References** must be cited consecutively in the text using square brackets [1] and collected together in a reference list at the end of the manuscript.
- **Appendix(-icies)** if any.

SPECIAL NOTES

Units: The SI system of units for nomenclature, symbols and abbreviations should be followed closely. Symbols for physical quantities in the text should be written in italics (e.g. *v*, *T*, *n*, etc.). Symbols for units that consist of letters should be in plain text (e.g. ms^{-1}, K, min, mm, etc.). Please also see: http://physics.nist.gov/cuu/pdf/sp811.pdf .

Abbreviations should be spelt out in full on first appearance followed by the abbreviation in parentheses, e.g. variable time geometry (VTG). The meaning of symbols and units belonging to symbols should be explained in each case or cited in a **nomenclature** section at the end of the manuscript before the References.

Figures (figures, graphs, illustrations digital images, photographs) must be cited in consecutive numerical order in the text and referred to in both the text and the captions as Fig. 1, Fig. 2, etc. Figures should be prepared without borders and on white grounding and should be sent separately in their original formats. If a figure is composed of several parts, please mark each part with a), b), c), etc. and provide an explanation for each part in Figure caption. The caption should be self-explanatory. Letters and numbers should be readable (Arial or Times New Roman, min 6 pt with equal sizes and fonts in all figures). Graphics (submitted as supplementary files) may be exported in resolution good enough for printing (min. 300 dpi) in any common format, e.g. TIFF, BMP or JPG, PDF and should be named Fig1.jpg, Fig2.tif, etc. However, graphs and line drawings should be prepared as vector images, e.g. CDR, AI. Multi-curve graphs should have individual curves marked with a symbol or otherwise provide distinguishing differences using, for example, different thicknesses or dashing.

Tables should carry separate titles and must be numbered in consecutive numerical order in the text and referred to in both the text and the captions as Table 1, Table 2, etc. In addition to the physical quantities, such as *t* (in italics), the units [*s*] (normal text) should be added in square brackets. Tables should not duplicate data found elsewhere in the manuscript. Tables should be prepared using a table editor and not inserted as a graphic.

REFERENCES:

A reference list must be included using the following information as a guide. Only cited text references are to be included. Each reference is to be referred to in the text by a number enclosed in a square bracket (i.e. [3] or [2] to [4] for more references; do not combine more than 3 references, explain each). No reference to the author is necessary.

References must be numbered and ordered according to where they are first mentioned in the paper, not alphabetically. All references must be complete and accurate. Please add DOI code when available. Examples follow.

Journal Papers:

Surname 1, Initials, Surname 2, Initials (year). Title. *Journal*, volume, number, pages, DOI code.

[1] Hackenschmidt, R., Alber-Laukant, B., Rieg, F. (2010). Simulating nonlinear materials under centrifugal forces by using intelligent cross-linked simulations. *Strojniški vestnik - Journal of Mechanical Engineering,* vol. 57, no. 7-8, p. 531-538, DOI:10.5545/sv-jme.2011.013.

Journal titles should not be abbreviated. Note that journal title is set in italics.

Books:

Surname 1, Initials, Surname 2, Initials (year). Title. Publisher, place of publication.

[2] Groover, M.P. (2007). *Fundamentals of Modern Manufacturing*. John Wiley & Sons, Hoboken.

Note that the title of the book is italicized.

Chapters in Books:

Surname 1, Initials, Surname 2, Initials (year). Chapter title. Editor(s) of book, book title. Publisher, place of publication, pages.

[3] Carbone, G., Ceccarelli, M. (2005). Legged robotic systems. Kordić, V., Lazinica, A., Merdan, M. (Eds.), Cutting Edge Robotics. Pro literatur Verlag, Mammendorf, p. 553-576.

Proceedings Papers:

Surname 1, Initials, Surname 2, Initials (year). Paper title. Proceedings title, pages.

[4] Štefanić, N., Martinčević-Mikić, S., Tošanović, N. (2009). Applied lean system in process industry. *MOTSP Conference Proceedings*, p. 422-427.

Standards:

Standard-Code (year). Title. Organisation. Place.

[5] ISO/DIS 16000-6.2:2002. *Indoor Air – Part 6: Determination of Volatile Organic Compounds in Indoor and Chamber Air by Active Sampling on TENAX TA Sorbent, Thermal Desorption and Gas Chromatography using MSD/FID.* International Organization for Standardization. Geneva.

WWW pages:

Surname, Initials or Company name. Title, from http://address, date of access.

[6] Rockwell Automation. Arena, from *http://www.arenasimulation.com,* accessed on 2009-09-07.

EXTENDED ABSTRACT:

When the paper is accepted for publishing, the authors will be requested to send an **extended abstract** (approx. one A4 page or 3500 to 4000 characters or approx. 600 words). The instruction for composing the extended abstract are published on-line: http://www.sv-jme.eu/information-for-authors/ .

COPYRIGHT:

Authors submitting a manuscript do so on the understanding that the work has not been published before, is not being considered for publication elsewhere and has been read and approved by all authors. The submission of the manuscript by the authors means that the authors automatically agree to publish the paper uder CC-BY 4.0 Int. or CC-BY-NC 4.0 Int. when the manuscript is accepted for publication. All accepted manuscripts must be accompanied by a Copyright Agreement, which should be sent to the editor. The work should be original work by the authors and not be published elsewhere in any language without the written consent of the publisher. The proof will be sent to the author showing the final layout of the article. Proof correction must be minimal and executed quickly. Thus it is essential that manuscripts are accurate when submitted. Authors can track the status of their accepted articles on https://en.sv-jme.eu/.

PUBLICATION FEE:

Authors will be asked to pay a publication fee for each article prior to the article appearing in the journal. However, this fee only needs to be paid after the article has been accepted for publishing. The fee is 380 EUR (for articles with maximum of 6 pages), 470 EUR (for articles with maximum of 10 pages), plus 50 EUR for each additional page. The additional cost for a color page is 90.00 EUR (only for a journal hard copy; optional upon author's request). These fees do not include tax.

Strojniški vestnik -Journal of Mechanical Engineering
Aškerčeva 6, 1000 Ljubljana, Slovenia, e-mail: info@sv-jme.eu

ISSN 0039-2480

http://www.sv-jme.eu

Contents

Papers